Study on the effect of the environment on internal fatigue crack propagation in Ti-6Al-4V

Louis Hébrard

N° d'ordre NNT : 2023ISAL0120

THÈSE de DOCTORAT DE L'INSA DE LYON
membre de l'Université de Lyon

Opérée au sein de

l'Institut National des Sciences Appliquées de Lyon

École doctorale : **ED n°34 - Matériaux de Lyon**
Spécialité de doctorat : **Matériaux**

Soutenue publiquement le 21 décembre 2023, par :

Louis Hébrard

Study on the effect of the environment on internal fatigue crack propagation in Ti-6Al-4V

Devant le jury composé de :

Véronique Aubin	Professeure des Universités *CentraleSupelec, Gif-sur-Yvette*	Présidente
Nathalie Limodin	Directrice de Recherche *CNRS, LaMcube, Centrale Lille*	Rapporteuse
Jonathan Cormier	Maître de Conférences - HDR *Institut P', ISAE-ENSMA, Poitiers*	Rapporteur
Charles Mareau	Maitre de Conférences *LAMPA, Arts & Métiers Sciences et Technologies, Angers*	Examinateur
Cédric Doudard	Professeur - HDR *ENSTA Bretagne, IRDL, Brest*	Examinateur
Jean-Yves Buffiere	Professeur des Universités *Matéis, INSA Lyon, Villeurbanne*	Directeur de thèse
Thierry Palin-Luc	Professeur des Universités *I2M, Arts & Métiers Sciences et Technologies, Bordeaux*	Directeur de thèse
Nicolas Ranc	Professeur des Universités *PIMM, Arts & Métiers Sciences et Technologies, Paris*	Directeur de thèse

INSTITUT NATIONAL DES SCIENCES APPLIQUÉES LYON

Département de la Formation par la Recherche et des Études Doctorales (**FEDORA**)

Bâtiment INSA direction, 1er étage
37, av. J. Capelle
69621 Villeurbanne Cédex
fedora@insa-lyon.fr

Référence : TH1050_HEBRARD Louis

L'INSA Lyon a mis en place une procédure de contrôle systématique via un outil de détection de similitudes (logiciel Compilatio). Après le dépôt du manuscrit de thèse, celui-ci est analysé par l'outil. Pour tout taux de similarité supérieur à 10%, le manuscrit est vérifié par l'équipe de FEDORA. Il s'agit notamment d'exclure les auto-citations, à condition qu'elles soient correctement référencées avec citation expresse dans le manuscrit.

Par ce document, il est attesté que ce manuscrit, dans la forme communiquée par la personne doctorante à l'INSA Lyon, satisfait aux exigences de l'Etablissement concernant le taux maximal de similitude admissible.

INSA LYON
Campus LyonTech La Doua
20, avenue Albert Einstein - 69621 Villeurbanne cedex - France
Tél. +33 (0)4 72 43 83 83 - Fax +33 (0)4 72 43 85 00
www.insa-lyon.fr

membre de UNIVERSITÉ DE LYON

Département FEDORA – INSA Lyon - Ecoles Doctorales

SIGLE	ECOLE DOCTORALE	NOM ET COORDONNEES DU RESPONSABLE
CHIMIE	**CHIMIE DE LYON** **https://www.edchimie-lyon.fr** Sec. : Renée EL MELHEM Bât. Blaise PASCAL, 3e étage secretariat@edchimie-lyon.fr	**M. Stéphane DANIELE** C2P2-CPE LYON-UMR 5265 Bâtiment F308, BP 2077 43 Boulevard du 11 novembre 1918 69616 Villeurbanne **directeur@edchimie-lyon.fr**
E.E.A.	**ÉLECTRONIQUE, ÉLECTROTECHNIQUE, AUTOMATIQUE** **https://edeea.universite-lyon.fr** Sec. : Stéphanie CAUVIN Bâtiment Direction INSA Lyon Tél : 04.72.43.71.70 secretariat.edeea@insa-lyon.fr	**M. Philippe DELACHARTRE** INSA LYON Laboratoire CREATIS Bâtiment Blaise Pascal, 7 avenue Jean Capelle 69621 Villeurbanne CEDEX Tél : 04.72.43.88.63 **philippe.delachartre@insa-lyon.fr**
E2M2	**ÉVOLUTION, ÉCOSYSTÈME, MICROBIOLOGIE, MODÉLISATION** **http://e2m2.universite-lyon.fr** Sec. : Bénédicte LANZA Bât. Atrium, UCB Lyon 1 Tél : 04.72.44.83.62 secretariat.e2m2@univ-lyon1.fr	**Mme Sandrine CHARLES** Université Claude Bernard Lyon 1 UFR Biosciences Bâtiment Mendel 43, boulevard du 11 Novembre 1918 69622 Villeurbanne CEDEX **sandrine.charles@univ-lyon1.fr**
EDISS	**INTERDISCIPLINAIRE SCIENCES-SANTÉ** **http://ediss.universite-lyon.fr** Sec. : Bénédicte LANZA Bât. Atrium, UCB Lyon 1 Tél : 04.72.44.83.62 secretariat.ediss@univ-lyon1.fr	**Mme Sylvie RICARD-BLUM** Institut de Chimie et Biochimie Moléculaires et Supramoléculaires (ICBMS) - UMR 5246 CNRS - Université Lyon 1 Bâtiment Raulin - 2ème étage Nord 43 Boulevard du 11 novembre 1918 69622 Villeurbanne Cedex Tél : +33(0)4 72 44 82 32 **sylvie.ricard-blum@univ-lyon1.fr**
INFOMATHS	**INFORMATIQUE ET MATHÉMATIQUES** **http://edinfomaths.universite-lyon.fr** Sec. : Renée EL MELHEM Bât. Blaise PASCAL, 3e étage Tél : 04.72.43.80.46 infomaths@univ-lyon1.fr	**M. Hamamache KHEDDOUCI** Université Claude Bernard Lyon 1 Bât. Nautibus 43, Boulevard du 11 novembre 1918 69 622 Villeurbanne Cedex France Tél : 04.72.44.83.69 **hamamache.kheddouci@univ-lyon1.fr**
Matériaux	**MATÉRIAUX DE LYON** **http://ed34.universite-lyon.fr** Sec. : Yann DE ORDENANA Tél : 04.72.18.62.44 yann.de-ordenana@ec-lyon.fr	**M. Stéphane BENAYOUN** Ecole Centrale de Lyon Laboratoire LTDS 36 avenue Guy de Collongue 69134 Ecully CEDEX Tél : 04.72.18.64.37 **stephane.benayoun@ec-lyon.fr**
MEGA	**MÉCANIQUE, ÉNERGÉTIQUE, GÉNIE CIVIL, ACOUSTIQUE** **http://edmega.universite-lyon.fr** Sec. : Stéphanie CAUVIN Tél : 04.72.43.71.70 Bâtiment Direction INSA Lyon mega@insa-lyon.fr	**M. Jocelyn BONJOUR** INSA Lyon Laboratoire CETHIL Bâtiment Sadi-Carnot 9, rue de la Physique 69621 Villeurbanne CEDEX **jocelyn.bonjour@insa-lyon.fr**
ScSo	**ScSo*** **https://edsciencessociales.universite-lyon.fr** Sec. : Mélina FAVETON INSA : J.Y. TOUSSAINT Tél : 04.78.69.77.79 melina.faveton@univ-lyon2.fr	**M. Bruno MILLY** Université Lumière Lyon 2 86 Rue Pasteur 69365 Lyon CEDEX 07 **bruno.milly@univ-lyon2.fr**

*ScSo : Histoire, Géographie, Aménagement, Urbanisme, Archéologie, Science politique, Sociologie, Anthropologie

Acknowledgements

Au moment où j'écris ces lignes de remerciements, je ne réalise pas encore que ces trois grosses années, passées au laboratoire Matéis et à Lyon, sont terminées. Ce que je réalise toutefois, c'est que de nombreuses personnes m'ont accompagné durant ce travail. Je vais tenter de remercier dans ces quelques paragraphes l'ensemble de ces rencontres qui m'ont permis de passer une thèse à la fois riche scientifiquement, mais aussi très agréable humainement.

Tout d'abord, je tiens à remercier les membres du jury qui ont accepté d'évaluer mes travaux. Merci beaucoup pour les échanges aussi bienveillants que scientifiquement poussés que nous avons pu avoir lors de ma soutenance. Je suis sûr que les perspectives à mon travail que nous avons soulevé ensemble à cette occasion sont en train de germer dans la tête de mes directeurs pour des travaux futurs. Un grand merci à Nathalie Limodin et Jonathan Cormier pour avoir rapporté mon travail avec précision. Merci aussi à Véronique Aubin d'avoir présidé le jury, Cédric Doudard (heureux de savoir que vous ne voyez plus un faciès de la même manière après avoir lu ma thèse) et Charles Mareau.

Un énorme merci à mes trois directeurs de thèse ! C'était un réel plaisir de travailler avec vous car vous êtes très complémentaires, mais aussi (surtout) car je ressentais que vous éprouviez un réel plaisir à travailler ensemble ce qui rendait nos interactions très sympas (et donc très efficace, je pense). J'ai vraiment apprécié venir travailler à Paris ou à Bordeaux. Pour cela, merci Thierry de m'avoir accueilli à I2M lors de mes quelques séjours. Je retiendrais ta rigueur à toute épreuve (même à 4h du mat' au synchrotron !) mais aussi la disponibilité que tu me consacrais malgré ton emploi du temps de ~~ministre~~ directeur de labo. Nicolas, merci pour tes explications patientes de phénomènes physiques qui m'étaient assez obscurs (notamment sur l'aspect thermique de mon travail) ainsi que pour les stocks de chocolat nécessaires pour faire tourner comme il se doit une manip synchrotron. Enfin, Jean-Yves, c'était un immense plaisir de travailler avec toi au quotidien. Les sessions de questions/réponses à ton bureau vont me manquer, tout comme ta bonne humeur et tes bons conseils. Je regrette un peu que nous ne soyons pas partis en conf' ensemble, mais ça n'est que partie remise !
Je croise les doigts pour que vous trouviez un doctorant ou une doctorante afin de poursuivre ces travaux et cette collaboration très fructueuse. Pour cette raison, j'ai essayé de détailler ce manuscrit du mieux que j'ai pu afin d'accompagner le plus possible le prochain ou la prochaine.

D'ailleurs, message pour cette hypothétique personne : n'hésite pas à me contacter si certains points ne sont pas très clairs, tout comme j'ai pu le faire avec Alexandre et Arnaud dont j'ai pris la suite et que je remercie pour leurs coups de mains éclairants lorsque j'avais besoin de détails au début de mon travail.

De manière plus générale, l'ensemble des données et des observations sur lesquelles sont basées les résultats présentés dans ce manuscrit sont le fruit d'un travail réalisé avec l'aide de nombreuses personnes. Notamment, je tiens à remercier Marta et Andrew, les *local contacts* à l'ESRF et à SOLEIL, mais aussi toutes les personnes m'ayant aidé lors des manips aux synchrotrons comme Ian (et ta passion pour Shohei), Matthieu (c'était toujours un plaisir d'avoir ton avis sur mes manips) ou Yves (merci de m'avoir expliqué ta vision de vieux routard de la fatigue), mais aussi Shawn, Viet Duc, Nicolas S, Mohamed, Vincent, Ruben, Milkhail et Guillaume ainsi que Maël, Florian et Julien dont je reparlerais ci-dessous.
Ces manips synchrotrons ont pu voir le jour grâce à l'aide d'Arnaud Weck (pour les entailles internes), de Florian M (pour l'aide sur le SPS) et de Jonathan M (pour le support technique à I2M) que je remercie chaleureusement. Tout comme Thierry Douillard avec qui on a passé du temps (toi encore plus que moi) devant le FIB puis le MEB pour faire du TKD. Mais aussi Nic (observations MET), Sylvain (calculs de facteurs de Schmid) et Bérangère (coupe polie à l'Illion) qui m'ont permis de post-traiter du mieux possible ces données.

Ces trois années seront inoubliables aussi en raison des nombreuses personnes rencontrées qui contribuent à l'ambiance très conviviale au laboratoire Matéis. Certaines m'ont donné, en plus, quelques coups de mains scientifiques comme Sophie (tu m'as autant aidé sur l'identification des macles que compliqué la vie devant un baby-foot), Joël (merci pour l'aide sur cette magie noire qu'est Linux), Jérôme (merci pour la tomo) ou Hélène qui fournit un support administratif (tout comme tes deux prédécesseures Frida et Véronique) ainsi que des discussions toujours sympas et détendues + de très bons cakes aux pommes !

Cette ambiance chaleureuse va probablement être la partie de mon quotidien qui va le plus me manquer et notamment mes cobureaux de qualité comme ma chère Justine (ou JuTo pour les intimes) ! Merci d'avoir partagé mon bureau pendant la majorité de nos thèses respectives (et ce, malgré les confinements, couvre-feux et déménagements !). Les petites discussions, nos poissons, les pauses dej en manif, les raccourcis Python, les vidéos de David Castello-Lopes sont autant de petits détails qui me donnaient envie d'aller au taf tous les matins. En parlant de poissons, ils te doivent aussi beaucoup à toi, Maël, mon deuxième bordelais préféré (faut pas que je me fâche avec TPL). Florian, tu as partagé mon bureau la dernière année, mais on a aussi partagé un directeur de thèse trois ans durant. C'était un plaisir de côtoyer tes pauses méditations, ton calme à toute épreuve allant de pair avec le temps que tu prends à finir ton assiette le midi. Mon brave Vié, tu étais toujours au top, surtout pour réparer ton vélo à toute heure du jour ou de la nuit. Je me rappellerai de ces quelques jours partagés chez Michel ponctués de paragraphes rédigés, d'attaques de Pogacar et de plongeons dans la piscine. Merci

aussi à tous mes autres cobureaux : Alex (it was a pleasure to watch you learn more French words than I did in Romanian), Felipe, Lucia, Esther, Camille et Marion.

Certains collègues n'étaient pas dans le même bureau que moi, mais ils n'en restaient pas moins contributeurs de la bonne ambiance générale. Dédicace aux voisins d'à côté, mes trois darteurs Sam, Julien et ChicheBoy Jr. Les doctorants de la même promo que moi, Théotime (on s'est bien amusés à organiser le team-building en compagnie de Florian), Vito et Yohan. Ma team *NBA watching party* le soir au labo : Adam et Jordan. Bonne chance aux nouveaux, Erwan, Sarah, Ronan, Matthieu et Paul. Profitez bien avant de devenir des vieux comme Arnaud Allera, Laurabelle (team tennis), Monzey, Quentin Saby et Ce.

Enfin un énorme merci à l'ensemble des autres personnes croisées à Matéis et qui m'on permis de passer trois années très agréables ; pêle-mêle : merci à Louis et Mathilde (souvenir de l'Ebbelwei Express), Maureen (bon courage à toi vu les cobureaux avec lesquels tu te retrouves), Fantou et la Fourne (beaux moments de lutte !), Xavier (petit prince du baby-foot), Bassem, Pierre-Antoine, Stéphanie, Quentin Gaillard, Michel (merci pour la semaine à nous confier ta maison - *cf.* plus haut), Eric (en souvenir des Cliffs de Moher), Aude, Aurore, Justine P, Lucas, Laura, Carole, Christophe, Patrice, Joël C, Véronique M, Masato et Benjamin ainsi que Hugo, Trunal et Simon d'I2M.

Un gros merci à mes amis d'avant la thèse, s'étalant du bqq de prépa jusqu'aux potes d'école. Dédicace à ma team tandoori (merci Mathilde, Lala et Tatane). Merci Francis (souvenirs d'une belle école d'été FabAdd sur le plateau !), Lucas et Sacha. Ainsi qu'une grosse pensée pour Antonin. Énorme remerciement à mes amis de Lyon (ceux qui n'ont rien à voir avec une thèse ou un labo de matériau) et notamment mes voisins et colocataires comme Marty, Marlon, Antwo et surtout le Chef Cantoro, tu m'as accompagné pendant 2 ans et demi lyonnais remplis de très bons moments.

Un remerciement spécial à toutes celles et ceux qui ne liront probablement jamais ce manuscrit, mais qui ont aussi contribué à leur manière à ces trois belles années : les gars de Champigny, les basketteurs de la Casi, Marwan, Lorenzo, Coach T. Lippens, Carbinche & Jam, le guépard, Boy Blue, Victor, Giannis, Nikola, Marine & Gaby, Youss, Zaho, Julien, Harry, Quillian et Yass.

Enfin, une énorme pensée à ma famille qui me soutient depuis toujours. J'espère que vous comptez sur moi autant que je tiens à vous ! Merci Suzanne, Guillaume, Cécile, Maguy, Marie, Paul, Anne et Inès. Une bise à Marie-Annick. Merci aux JJJ (Joohee, Jean-Marie et Julien) pour votre soutien le jour J.

Merci du fond du ♡, Léna ! On a quasiment réussi nos thèses à 2h24 de TER l'un de l'autre (ça n'est plus qu'une question de semaines au moment où j'écris ces lignes). J'ai hâte de partir vers de nouvelles aventures avec toi !

Summary

In the Very High Cycle Fatigue regime (fatigue lives longer than 10^7 cycles), fatigue cracks tend to initiate internally. This makes visual detection impossible during maintenance operations. Consequently, engineers need robust fatigue datasets to prevent such internal crack initiations that may lead to the fracture of a critical part. To obtain such data, in-situ experimental techniques are developed. In particular, micro-computed tomography allows to acquire direct images of internal fatigue cracks. In this study, a combination of in-situ micro-tomography and ultrasonic fatigue cycling has been applied to specimens that contain an internal sharp notch to study the propagation of internal fatigue cracks. More precisely, the crack shape of internal fatigue cracks has been monitored in 3D at different instants of their propagation up to the Very High Cycle Fatigue regime.

Some internal notches have been linked to the specimen surface given access to the ambient atmosphere. This was done to study the influence of the environment on internal fatigue cracks. This experimental procedure allowed to acquire for the first time, in-situ observations of internal fatigue cracks propagating with and without air in a Ti64 alloy. Temperature measurements were also carried out to evaluate the effect of the environment on the plasticity at the crack tip. Finally, the fatigue data obtained at ultrasonic frequencies allowed to evaluate the influence of the cycling frequency on the crack growth rates.

Contents

Introduction

The fatigue phenomenon is a crucial aspect to consider during the design of the metallic parts of a mechanical system [SCH 09]. To do so, many engineers use the concept of fatigue limit, the maximum stress amplitude - for a given mean stress - under which the parts theoretically have infinite fatigue lives. With the development of ultrasonic fatigue testing machines, the Very High Cycle Fatigue (VHCF) regime (*i.e.* fatigue lives beyond 10^7 cycles) could be extensively studied by many researchers who demonstrated that fatigue failures eventually occur in metallic alloys under stress levels equal to or lower than the fatigue limit [BAT 99]. It was also observed by many scientists that, for such low values of applied stress amplitude leading to very high numbers of cycles, fatigue crack initiation usually occurs in the bulk of the fatigue specimens (or industrial components). Such observations have been reported also for metallic materials without internal defects (porosities, inclusions, etc.) such as forged titanium alloys [NIK 16b, YOS 16a]. From an industrial perspective, internal fatigue crack initiation is critical because it is invisible to the classic visual surface inspection methods which are used to detect initiated fatigue cracks during maintenance inspections. This can be illustrated by some examples of critical component failure as shown in Figure 1 on a steel train axle [KLI 13] and a Ti64 fan hub of a turbojet engine [BEA 20] (other VHCF fracture examples are reported in the literature such as a compressor disk of an aircraft engine [SHA 23]). Even if most of these events resulted only in material casualties, they illustrate the fact that robust fatigue datasets are needed to prevent fractures provoked by internal fatigue cracks from happening.

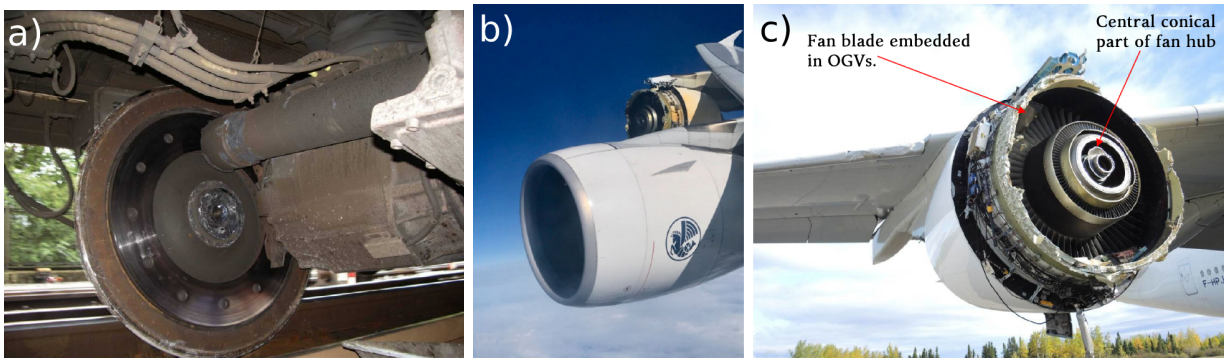

Figure 1 | **Examples of component failure due to internal fatigue crack initiation and propagation** (a) Fracture of a 34CrNiMo6 steel axle of a German high-speed train. As the initiation location has not been properly identified, this fatigue fracture is supposed to be subsurface initiated because of the presence of numerous non-metallic inclusions in the initiation region [KLI 13]. (b) & (c) Fracture of a Ti64 part from an Airbus A380 motor which occured during the flight. The analyses concluded on an internal fatigue crack initiation in the Very High Cycle Fatigue regime enhanced by dwell fatigue [BEA 20].

For this purpose, some recent studies are focused on the development of in-situ experimental techniques such as temperature monitoring [KRE 13, RAN 22], evaluation of the cycling system nonlinearities [KUM 09], X-ray radiography [LIU 11] or X-ray micro-computed tomography [CHA 15, YOS 16a, MES 19, JUN 23] to study internal fatigue crack initiation and propagation. Among these methods, the use of X-rays is the only way to directly observe internal cracks in a non-destructive way. The present study on internal fatigue cracks will extensively use this technique with synchrotron X-rays.

Literature reports much evidence of the effect of the environment on the fatigue behavior of metallic alloys. The cracks propagating in air present shorter fatigue lives and faster growth rates than fatigue cracks propagating in vacuum [HEN 23]. Since internally initiated cracks are not in contact with the ambient atmosphere (until they reach the specimen surface), the environment in which they propagate might explain the differences with surface cracks concerning fatigue lives and crack growth rates.

To adapt internal fatigue crack observation tests to the constraints of a synchrotron experiment, an internal notching procedure will be employed to foster internal fatigue crack initiation. Also, as studying internal fatigue cracks raises the topic of the environment effect, an adaptation of this notching procedure will be employed to artificially bring air molecules to the artificial internal notch in order to evaluate the environment influence on fatigue properties of internal cracks.

Hence, this work is based on an experimental protocol that combines in-situ micro-computed tomography and internally notched specimens to carry out the first in-situ observations of in-

ternal cracks propagation in Ti64 with and without air in order to collect fatigue data to help understand the effect of environment on internal fatigue crack propagation in Ti64.

This PhD thesis has been built as the continuation of two previous PhD theses which were realized in parallel and funded by the French National Research Agency (GIGADEF ANR project, grant number ANR-16-CE08-0039). Alexandre Messager's thesis was focused on a cast aluminum alloy and allowed to develop a first version of the machine used in the present study to carry out ultrasonic cycling tests with in-situ synchrotron micro-tomography [MES 20]. Arnaud Junet's thesis focused on low frequency cycling of internally notched Ti64 specimens also with in-situ synchrotron micro-tomography monitoring of the fatigue cracks. He developed the artificial notching procedure used in the present work [JUN 21].

The present study focuses on an adaptation of the in-situ ultrasonic testing procedure to the Ti64 alloy which presents a finer microstructure than the cast Al alloy studied by A. Messager. Consequently, the cracks will have a smoother front and a more continuous propagation because the influence of a fine microstructure on the propagation is reduced. A smoother crack shape allows to more accurately estimate the crack growth rates and also to more easily generate meshes to set up finite element simulations. Finally, using ultrasonic cycling frequencies allows to carry out temperature field measurements during the fatigue cyclings because when a low cycling frequency is used, the heat sources per unit of time are too weak to obtain consistent measurements.

This manuscript is divided into four chapters:

- The first chapter introduces the basics of fatigue in Ti64. Also, a summarized state of the art is presented concerning ultrasonic fatigue cycling tests, experimental evidence of the effect of environment and cycling frequency on fatigue propagation and methods used to characterize fatigue crack propagation (post-mortem and in-situ).

- A second chapter describes the experimental and numerical techniques used in this study to observe and characterize internal fatigue crack propagation in Ti64 with and without air molecules at the crack tip.

- The third chapter presents the experimental fatigue results (micro-computed tomography data, fatigue lives and crack growth rates, fractographic observations with SEM and EBSD) obtained on specimens containing an internal sharp notch not linked with the ambient atmosphere. The propagation mechanisms of the fatigue cracks obtained with this procedure are then analyzed.

- Finally, the fourth chapter is focused on the effect of environment by presenting experimental results (micro-computed tomography data, fatigue lives and crack growth rates, fractographic observations with SEM and EBSD, temperature field measurements) obtained on specimens with an internal sharp notch connected with ambient atmosphere. They will be analyzed to evaluate

if the fatigue data obtained in such a way are comparable with surface crack propagation in a Ti64 specimen put in an ambient atmosphere. This will allow to study the fatigue crack propagation mechanisms when air molecules are present at the crack tip.

Chapter 1

State of the Art

Contents

1.1 Basics on Fatigue of Metallic Alloys

1.1.1 S-N Curves & Fatigue Regimes

Fatigue is the phenomenon leading to the failure of a material or a component when it is submitted to a cyclic loading. This phenomenon was studied first in the 19th century by Jean-Victor Poncelet in France who introduced the term «fatigue» [FAT23]. Fifteen years later in Germany, August Wöhler introduced a curve bearing his name since then. This formalism - also called S-N curves - is used to represent the fatigue lives of the tested specimens: for a given mean stress, the applied stress is represented versus the number of cycles before failure (Figure 1.1). The fatigue life represented on such curves is the sum of the number of cycles needed to initiate a fatigue crack that will lead to fracture and the number of cycles during which this crack propagates until the specimen fracture. The applied stress can be defined as the maximal stress σ_{max}, the stress amplitude $\sigma_a = (\sigma_{max} - \sigma_{min})/2$ or its range $\Delta\sigma = \sigma_{max} - \sigma_{min}$.

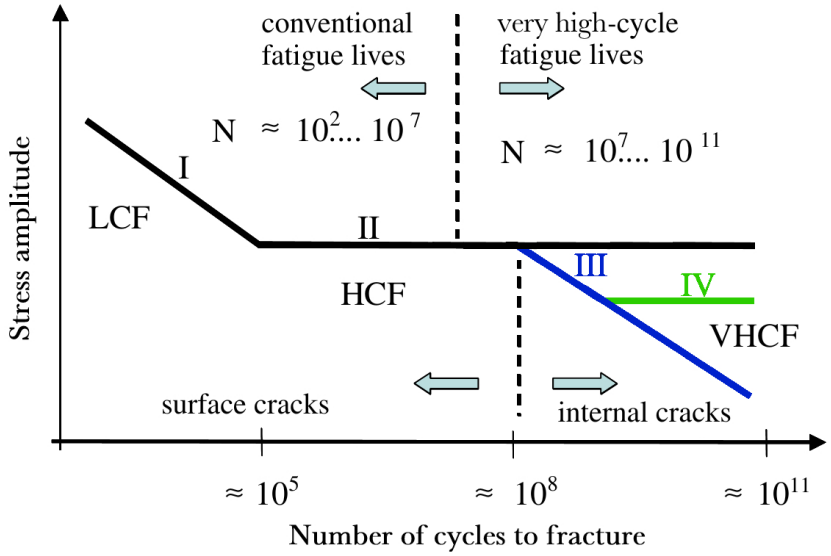

Figure 1.1 | **Schematic S-N curves considered in the literature** (adatped from the work of Mughrabi [MUG 06]). In black, the conventional S-N curve with a HCF fatigue limit. The fatigue limit is replaced by the curve in domain III (in blue) if Very High Cycle Fatigue is considered and the green curve in domain IV represents the VHCF limit sometimes considered in the literature. Surface crack initiations usually occur in LCF and HCF regimes whereas fatigue cracks tend to internally initiate in VHCF.

Usually, the literature divides the fatigue behavior into three regimes (see for example the description of Mughrabi [MUG 02]): the *Low Cycle Fatigue* regime (LCF) where the applied stress amplitude is producing macroscopic plastic strains in the material and the fatigue endurance is limited (typically below $\sim 10^5$ cycles). If the stress amplitude is smaller, the fatigue life is

longer and it corresponds to the *High Cycle Fatigue* regime (HCF) where there is no macroscopic plasticity and the fatigue life is approximatively between 10^6 and 10^7 cycles. Finally, for even smaller stress amplitude, the number of cycles to fracture can be higher than 10^7. This is the *Very High Cycle Fatigue* (VHCF) regime. This fatigue domain will be studied in this work and is presented in Section 1.1.2. These fatigue regimes can be linked with different domains on the S-N curves as illustrated in Figure 1.1: **Domain I** corresponds to LCF and the beginning of HCF where fatigue cracks are due to macroscopic plastic strain (such as persistent slip bands at the specimen surface). **Domain II** concerns the conventional fatigue limit located in the HCF regime where a cyclic strain localization threshold is reached. **Domain III** concerns VHCF where only microplastic strains occur.

Up to the end of the 20th century, the first studies on fatigue brought the concept of *fatigue limit* for a given mean stress or loading ratio ($R = \frac{\sigma_{min}}{\sigma_{max}}$): it is the stress amplitude below which the material theoretically has an "infinite" fatigue life. This concept lies in the fact that a plateau can generally be observed on the S-N curve for several metallic materials above 10^6 or 10^7 cycles. It was however difficult to reach such a large amount of cycles because carrying fatigue tests beyond 10^7 cycles is very long with classic servo-hydraulic or electromagnetic testing machines (usually operating around 30 Hz and 200 Hz respectively). However, with the development of ultrasonic fatigue testing machines at the end of the 20th century, it has become possible to test specimens with a 20 kHz (or even higher) frequency and to reach the gigacycle regime in a reasonable time [BAT 05]. This type of loading procedure is based on making the specimens resonate at 20 kHz. Hence, at such a high frequency, 10^9 cycles can be applied in less than 14 hours whereas at conventional frequencies (a few hundreds of Hertz), it takes months to reach the same number of cycles. With this type of test, researchers found out that fracture could occur beyond the HCF region of the S-N curve - *i.e.* in the VHCF regime - when the stress amplitude is lower than the conventional fatigue limit. These observations brought the idea of the existence of Domain III *i.e.* the absence of infinite fatigue life meaning that there is no fatigue limit in materials, particularly in metals. This justifies the necessity to study VHCF regime more precisely [BAT 99]. Consequently, it was considered to replace the horizontal asymptote of the S-N curve with a multi-step curve as illustrated in blue in Figure 1.1 and the notion of fatigue limit should be replaced by the fatigue strength at a given number of cycles. However, this consideration is questioned by several papers which report that a **Domain IV** can be observed when a strain reversibility threshold is reached leading to possible "infinite" VHCF lives (green curve on Figure 1.1) [MUG 02, SAK 09, BAT 10].

1.1.2 Very High Cycle Fatigue

As evoked in last section, ultrasonic fatigue testing machines allow to reach the VHCF regime in a reasonable amount of testing time. In this regime, Mughrabi distinguished two types of materials [MUG 02]: type I which are single-phase pure materials without microstructural defect

and type II materials comprising defects such as inclusions or porosities that act as preferred sites for fatigue crack initiation (*e.g.* steels or cast alloys).

In the case of type II materials, a remarkable feature in the VHCF regime is that crack initiation mechanisms change and fatigue cracks tend to initiate from the defects in the bulk of the material and not at the surface anymore as it is usually the case in LCF and HCF [ATR 83, UME 97, PET 06, ZUO 08, BAT 10, EVE 16, CAO 17]. In Domains I & II of the S-N curves, the cracks tend to initiate from the surface were cyclic plastic strains are easier to develop whereas in Domain III, the stress amplitude is too weak for macroscopic plastic strains to be localized and an accumulation of microplastic strain inside the material occurs leading to internal fatigue fracture after a very large number of cycles. Figure 1.2 summarizes the crack initiation mechanisms in a two-stage S-N curve to illustrate the shift in initiation location when the fatigue stress amplitude decreases. It points out that many different fatigue crack initiators have been referenced in the literature for these two types of initiation locations. Most of them are related to the microstructure (grain boundaries, slip bands, inclusions, cleavage) or linked with the manufacturing process (machining flaws, porosities, shrinkages, microcracks).

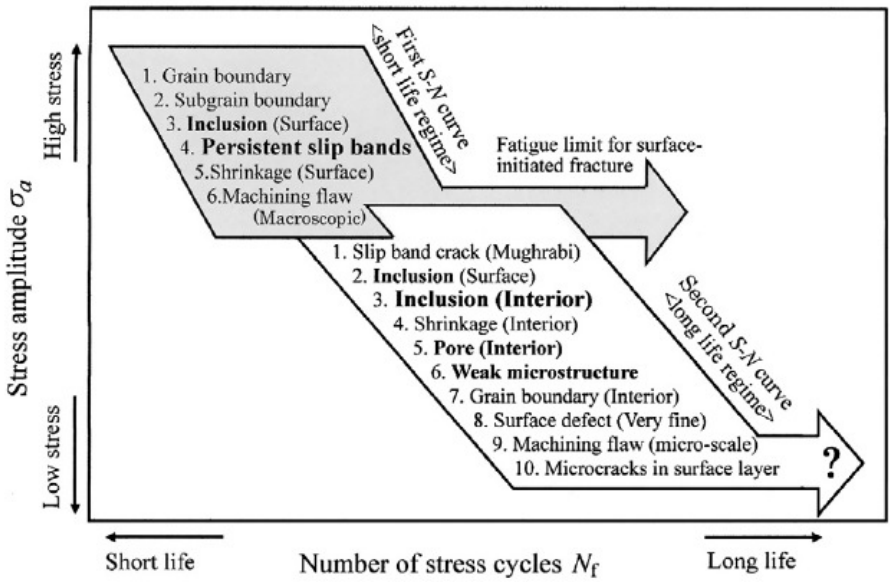

Figure 1.2 | **Summary of fatigue crack initiation origins** for low-cycle fatigue and surface initiation (in grey) or high-cycle fatigue and internal initiation (in white) [SAK 16]. In general, fatigue cracks tend to initiate from microstructural or machining-induced features.

Most of the ultrasonic fatigue test protocols used to study the VHCF regime load the specimens with a fully reversed loading (nominal stress ratio $R = \frac{\sigma_{min}}{\sigma_{max}} = -1$) under tension-compression resonance. However, as explained by Mayer, it is possible to change the ultrasonic load ratio by adding a static force to the specimen during the ultrasonic loading [MAY 15].

A lot of different examples of tests carried out on different materials exist in the literature with various experimental conditions (fatigue testing of welded joints, ultrasonic three points bending test,etc.) as reviewed by Stanzl-Tschegg or Mayer [STA 13, MAY 15]. Quite a few of these studies deal with the Ti64 used in this work [HEI 13, LIU 16, FU 22, HUA 14].

As summarized in Stanzl-Tschegg's review, ultrasonic fatigue testing procedures have however several limits [STA 13] such as the specific geometry of the specimens necessary to reach the resonance (making it very difficult to test components). Also, depending on the material, because of the high strain rate, the temperature might increase during cycling and influence the fatigue behavior. That is the reason why most of the specimens in ultrasonic fatigue tests are cooled with dry compressed air passing through an air gun [BAT 05]. Furthermore, using very high strain rates may have an impact on fatigue life. This will be discussed in Section 1.3.4.2. Finally, with such a high loading frequency, it is necessary to adapt the measurement methods used to monitor the cracks during their propagation as it will be presented in Section 1.4. For example, very few crack growth rate data are available in the literature for ultrasonic cycled specimens [STA 80, HOL 03, PAL 10, PER 15, OUA 18, GEA 22]. The present work focuses on a method to collect such dataset for internal cracks in a Ti64 alloy.

1.2 Fatigue of Ti64 Titanium Alloy

1.2.1 Ti64 Microstructure

As evoked above, the material studied in this project is a titanium alloy. Two different crystallographic structures can be found in pure titanium (*cf.* Fig. 1.3): a hexagonal close-packed (HCP) α phase and a body-centered cubic (BCC) β phase [LUT 07]. At ambient temperature, the α phase is stable (transus temperature is 882°C). For this HCP phase, the most densely packed planes are the $\{0002\}$ *basal* plane and three $\{10\bar{1}0\}$ *prismatic* planes (*cf.* Fig. 1.3).
In this α phase, different slip systems can be activated during plasticity. They are listed in Table 1.1 and have different critical resolved shear stress values. This means that some of them are easier to activate. As reported by Castioni *et al.* [CAS 21] the basal, prismatic and first order pyramidal are usually the first activated slip systems.

As the two phases are responsible for different characteristics of the alloy, different alloying elements have been used to stabilize either one or the other phase. Aluminum is an α stabilizer which increases the material strength and vanadium stabilizes the β phase to increase its ductility. These two alloying elements are predominant in the Ti64 titanium alloy (also called Ti-6Al-4V) which is an $\alpha+\beta$ alloy covering more than 50% of the titanium market [LEY 03]. It is very frequently used for biomedical and aeronautics applications because of its good mechanical properties, good corrosion resistance and workability [LUT 07].

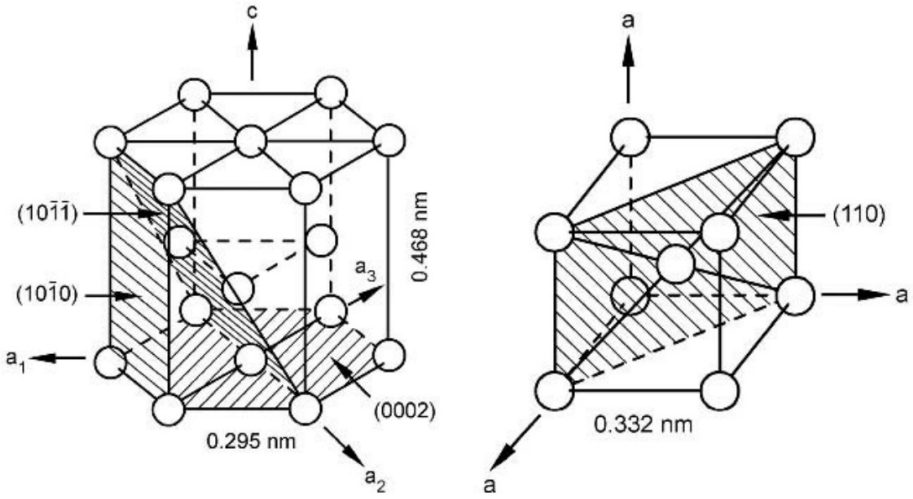

Figure 1.3 | Unit cells of pure titanium α (left) and β (right) phase [LUT 07]. The hexagonal close-packed α phase is the stable phase at room temperature. The β phase is body-centered cubic. Several slip planes are dashed.

Slip system	Slip plane	Slip direction	Burgers vector
Basal	(0002)	$< 11\bar{2}0 >$	$\vec{a}$
Prismatic	$\{10\bar{1}0\}$	$< 11\bar{2}0 >$	$\vec{a}$
First order pyramidal (π_1)	$\{10\bar{1}1\}$	$< 11\bar{2}0 >$	$\vec{a}$
First order pyramidal (π_1)	$\{10\bar{1}1\}$	$< 11\bar{2}3 >$	$\vec{c}+\vec{a}$
Second order pyramidal (π_2)	$\{11\bar{2}2\}$	$< 11\bar{2}3 >$	$\vec{c}+\vec{a}$

Table 1.1 | Slip systems in the Ti64 α phase [LUT 07, LEC 00]

Depending on the required properties, different heat treatments can be applied to this alloy resulting in three main types of microstructure:

- The lamellar microstructure (also called *basketweave*) has large lamellar-shaped α colonies with β zones at the grain boundaries (Figure 1.4a). It is obtained from an annealing treatment and a martensitic structure can be obtained if quenching is applied to this microstructure leading to very high strength properties.
- The bi-modal microstructure is obtained from a lamellar Ti64 which is hot worked and recrystallized. It is composed of globular α grains surrounded by lamellar-like α zones (Figure 1.4b). The size of the two different types of grains is determined by the cooling rate.
- Finally, the equiaxed microstructure can be obtained the same way as the bi-modal one but the cooling rates from the recrystallization temperature have to be slower. This type of microstructure is used in the present study and is composed of α grains surrounded by intergranular β zones located at the grain boundaries (Figure 1.4c). This microstructure

configuration has a high level of ductility, strength and a good fatigue resistance. The latter can be increased if the grain size is smaller.

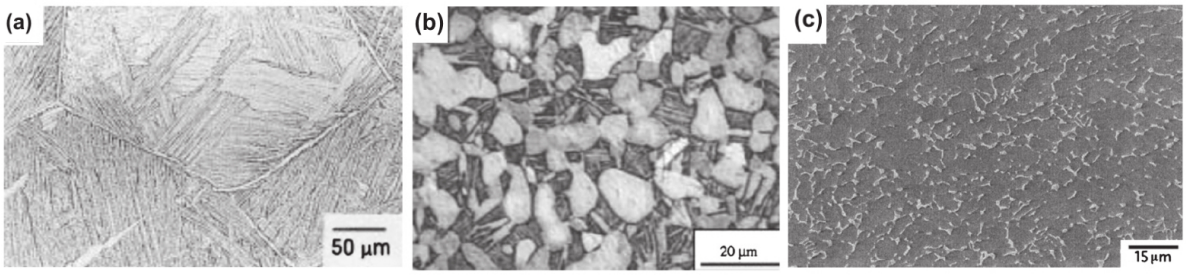

Figure 1.4 | **The three different types of Ti64 microstructures** [WU 13] (a) lamellar (large lamellar-shaped α colonies with β zones at the grain boundaries), (b) bi-modal (globular α grains surrounded by lamellar-like α zones) and (c) equiaxed microstructure (α grains surrounded by intergranular β zones located at the grain boundaries)

Macrozones can be observed in the wrought Ti64 alloy. These are large microstructural zones containing a lot of grains with their $\vec{c}$ -axis oriented more or less in the same direction. For instance, these zones can be formed during hot rolling and might have an impact on the HCF [LEB 00] and VHCF [NIK 15, NIK 16a] resistance of the alloy. More details on macrozones formation and characterization can be found in the thesis of Lunt (and particularly in his Section 2.6) [LUN 14].

1.2.2 Fatigue Crack Initiation in Ti Alloys

The fatigue strength of a material depends on its resistance against fatigue crack initiation and its ability to limit crack propagation as illustrated by S-N curves (representing the sum of the numbers of cycles required to initiate and to propagate cracks leading to fatigue fracture). The different Ti64 microstructures do not have the same fatigue strengths. However, those differences are not systematic: for example, Welsch *et al.* observed *higher* fatigue strength for the bi-modal microstructure [WEL 94] whereas Lütjering but also Zuo *et al.* report *lower* strength for bi-modal than for lamellar microstructures [LUT 98, ZUO 08]. More generally, Wu *et al.* compare the fatigue lives for three Ti64 microstructures by compiling the results from different studies [WU 13]. They report that the fatigue life is scattered for each microstructure type and they claim that one of the most important parameters that control the fatigue resistance of Ti64 is the α grain size (or the size of the lamellar zones): smaller grain size entails better fatigue resistance. This can be explained by the fact that grain boundaries act as natural barriers slowing down the crack propagation specifically when the crack is microstructurally or mechanically short (*i.e.* it is short enough to interact strongly with the microstructure) [DAV 03].

As evoked in Section 1.1.2, the location of crack initiation shifts from the surface in the HCF regime to the interior of the specimen in VHCF (*i.e.* when the stress amplitude is low). As most of the titanium alloys do not contain any inclusions or porosity (in the case of forged material), the internal fatigue cracks tend to initiate from microstructural heterogeneities such as macrozones or α/β interfaces (where the deformation is incompatible between the two phases) [ZUO 08, CHA 10]. Nikitin *et al.* reported four different fatigue crack initiation types which compete and might lead to the final fracture in a forged VT3-1 titanium alloy (presence of macrozones, of elongated α grains, of surface defects and molybdenum segregation zones) [NIK 16a]. Heinz observed that internal cracks initiate from microstructural inhomogeneities in the α and β phase distribution [HEI 13]. Wu *et al.* reported, in a Ti-7Mo-3Nb-3Cr-3A β stable alloy, that fatigue crack initiation tends to occur in elongated α grains [WU 21]. Finally, in the HCF and VHCF regimes, a lot of studies observe that crack initiation occurs at α grains clusters leading to the formation of cleavage facets [NEA 75, OGU 10, NIK 15, HON 17].

1.3 Fatigue Crack Propagation

After its initiation, a fatigue crack may propagate until the final fracture of the specimen. The propagation will be controlled by different mechanisms. This section summarizes the formalism classically used to describe crack propagation. The mechanisms and the parameters influencing fatigue crack propagation are also briefly presented.

1.3.1 Stress Intensity Factor, Plastic Zones and Crack Closure

As extensively explained in Chapter 5 of J. Schijve's book [SCH 09], in a Linear Elastic Fracture Mechanics (LEFM) situation, for which plasticity is supposed to be localized at the vicinity of the crack tip (small radius of the plastic zone size compared with the crack length), the stress field around a crack can be written as follows (in the polar coordinates system depicted in Figure 1.5) [IRW 58]:

$$\sigma_{i,j}(M) = \frac{1}{\sqrt{2\pi r}} \left(K_I f_{i,j}^{I}(\theta) + K_{II} f_{i,j}^{II}(\theta) + K_{III} f_{i,j}^{III}(\theta) \right), \tag{1.1}$$

with r the distance to the crack front, $f_{i,j}^{I,II,III}(\theta)$ the functions which defines the polar stress spatial distribution and $K_{I,II,III}$ the Stress Intensity Factors (SIF) respectively for the three fracture modes (Fig. 1.6). The SIF represents the severity of the stress at the crack tip, it takes into account the loading and the crack geometry and can be considered as the crack driving force.

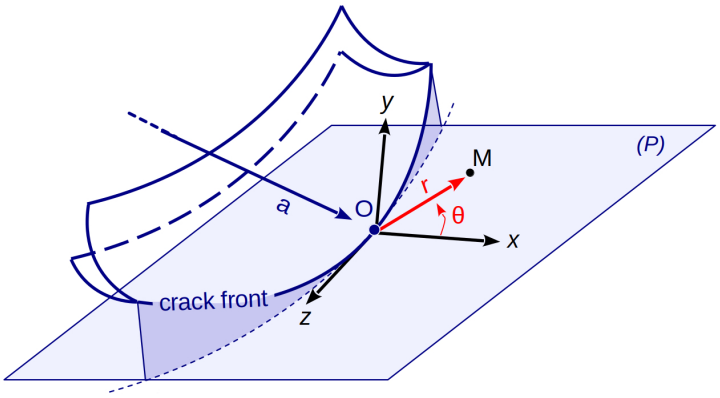

Figure 1.5 | **Polar coordinate system used to describe the stress field around a 3D crack** (Eq. 1.1). O is a point of the crack front. z is the unit vector tangent with the crack front in O. x is defined in order to have $P = (O, x, z)$ as the crack front tangent plane in O. Finally, y is normal to the P plane to have a (xyz) orthonormal basis. The dashed line is the projection of the crack front on the P plane.

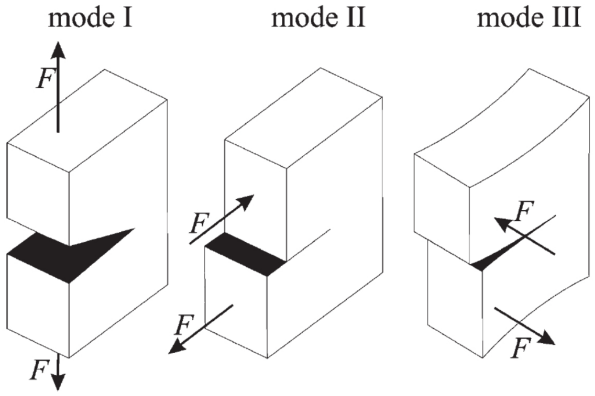

Figure 1.6 | **Three typical fracture modes** [KRU 07]

In a simplified case of a 2D crack submitted to a stress that is normal to the propagation direction (*e.g.* loading in mode I), the SIF can be written as follows:

$$K = \Gamma(a)\sigma\sqrt{\pi a}, \tag{1.2}$$

with σ the applied far-field stress and $\Gamma(a)$ a dimensionless function that depends on the crack length a, the loading applied to the component and the component geometry.

Equation 1.1 theoretically states that the stresses become infinite when r tends towards zero (*i.e.* for a point very close to the crack tip). Metallic materials have, at least, a minimum ductility, consequently (in the case of a perfect elastic-perfectly plastic behavior), one can observe a plastic zone around the crack front inside which the stress equals the local yield stress, σ_Y, as illustrated in Figure 1.7. In this small volume, the above equations are not valid as they have

been defined in the context of LEFM. Usually, this plastic zone is approximated, in 2D, as a disk. It is possible to find in the literature some estimations of its radius, $r_{p,mono}$ (Eq. 1.3 in the case of plane strain) [IRW 58]. In a fatigue loading situation, the portion of the cycle when the stress decreases induces a zone where the plastic flow is reversed. The size of this so-called reverse cyclic plastic zone, $r_{p,cycl}$, has been evaluated by Rice thanks to the superposition principle [RIC 67a]. In the case of an elastic-perfectly plastic behavior, $r_{p,cycl}$ is four times smaller than $r_{p,mono}$ as shown in Eq. 1.4 (in the case of plane strain). More details on crack tip plasticity can be found in the literature (*cf.* Section 2.3.2 of U. Krupp and Section 5.8 of J. Schijve respective books [KRU 07, SCH 09]).

$$r_{p,mono} = \frac{(1-2\nu)^2}{\pi}\frac{K_{I\ max}^2}{\sigma_Y^2} \tag{1.3}$$

$$r_{p,cycl} = \frac{(1-2\nu)^2}{\pi}\frac{\Delta K_I^2}{4\sigma_Y^2} \tag{1.4}$$

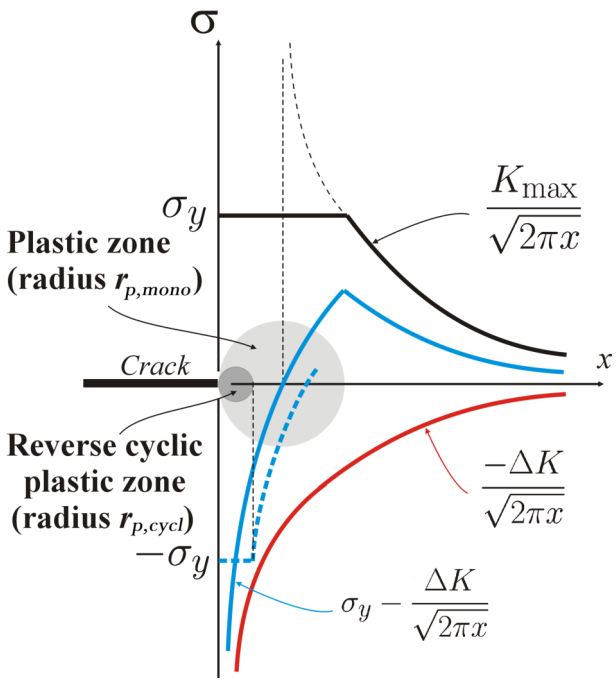

Figure 1.7 | Stress field evolution around a crack tip where $r_{p,mono}$ is the radius of the monotonic plastic zone and $r_{p,cycl}$ is the radius of the reverse cyclic plastic zone appearing in reason of the alternating aspect of the fatigue loading.

As explained in Section 8.4 from J. Schijve's book [SCH 09], at the end of the unloading portion of a fatigue cycle, the crack is closed while the stress is still positive (*i.e.* tensile part of the cyclic loading). This phenomenon is called *fatigue crack closure* and is important because

when the crack is closed, it is usually assumed that the crack does not propagate. Consequently, an effective SIF range, ΔK_{eff}, has been defined to more precisely quantify the crack driving force.

$$\Delta K_{eff} = K_{max} - K_{op} \tag{1.5}$$

with K_{op} corresponding to the higher SIF value at which the crack is closed.

As described above, during fatigue crack propagation, a plastic wake is formed in the material located near the crack lips. This is one of the reasons explaining crack closure because the region impacted by cyclic plasticity is extended in the loading direction which forces the crack lips to touch before the end of the unloading. This mechanism has been called *plasticity-induced crack closure*. Other phenomena can provoke crack closure such as the presence of oxide layers on the freshly created crack lips (*oxyde-induced crack closure*), but also the contact between the crack lips which induces mode II and mode III residual stresses because of the fractographic roughness (*roughness-induced crack closure*). A recent review of this phenomenon has been written by Pippan & Hohenwarter [PIP 17].

1.3.2 Crack Propagation Mechanisms

Different mechanisms are involved in the propagation of a fatigue crack that can be separated into four successive regimes as detailed in the literature [LAN 85, KRU 07, BAT 10]. Those regimes are summarized in Table 1.2 and described hereafter.

Crack propagation regime	Crack size	Plastic zone size	Propagation mode	Closure effect	LEFM
Microstructurally short	≈ Grain size	Negligible	II (shear)	Due to roughness	Non valid
Mechanically short	≈ Grain size	Large compared to the crack size	I (tension)	Limited	Non valid
Physically short	>> Grain size	Small compared to the crack size	I (tension)	Limited	Valid
Long	>> Grain size	Small compared to the crack size	I (tension)	Due to the plastic zone	Valid*

Table 1.2 | Fatigue crack propagation regimes

*If the crack is large compared to the dimensions of the specimen section (*i.e.* the final stage of the crack propagation), the value of the SIF range is important and the amount of section not fractured is small compared to the crack size. In this case, the plastic zone is big and LEFM cannot be applied even if the last line of Table 1.2 is valid.

At the beginning of its propagation (called the propagation *Stage I*), a fatigue crack is sensitive to the microstructure because of its small size so, even if the crack growth rate may be relatively high, microstructural features such as grain boundaries, non-metallic inclusions, pores, etc. can slow down and even arrest the cracks. When the crack size and its plastic zone increase, those microstructural barriers have less and less impact on the propagation (*Stage I-like* as defined by Petit & Sarrazin-Baudoux [PET 10]) so the crack is propagating in Stage I in the different grains (*i.e.* shear mode, II or III) but, macroscopically, it is perpendicular to the loading direction (*i.e.* mode I). Finally, when the crack is long enough, the microstructure does not affect anymore the propagation (*Stage II*, mode I). The transition from Stage I to Stage II occurs when the crack is **mechanically short**. Different conditions on the crack size compared to the grain size can be found in the literature to characterize this transition (transition when $\frac{crack\ size}{grain\ size} > X$ with $X = 1$ [LAN 85, ROD 02, YOD 82], $X = 5$ [TAY 81], $X = 8$ [TOK 92] or $X = 10$ [ZHA 02]). A mechanically short crack is small enough to be still influenced by the heterogeneous stress field around the initiation location. The crack enters the **physically short** regime when it is long enough not to be influenced anymore by the microstructure and its plastic zone is still small compared to the crack size. The main difference between physically short and **long** cracks is their plastic zone size which is larger for long cracks. Consequently, there is more closure effect (due to plasticity) for long cracks. Their crack growth rates are slower than for physically short cracks.

1.3.3 Crack Growth Rate

To rationalize crack growth rates in different fatigue experimental conditions, Paul C. Paris empirically proposed a relation between the SIF range, ΔK, and the crack growth rate, da/dN (with N the applied number of cycles), which is valid in a stable propagating stage (since then, called the Region II or Paris region in Figure 1.8) [PAR 63]:

$$\frac{da}{dN} = C\Delta K^m, \tag{1.6}$$

with $\Delta K = K_{max} - K_{min}$ the SIF range (K_{max} and K_{min} corresponding respectively to σ_{max} and σ_{min}), C and m two empirical constants depending on the testing conditions: applied loading (in particular the SIF ratio $R_K = K_{min}/K_{max}$), material, temperature, environment...

In this type of diagram, a stable crack growth region called the *Paris region* can be seen between two regimes: the threshold region (on the left of the diagram) and a region of very rapid crack growth (on the right) corresponding to crack instability or material tearing. The *threshold region* corresponds to a SIF range value ΔK_{th} below which a long crack does not propagate. For SIF range values smaller than ΔK_{th}, only short cracks can initiate and propagate. In the mid-70s, Pearson reported for the first time such short crack propagation for SIF ranges below the ΔK_{th} value [PEA 75]: the crack growth rate behavior of short cracks can decrease or increase

with increasing SIF as explained by Davidson *et al.* [DAV 03] and illustrated by the blue curves from Figure 1.8. This variety of short crack behaviors is due to their strong interactions with microstructure because of their small size. Finally, the *sudden crack growth region* concerns the propagation which occurs just before the final fracture. The crack growth rate curves can be used to compare the effect of different testing conditions on crack propagation at a given SIF value or to visualize the influence of different microstructures on crack resistance [SUR 98]. A more comprehensive description of fatigue crack propagation can be found in Chapter 8 of J. Schijve's book [SCH 09]. Several parameters can influence the fatigue crack propagation rates, they will be described in the next sections.

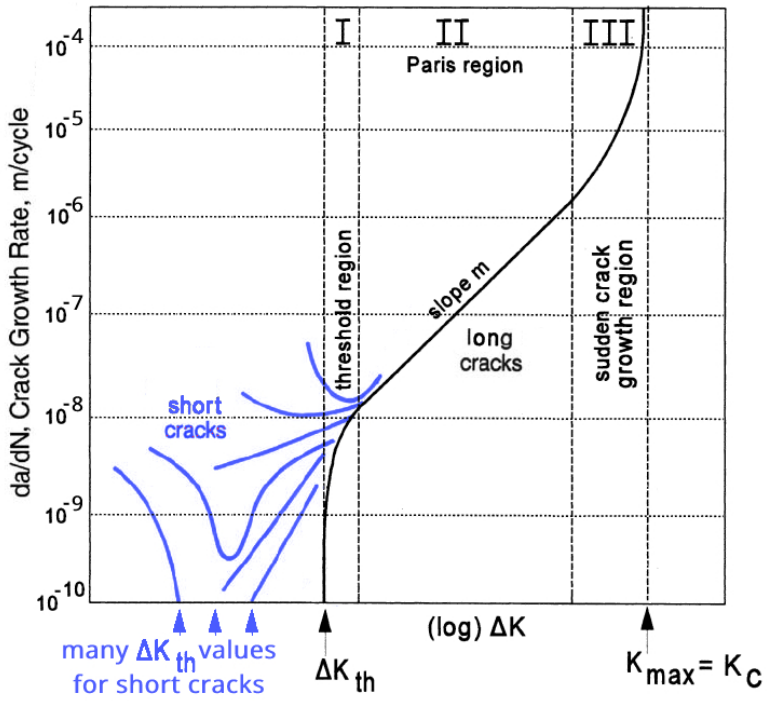

Figure 1.8 | **Crack growth rate curve** with the three regions, I, II and III, corresponding to the stages of long-crack fatigue propagation. The blue curves represent the variety of typical small-crack growth rate behavior that have been observed below the SIF range threshold value, ΔK_{th}. This graph is an adaptation from two different sources [DAV 03, SCH 09].

1.3.4 Impacting Factors on Fatigue Crack Propagation

Various factors are reported in the literature to have an influence on fatigue crack propagation in metallic alloys. For example, Grinberg reports that the microstructure, the mean stress and the environment have an important influence on the near-threshold region of the crack growth rate diagram whereas it is not the case in the Paris regime [GRI 82] (also highlighted in another

review [SIN 12]).

As explained above, short cracks are largely influenced by the microstructure through which they propagate. Hence the **microstructure** has an influence on fatigue properties. Wu *et al.* reviewed some results from different studies to evaluate the influence of the Ti64 microstructure types on fatigue life [WU 13], this has been detailed in Section 1.2.2.

The nominal **stress ratio** $R = \frac{\sigma_{min}}{\sigma_{max}}$ (with σ_{min} and σ_{max} the extrema stress values when no crack is considered in the specimen *i.e.* the nominal stress values) has also a huge impact on the fatigue properties as detailed in many studies [BOY 01, OBE 11, LIU 15, MAY 15]. These studies report a smaller value of ΔK_{th} (fatigue crack propagation threshold) for higher stress ratios and link it with the closure effect [PIP 17]. The influence of the stress ratio can be considered together with the influence of the environment because the chosen stress ratio plays a role in the time during which the crack is open: a key parameter when the effect of environment is considered. For example, Grinberg claims that the stress ratio has an impact on ΔK_{th} only in air and not in vacuum [GRI 82]. In the present work, all our experiments were carried out under $R = -1$.

The **temperature** has an influence on the fatigue behavior of metallic alloys (fatigue life and crack growth rate) particularly at high temperatures (*cf.* Chapter 17 from J. Schijve's book for more details [SCH 09]). This influence on fatigue properties is crucial in aeronautics and in particular for turbine blades which can be cycled at 300°C [SAR 97].
Other phenomena can influence the fatigue properties, for example, the **dwell effect** can impact the fatigue life of titanium alloys as extensively reported in the literature [BAN 78, BAC 03, LAV 20, JUN 21]. This effect consists of an increase in crack growth rates provoked when a static loading is imposed on the specimens in between their cyclic blocks.

The present work uses ultrasonic cycling to study internal crack propagation in a nondestructive way thanks to in-situ synchrotron computed tomography. The **environment** and the **loading frequency** are two parameters which will be relevant in the present work. A literature review on these topics is presented in the next sections.

1.3.4.1 Environment Influence

The environment in which a fatigue crack propagates is known to have an important impact on the fatigue behavior of many metallic alloys. This phenomenon has been documented for decades as illustrated by the numerous reviews available in the literature [HUD 76, GRI 82, PET 06, SIN 12, HEN 23]. For example, environment effect has been observed for titanium alloy [PET 07, OGU 13, CHA 15, GEA 15, SAR 16], for aluminum alloys [BON 12] and for steel [HEN 95].

The majority of experimental evidence of the environment effect on various metallic alloys (Al alloys, steels, Ti alloys or pure Cu) cycled at conventional frequencies report shorter fatigue

lives if the specimen is in air than if it is in a vacuum environment [PET 03, HEN 23]. This difference has also been reported at ultrasonic frequencies as presented by Petit *et al.* in Ti6246 alloy (Figure 1.9) [PET 07].

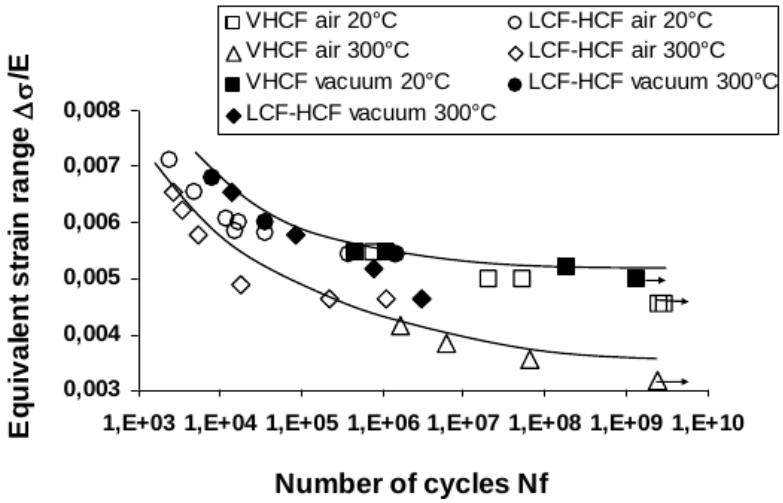

Figure 1.9 | **Differences in fatigue lives between cracks propagating in air and in vacuum** at 20 kHz in Ti6246 [PET 07]. Cracks in contact with air present shorter lives than vacuum-propagating ones.

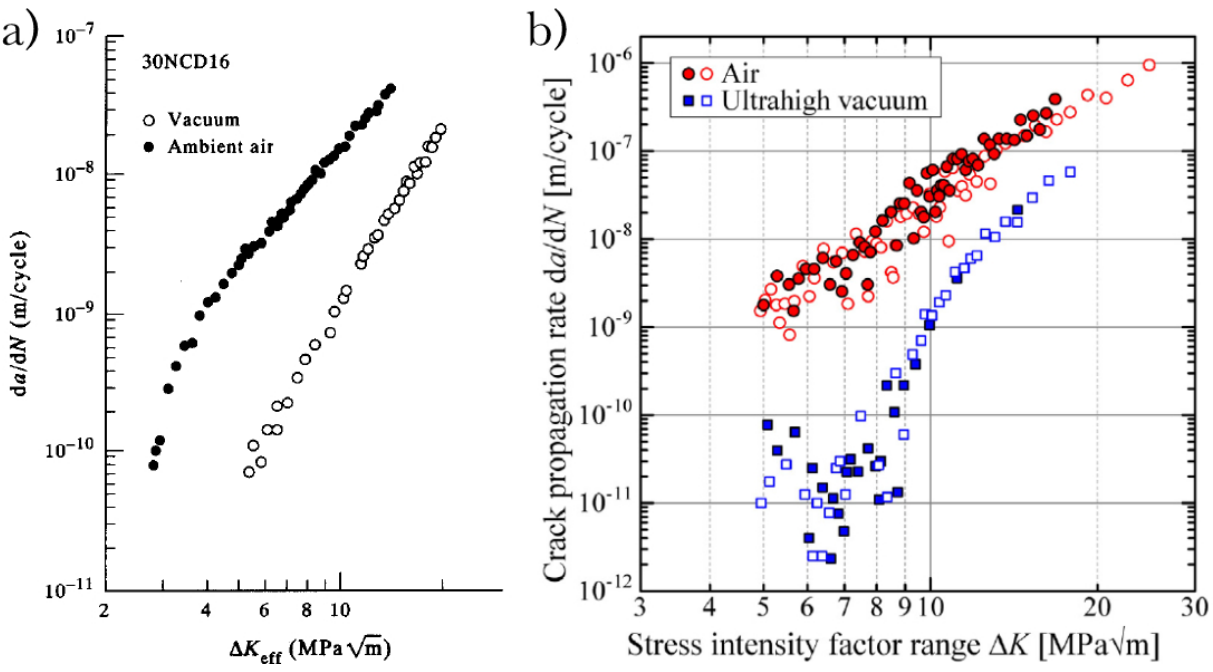

Figure 1.10 | **Crack growth rate curves obtained for specimens cycled in air or in vacuum** (a) for a high-strength low-alloy steel by Henaff *et al.* [HEN 95] and (b) for Ti64 by Yoshinaka *et al.* [YOS 16b]. For similar SIF range values, the growth rates are higher for cracks propagating in air than in vacuum.

Also, for long cracks with similar SIF range values, air-propagating cracks growth rates are reported to be higher than those obtained in vacuum (Figure 1.10) as observed by Henaff *et al.* and Yoshinaka *et al.* respectively in high-strength low-alloy steels and in Ti64 cycled at conventional frequencies [HEN 95, YOS 16b]. Petit *et al.* reviewed similar observations from many studies on a 7075 Al alloy, a nodular cast iron, an En24 steel and a high-strength low-alloy steel [PET 03]. Similarly, Oguma *et al.* compared Ti64 fatigue crack growth in air and in vacuum, they reported the same observations concerning fatigue lives and crack growth rates [OGU 13].

The different fatigue behaviors of Ti64 in various environments can be observed from fractographic observations. As it will be explained in Section 1.4.1, the fractographic aspect of a crack that propagated under vacuum conditions does not present the same characteristics as a fatigue crack propagating under air environment (for example, *the striation phenomenon is, in general, known to occur only in presence of air and not in vacuum* [SUR 98]).

The described influence of the environment on fatigue properties has also been studied at ultrasonic frequencies to evaluate the link it has with the frequency effect concerning fatigue crack growth rates, this will be detailed in Section 1.3.4.2.

As explained by Petit & Sarrazin-Baudoux [PET 06], the model from Wei is usually used to explain this difference in propagation [WEI 81]. Two different mechanisms emerge from this model:
(i) the *adsorption-induced dislocation emission (AIDE)* where water vapor molecules are adsorbed at the freshly created surface crack to create an oxide layer [GRI 82, SUG 89]. Some researchers claim that this layer increases dislocations movements [LYN 88], reduces slip irreversibility and crack front surface energy [DUQ 71] or increases plasticity [HEN 95] resulting - in all cases - in an increase in crack growth rate.
(ii) *the hydrogen enhanced localized plasticity (HELP)* which claims that the adsorbed hydrogen diffuses in the material around the crack tip reducing the stress needed to unpin dislocations. As reviewed by Henaff & Sarrazin-Baudoux [HEN 23], a two-step model composed of the succession of adsorption and hydrogen crack propagation assistance is sometimes developed in the literature. It has been considered for titanium alloys by Smith & Piasick [SMI 98]. The *HELP* phenomenon has been experimentally observed only for small values of the SIF range [PET 06] whereas the *AIDE* one seems to occur for larger values of the SIF range [HEN 07]. Also, Sinha & Larsen [SIN 12] report that oxidation has a higher influence on the crack growth rate than hydrogen in Ti alloys.

In addition to these two mechanisms, Hudson & Seward present *cold-welding* as a reason why vacuum propagating cracks can be slower [HUD 76]: when there is no oxide layer, the two lips of a freshly created fatigue crack might reweld during the compression phase of the cycling. Several studies have reported observations justifying this assumption [WAN 75, ZHA 98, BON 12, BAR 23].

To study the influence of environment on fatigue behavior, most researchers are using adapted fatigue testing machines fitted with a vacuum chamber to cycle a specimen with a surface crack in a controlled environment [SUG 89, YOS 16b, PET 07]. An original example of vacuum chamber has been used by Geathers *et al.* who carry out their observations in the primary vacuum of a Scanning Electron Microscope [GEA 22].
Another uncommon solution to study the effect of environment consists of bringing air to internal cracks instead of putting surface cracks in a controlled vacuum environment. To do so, Schijve drilled an axial hole connecting the top surface of some fatigue specimens to the volume center [SCH 78]. As detailed in Chapter 2, a similar approach has been used in the present study.

1.3.4.2 Loading Frequency Influence

The present work is focused on internal fatigue cracks which principally initiate in VHCF regime. As it will be explained in Chapter 2, an ultrasonic system working at 20 kHz is used to reach this gigacycle regime in a reasonable amount of time. For this reason, it is important to know the influence of the cycling frequency on the crack behavior because the majority of fatigue experimental protocols use servo-hydraulic, electro-magnetic or electrodynamic resonance types of equipment whose cycling frequencies are generally of the order of several tens or hundreds of Hertz. The influence of the cycling frequency can be linked with strain rate effects and time-dependent influences of the environment.

To address those issues, it is necessary to differentiate the materials. For example, steel or copper alloys which are strain rate sensitive might be influenced a lot by the cycling frequency. Kikukawa *et al.* - who wrote one of the first papers reporting a study on the frequency effect - observed that for their studied steel, higher frequencies led to longer fatigue strengths [KIK 65]. Mayer reports that - contrary to body-centered cubic alloys - the face-centered cubic metals (*e.g.* Al alloy) are weakly dependent on the strain rate [MAY 15]. However, these assertions need to be taken with caution as illustrated by Engler-Pinto *et al.* [ENG 07] who studied two different Al-Si cast alloys used for an automotive component and observed that one alloy did not present any noticeable differences in fatigue behavior between ultrasonic and conventional frequencies whereas for the other one, the difference was very pronounced.

For strain rate insensitive alloys, as studied by Stanzl-Tschegg, Sarrazin-Baudoux and coworkers [STA 06, SAR 16], the frequency effect is mainly explained by environment considerations because, at ultrasonic frequencies, a surface fatigue crack is in contact with the air molecules present in the ambient atmosphere during very short time intervals. Hence, by taking into account the environment effect presented in Section 1.3.4.1, it is possible to claim that the crack growth rates might not be impacted by high frequencies if the cracks are in a non-corrosive environment (*i.e.* in primary vacuum) [SAR 16, GEA 22]. In the study on frequency effect made by Holper et al. on a 2024-T3 Al alloy cycled with $R = -1$ [HOL 03, STA 06], it has

been observed that the crack growth rates in vacuum appear similar for high and low cycling frequencies whereas in air, the crack growth rates at ultrasonic frequencies decrease to meet those measured under vacuum conditions at high SIF ranges (long cracks) (*cf.* their summarized results in Figure 1.11). To explain these observations, the authors claim that, at ultrasonic frequencies, the amount of time during which the crack is open is too short for the air molecules to reach the crack tip and provoke oxidation of the freshly created crack surfaces.

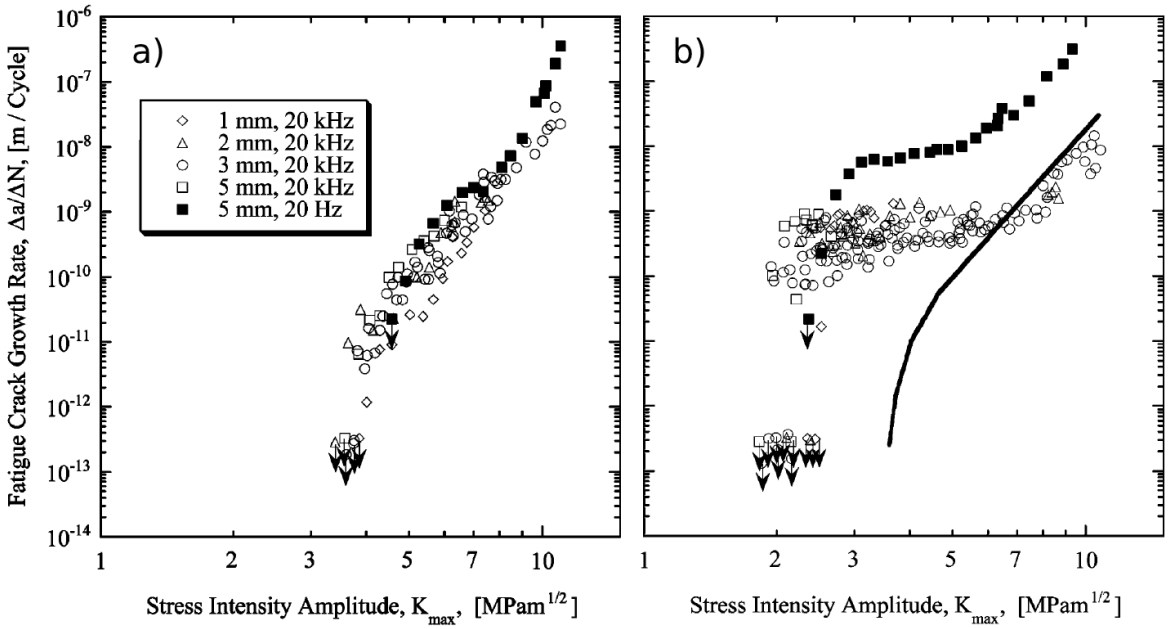

Figure 1.11 | Crack growth rate graphs showing a frequency effect for 2024-T3 aluminum alloy [HOL 03] (a) Dataset cycled under vacuum conditions: no difference between 20 Hz and 20 kHz crack growth rates (b) Dataset cycled under air conditions: the crack growth rates obtained at 20 kHz are lower than the one obtained at 20 Hz. The continuous curve in (b) corresponds to the data from (a): for high SIF amplitudes, the growth rates for cracks cycled in air at 20 kHz are comparable to the rates measured in vacuum.

However, the results reported by Sarrazin-Baudoux *et al.* on a comparable 2024-T351 Al alloy present no difference in crack growth rate between cracks propagated at 20 Hz and 20 kHz [SAR 16]. In this last study, the stress ratios used were all positive. This reminds the conclusions of Petit *et al.* for results obtained at conventional frequencies: if the effect of environment is «saturated» (*i.e.* if the specimen is cycled in ambient air at positive stress ratio), the air molecules are reaching the crack front whatever the frequency, so in that case, the frequency effect might be limited [PET 06].

These considerations bring elements to understand the different literature results concerning frequency effect on titanium alloys [PAN 20]. For example, Morrissey & Nicholas observed longer

fatigue lives for tests carried out at ultrasonic frequency and $R = -1$ [MOR 05] whereas, for the same Ti64 alloy, Atrens *et al.* did not report any frequency influence on fatigue life with a stress ratio of zero [ATR 83]. Similarly, Furuya & Takeuchi claim that no frequency effect is observed for positive stress ratios for Ti64 [FUR 14]. Finally, in the review on ultrasonic fatigue testing written by Mayer [MAY 15], a comparison between different studies was made which reported no frequency effect for internal cracks [TAK 08] contrary to the case of surface cracks [GEA 15].

1.4 Experimental Analysis of Internal Fatigue Cracks Initiation and Growth in Metals

Different experimental approaches have been used to study internal fatigue cracks and will be presented in this section, from the classic post-mortem optical surface analysis to the in-situ microcomputed tomography monitoring which is less frequently used in the literature.

1.4.1 Fracture Surface Analysis

As presented in Section 1.1.2, in VHCF, fatigue crack initiation occurs very often inside the material. Consequently, the experimental methods to study this type of crack are very limited. That is the reason why most of the experimental references on internal fatigue cracks are focused on the total number of cycles and use post-mortem observations of the final fractured surfaces to determine the mechanisms occurring before the final fracture [ASM 04]. This fractographic analysis method is used to locate the crack initiation site and also to determine the crack propagation mechanisms from the aspect of the fractured surface. To obtain this type of information, optical microscope and Scanning Electron Microscope (SEM) observations are usually carried out. But the crack surface can also be analyzed with 3D profile measurements [YOS 21], roughness measurements [EVE 17a, JUN 21], Energy-Dispersive X-ray spectroscopy (EDX) [NIK 15] or even by using the Focused-Ion Beam (FIB) technology to extract a section view perpendicular to the crack surface in order to reveals the microstructure in the volume just below the crack [SU 17] (this method, used in the present study, will be detailed in Chapter 3).

Generally, the initiation site is located on the fractographic surface thanks to several fracture characteristics such as clusters of facets or step lines which are directed toward the initiation location as it can be observed in Figure 1.12a [SCH 09].

Immediately after initiation, an internal crack in a Ti64 alloy has strong interactions with the microstructure; this can be seen on the fracture surface as a "chaotic-looking" zone called the *Rough Area* (RA) as illustrated in Figure 1.12a. In this zone which comprises the initiation site, a relatively large roughness is observed. More precisely, the zone is composed of smooth facets dispersed within granular areas (*cf.* Fig. 1.12b). This *Rough Area* is referenced in a lot of studies on Ti64 [LIU 15, OGU 13].

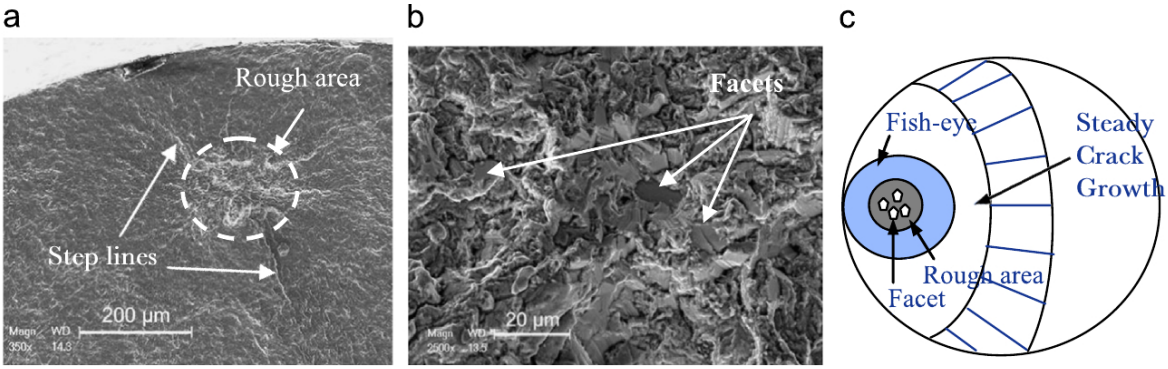

Figure 1.12 | Aspects of the fracture surface for a sub-surface crack in Ti64 observed with SEM [LIU 15]. It presents all the typical fractographic features of an internal fatigue crack in Ti64. (a) global view of the *Rough Area* around the initiation location, (b) detailed view located in the *Rough Area*: some facets surrounded by granular zones, (c) scheme of the fracture surface for an internal crack in Ti64.

When the crack is long enough not to be influenced by the microstructure anymore, the fracture surface starts to present a more planar aspect. This zone surrounding the *Rough Area* has a circular shape, for this reason, it forms with the *Rough Area*, the so-called *Fish-eye* zone (FiE). Beyond this region, the crack enters the Steady Crack Growth region and propagates until the final fracture when the maximum value of the SIF approaches the material toughness. These different zones are summarized in Figure 1.12c and described with more details in Hong & Sun's review [HON 17].

To explain those different regions of the fracture surface, some authors claim that the crack exits the *Rough Area* region when the plastic zone radius at the crack tip is larger than the grain size [WAN 89, ZHA 12, JUN 21]. Such an assumption has also been made by Birkbeck *et al.* who studied a low-carbon steel and stated that the crack is not influenced by the microstructure when the plastic zone radius is four times larger than ferrite grain diameter [BIR 71].

In their review, Hong & Sun present a model to explain the formation of a *Fine Grain Area* (FGA) in steels with internal fatigue crack initiation (the *Fine Grain Area* is the steel equivalent of the *Rough Area* observed in Ti alloys) [HON 17]. This so-called Numerous Cyclic Pressing (NCP) model states that the repeated pressing between crack surfaces during fatigue cycling can lead to the formation of a nanograin layer immediately below the crack lips as confirmed by several works [JIA 16, CHA 20, FU 22]. Other models can be found in the literature to explain the formation of the *Fine Grain Area*, they are detailed in Section 4.1 from Hong & Sun's paper, however, they concern most of the time alloys with inclusions such as steels. For example, the environment effect of the hydrogen contained in the inclusion from which the crack initiated is considered as the origin of *Fine Grain Area* formation by different researchers [MUR 00, LI 12]. Finally, because the *Fine Grain Area* is only present for specimen cycled in vacuum and not

in air, Oguma & Nakamura supposed that cold-welding occurring between the two lips of an internal crack might be the reason for the formation of this zone [OGU 13].

The aspect of the fracture surface is influenced by the environment in which the fatigue crack has propagated [ZIM 12]. For example, the fractographic features of a crack that initiated at the surface of a Ti64 specimen put in air are different from those of an internal crack not in contact with the ambient atmosphere. As described by Yoshinaka *et al.*, surface crack fractography does not present any *Rough Area* with facets and granular aspect but an «angular and sharp» zone nearby the initiation site surrounded by a «larger flat striated zone» (*cf.* Fig. 1.13) [YOS 21]. In this work, the authors studied the propagation of fatigue cracks from an artificial notch at the surface of Ti64 under various controlled environments. They report that the «angular and sharp» zone around the initiation location - observed when the specimen is in ambient air - progressively changes when the atmospheric pressure is modified and a «granular and rounded» aspect is observed when a 10^{-6} Pa pressure is applied. The latter reminds the granular *Rough Area* typically reported for internal fatigue cracks (depicted in Figure 1.12).
The fact that the influence of the environment on the fracture aspect can only be observed near the initiation site (*i.e.* for short cracks) is in agreement with the observations of Grinberg who claimed that the crack growth rate depends on the environment only in the near-threshold region [GRI 82].

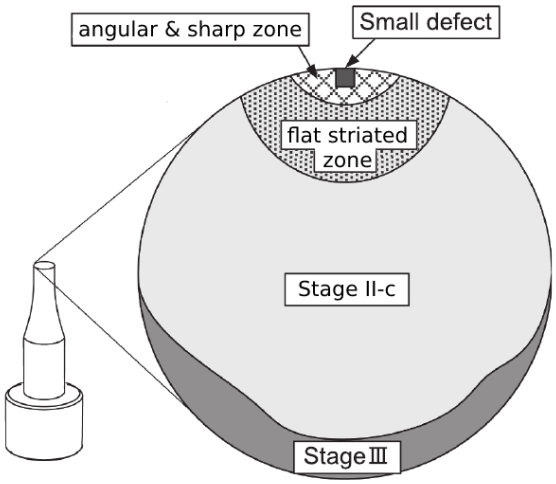

Figure 1.13 | **Scheme of the fracture surface for a surface crack propagating in Ti64 in ambient atmosphere** No Rough Area is observed around the initiation site but an angular and sharp zone located inside a flat striated one. Illustration adapted from the work of Yoshinaka *et al.* [YOS 21].

The striations on the fracture surface are typical of fatigue cracks propagating in air as reported by many studies in the literature [SUR 98]. It consists in many parallel marks visible on the planar regions of the crack surface. This phenomenon is described as specific to crack propagation under air environment as remarked by Yoshinaka *et al.* [YOS 21] who observe that striations disappear when the pressure around the fatigue specimen decreases. Two possible mechanisms have been proposed to explain the striations formation: Newmann [NEW 83] postulated that, in a vacuum environment, the absence of any oxide layer will enhance the rubbing marks on the crack surfaces and will obliterate the fatigue striations; a different hypothesis from Pelloux suggests that, in air, the oxide layer prevents the shear process in the plastic region around the crack tip to be reversible and leads to the formation of a striation pattern [PEL 69].

These striations are frequently used to calculate a crack growth rate by assuming that one striation is created during each fatigue cycle [LEN 00, BUL 10, CAT 12]. Measuring crack growth rates from inter-striation spacings gives a local estimation measured at the scale of a facet (several dozen micrometers) whereas macroscopic crack growth rates usually reported in the literature are averaged along a longer crack length and during the given amount of cycles between two measurements (which obviously depends on the cycling frequency). The very different nature of these two types of measurements might explain why such a striation-based method to estimate the crack growth rate frequently gives higher values than the macroscopic averaged ones [WAN 89, PIL 13, YOS 21]. Some researchers [WIL 11] claim that those differences in crack growth rates lie in the fact that the propagation is not homogeneous along the crack front so the macroscopic crack growth rate - which is an averaged value - can differ from the local one, measured in the facets for example. This hypothesis might be valid only for short cracks because when a crack is long, the microstructure no longer influences the propagation. In that case, other researchers insist on the fact that the crack in the flat facets (where striations can be observed) could stay arrested during several cycles (between 10 and 100) before propagating again. For example, Grinberg reported different observations on an iron and a copper alloy to state that the number of cycles needed to form one striation varies during the propagation depending on the value of the SIF range at the moment of the creation of the striations [GRI 82].

1.4.2 In-Situ Observation of Propagating Cracks

Studying the internal fatigue crack growth mechanisms thanks to the number of cycles to failure and the observation of fractured surfaces brings crucial information on the fatigue behavior of the studied material but this approach is carried out *post-mortem*. Consequently, a lot of information is still missing or is assumed. For this reason, several non-destructive in-situ methods have been developed to monitor fatigue cracks during their growth and to better understand the initiation and propagation mechanisms.

1.4.2.1 Thermal Measurements

Following the temperature field evolution at the surface of a specimen submitted to cyclic loading is an example of an in-situ non-destructive way to observe internal fatigue cracks. Such an indirect technique allows only to observe the consequences of the crack presence and propagation on the temperature field at the specimen surface. The thermal evolutions of cycling specimens depend on the different heat sources in the material but also on the material thermal properties, the specimen geometry and the heat losses caused by convection and radiation. The challenge is to separate these sources from the temperature measurements to quantitatively study the heat source due to the crack presence.
When a metallic material is cycled below its macroscopic yield strength, plastic strain heterogeneously occurs at the scale of the microstructure. This cyclic localized microplasticity activity is at the origin of the so-called self-heating thermal source. It can be considered to be homogeneous at the scale of the representative elementary volume and directly depends on the applied stress amplitude [RAN 22].
The presence of a propagating fatigue crack inside a specimen contributes to the heterogeneous temperature increment field because of the energy dissipation provoked by the plastic activity in the reverse cyclic plastic zone near the crack front but also because of the friction between the crack lips during cycling. No study has been found in the literature to evaluate the heat source due to crack lips friction but it is usually negligible in the case of mode I loading. As shown by Rice & Rosengren [RIC 67b], the plastic energy for an elastic-perfectly plastic material is linear versus the square value of the reversed cyclic plastic zone size $r_{p,cycl}^2$. In the case of cyclic loading, the radius of this plastic zone size should be linear versus ΔK^2 as presented by Equation 1.4. Hence, the heat source due to the cyclic plastic zone at the crack tip is linear with ΔK^4. Experimental observations from Pippan & Stüwe and numerical simulations from Klingbeil [PIP 83, KLI 03] also confirm this.

Several studies report the contactless monitoring of temperature evolution of cycling specimens containing internal fatigue cracks. Most of them observe a typical temperature evolution [KRE 13, RAN 08, RAN 22, MES 20] which starts, as represented in Figure 1.14, with **(i)** a rapid increase of the temperature corresponding to a thermal transient regime where a quasi-homogeneous heat source is generated in the whole specimen due the microplastic activity (*i.e.* specimen self-heating) [WAG 09]. The fact that this source predominates on the heat losses is the reason for the strong increase. **(ii)** After the transient regime, the temperature keeps increasing but the increment is slower because the heat losses caused by convection and conduction become predominant. The heat source originates also from microplastic activity as illustrated by the fact that the slope of this temperature increment depends on the stress amplitude applied on the specimen. **(iii)** Once a crack has initiated, the heat source in the plastic zone provokes a strong temperature increase because of a high cyclic plastic activity around the crack tip. This

thermal increment can be detected in the temperature measurements.

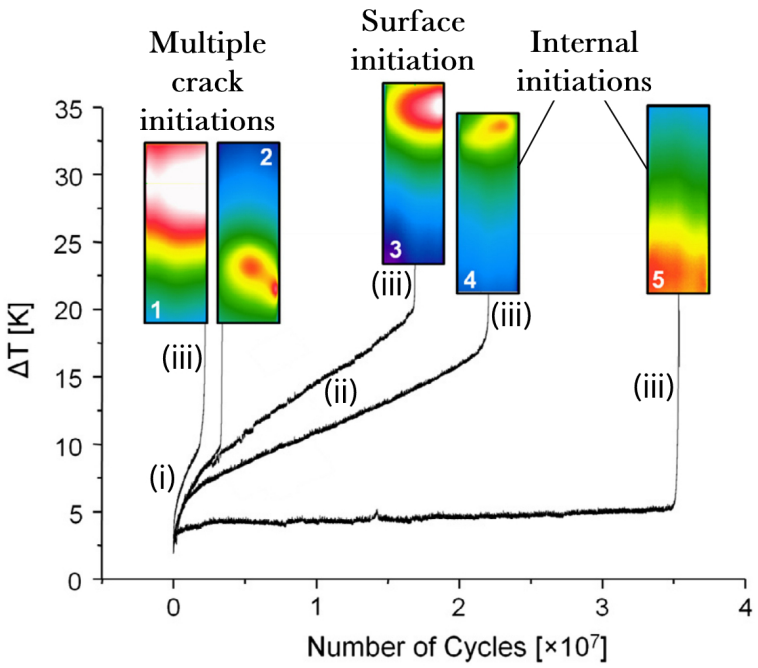

Figure 1.14 | **Typical surface temperature field evolutions for AlSi7Mg specimens containing propagating fatigue cracks** Graph extracted from the work of Krewerth *et al.* [KRE 13]. The transient temperature increase due to microplastic self-heating is labeled as (i). The small temperature increase due to the slight evolution of the microplastic heat source with the number of cycles is labeled as (ii) and the final strong increase provoked by the crack initiation and propagation is labeled as (iii).

Most of the literature references reporting fatigue crack temperature monitoring use thermal approaches to detect internal fatigue crack initiation. For example Wagner *et al.* estimated the initiation proportion of the VHCF life to 92% under tension ($R = 0.01$) at ultrasonic frequency for two aluminum-silicon alloys and three low alloyed steels [WAG 09]. Huang *et al.* carried out a fatigue experiment on a titanium alloy while monitoring the surface radiation in the infrared domain to obtain data to calibrate a dissipation model [HUA 14] and to predict the fatigue life with a Weibull model [HUA 15]. However, internal crack detection carried out with thermal measurements can be complicated because an initiated crack remains small for an important number of cycles so the SIF range and consequently the heat sources also remain small. In practice, as the thermal measurement is performed at the surface of the specimen, the heat diffusion and conduction in the material prevent the surface from undergoing a measurable thermal increment if the crack initated far away from the monitored surface. These limitations are pointed out by Ranc *et al.* who compared experimental and simulation data to evaluate the smaller internal crack thermally observable [RAN 08]. In this paper, the crack propagation

has also been monitored with thermal data and compared with simulation results under the assumption of a simple penny-shape crack geometry.

As evoked above, the plastic dissipation at the crack front is proportional to ΔK^4 with η being the proportionality coefficient. Consequently, the lineic heat source at the crack tip, S, can be written: $S = \eta \Delta K^4$. The η material parameter can be used to quantify the influence of various parameters on the local crack tip plastic activity occurring during fatigue loadings. To do this, Ranc *et al.* [RAN 08, RAN 22] supposed that all the mechanical energy is dissipated in heat (with perfect plasticity and no closure effect). Then, during the PhD thesis of A. Messager, temperature field measurements were used to evaluate the value of η in a cast aluminum alloy [MES 20]. For that purpose, the heat source located in the reversed cyclic plastic zone has been modeled as lineic along the crack front in finite element simulations carried out with the crack geometry obtained from micro-tomography acquisitions. As presented in Section 2.4.3, this approach will be carried out to evaluate the influence of the environment in which cracks are propagating, on the plastic activity at the crack tip.

1.4.2.2 System Nonlinearities Measurements

A specimen can be put in vibrations to measure its acoustic parameters in order to detect [JHA 99] or even quantify its damage from the nonlinearities of this signal, as reviewed by Jhang [JHA 09]. This approach can be applied to fatigue tests such as presented by Frouin *et al.* who regularly stopped their low-frequency fatigue tests to carry out ultrasonic nonlinearities measurements and to detect fatigue crack initiation [FRO 99a, FRO 99b]. In the case of ultrasonic fatigue tests, the specimen ultrasonic vibrations can directly be measured during cycling (*i.e.* in-situ approach) to detect crack initiation. As reviewed by Matlack *et al.* (cf their Section 4.1 [MAT 15]), different methods to measure these ultrasonic vibrations can be found in the literature, either in contact with the specimen (strain gauge [FIT 14, MAY 13, MAY 15]) or contactless (laser vibrometer [CAM 06], capacitive displacement sensor [KUM 09]).

If the free-end velocity of a vibrating specimen is measured, it is possible to determine - thanks to a Fast Fourier Transform (FFT) - the amplitudes of its harmonics which depend on the nonlinearities of the whole fatigue experimental system. Such nonlinearities originate from the presence of cracks in the specimen but also from the specimen material itself (micro plasticity provoked by micro-cracks, local plasticity at the crack tip) and the experimental assembly (intrinsic apparatus nonlinearities, unperfect contacts between parts, temperature evolution of the piezoelectric actuator, or even high voltage electric power). Consequently, in order to use this approach to detect fatigue crack initiation, the nonlinearity due to the presence of a crack has to be distinguished from the others. For this reason, Kumar *et al.* [KUM 09] used a relative nonlinearity parameter, β_{rel}, to detect an initiated fatigue crack.

Their parameter depends on the amplitude of the second harmonics and is normalized by its initial value as follows:

$$\beta_{rel} = 20\log_{10}\left(\frac{V_2}{V_1^2}\right) - 20\log_{10}\left(\frac{V_2}{V_1^2}\right)_0 \tag{1.7}$$

with V_1 and V_2 the vibration velocity amplitudes of respectively the fundamental and the second harmonics where $(.)_0$ means the initial value of a parameter at the beginning of the considered cycling test.

This in-situ crack detection procedure is illustrated in Figure 1.15 which represents the evolution of the described nonlinearity parameter during cycling. It is possible to observe an increase just before the final crack propagation. For this reason, this method has been used by other researchers to detect crack initiation [MES 19]. However, this approach did not suppress all the parasitic nonlinearity contributions. For example, piezoelectric converter nonlinearities might depend a lot on the converter temperature which can increase during ultrasonic cyclings (even when dry air cooling is used). Furthermore, the described parameter does not consider the other harmonics that might be more sensitive to specific nonlinearities (the ability to study numerous harmonics depends on the recording system bandwidth).

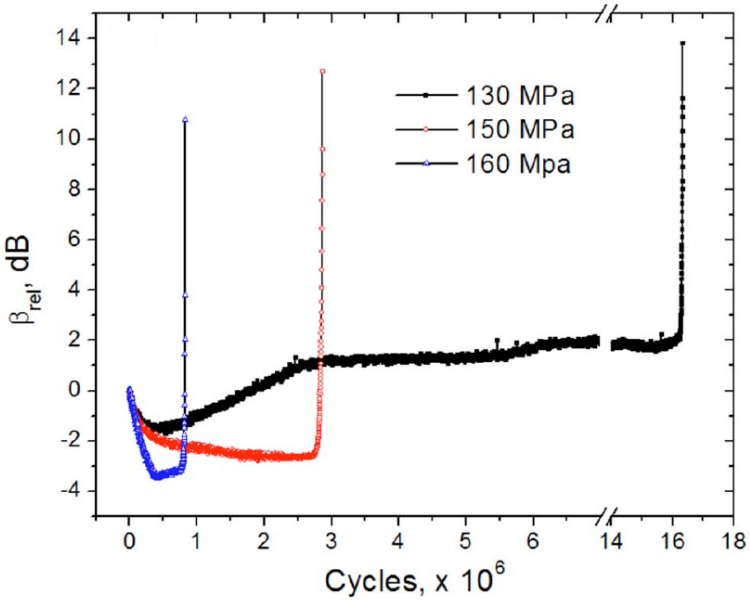

Figure 1.15 | Normalized nonlinearity parameter (Eq. 1.7) evolution during fatigue cycling. The sudden increase observed at the end of cycling is due to crack initiation and fast crack propagation. This increase can be used to detect internal fatigue crack initiation. Data extracted from the work of Kumar *et al.* [KUM 09].

Hence, such an approach allows the detection of fatigue crack initiation but remains influenced by other nonlinearities from surrounding elements of the experimental setup. Despite this, the

technique could be used to detect a fatigue crack in its early stages of propagation in order to stop the cyclic loading before the crack is too big. X-ray imaging methods - such as micro-computed tomography - can then be used to obtain direct images of such a fatigue crack at different instants of the propagation [MES 19].

1.4.2.3 Direct Crack Imaging Methods Using X-Rays

The experimental methods described above to detect and monitor an internal fatigue crack during its propagation are based on *indirect measurements*. During the last two decades, many studies have adapted X-ray techniques (either in laboratories or in large instruments) to monitor in a non-destructive way fatigue cracks during their propagation. For example, X-ray diffraction has been used to study the crack closure effect [THI 19] or the role of slip bands and dislocations in fatigue crack initiation [IST 14]. X-rays can also give *direct measurements* of the crack size in 2D using X-ray radiography [LIU 08, LIU 11] or in 3D thanks to X-ray micro-computed tomography (μCT) [WU 17, LUO 18].

X-ray micro-computed tomography allows to non-destructively monitor a 3D volume thanks to the acquisition of a set of 2D radiographs. During the acquisition, the studied specimen is located on a rotating stage to acquire successive radiographs at different angular positions of the specimen. From the set of radiographs, a 3D volume is then reconstructed. Figure 1.16 illustrates this type of data by showing some different views of a 3D volume containing a fatigue crack which has been acquired with micro-tomography.

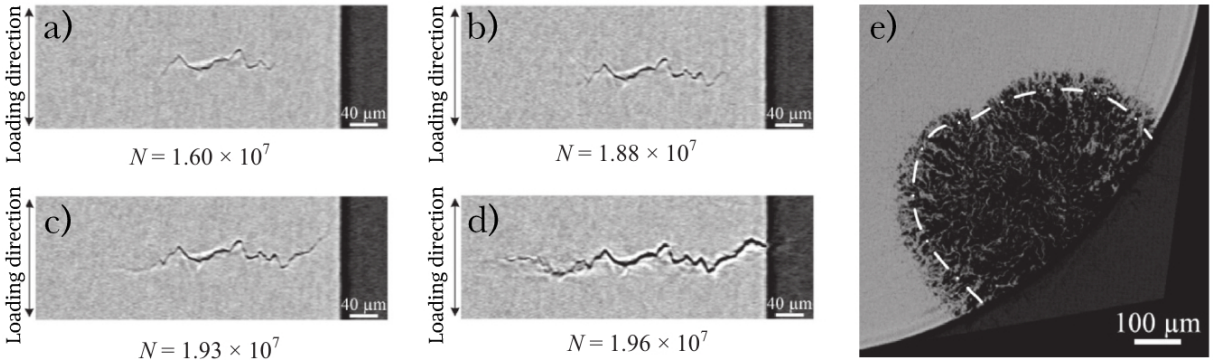

Figure 1.16 | Typical example of direct 3D crack imaging with micro-tomography (a-d) Longitudinal sections extracted from different 3D μCT volumes acquired at different instants of the crack propagation. (e) Projection along the specimen loading axis of the tomographied crack. This type of data can be used to obtain the 3D shape of a fatigue crack at different instants of the propagation. Images taken from Yoshinaka *et al.* on Ti64 [YOS 16a]

The access to the 3D aspect of the cracks allows to measure the local crack growth rates in a more precise way than with post-mortem, indirect or 2D analyses. For these reasons, micro-

tomography experiments are employed in the present study to acquire the shape of internal cracks with different experimental conditions. To carry out this type of imaging, specific fatigue testing machines adapted to X-ray recording have been developed [BUF 06, TER 16]. A lot of studies using in-situ tomography to monitor material damage and in particular fatigue crack propagation have been published in the literature, see for example the following reviews [WU 17, LUO 18]. However, there are very few examples focused on *internal* fatigue cracks.

Those rare observations have been obtained in different titanium alloys as reported by some authors who observed internal cracks initiated from microstructural defects (natural cracks) [CHA 15, NAK 16, YOS 16a, XUE 22]. Artificial internal defects have also been used by some authors to locate the fatigue crack initiation in the observed area of Ti64 specimens [JUN 19]. Also, an internal fatigue crack initiated from a casting defect could be monitored with tomography in an Al alloy [SER 17, MES 19] or another one initiated from an internal inclusion in a Ni-based superalloy [NAR 17].

The use of the X-ray technology to acquire tomographic data of fatigue cracks needs adapted experimental setups allowing to cycle the specimens and to let the X-rays pass through the tomographied volume [BUF 06]. Consequently, the in-situ fatigue testing machines used in that case are generally quite bulky so the recorded specimen cannot be brought very close to the X-ray detector. Hence, this type of experiment has to be carried out in synchrotron facilities in order to use a parallel X-ray beam which ensures a good spatial resolution (typically around 1 μm) even if the specimen is far from the detector. This is crucial because, usually, the opening of a fatigue crack is small (the crack tip opening displacement is typically below 1 μm). Furthermore, the use of synchrotron X-rays allows to have an important phase contrast in the acquired data. With this type of contrast, it is possible to distinguish cracks at a resolution below the voxel size [CLO 97]. Finally, synchrotron facilities provide a monochromatic (or quasi-monochromatic) beam, which allows to acquire good quality pictures in a short amount of time: usually, the time needed to record the set of radiographs from which the 3D image is obtained (scan) takes between 5 and 10 minutes in synchrotron facilities and approximately one hour with a laboratory tomograph.

The limit of using a parallel beam is that the specimen size is limited by the size of the X-ray detector. So, even if a half-acquisition setup is used (the specimen size is twice bigger than the detector size), the specimens cannot be too thick. For example, the width of the detector available at PSICHE beamline (Soleil synchrotron in France) is 4600 pixels, so with a 0.7 μm voxel resolution, the specimen cannot be thicker than 3.2 mm (without half-acquisition). Therefore, a compromise has to be found because the specimen diameter should be big enough for the crack to propagate internally the longest possible before reaching the surface and small enough to be fully tomographied. For example, Junet *et al.* [JUN 19] have used Ti64 specimens with a cylindrical diameter in the gauge section of 1 mm and Messager *et al.* [MES 19] used specimens in cast Al alloy with a diameter of 3 mm.

In-situ testing micro-tomography has several specific limits such as the fact that the specimen cycling has to be stopped during the acquisition; consequently, such *in-situ* procedures consist, in fact, in acquiring «screenshots» of the crack shape at different instants of its propagation. Also, the file size of the tomographic scans is quite large (*e.g.* 4.5 Go for an 8-bit $3000 \times 3000 \times 500$ volume) so if they have to be analyzed immediately after the acquisition (for example to check if a crack is present in the acquired volume), it is necessary to have an optimized analysis procedure that does not take too much time because synchrotron in-situ experiments usually last a few days (typically three or four days).

1.5 Chapter Synthesis

For decades, fatigue crack initiation and propagation have been studied in metallic alloys. Since the development of ultrasonic cycling techniques, the Very High Cycle Fatigue regime has been extensively studied showing that fatigue fracture could occur at stress amplitudes lower than the conventional fatigue limit (*i.e.* beyond 10^7 cycles) [BAT 99]. Contrary to Low Cycle Fatigue where cracks initiate from the specimen surface, in VHCF, the fatigue cracks tend to initiate internally. A major difference between the two cases is the environment in which the crack propagates because, contrary to internal ones, surface cracks are in contact with the ambient atmosphere.

The environment effect on surface fatigue crack behavior has been widely reported in the literature: cracks in contact with air present shorter fatigue lives and higher crack growth rates than cracks propagating in a vacuum environment [PET 03, HEN 23]. These observations have been explained, for metallic alloys, by the impact of the water vapor and hydrogen present in the ambient atmosphere on fatigue propagation mechanisms [WEI 81]. According to our knowledge, there is no literature reference on the effect of the environment on the propagation of internal cracks. That is one aim of this study.

Because ultrasonic frequencies are needed to cycle fatigue cracks to the VHCF regime, the frequency influence on fatigue has been studied by many researchers [STA 06, SAR 16]. For strain rate insensitive alloys, it is closely linked with the environment effect because, at such high cycling frequency, if a negative stress ratio is imposed, the time required to allow the atmosphere molecules to reach the crack front is reduced. Consequently, for some materials, ultrasonic frequency applied to cracks propagating in air leads to crack growth rates close to those of long cracks propagating in vacuum (as claimed by Holper *et al.* in Al alloy [HOL 03]).

To study the impacting parameters on fatigue behavior, different types of experimental methods are reported in the literature. *Post-mortem* analysis are typically carried out on specimen fracture surfaces with optical microscopes and Scanning Electron Microscopes to identify the propagation regimes of the cracks and the local mechanisms occurring during the whole propagation [HON 17]. The parameters impacting fatigue behavior - such as the environment in

which fatigue cracks propagate [YOS 21] - can be analyzed through the different influences they have on fractographic features. For example, striation marks are typical of fatigue propagation in an air environment.

To monitor the crack behavior all along the fatigue life, many different *in-situ* experimental methods have been developed such as the monitoring of the specimen acoustic nonlinearities to detect crack initiation and to follow the fatigue damage evolution [KUM 09]. This type of method is however limited by the numerous parasitic nonlinearities which can influence such measurements. Thermal monitoring is also used for initiation detection purposes and to record the temperature evolution of a specimen in which a fatigue crack propagates [WAG 09]. This approach can however be limited when cracks initiate far away from the observed specimen surface. Finally, in-situ X-ray 3D imaging allows one to precisely follow the crack propagation because it allows the record of non-destructive direct pictures of the crack 3D shape at different instants of its propagation inside an optically opaque specimen. The limits of such an approach are the heavy required experimental setup, the relatively small specimen size needed for X-ray transmission purposes and the necessity to get access to synchrotron beamlines. Nevertheless, in the present study, this technique is used in combination with temperature measurements carried out all along the in-situ synchrotron fatigue tests.

Graphical Overview

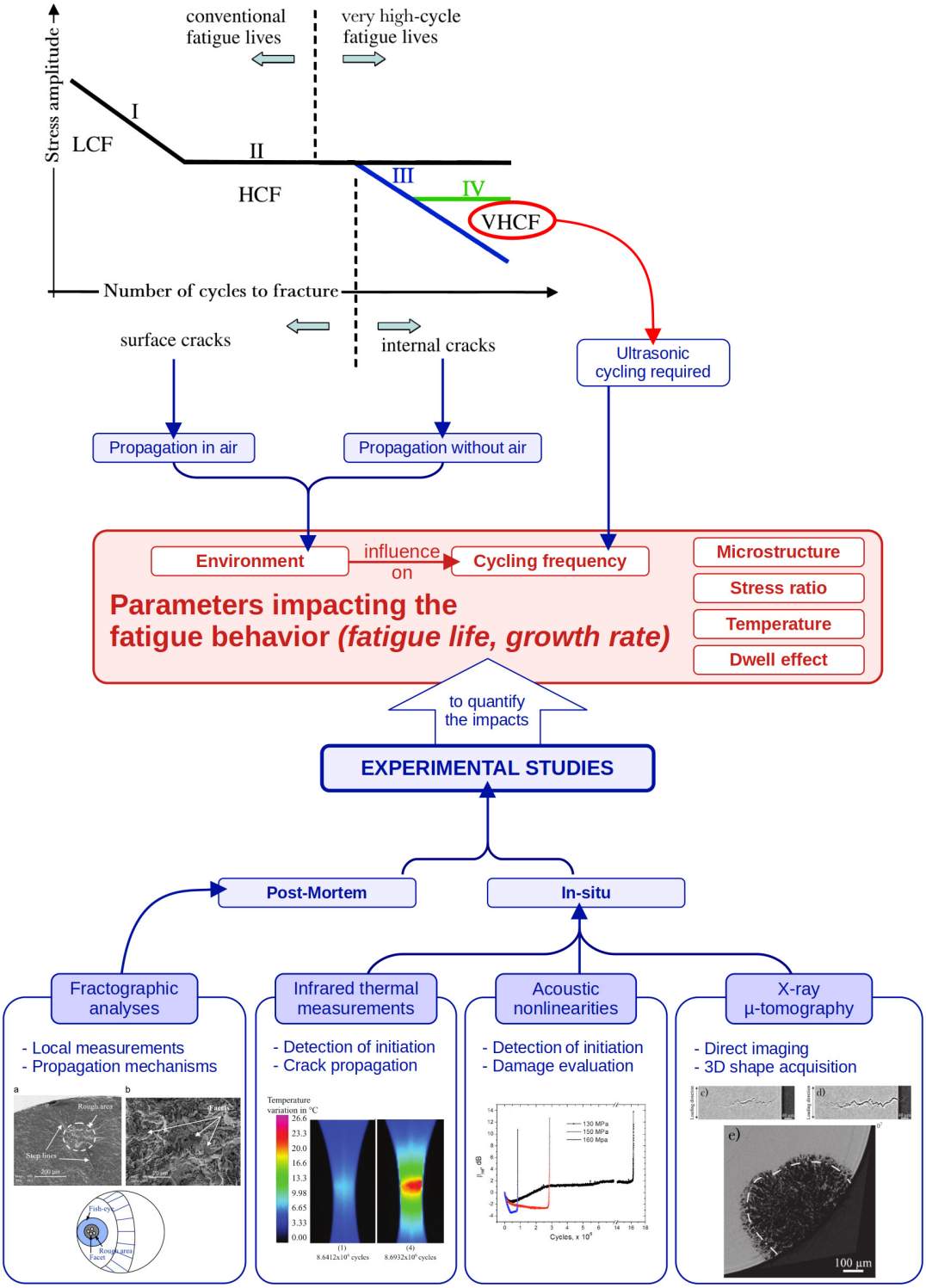

Figure 1.17 | Synthesis of the state of the art chapter

Chapter 2

Material, Experiments & Numerical Protocols

Contents

This work is the continuation of two PhD theses during which synchrotron micro-tomography (μCT) was applied to study internal fatigue cracks. The first one studied the Very High Cycle Fatigue regime of a cast Al alloy with an in-situ ultrasonic machine [MES 20] and the second one was focused on low frequency (20 Hz) high-cycle fatigue of Ti64 [JUN 21]. For both materials, specimens containing artificial defects were used. The present work consists of the adaptation of the ultrasonic in-situ micro-tomography approach to Ti64 in order to study VHCF for a material with smaller grain size than the cast aluminum material studied in the first thesis. A finer microstructure should allow to obtain cracks with a more regular 3D shape which should make the micro-tomography data post-processing easier.

2.1 Studied Titanium Alloy

2.1.1 Microstructure

The material studied in this work is a Ti64 alloy bought from the *Timet* company as a 15-mm-thick plate. This so-called Timetal 64 has been hot-rolled and annealed at 750°C. Its chemical composition is given in Table 2.1.

Al	V	Fe	O	C	N	H	Y	Ti
6.43	4.10	0.15	0.18	0.01	0.004	0.004	<0.001	Bal.

Table 2.1 | **Chemical composition of the studied Ti64** (weight%) according to the technical datasheet provided by the company.

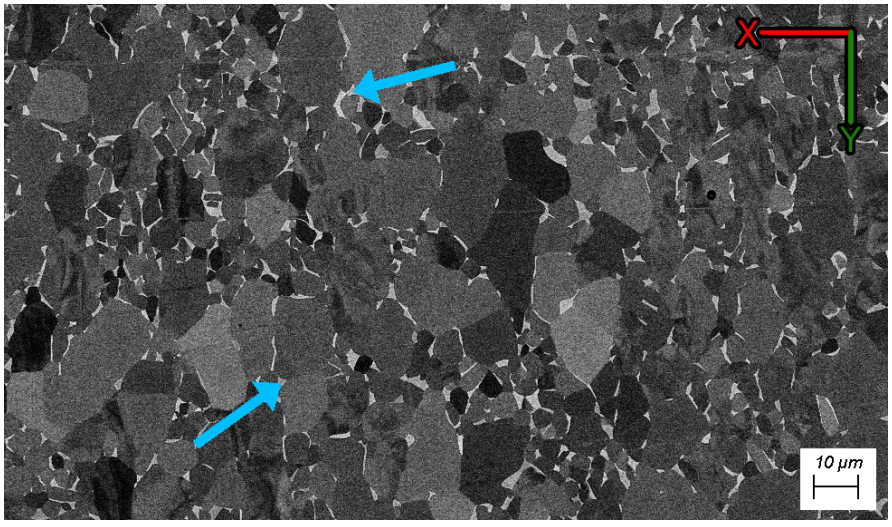

Figure 2.1 | **Phases in the studied Ti64 microstructure** observed with SEM backscattered electron mode. Predominant α phase (in dark grey levels) with β phase at the grains boundaries (light grey levels such as pointed by the blue arrows).

The equiaxed microstructure of the studied material is represented in Figure 2.1. It is composed of small BCC β zones located at the boundaries between larger HCP α regions which compose around 94 % of the surface fraction. The average α grain size has been determined from Electron Backscatter Diffraction (EBSD) acquisitions (*cf.* Fig. 2.3) with Equation 2.1:

$$D_{average} = \sum_{i=1}^{n} \frac{A_i}{A_{tot}} D_i \tag{2.1}$$

with n the number of grains, A_i the area of grain i, A_{tot} the total area of the EBSD map and $D_i = 2\sqrt{A_i/\pi}$ the equivalent diameter of grain i [JUN 19].

This method allows to avoid the large number of small grains to bias the result whereas they constitute only a small fraction of the total observed surface. Figure 2.2a can be compared to Figure 2.2b to point out the difference in grain size if we consider the number of grains or the fraction area. Hence, the grain size will be considered to be $10.8 \pm 1\mu$m.

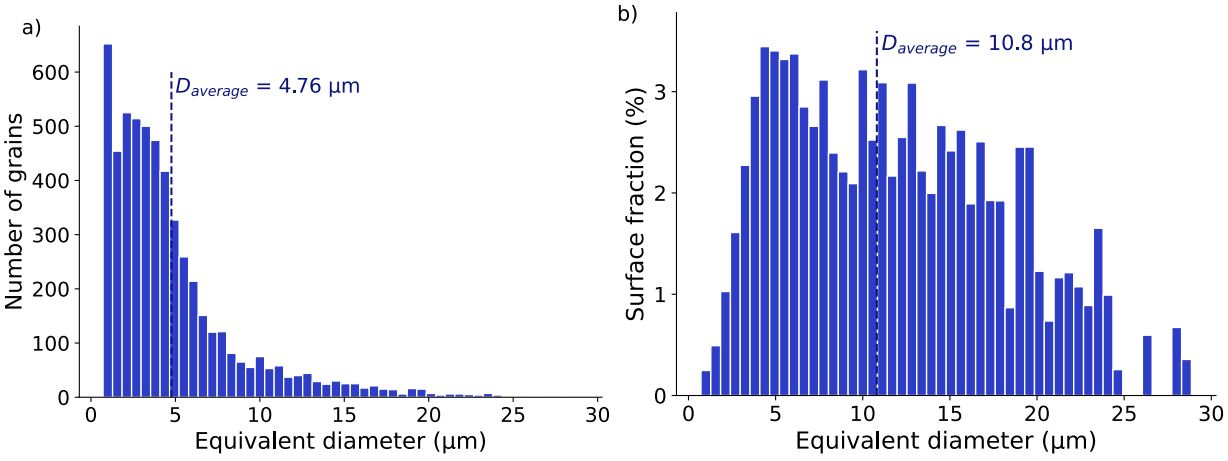

Figure 2.2 | Distribution of equivalent grain diameters of the studied Ti64 estimated with (a) the number of grains per class of equivalent diameter. (b) the grains relative surface fraction A_i/A_{tot} with regard to the whole observed surface A_{tot}. The second approach allows to reduce the influence of small grains on the measurement.

As presented in Section 1.2.1, macrozones can be found in the Ti64 alloy. Some EBSD maps have been obtained on different sections of the original plate to check the presence of such zones. Figure 2.3 represents - for the X, Y and Z directions of the laminated plate - in red the grains whose basal plane normal direction (*i.e.* the $\vec{c}$ -axis) is parallel to the orange line of the figure and in blue the ones with a prismatic plane normal parallel to this orange line. Extended red zones can be observed in the first two cubes of this figure which means that there are macrozones with the $\vec{c}$ -axis aligned with the longitudinal transverse and rolling directions (respectively Y and Z) of the rolled plate. As described by Lunt [LUN 14], this is typical for rolled material.

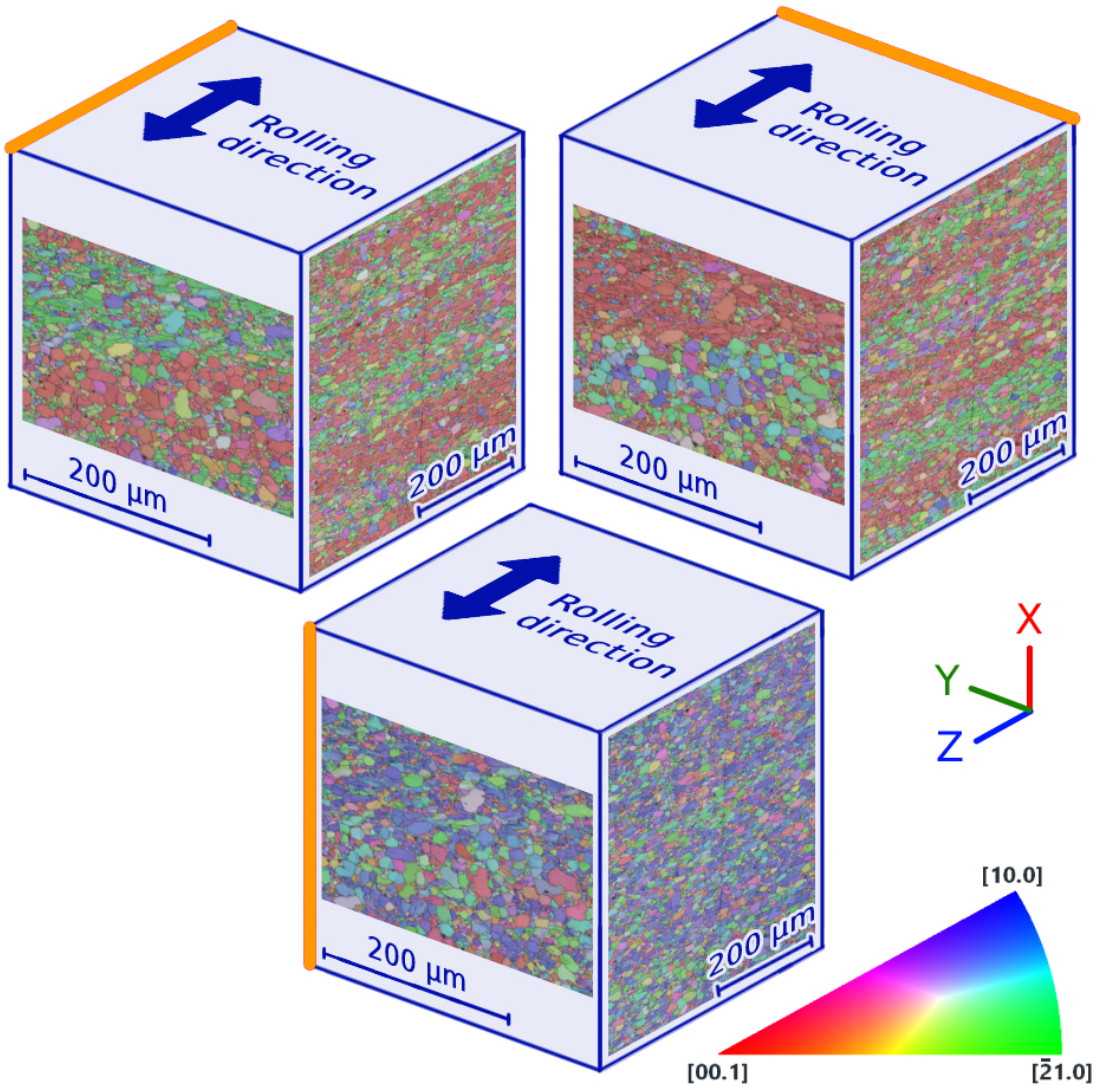

Figure 2.3 | **Microstructure of the rolled sheet used in this study** Each cube presents the IPF showing the crystal directions parallel to the orange line represented in each cube. The rolling process appears to have aligned most of the grains $\vec{c}$-axis in the Y and Z directions leading to the formation of macrozones. A 5°misorientation is used to obtain those EBSD maps.

2.1.2 Mechanical Properties

Table 2.2 gives the nominal mechanical properties of the alloy. Before designing the specimens used for the ultrasonic fatigue tests, a volumetric mass measurement of the material, ρ, has been done. Also, the Young modulus was measured in the case of ultrasonic loading, E_{US}. To do so, a classic procedure has been applied (cf Appendix D). The measured values are $\rho = 4422\ \mathrm{kg\,m^{-3}}$ and $E_{US} = 117.4\ GPa$.

Young Modulus (20°C)	0.2% yield stress	Ultimate Tensile Stress	Elongation
107-122 GPa	830 MPa	900 - 1160 MPa	10 %

Table 2.2 | **Timetal 64 mechanical properties** at room temperature (according to the technical datasheet provided by the company)

The Vickers hardness (500 g) of the material has been measured and compared with Ti64 values reported in the literature (Fig. 2.4). The measured values, around 350 HV, are in good agreement with the literature data. A series of measurements across the plate thickness showed no significant variation in the hardness between the bulk and the surface of the plate.

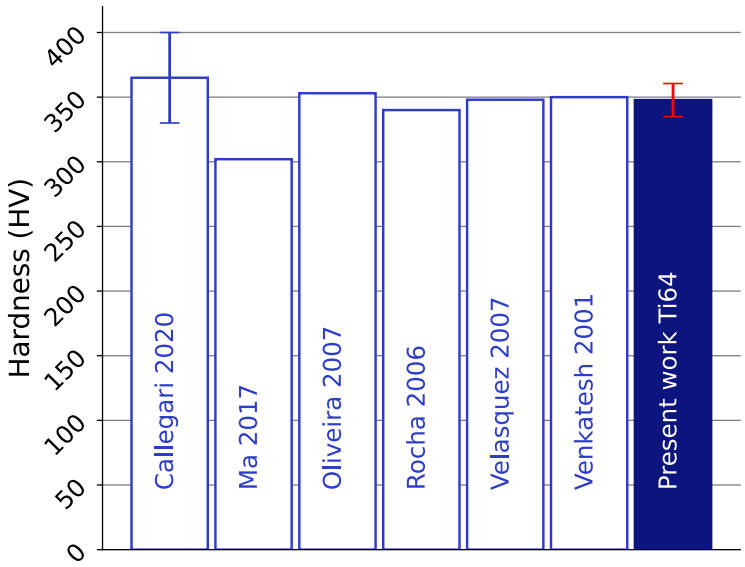

Figure 2.4 | **Literature and measured Vickers hardness.** The uncertainty bars represent the standard deviations in the case of a dataset with many measurements [CAL 20, MA 17a, OLI 07, ROC 06, VEL 07, VEN 01].

2.2 Experimental Procedures

2.2.1 Synchrotron In-Situ Ultrasonic Fatigue Testing Machine

2.2.1.1 Concept

A first ultrasonic fatigue machine was developed in a previous study [MES 20] for in-situ micro-computed tomography at synchrotron facilities; it has been improved in the present thesis.

This apparatus is represented in Figure 2.5 and its components are schematized in Figure 2.7. The machine is composed of a piezoelectric converter (Branson CR-20) which is powered by a 20 ± 0.5 kHz ultrasonic generator (Branson DC922b) and cooled by compressed dried air. Between this converter and the specimen, there are a booster and a horn that mechanically amplifies the ultrasonic signal in order to cycle the specimens. The tension-compression cyclic loading is carried out with a load ratio of $R = -1$. A laser vibrometer monitors the free-end surface velocity of the specimen during cycling to detect potential nonlinearities that may be caused by a crack. This signal is treated by a laser conditioner and used to automatically stop the piezoelectric converter when the nonlinearities increase (this aspect of the protocol is described in detail in Section 2.2.2). A cylindrical PMMA tube surrounds the specimen and transfers the mechanical load with a constant and negligible X-ray attenuation. This tube is not transparent to infrared signal, hence some holes are machined in the structural metallic tube to allow the monitoring of the thermal radiation of the specimen gauge length during the cycling blocks with an infrared camera. Finally, the vibration nodes of the booster are clamped with the structural tube (*cf.* detailed section in Figure 2.5). During tomography acquisitions, a static load is applied to the specimen. This load is controlled thanks to a force sensor (*cf.* Fig. 2.7b). The value of such a load is set at 80% of the stress amplitude to open the cracks in the loading direction and to distinguish them better on the tomographic data [NAK 16].

Because the setup was originally designed to test aluminum specimens, several parts had to be redesigned to support larger static loads (force sensors, loading motor and its support parts). The booster was also added to be able to impose larger stress amplitudes.
Excessive parasitical vibrations occurred during the first tests because the vibration line lay on the vibration nodes of the horn. To reduce those, it has been decided to clamp the whole line on the vibration nodes of the booster. Besides improving the stiffness of the whole setup, this clamping system shown in the section view (S) from Figure 2.5 also allows to avoid a potential rotation along the machine axis. This could prevent successive tomographic scans from having a different reference.

2.2.1.2 Test Calibration for Undamaged Ultrasonic Specimens

The ultrasonic fatigue testing protocol has to be calibrated for the chosen specimen geometry before carrying out crack propagation tests. The following calibration protocol has been applied to a specimen (such as the one represented in Figure 2.21) without any internal notch or any initiated fatigue crack. The specimen was mounted on the vibration line composed of the piezoelectric converter, a 1.5× Booster (serial nb 101-149-052) and a horn (serial nb FR2021-0430). A strain gauge (with a small grid of 0.5×0.5 mm) was glued on the region of interest of the specimen and inserted in a Wheatstone bridge.

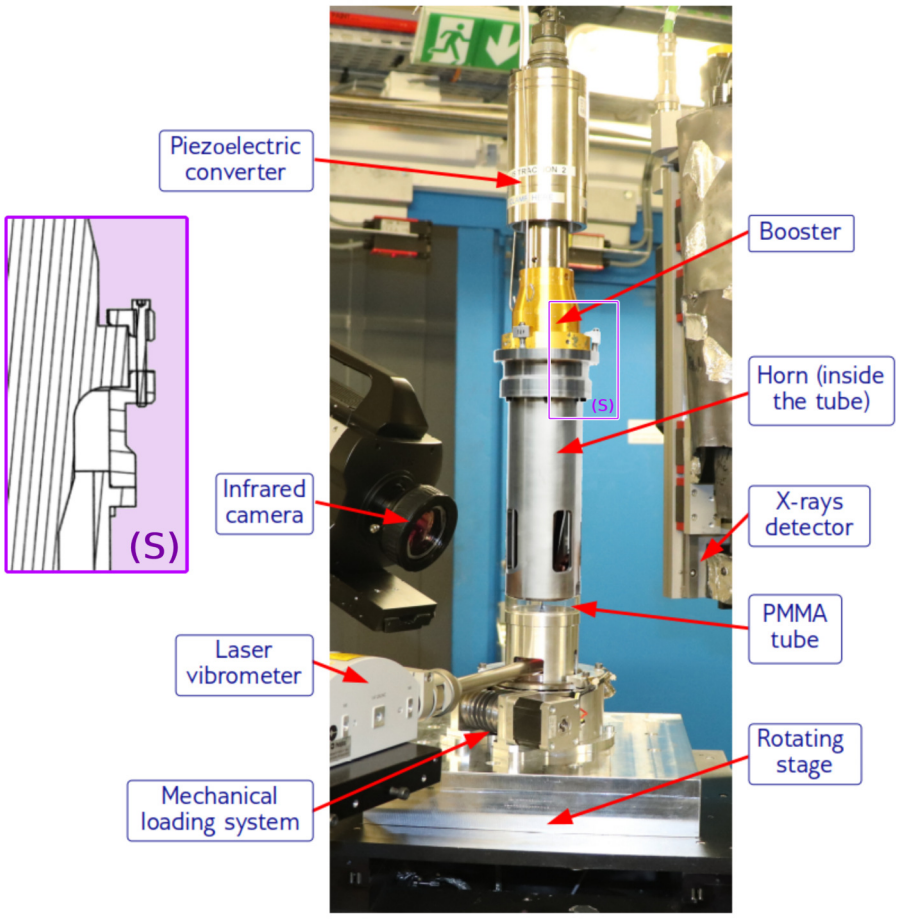

Figure 2.5 | **Ultrasonic fatigue testing machine** installed on PSICHE beamline of the Soleil synchrotron facility. (S) represents a detailed section of the clamping system at the vibration nodes of the booster. All the parts of the machine are schematized in Figure 2.7.

The calibration protocol consists of inputting different control voltages, V_{ctrl}, to the ultrasonic generator and measuring the corresponding strain amplitude to link it to a stress amplitude, σ_a, using the Young modulus, E_{US}, evaluated in Section 2.1.2. However, as the radius of the specimen cross-section in its neck part is small (1.25 mm - *cf.* Section 2.3), the double curvature of the specimen surface on which the strain gauge is glued reduces the fatigue life of the latter. Hence, the strain gauge broke when the stress amplitude was above 250 MPa. Consequently, very few data points could be acquired (*cf.* Table 2.3).

V_{ctrl} (V)	σ_a (MPa)	d_{bot} (μm)	R_a (MPa/μm)
-7.40598	116.5	4.74	24.6
-5.06654	227.1	9.31	24.39

Table 2.3 | **Stress amplitude datapoints acquired with a strain gauge** below 250 MPa

To solve this problem, the laser vibrometer has been used to monitor the specimen free-end displacement amplitude, d_{bot}, for different power control voltage values, V_{ctrl}. As shown in Figure 2.6, this allowed to point out that the relation between d_{bot} and V_{ctrl} is linear (at least below $d_{bot} = 16.5$ μm).

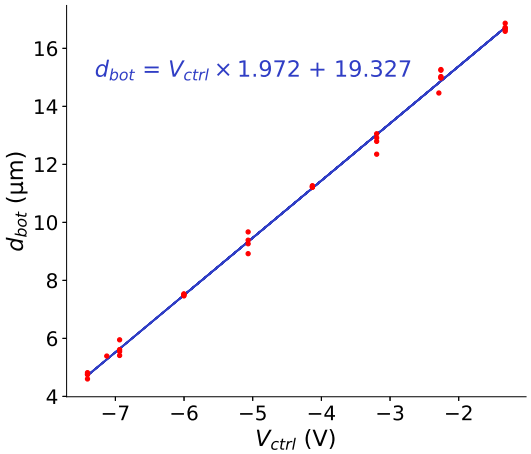

Figure 2.6 | Linear regression and experimental measurements of the specimen free-end surface displacement amplitude, d_{bot}, for different values of power control voltage, V_{ctrl}

The specimen free-end displacement measurements permitted also to estimate a value of the line amplification ratio, R_a, which is the proportionality coefficient between σ_a and d_{bot}. It has been evaluated to be $R_a^{exp} = 24.5$ MPa/μm $\pm\, 2.5\%$ (*cf.* Table 2.3). This value was compared to the one obtained from finite element calculations carried out to design the ultrasonic specimen geometry (in Section 2.3): a harmonic calculation on the geometry at the frequency obtained with a numerical modal analysis gave $R_a^{num} = 22.7$ MPa/μm. So there is an 8% difference between the experimental and the numerical amplification ratio values.

Finally, because there is a linear relation between d_{bot} and V_{ctrl}, the experimental value of the amplification ratio, R_a^{exp}, was chosen to obtain the relation between σ_a and V_{ctrl}:

$$\sigma_a \text{ (MPa)} = R_a^{exp} \times d_{bot} \text{ (μm)} = V_{ctrl} \text{ (V)} \times 48.322 + 473.506 \tag{2.2}$$

Nota: This equation is valid for a tension, V_{ctrl}, used to control the generator ranged between -7.5 V and +7.5 V.

This protocol has been applied to specimens without internal notch or crack but the local stress field around the crack evolves during its propagation. It makes it impossible to compare the fatigue lives of different specimens in a similar graph. In S-N diagrams, the represented stress amplitudes do not take into account the presence of the cracks in the specimens because

such diagrams have an engineering purpose which is to know the number of cycles an initially undamaged part can withstand at a given nominal stress amplitude. So, to compare stress amplitudes calculated in a similar way, **it has been decided, in this work, to consider only nominal values *i.e.* the average stress amplitudes dynamically calculated over the middle cross-section of the specimen without considering the presence of the notch or the crack.**

2.2.2 In-Situ Synchrotron Internal Crack Propagation Experimental Protocol

The in-situ experimental procedure is divided into two phases: crack initiation and crack growth monitoring.

- The initiation phase consists in cycling the specimen with the machine described in Section 2.2.1. This phase is carried out at room temperature, the specimen is not cooled down during cycling and its surface temperature is monitored with an infrared camera. It will be shown in Section 2.4.3.1 that the specimen self-heats by only a few degrees. When the machine is in cycling mode (Figure 2.7a), there is no tensile static force applied on the specimen during its vibration at 20 kHz (so the nominal stress ratio is R=-1). The laser vibrometer monitors the bottom-surface velocity and a real-time Fast Fourier Transform (FFT) of this signal allows to obtain in real time the amplitudes of its fundamental, V_1, second, V_2, and third, V_3, harmonics. The FFT is carried out with a moving average (of 3 timesteps length) on the measured velocity amplitudes. A 80 kHz frequency bandwidth is used and no numeric filters are activated. Based on the work of Kumar *et al.* [KUM 09], a nonlinear parameter, α, depending on the value of the second harmonic which is normalized by the fundamental amplitude can be computed. It is presented in Equation 2.3 where $(.)_0$ represents the value of $(.)$ at the beginning of the cycling, *i.e.* when the material is not damaged (reference state).

$$\alpha = 20\log_{10}\left(\frac{V_2}{V_1^2}\right) - 20\log_{10}\left(\frac{V_2}{V_1^2}\right)_0. \tag{2.3}$$

The α notation - which differs from the one used by Kumar *et al.* [KUM 09] presented in Section 1.4.2.2 - is proposed to avoid any confusion with the nonlinear parameter β used in the nonlinear acoustic community for the quadratic term of the nonlinear Hooke's law [KUM 09]. This α parameter characterizes the nonlinearities of the whole testing system: nonlinearity of the material in the specimen, nonlinearities due to the potential initiation of a crack and nonlinearities coming from the horn, the booster, the converter and their connections. The experimental surroundings may have an impact on this nonlinearity. Consequently, to ensure a good reproducibility of the ultrasonic fatigue tests and an accurate crack detection by this technique, the dry compressed air used to cool the converter has to be stable and the temperature of the testing room has to be stabilized with air con-

ditioning all along the test. Hence, the ultrasonic cycling can be automatically stopped by setting a threshold on the velocity second harmonic, V_2. Once the cycling is automatically stopped because of the detection of a potential crack, a static load is manually applied to the specimen (80% of the stress amplitude). A micro-tomography acquisition is then carried out (machine in its acquisition mode - Figure 2.7b).

The experiments reported in this PhD thesis have been carried out at SOLEIL and ESRF synchrotrons. On the PSICHE beamline (SOLEIL synchrotron facility), a 65 keV pink beam (multi-bunch mode) obtained by filtering the white beam with a 3mm Al + 0.304mm W plate was used. With a 4608 × 2592 pixels Hamamatsu ORCA Lightning camera, a $1.5 \times 3.2 \times 3.2$ mm^3 volume (1.5 mm being along the specimen loading direction) with a voxel size of 0.7 μm can be acquired with a 360 degrees acquisition containing 7000 projections (for better statistics and fewer artifacts). The scan takes approximately 10 minutes. Because exposure times needed for the tomography of metallic alloys are relatively long ($\sim$ 100 μs), a continuous beam signal can be supposed when the camera shutter is open.
On the ID19 beamline (ESRF synchrotron), a multi-bunch wiggler 70 keV pink beam was used (filtered with a 2.8mm Al + 0.7mm Cu plate). With a 2160×2560 pixels detector and a half-acquisition setup (5300 projection and exposure time of 0.1s), the $1.5 \times 3.2 \times 3.2$ mm^3 volume can be acquired in 10 minutes with a voxel size of 0.7 μm.
The reconstruction time takes typically 15 minutes for the $1.5 \times 3.2 \times 3.2$ mm^3 volume. Consequently, at the two beamlines, the 3D data from the tomography acquisition are available in less than half an hour.
When an automatic stop happens, a tomographic scan has to be acquired to carefully check if the stop is really due to a crack initiation. That is necessary because some false detections can occur in reason of the very high sensitivity of the technique to parasitic vibrations (*cf.* Appendix C). If no crack is detected on the 3D data, the initiation phase continues as described above but if an initiated crack is observable on the tomographic data, the procedure shifts to the propagation phase.

- During the propagation phase, the number of cycles is pre-set so that the ultrasonic cycling is not controlled by the laser vibrometer anymore. Even if this detection system is still active, to prevent the initiated crack from propagating too quickly, each loading block is limited in number of cycles (typically between 10^4 and 5×10^6 cycles corresponding to a cycling time ranging from 0.5 to 250 seconds at 20 kHz) to more precisely control the crack propagation between two successive tomography acquisitions. These number of cycles have been chosen so that the crack advance during each loading block would be detectable for a crack growth rate maximum value of 5×10^{-7} m.cycle^{-1} (*i.e.* larger than a 5 μm crack propagation at ultrasonic frequency). This propagation phase is carried out

until the crack has grown as far as the specimen cannot be put in resonance anymore. In that case, the crack reaches the specimen surface and it usually covers more than 85% of the specimen section. Consequently, **in the rest of this work, the total number of cycles applied to the specimen until it cannot resonate anymore (because of the propagated crack) will be considered as the number of cycles to fracture.**

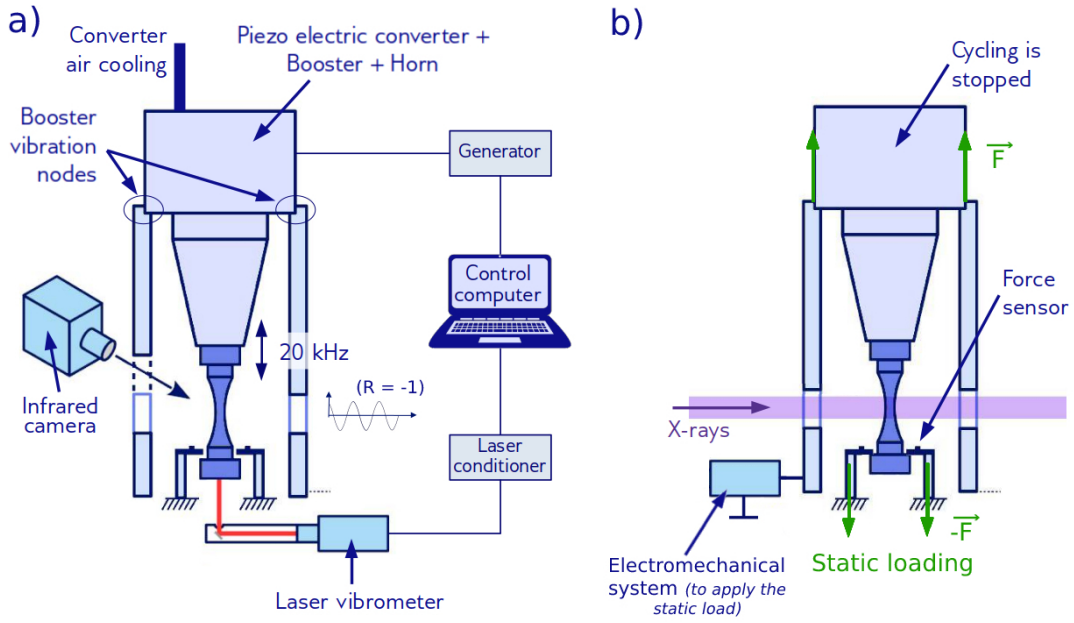

Figure 2.7 | **Schematic representation of the ultrasonic machine in the two used experimental modes** (a) cycling mode: ultrasonic loading is on but no static load is applied, the measurement systems (IR camera, laser vibrometer) are recording. (b) tomography acquisition mode: no fatigue cycling but a static loading, X-rays are used to carry out micro-tomography.

Two specimens were cycled without the use of a threshold set on any velocity harmonic amplitude in order to record the signal acquired by the laser vibrometer during a whole cycling test carried out without any stop until the fatigue fracture. Figure 2.8 represents the amplitudes of the second and third harmonics for the two specimens. It is possible to remark that the second harmonic amplitude starts to increase before 70% of the total fatigue life and undergoes a strong increase just before the final fracture whereas the third harmonic one does not seem to vary until the very end of the fatigue life. For this reason, a threshold on the amplitude of the second harmonic was used to detect internal crack initiations. However, because it was required by the software, a threshold on the amplitude of the third harmonic was also activated.

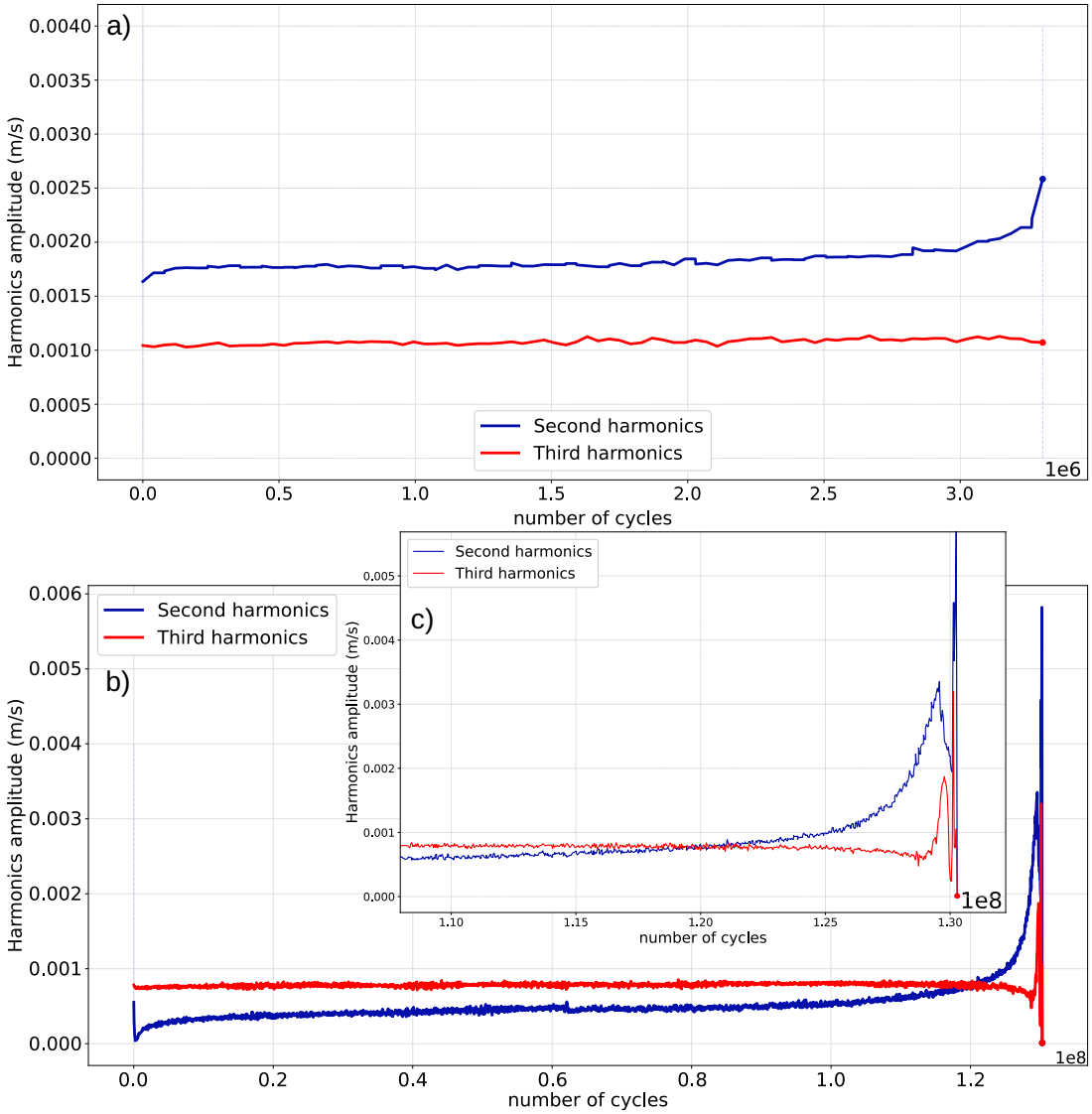

Figure 2.8 | **Evolution of the second and third amplitude of the ultrasonic velocity signal acquired by the laser vibrometer during the whole fatigue life of two specimens** (a) Specimen 59 cycled at 500 MPa. (b) Specimen 55 cycled at 330 MPa and (c) Detailed view of the end of the cycling represented in (b). The second harmonic amplitude seems more sensitive to crack propagation than the third harmonic one.

The typical evolutions of the velocity second harmonic amplitude used to detect crack initiation during an ultrasonic loading are represented in Figure 2.9. For Specimen nb 45, a sudden increase of the harmonic amplitude stopped the ultrasonic cycling (red point in Fig. 2.9a) whereas for Specimen nb 61 (Fig. 2.9b), this parameter progressively increased to reach the specified threshold (at 10^{-3}m/s in this case). These two cases are typical of the two types of internal crack detection which occurred during the in-situ synchrotron experiments.

However, for Specimen nb 53, the first internal crack imaging with tomography was after the cycling had been stopped by an important increase in the velocity third harmonic but without any evolution of the second one (*cf.* the corresponding red point in Fig. 2.9d). Such an increase in the third harmonic without any evolution of the second one was frequently observed when false detections occurred. For Specimen nb 53, it allowed to detect an internal crack very early in its fatigue life so the crack could be imaged while it was still very short.

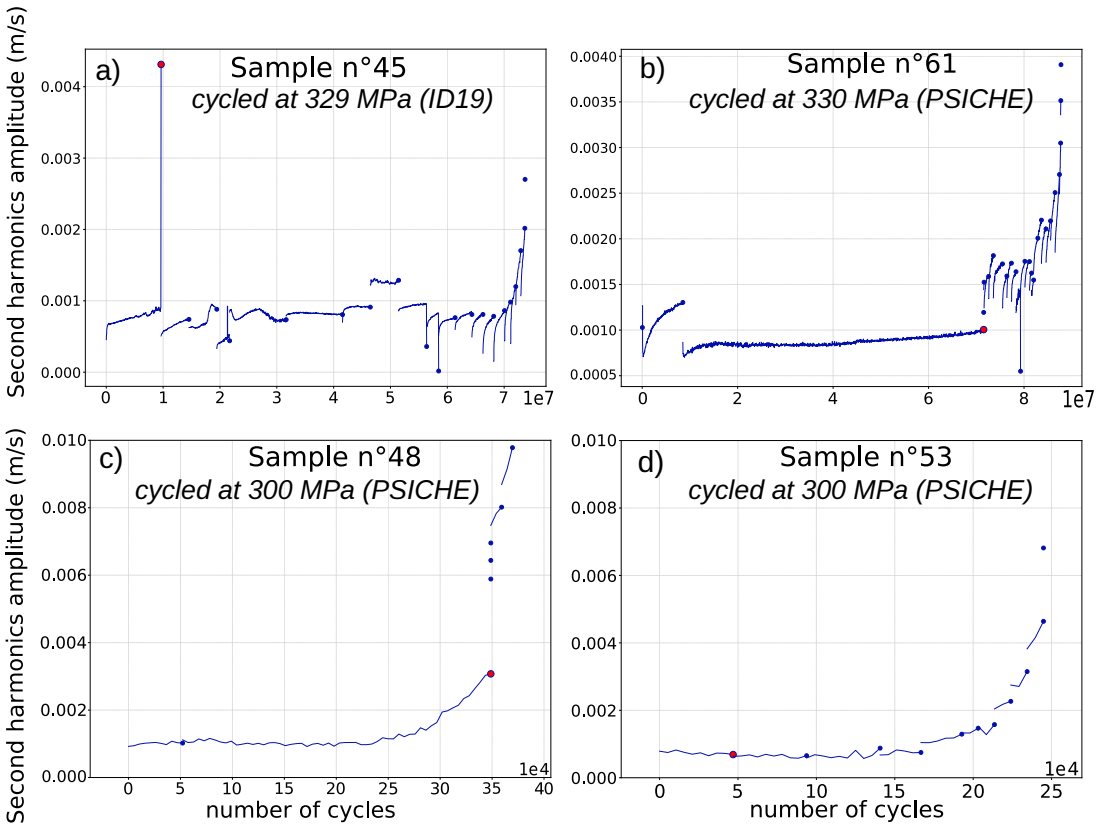

Figure 2.9 | **Second harmonic of the specimen free-end surface velocity monitored with the laser vibrometer during the cycling blocks of in-situ synchrotron experiments** (a) & (b): Two specimens cycled during long cycling blocks (data used to control the ultrasonic generator during the cyclings). (c) & (d): two specimens cycled during short cycling blocks (data acquired during the experiment and post-processed afterward). Each blue dot represents a tomographic acquisition and the red dots correspond to the moment where the internal crack was detected for the first time on the tomographic data. Nota: (c) & (d) were plotted from the signal acquired by another ultrasonic signal acquisition system (which has a 1 MHz acquisition frequency).

These previous examples illustrate clearly the difficulty of using the velocity second harmonic (*i.e.* the α parameter) to reliably detect internal fatigue crack initiation. As explained before, this parameter depends on the nonlinearities of the whole experimental system. This is the

reason why using this parameter to detect internal fatigue crack initiation can be biased by external parasites (false detections where the threshold was reached for the second or third harmonic but no internal crack could be observed in the tomographic data, Specimen nb 53 being the only exception).
Another argument justifying the influence of the experimental surroundings on the vibrometer signal quality is that the first crack detections that occurred during the synchrotron experiment at ID19 beamline (ESRF synchrotron) were some sudden second harmonic amplitude increases (Figure 2.9a). However, for the experiment at PSICHE beamline (SOLEIL synchrotron), only progressive ones (Fig. 2.9b and 2.9c) allowed to detect cracks for the first time in the different specimens.

2.2.3 Long Crack Propagation Test in Air at Ultrasonic Frequency

Another experimental procotol has been used to measure the crack growth rates of long surface cracks in Ti64 specimens loaded at 20 kHz (without the use of synchrotron tomography). For that purpose, the experimental protocol has been adapted from the works of Perez Mora, Ouarabi and Messager [MES 20, OUA 18, PER 10].

2.2.3.1 Ultrasonic Propagation Specimen Design

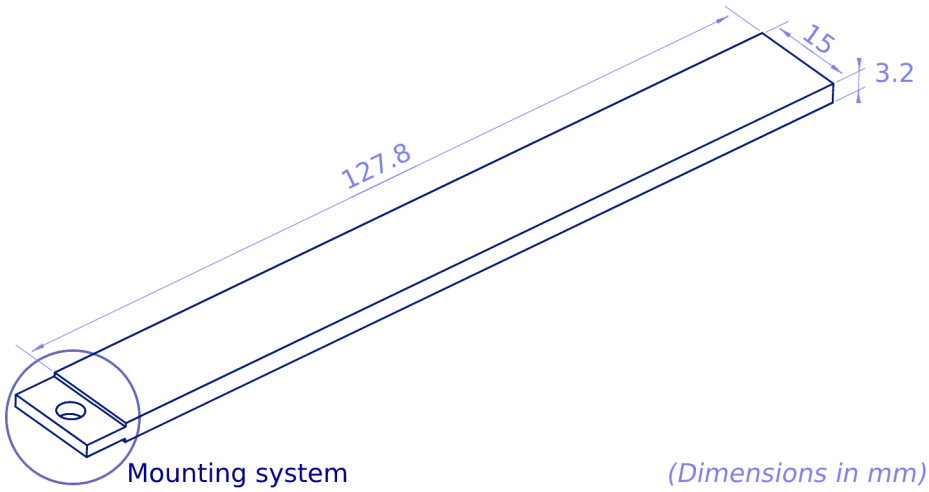

Figure 2.10 | **Drawing of the ultrasonic fatigue propagation specimen** used in this study.

The specimen geometry used to study ultrasonic fatigue crack propagation has been determined as described in Section 2.3.1.1 of A. Messager's thesis [MES 20]. With the same thickness, the same width and the same mounting system, the specimen length l is determined with Equation 2.4.

$$l = \frac{1}{2f}\sqrt{\frac{E_{US}}{\rho}} = 127.8\text{mm} \tag{2.4}$$

with $f = 20$ kHz the aimed resonance frequency, $E_{US} = 117.4$ GPa the Ti64 Young modulus and $\rho = 4422$ kg/m^3 its volumetric mass.
The resulting Ti64 specimen dimensions are shown on the technical drawing from Figure 2.10. As described in Section 2.2.3.3, the specimens will be notched before the tests to force the crack to initiate at a precise location (in the middle of the specimen, where there is the highest stress amplitude) and to shorten the initiation duration.

2.2.3.2 Test Calibration

In the case of ultrasonic cycling, as detailed in A. Messager's thesis [MES 20], Wu & Bathias proposed, for a test run under displacement control (like an ultrasonic test) with the amplitude, U_0, imposed at the top of the specimen, to write the mode I stress intensity factor range as follows [WU 94]:

$$\Delta K_I = \frac{E_{US}}{1-\nu^2} U_0 \sqrt{\frac{\pi}{a}} F\left(\frac{a}{W}\right) \tag{2.5}$$

with E_{US} and ν, respectively the Young modulus and the Poisson ratio for Ti64, a the crack length and W the specimen width as summarized in Figure 2.11.

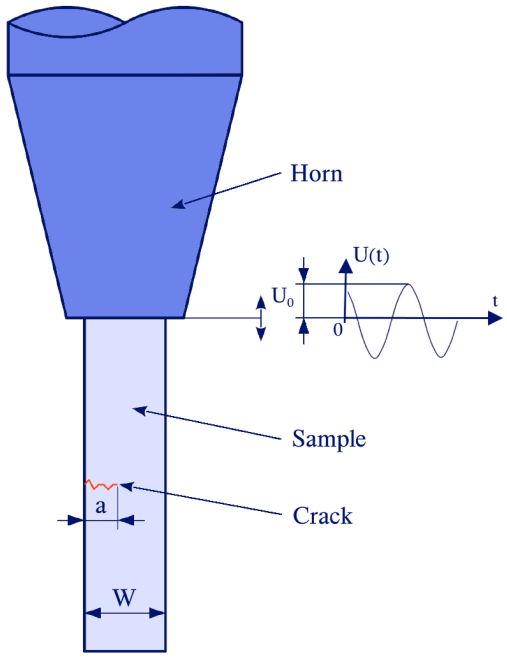

Figure 2.11 | **Summary of the parameters used in Equation 2.5** (Figure from A. Messager's thesis [MES 20]).

The procedure required to determine the $F(a/W)$ function [PER 10, OUA 18, MES 20] has been done with the finite elements software *Abaqus* and is decomposed in two steps:

- First, for different crack lengths, a modal analysis is carried out on a geometry that includes the whole horn (made of Ti64) and the specimen to obtain - for each crack length a - the value of the first longitudinal eigen mode which should be around 20 kHz. As explained below, some other resonance modes are close to this one and might influence the loading mode when the crack is too long. For this type of finite element analysis, a mesh as shown in Figure 2.12 is created for different values of a (it is refined near the crack tip and the crack opening is equal to 10 μm to avoid volume interpenetration in the software). The results are presented in Figure 2.14 and reveal that the resonance frequency decreases when the crack size increases as pointed out in Ouarabi's thesis [OUA 18].

- A 2D harmonic calculation is then carried out for each crack length with the resonance frequency - determined from the modal analysis - applied to the model. As the geometry is thin the finite element calculation is carried out in plane stress. Furthermore, it has been decided to model only half of the geometry because the frequency is set to be the resonance frequency of a free specimen. Hence, the nodes at the bottom boundary of the geometry which do not constitute the crack are fixed and a sinusoidal displacement with an amplitude $U_0 = 1$ μm is applied to the top nodes (*cf.* Figure 2.13a). As explained just below, the crack tip opening displacement (CTOD) will be computed to deduce the stress intensity factor range. For this reason, the mesh around the crack tip is refined (Figure 2.13b). Finally, for each crack length, the SIF factor range is estimated and the $F(a/W)$ function can be identified from Equation 2.5 (*cf.* Figure 2.16).

The CTOD method used to estimate the SIF range is based on Linear Elastic Fracture Mechanics assumptions. It is valid to use these hypotheses in the present case because the plastic deformations are only localized in the close vicinity of the crack tip. In this case, the displacement field in the vicinity of the crack tip can be written at any point as follows:

$$u_x = \frac{K_I}{4G}\sqrt{\frac{r}{2\pi}}\left((2k+1)cos\left(\frac{\theta}{2}\right) - cos\left(\frac{3\theta}{2}\right)\right) - \frac{K_{II}}{4G}\left((2k+3)sin\left(\frac{\theta}{2}\right) - sin\left(\frac{3\theta}{2}\right)\right) \quad (2.6)$$

$$u_y = \frac{K_I}{4G}\sqrt{\frac{r}{2\pi}}\left((2k+1)sin\left(\frac{\theta}{2}\right) - sin\left(\frac{3\theta}{2}\right)\right) - \frac{K_{II}}{4G}\left((2k+3)cos\left(\frac{\theta}{2}\right) - cos\left(\frac{3\theta}{2}\right)\right) \quad (2.7)$$

$$u_z = \frac{2K_{III}}{4}\sqrt{\frac{r}{2\pi}}sin\left(\frac{\theta}{2}\right) \quad (2.8)$$

with $G = \frac{E_{US}}{2(1+\nu)}$ the dynamic shear modulus, $k = \frac{3-\nu}{1+\nu}$ in the plane stress conditions, r and θ the radial coordinates around the crack tip of the given point as illustrated in Figure 2.15.

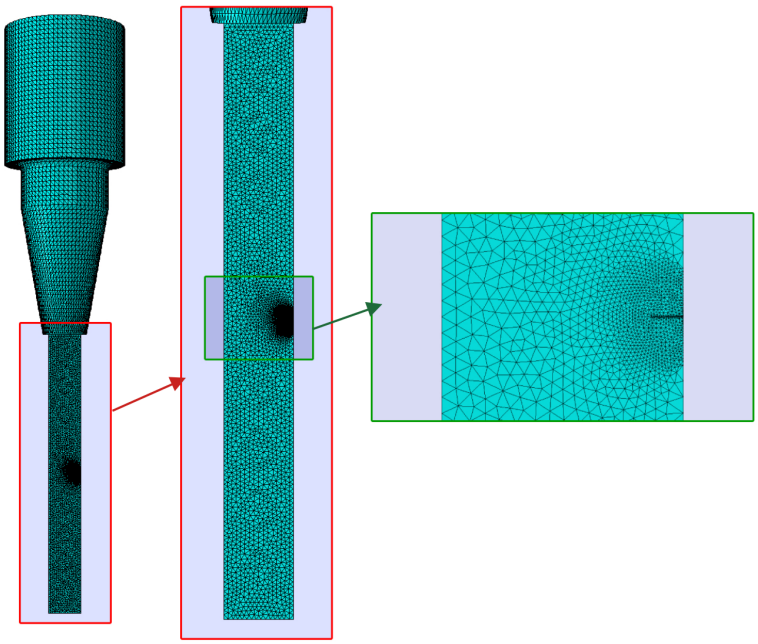

Figure 2.12 | **Mesh used for the modal analysis in Abaqus** The horn and the specimen are meshed with a refinement around the crack.

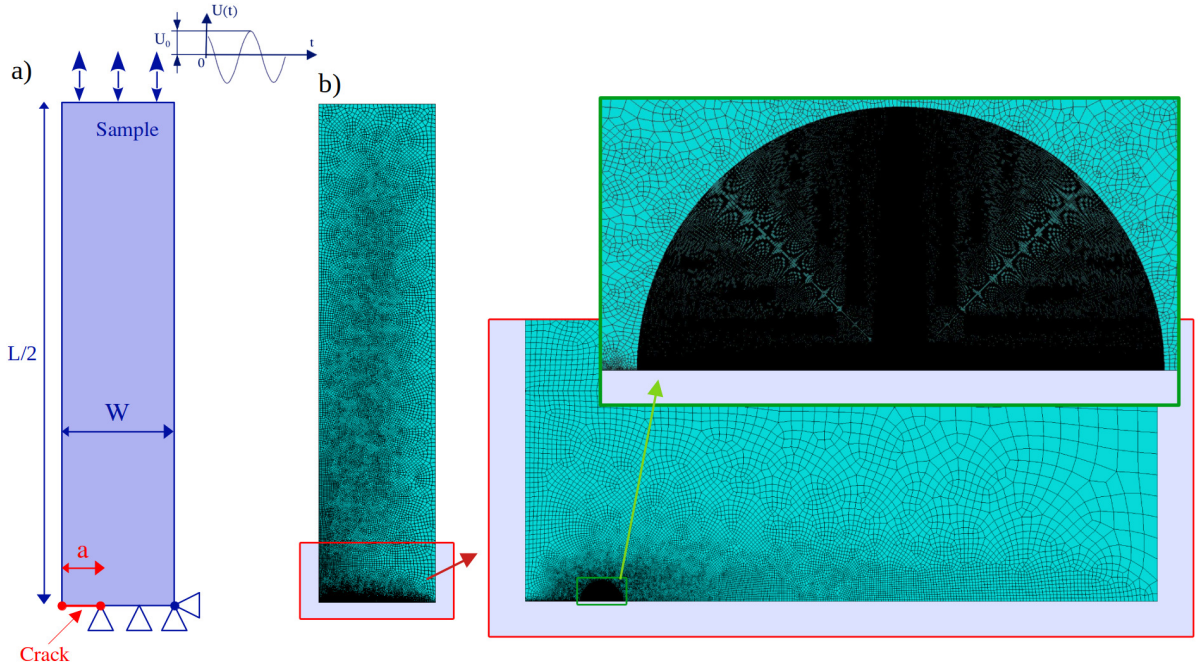

Figure 2.13 | **Geometry used in the 2D plane stress harmonic calculation in Abaqus** (a) Dimensions and boundary conditions used in the calculation. (b) Refined mesh at the crack tip.

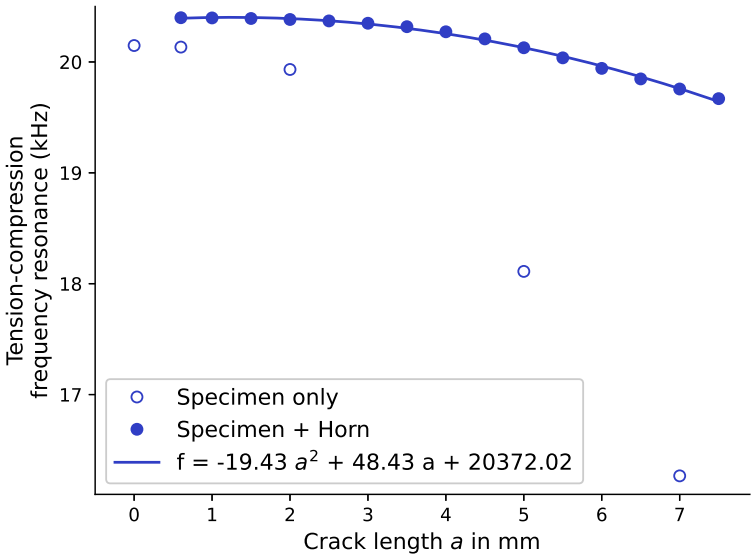

Figure 2.14 | **Resonance frequency drop when the crack length increases** according to finite element simulations. A more important drop is obtained when the simulation is carried out without the horn so it is necessary to consider it in the finite element simulations.

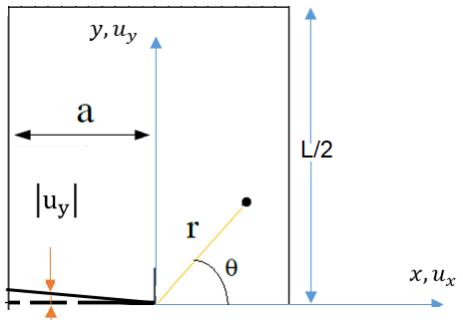

Figure 2.15 | **Notations and axis used in the CTOD method** for evaluating the SIF (Figure from Ouarabi's thesis [OUA 18]).

It is generally supposed that the crack does not propagate when it is closed. Consequently, the effective SIF range ΔK_{eff} is approximated as $\Delta K_{eff} = K_{max} - K_{op}$ with K_{op} the minimum SIF value for which the crack is open. With an ultrasonic loading at 20 kHz, the literature does not report any way to experimentally determine the value of K_{op}. Hence, as the cycling was carried out under a nominal stress ratio of $R = -1$, the crack is supposed to be closed when the applied stress is negative ($K_{op} = 0$) and only the positive part of ΔK is considered to make the crack propagate: $\Delta K_{eff} = \Delta K^{+}$. For this reason, Equation 2.7 can be applied along the crack

(*i.e.* $\theta = 180°$ and r between 0 and a) to obtain the SIF range from the CTOD as follows:

$$\max(u_y(t)) = \frac{K_{I,max}}{2G}\sqrt{\frac{r}{2\pi}}(1+k) = \frac{\Delta K^+}{2G}\sqrt{\frac{r}{2\pi}}(1+k) \iff \Delta K^+ = u_y^{max}\frac{2G}{1+k}\sqrt{\frac{2\pi}{r}} \quad (2.9)$$

Finally, as this approach provides a ΔK value for each crack length a, it is possible to use Equation 2.5 to determine the $F(a/W)$ function (*cf.* Figure 2.16). As explained in A. Messager's thesis [MES 20], this numerical procedure is used for a a/W ratio up to 50% because, for larger cracks, the resonance mode becomes too much influenced by the crack and does not correspond to tension-compression loading anymore (parasitic modes with a resonance frequency too close to the longitudinal one are present).

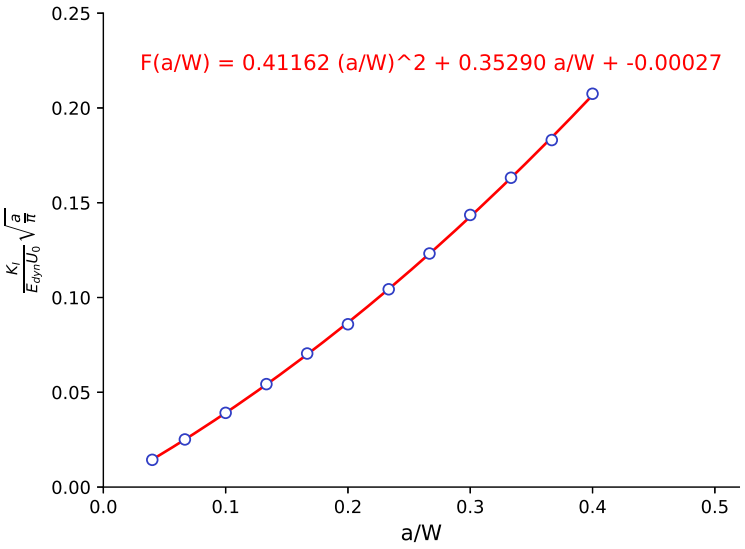

Figure 2.16 | **Polynomial regression used to estimate the $F(a/W)$ function** (for our specimen in Ti64) from Abaqus calculations carried out on the geometry shown in Figure 2.10

2.2.3.3 Ultrasonic Crack Propagation Protocol

The experimental protocol used in the present work to measure surface crack growth rates at 20 kHz has been presented in A. Messager's thesis and is summarized in the following paragraphs [MES 20].

The ultrasonic (US) crack propagation specimens are notched on one side with a micro-cutting machine. The size of the initial notches ranges between 500 and 1000 μm (this length is taken into account in the measurement of the crack size as indicated in Figure 2.17b)). Before the tests, the observed surface is polished down to 4000 grit SiC paper, then a super-polishing is carried out for 10 minutes with an Oxide Polishing Suspensions (OPS) preparation (*cf.* Figure 2.17a).

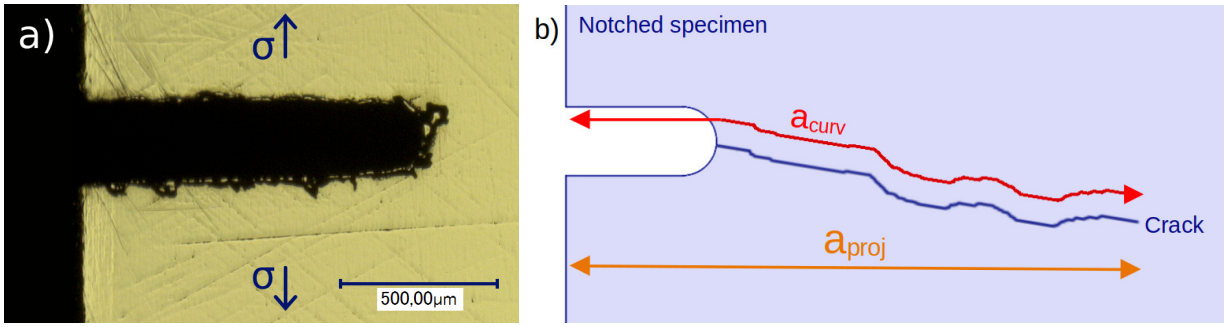

Figure 2.17 | **Notch machined on one edge of the specimen** (a) Optical microscopy picture of the polished specimen surface. (b) Scheme of the crack length measurements: a_{curv} is used to calculate crack growth rates and a_{proj} is used to determine SIF ranges.

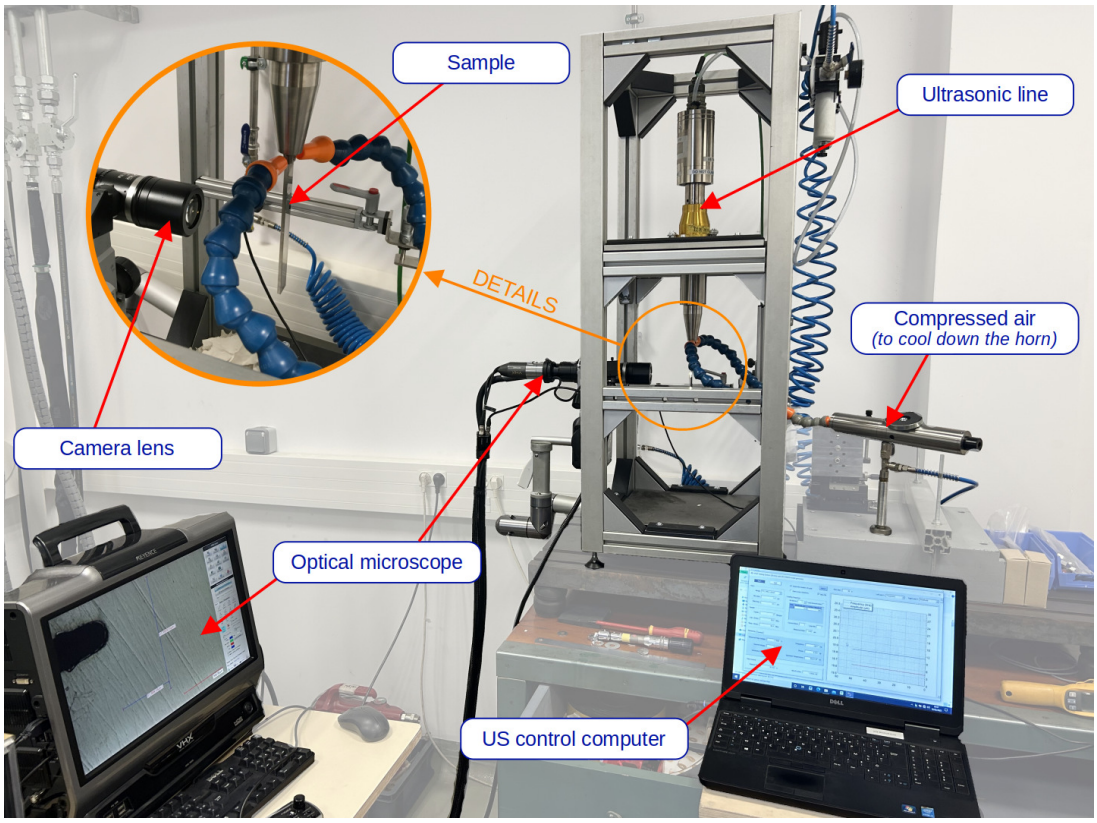

Figure 2.18 | **Ultrasonic fatigue propagation setup**

To carry out the ultrasonic fatigue crack propagation tests, the same ultrasonic line as the one described previously for in-situ tests (ultrasonic generator + piezo-electric converter + booster + horn) is used without the synchrotron tomography adapted support part and the static loading cell (*cf.* Fig. 2.18). The specimens are observed with a *Keyence* ® optical microscope to measure the crack size after each cycling block. However, as the specimen is vibrating at 20 kHz, the

cycling has to be stopped to measure the crack length with good accuracy (which is around 8 μm with the higher magnification lens of the used microscope).

The ultrasonic crack propagation tests are divided into an initiation and a propagation phase:

- **Initiation** - The aim is to initiate a crack from the artificial notch at the lowest possible SIF range. For this, an initial imposed displacement amplitude is estimated with Equation 2.5 from the initial crack length (*i.e.* the notch length) and an initial SIF range value. If the crack does not initiate after 10^7 cycles under this displacement amplitude, the SIF range is increased by 0.1 MPa $\sqrt{\text{m}}$ steps until a crack propagation is observed with the optical microscope. The crack has to propagate more than 500 μm from the initial notch to consider that the stress field at the crack tip is not influenced anymore by the notch. Once this is the case, the crack is considered to be initiated.
- **Propagation** - The propagation is divided into successive cycling blocks to be able to measure the crack length when the ultrasounds are turned off between two blocks. Usual low-frequency fatigue crack propagation tests follow the ASTM E647 standard test method [AST13] which recommends that the propagation tests have to be carried out with a constant SIF range. At ultrasonic frequencies, it is not possible to control in real time this parameter while cycling. Since this standard test method imposes keeping a maximum ΔK variation of 7% during a cycling block, this method has been adapted as it was done in the thesis of Perez Mora, Ouarabi and Messager [PER 10, OUA 18, MES 20]. For this reason, before starting a block during which the crack will propagate, **(i)** a maximum crack length is estimated to be sure that the SIF range will not exceed 1.07 times its initial value given that the displacement amplitude is fixed during a whole cycling block.
  Another crack length condition is set to be sure that the crack propagation distance is larger than the cyclic plastic zone of the previous block. That means that **(ii)** the crack has to propagate at least during more than two times the cyclic plastic zone radius of the previous block.
  If these two conditions (i) & (ii) are respected, the cycling block is considered to be valid.
  Once the crack has been initiated, the displacement amplitude is kept constant and cycling blocks are carried out to make the crack propagate. This procedure is maintained until the crack growth rate reaches 10^{-8} m/cycle. When this maximum crack growth rate is reached, the first part of the propagation phase is finished and the second part starts: the displacement amplitude is progressively decreased for the following cycling blocks until there is no observable propagation at all during a 10^7 cycles-long block. This means that with the spatial resolution of our optical microscope ($\approx$ 8 μm) the smallest detectable crack growth rate is around 10^{-12} m.cycle^{-1}. During the final part of the protocol, the displacement amplitude is kept constant as it was done in the first part and cycling blocks are carried out until the overall crack length is larger than 50% of the specimen width.
  This three-part protocol allows to run three times through the ΔK range in order to obtain

crack growth rate data. Such an increasing SIF range procedure followed by a decreasing and another increasing one satisfies the ASTM standard method recommendations.

2.3 Specimen Design and Fabrication for Synchrotron In-Situ Internal Crack Propagation Tests

The in-situ ultrasonic cycling specimens are designed to have their first longitudinal eigen mode at 20 ± 0.5 kHz. For that purpose, the geometry is first approximated in the case of an axisymmetric specimen by a 1D-model [BAT 05]. For this simplified configuration (*cf.* Fig. 2.19), the geometric parameters can be linked with Equation 2.10.

$$L_2 = \frac{1}{k_1} \arctan\left(\frac{1}{k_1}\left(\frac{k_3}{\tanh\left(k_3 L_1\right)} - k_2 \tanh\left(k_2 L_1\right)\right)\right) \text{ with } \begin{cases} k_1 = 2\pi f \sqrt{\rho / E_{US}} \\ k_2 = \operatorname{arcosh}(R_2/R_1)/L_1 \\ k_3 = \sqrt{k_2^2 - k_1^2} \end{cases} \quad (2.10)$$

with R_1, R_2, L_1 and L_2 the geometric parameters from Figure 2.19, f the resonance frequency, ρ and E_{US} respectively the volumetric mass and the Young modulus of the material.

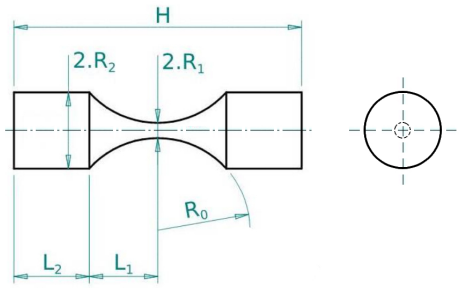

Figure 2.19 | **Simplified specimen geometry** considered by the 1D-model from Bathias & Paris [BAT 05]

The time needed to acquire a micro-tomography scan depends on the thickness of the specimen. As a synchrotron experiment only lasts a few days (4 days max.), it has been decided to impose the thickness of the region of interest of the in-situ specimens to be 2.5 mm in order to be able to acquire a consistent amount of tomographic data during the synchrotron experiments. So with $R_1 = 1.25$ mm and $R_2 = 5$ mm (to keep enough space for the threading), the L_1 dimension is chosen to have a long enough specimen with a not-too-short L_2 dimension. Most importantly, R_0 has to be as large as possible to induce a nearly constant longitudinal stress value around the center of the specimen. The specimen geometry resulting from this approach is then imported in the Finite Element Analysis software *Abaqus* to carry out several modal analyses to optimize

the design: heads with a specific geometry allowing to apply the static loading during tomography will be added and the final geometry needs its first longitudinal eigen mode to be equal to 20 ± 0.5 kHz. The stress distribution around the central region of interest is determined and one can check if the other eigenmodes are not in the 20 ± 2 kHz range to avoid any parasitic mode. The final geometry is illustrated in Figure 2.21; it has a longitudinal stress decrease of 3% maximum in a 1.64 mm-thick region around the specimen center as depicted in Figure 2.20.

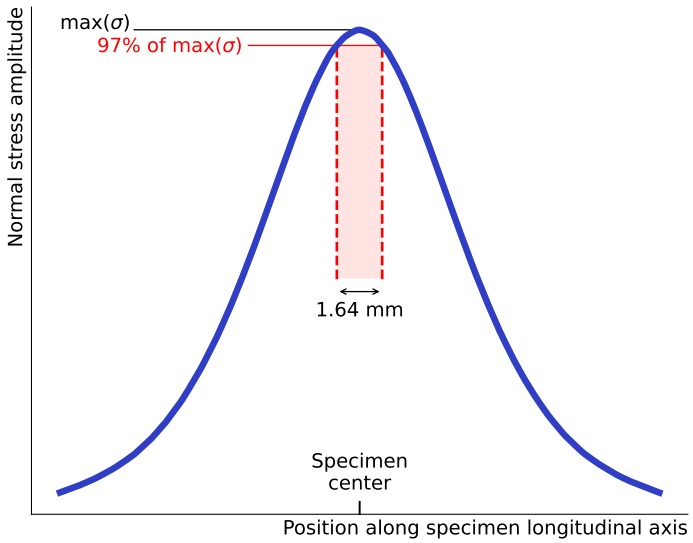

Figure 2.20 | **Distribution of the normal stress amplitude along the specimen longitudinal axis** (schematic drawing). For the design used in this study, there is a stress decrease of 3% maximum in a 1.64 mm-thick region around the specimen center.

Reminder: All stress amplitude values given in this work are the nominal values *i.e.* the average stress amplitudes dynamically calculated over the middle cross-section of the specimen without considering the presence of the notch or the crack. The chimney presence is neglected too for the stress calculation.

To ensure **internal crack initiation** but also to know its precise location (to facilitate the observations with tomography), an artificial internal notch is inserted inside the specimen following the procedure proposed by Junet *et al.* [JUN 19, JUN 23]. To obtain experimental evidence of the environment effect on fatigue crack propagation, it is also possible to add a narrow path (which will be called *chimney* hereafter) to link the notch to the surface of the specimen in order to bring air molecules to the internal notch. The procedure used to produce the notched specimens with or without the chimney is illustrated in Figure 2.22.

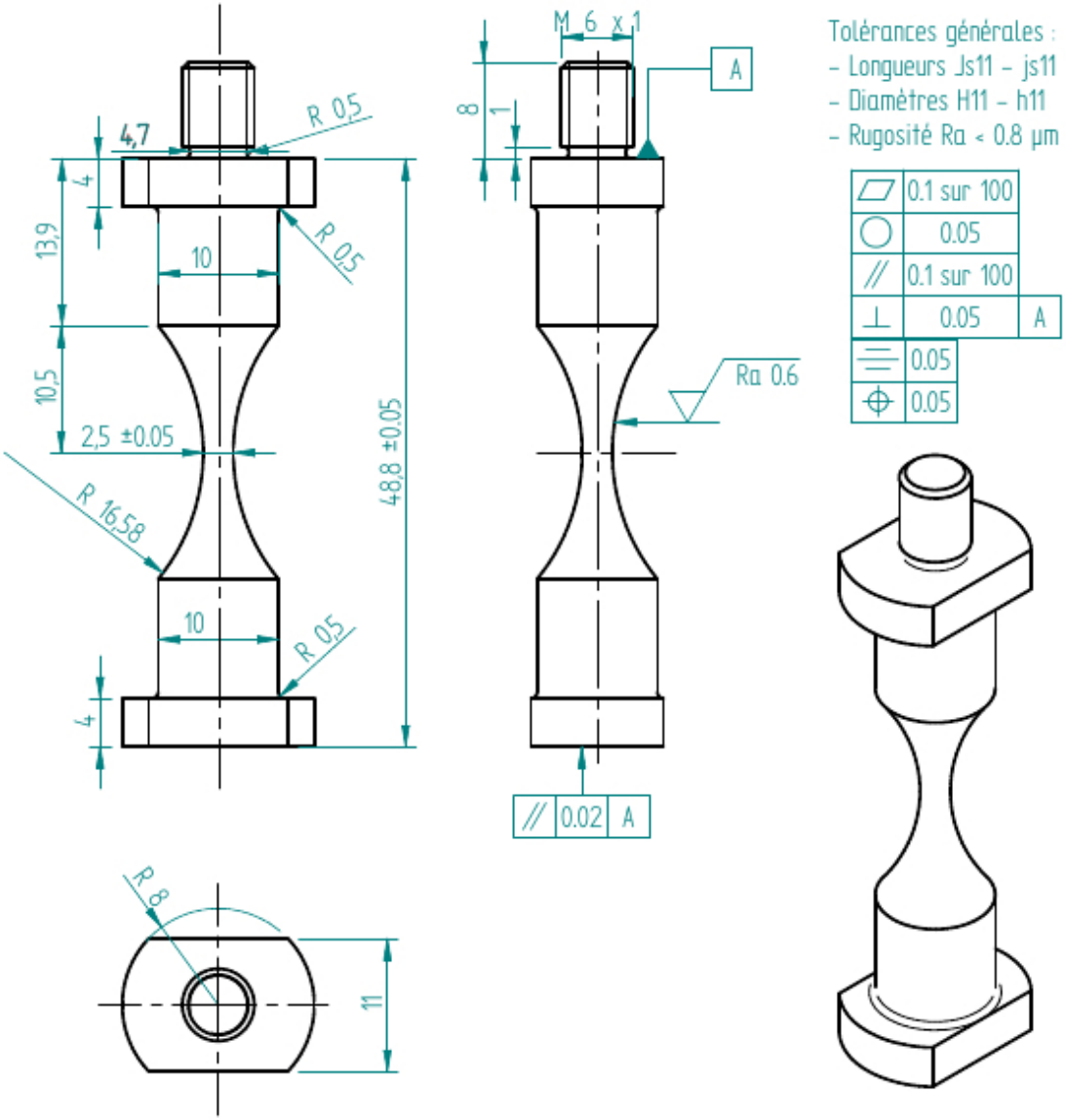

Figure 2.21 | **Drawing of the ultrasonic fatigue specimen geometry** designed for in-situ synchrotron micro-tomography fatigue tests carried out in the present study.

Step	SiC Paper	Buehler support	Used suspension	Plate rotation	Head rotation	Applied pressure	Polishing duration
1^{st}	320 Grit	/	/	220 rpm	50 rpm (same rotation)	25 N	Until plane
2^{nd}	/	Verdutex	9 μm	150 rpm	50 rpm (opp. rotation)	25 N	15 min
3^{rd}	/	Chemomet	Oxide Polishing Suspension	150 rpm	50 rpm (opp. rotation)	20 N	15 min

Table 2.4 | **Polishing protocol for Ti64** applied before the SPS bonding [BUE23].

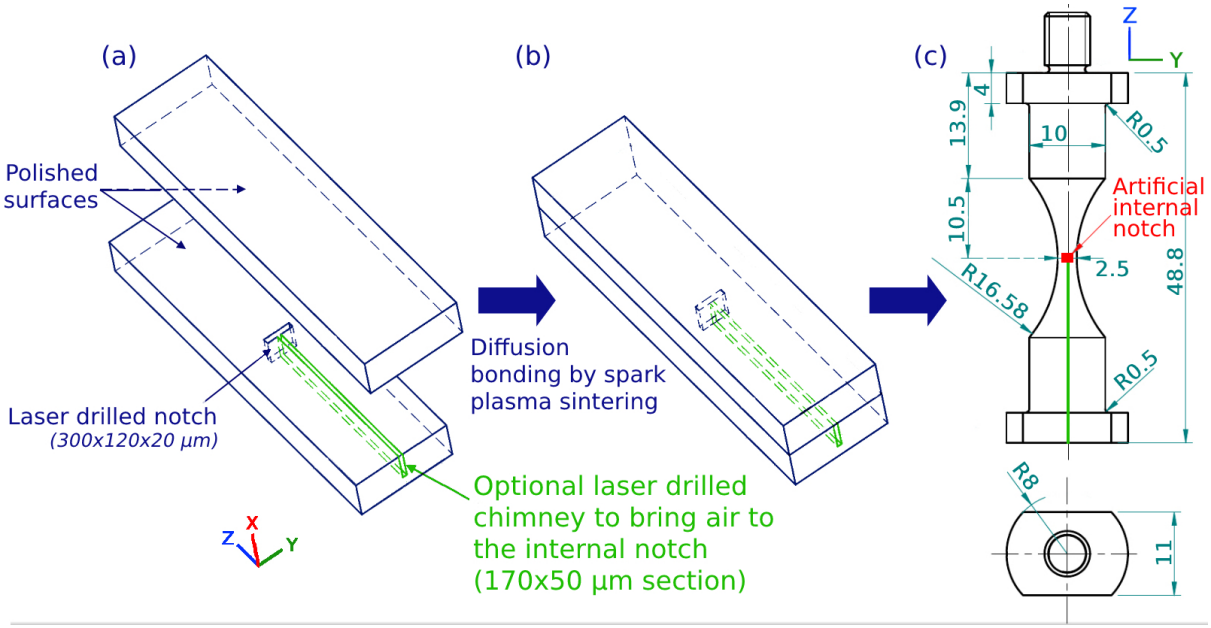

Figure 2.22 | **Schematic illustration of the specimen fabrication process** (a) one half-sheet with an artificial notch is diffusion bonded with an unnotched one by Spark Plasma Sintering. (b) Diffusion-bonded block used to manufacture the specimen. (c) specimen geometry (dimensions in mm). The green chimney is optional and can be added to link the internal notch to the ambient atmosphere.

The fabrication steps are as follows:

- A 15-mm-thick Ti64 sheet is cut in its middle in two parts using electrical discharge machining. The two halves are mechanically polished (with an automatic polishing machine) down to 1-μm-diamond suspension according to the titanium polishing protocol from *Buehler* [BUE23] which is summed up in Table 2.4. The polished half-sheets are then ultrasonically cleaned in acetone.

- One half-sheet is notched with a femtosecond laser* as described by Junet *et al.* [JUN 19] in order to have minimal residual damage and reduced microstructure alteration around the notched micro defects (for details, see the paper of Junet *et al.*). The notch dimensions are approximately $300 \times 120 \times 20$ μm (*cf.* Fig. 2.22a). For the second type of specimen, a narrow chimney (with a 170×50 μm cross-section) links the central notch to the bottom surface of the specimen (*cf.* green volume in Fig. 2.23c). As the notching protocol is easily reproducible, every notch is geometrically quasi-similar to the others (*cf.* Figure 2.23 and 3.3). As depicted by Figure 2.23a, the voxel size is too large to determine if the opening created by the laser in the central part of the notch exists or if it has been rewelded

*We sincerely thank Prof. Arnaud Weck from the University of Ottawa for the realization of the femtosecond notches.

during the following thermal treatment. However, such internal notches allow the cracks to initiate which is their primary objective as this study focuses on the early phases of crack propagation.

- The two plates are then diffusion bonded using Spark Plasma Sintering (SPS) as described in Section 1.5.3.2 from A. Junet's thesis [JUN 21]: the thermal bonding protocol starts by applying a 1 MPa initial normal load on the two plates while a primary vacuum is pumped down to 100 Pa. A force creating a pressure of 15 MPa is then applied before increasing the temperature up to 750°C with a heating rate of 100°C/min. This value is maintained for 10 minutes before decreasing the temperature down to 450°C with a controlled rate of 25°C/min (to obtain a microstructure similar to the original one). The last step is the natural cooling in the SPS chamber down to 200°C. A very good bonding of the interfaces is obtained with this protocol as shown in the thesis of A. Junet [JUN 21] and corresponds to the observations made during the present work. Some considerations on the potential impact of this welding procedure on the crack propagation will be presented in Chapter 3. The vacuum level inside the internal notches has been studied by Junet *et al.* [JUN 23] and experimental evidence allows to claim that the few air molecules present in the notch before the SPS diffuse in the material during the welding because of the imposed high temperature. Consequently, the vacuum level is estimated to be higher than the vacuum applied during the bonding of the two Ti64 half sheets ($<$ 100 Pa) but no quantitative measurements could be carried out.

- After SPS, the internal notch position is checked with X-ray radiography before specimen manufacturing. This is necessary to ensure that the internal notch will be machined in the center of the specimen cross-section and in the middle of the specimen longitudinal axis.

- Finally, when the specimen has been manufactured (Fig. 2.22c), the gauge length is manually polished (down to 4000 grit SiC paper) to avoid surface crack initiation due to the lathe machining marks.

2.4 Data Post-Processing

2.4.1 From Micro-Computed Tomography Data to 3D Mesh

A tomography acquisition provides a stack of 32-bit slices which is converted to an unsigned 8-bit stack (otherwise the file size is too large for an easy treatment). The automated thresholding protocol developed with the *Fiji* software to convert each 8-bit tomographic stack dataset into a binary stack representing the propagated crack is described below and illustrated in Figure 2.24.

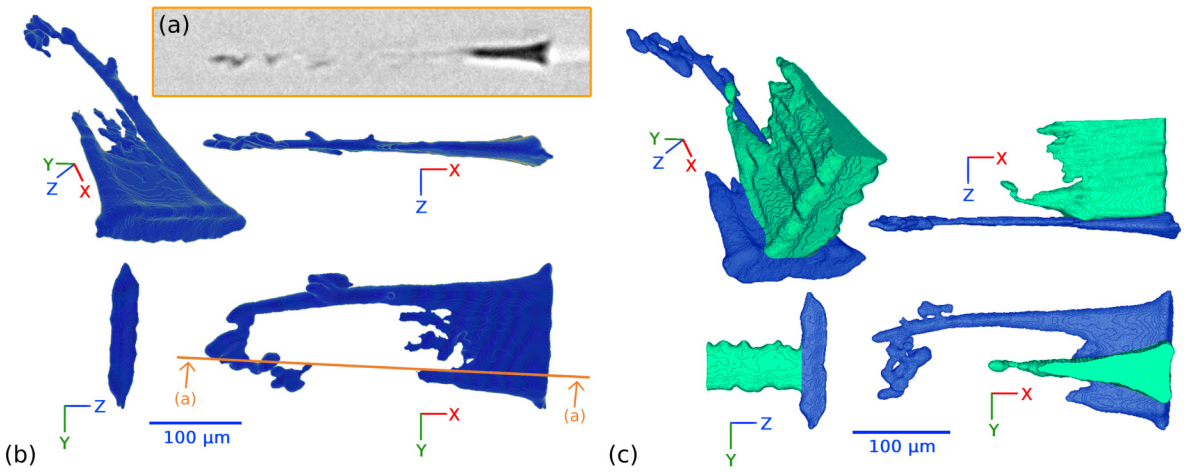

Figure 2.23 | **3D renderings of an internal notch** (b) without and (c) with the chimney which links the internal crack to the ambient atmosphere. The chimney is displayed in green. (a) Section of a notch without the chimney. The loading direction is along z. The voxel size is too large to determine if the opening created by the laser in the central part of the notch exists or if it has been rewelded during the thermal treatment

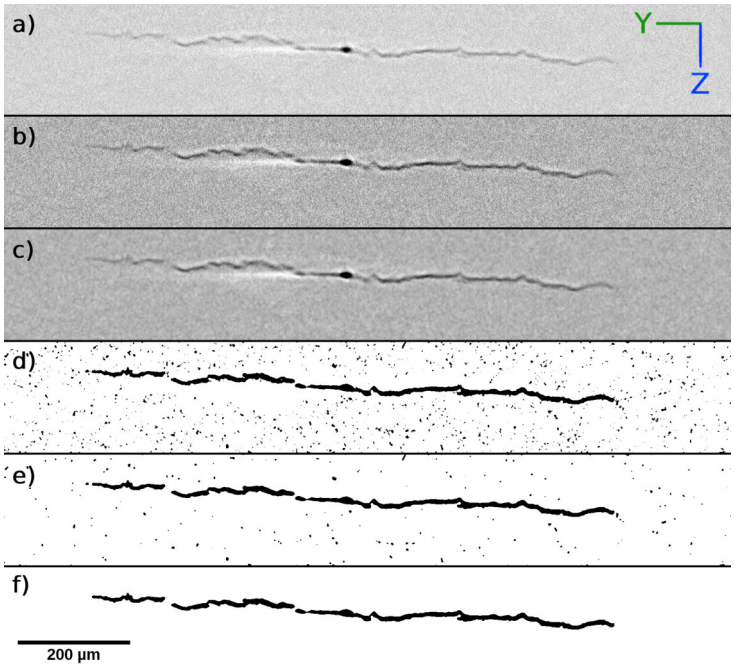

Figure 2.24 | **Successive steps of the thresholding protocol** for a reconstructed slice of an internal crack after 4.4×10^7 cycles of propagation under a stress amplitude of 330 MPa. (a) Initial grey-level image. (f) binary image after the thresholding protocol. See the text for a detailed explanation of the successive steps (b to e). All the pictures have the same scale as (f).

- Figure 2.24a - Initial 8-bit grey level reconstructed slice of the crack.
- Figure 2.24b - The contrast is manually adjusted to increase the grayscale difference between the propagated crack and the titanium bulk. The contrast extrema are similarly adjusted for each scan of the same specimen recorded after a different number of cycles.
- Figure 2.24c - A 3D-median filter with a 3 voxels radius is applied to reduce the noise.
- Figure 2.24d - A small volume around the notch is selected to shorten the procedure. This volume has a cuboid shape which comprises the notch and several hundreds of voxels around it. The threshold value is determined from the grayscale distribution of the voxels in this small volume of interest. With $D(gs)$ the number of voxels having a grayscale equal to gs in the volume, the threshold value gs_{20} is chosen to be the grey level for which $D(gs_{20}) = 0.2\max(D)$. Using this value, the overall volume is binarized (*cf.* Fig. 2.25). The 20% value has been fixed after comparison with several sections from the original dataset (Fig. 2.24a) to be sure that no important part of the crack is omitted.

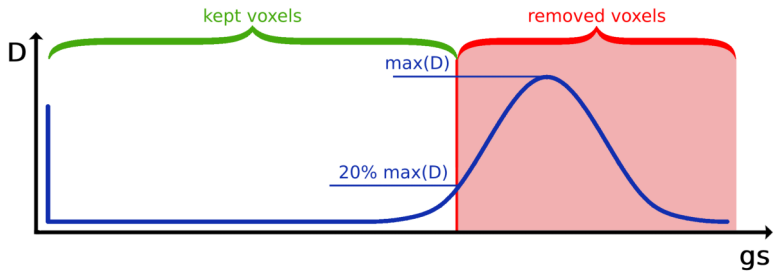

Figure 2.25 | Typical grey level histogram used to determine the threshold value applied to a tomographic stack.

- Figure 2.24e - Another 3D-median filter with a 3 voxels radius is applied to smooth the binarized volume and to remove the isolated voxels.
- Figure 2.24f - Finally, a 3D labelling tool is applied to select and delete all 3D objects composed of less than 2.5×10^5 voxels. This last step allows to keep only the thresholded volume that comprises the internal notch and the propagated crack and removes spurious voxels that result from noise.

The protocol described above allows to obtain the thresholded 3D volume of the acquired crack geometry. The shape of the crack fronts obtained with such a method can be jagged (*cf.* Fig. 2.26a). Because near the front, the crack opening is very narrow, it is not possible to estimate if this aspect is the real front aspect or if it is due to the thresholding procedure. Consequently, the uncertainty on the crack front is evaluated to 5 pixels based on the capacity to distinguish the crack front in tomography data. The thresholded crack volume is then treated to obtain a surface mesh of the crack which will be used in a Finite Element Analysis (FEA)

to compute the SIF along the crack front. The meshing protocol is presented as follows (it comprises a smoothing step that mitigates the jagged aspect of the front).

- Smoothing of the 3D volume with the Fiji tool *Smooth (3D)* from the *Process* menu. The Gaussian method is chosen with a sigma value of 3.0. The output of this averaging tool is an 8-bit stack which needs to be thresholded to keep a binarized volume. For this, the pixels with grayscales higher than 20 are kept: $20 < gs < 255$.
- The binary volume is then treated to create a surface mesh with the *gmsh* plugin of Python. For each coordinate in the XY plane, the average Z position of the pixels corresponding to the crack is measured. A surface mesh is created from all these average Z positions.
- The obtained mesh has to be smoothed to remove the discontinuities due to the Z-averaging step but also to smooth the crack front which can be quite chaotic after the thresholding procedure. The *Meshlab* software is used for this and particularly the *Laplacian Smooth* tool [SOR 05]. Such a smoothing tool is employed with approximately a hundred smoothing steps with a remeshing every ten steps.
- Finally, the obtained mesh is manually cleaned (removing of the folded elements and local remeshing of the distorted ones) before being imported into a finite element software. A typical crack mesh is presented in Figure 2.26.

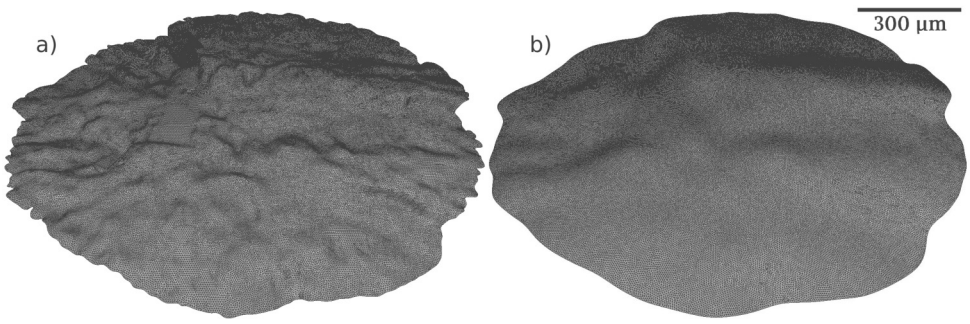

Figure 2.26 | **Meshed crack** (a) before and (b) after smoothing procedure

2.4.2 Numerical Stress Intensity Factor Estimations

The mesh of the crack is then used to carry out finite elements analysis thanks to the *Zcracks* module from the material and structure analysis suite *Zset* [ZCR21]. This module allows to insert a meshed crack in a volume and to evaluate the SIF values all along its front. This method is useful to obtain an estimation of the SIF for complex 3D cracks for which no analytical solutions exist (as penny-shape cracks do have).

The crack insertion in the meshed specimen is carried out by *Zcracks*. Then, the whole volume containing the inserted crack is remeshed. All the remeshing steps are carried out with the use of several software modules from *MeshGems* suite which is distributed by the *Distene* company.

In the present study, the crack is inserted in a specimen which is modelled as a short cylinder (with a $R_1 = 1.25$ mm radius). A stress amplitude is applied on its top surface and the boundary conditions are set on its bottom one (no displacement along the specimen axis).

The SIF evaluation along the crack tip is done with the G-θ method (detailed in software users manual [ZCR21] as reproduced in Appendix E). This approach estimates the stress-energy release rate, G, which is the Lagrangian derivative of the potential energy, W.
With this value, the software computes the SIF in mode I using the classical plane strain equation:

$$K_I = \sqrt{\frac{EG}{1-\nu^2}} \tag{2.11}$$

The software also enables to estimate directly the $K_{I,II,III}$ values with Westergard displacement solutions $v^{I,II,III}$ applied to an interaction integral in the crack front vicinity. It is then possible to integrate the stress-energy release rate G_j at each control point j distributed along the crack front for pure mode I, II or III. Finally, in the assumption of isotropic linear elastic behavior (justified by the fact that only a small volume at the crack tip underwent plastic deformation *i.e.* small scale yiedling assumption), applying the Irwin formula (*cf.* Equation 2.12 [IRW 48]) to this system of equation gives the SIF value for each mode at every control points depending on the material parameters (E, the Young's modulus, ν the Poisson ratio and μ, the shear modulus).

$$G = \frac{1-\nu^2}{E}\left(K_I^2 + K_{II}^2\right) + \frac{K_{III}^2}{2\mu} \tag{2.12}$$

With this approach, the equivalent value ΔK_{eq} can be calculated as the mode I SIF whose energy release rate equals a mixed mode I+II+III:

$$\Delta K_{eq} = \sqrt{\Delta K_I^2 + \Delta K_{II}^2 + \frac{\Delta K_{III}^2}{2\mu}} \tag{2.13}$$

These two different approaches (Eq. 2.11 & Eq. 2.13) used to numerically estimate the SIF range for complicatedly-shaped cracks are compared in Figure 2.27. It represents the mode I SIF range ΔK_I evaluated with these two approaches along a meshed crack tip which has the shape depicted in the top left corner of the figure. The SIF range value analytically calculated for a penny-shape crack having the same area (inserted in the center of an infinitely long volume with a circular section from the Equation 3.2 presented in Chapter 3 [TAD 00]) is indicated by the red line in this figure. This value is closer to the average SIF range obtained with Equation 2.11 (dark blue curve) than to the one obtained with Equation 2.13 (light blue curve). It is due to the numerical errors on the SIF range obtained with Equation 2.13 in some portions of the crack front when the meshed crack is not regular enough (*cf.* black arrows in the figure). For this

reason, Equation 2.11 has been used in the rest of this work to numerically estimate the SIF range evolution along the crack front.

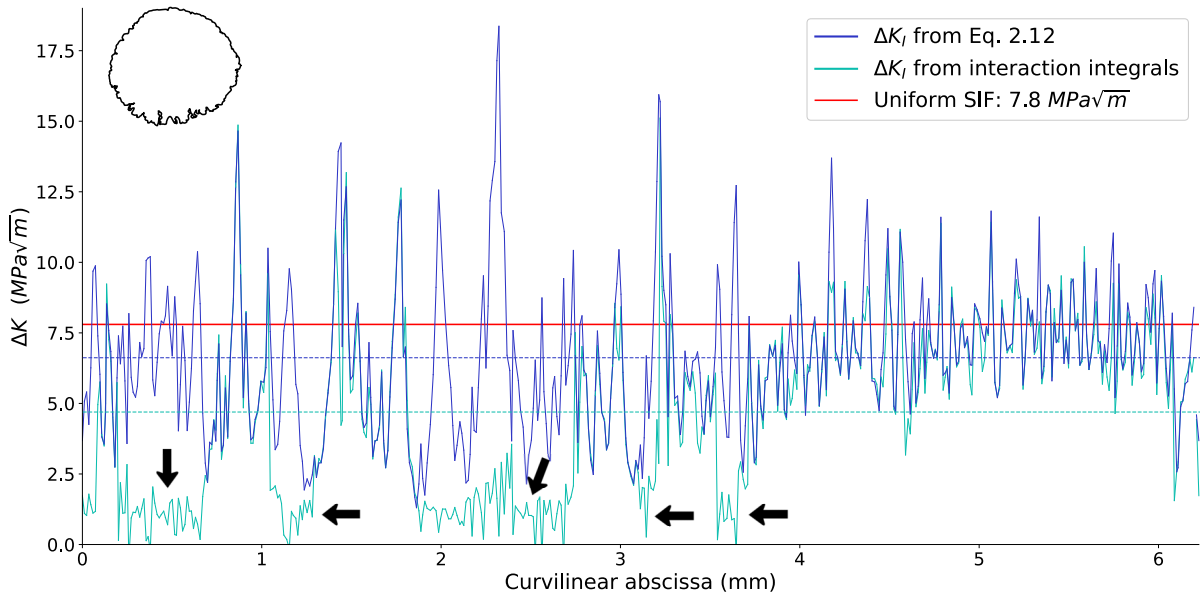

Figure 2.27 | **Mode I SIF range ΔK_I evaluated along a meshed crack tip** with the two approaches described in Eq. 2.11 & Eq. 2.13. Dashed lines are the corresponding average values. The red line represents the SIF value analytically estimated for a penny-shape crack having the same area as the projected crack (Eq. 3.2). The black arrows point at the crack front portions where there are errors in the SIF range evaluation by Equation 2.13. The black closed curve displayed at the top left corner corresponds to the studied meshed crack front.

2.4.3 Thermal Analysis

As described in Section 2.2.1.1, the experimental protocol is designed to be able to monitor the temperature field on the specimen surface while they are submitted to ultrasonic fatigue cycling. Such measurements have been carried out and presented in Chapter 4 to evaluate if a difference in generated heat source due the cyclic plastic deformation can be detected during internal crack propagation between specimens with and without a chimney. For that purpose, the η parameter is estimated. This proportionality coefficient between the linear heat source and ΔK^4 characterizes the heat source due to the cyclic plasticity along the crack front independently of the applied stress intensity factor range. Thus, an environment effect on this cyclic plasticity along the crack front will directly affect the eta parameter.

2.4.3.1 Experimental Thermal Data Analysis

An infrared camera has been used to monitor the temperature field (*cf.* Figure 2.28) at the surface of a specimen containing an internal crack under ultrasonic cyclic loading. For that

purpose, before the first cyclic loading, the specimen surface is covered by black matte paint to reduce the light reflections and have an emissivity close to the unit. The used camera is a FLIR X6900SC which has a spectral range between 3 and 5 μm and a resolution of 40 μm/pixel. It was configured with a 200 Hz frame rate, a temperature range between 10 and 90°C, and an integration time of 0.2539 ms.

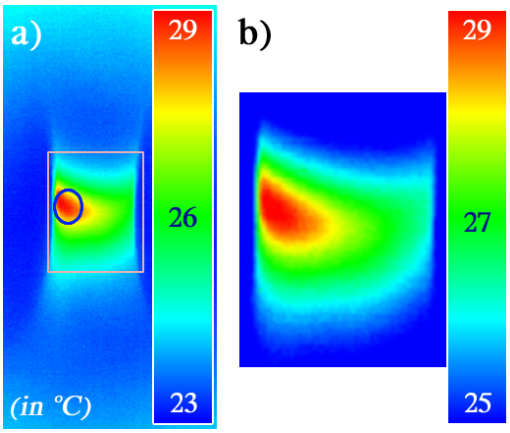

Figure 2.28 | **Example of thermal data acquired during a synchrotron in-situ cycling block** representing the temperature increase after 0.7s of a specimen loaded at 20 kHz with an internal chimney (Specimen nb 53). The pink rectangle of (a) locates the detailed view represented in (b). The blue ellipse is used to evaluate the average temperature around the crack location.

To evaluate the temperature increase due to the presence of a crack in the specimen, the temperature is averaged in a circle around the hot point (blue ellipse in Figure 2.28). With the initial value, T_0^{exp}, of this average temperature, the temperature evolution $\vartheta_{exp} = T_{surf}^{exp} - T_0^{exp}$ can be extracted during the different cycling blocks as shown in Figure 2.29 where the blocks are presented one after each other for a specific specimen. In this example, the internal crack initiated during Block nb 4 and the final fracture occurred during Block nb 26.

Plotting the evolution of the temperature increments versus time for different blocks with the same temporal origin allows distinguishing the differences between them more easily. For example, in Figure 2.30 where the specimen was loaded at the same stress amplitude for each block, the crack was observed on tomography data for the first time at the end of Block nb 4 (with $a_{eq} = 243$ μm). As explained in Section 1.4.2.1, the only active heat source before crack initiation is self-heating due to microplastic activity. For this reason, the increments in temperature for the cycling blocks before crack initiation (all cycled at the same stress amplitude) look similar. However, once the crack starts to grow, the temperature increments are more and more important because the heat source due to the plastic activity at the crack tip is added to the microplastic source and increases with the crack size. So the temperature increment is due to these two sources and, as the heat equation is linear versus its sources, it is possible

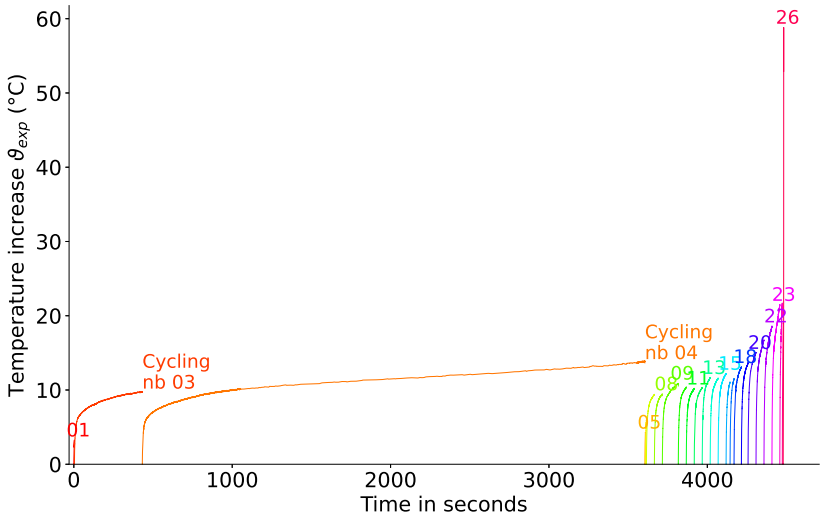

Figure 2.29 | **Temperature increase monitored at the specimen surface during in-situ synchrotron cycling blocks** The temperature depicted here is a value averaged around the hot spot (*i.e.* in a circle such as the blue one from Figure 2.28). These data were collected for Specimen nb 61 which was cycled at a constant 330 MPa stress amplitude without a chimney. The internal crack initiated during Block nb 4 and the final specimen fracture occurred in Block nb 26.

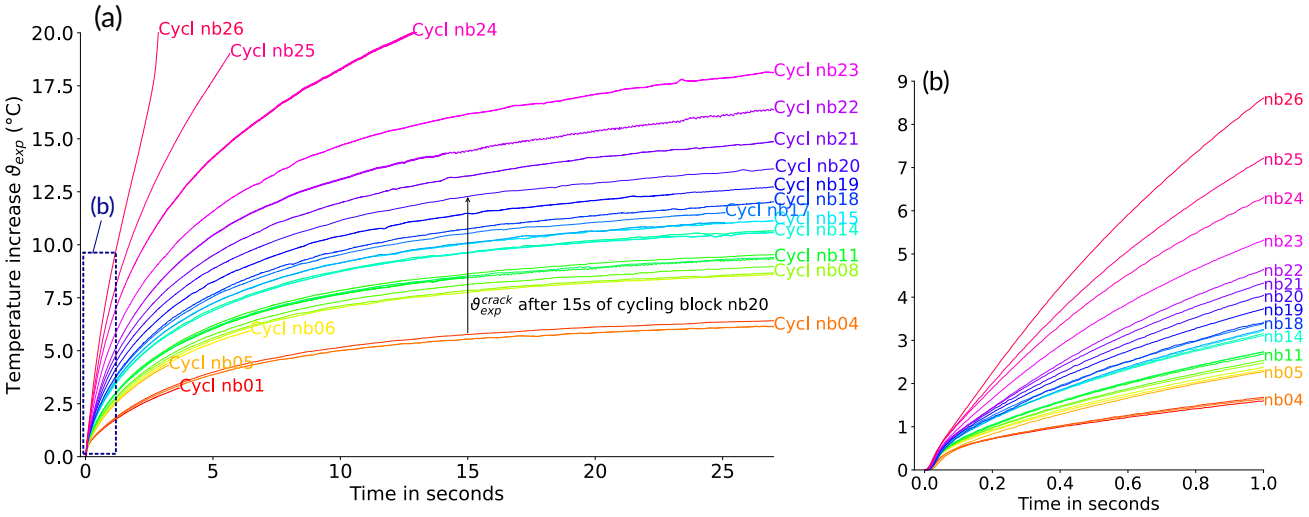

Figure 2.30 | **Temperature increments from Figure 2.29 plotted with the same origin** (a) global temperature increments. (b) presents the increments during the first second of cycling. The internal crack initiated during the cycling Block nb 4. The thermal increase is higher when a crack has initiated than before the initiation.

to separate the thermal increase induced by the plasticity at the crack tip from the one due to the microplastic source. If the microplastic source is supposed to be constant during crack propagation (*i.e.* the influence of the crack on the stress field is limited), it is possible to consider the temperature increment of the cycling blocks before crack initiation to be the thermal increase only due to the self-heating. Consequently, the temperature increment obtained for Block nb 4 can be subtracted from the increments measured after initiation to deduce the temperature increment, ϑ_{exp}^{crack}, resulting from the sole presence of the crack (as represented by the black arrow in Figure 2.30a).

2.4.3.2 Numerical Finite Elements Thermal Analysis

As it is possible to experimentally measure the temperature increase provoked by the presence of an internal crack in a specimen, a numerical analysis will be used to evaluate the corresponding heat source due to plastic activity at the crack tip. For that purpose, the η proportionality coefficient between the plastic dissipation at the crack tip and ΔK^4 will be determined. This will be carried out for specimens with and without a chimney to quantify the impact of the chimney on the reverse cyclic plastic zone activity.

To do this, a Matlab finite element code is used to solve the heat equation for a 3D meshed geometry of the specimen in order to model the temporal evolution of the temperature at its surface. The thermal model is described hereafter and all the heat sources modeled in the finite element procedure are summarized in Figure 2.31.

Since the specimen temperature increments are small (Fig. 2.29), thermal radiations can be neglected if they are compared with convection. The whole exterior surface of the specimen is supposed to only undergo a convection heat flux which is modeled as follows:

$$\varphi = h(T^{surf} - T^{amb}) = h\vartheta \tag{2.14}$$

with h the convection coefficient (supposed equal to $h = 10$ W.m^{-2}.K^{-1} [MES 20]) and T^{amb} the ambient temperature which is supposed to be equal to the initial value of the specimen surface temperature.
The thermal exchanges between the horn and the specimen are not modeled but are supposed to have a negligible effect on the results near the center of the specimen, particularly for short-time simulations.

As explained in Section 1.4.2.1, the temperature increase undergone by a cycled specimen that contains an internal fatigue crack is induced by two heat sources:

- the microplastic heat source per unit of volume (also called self-heating or intrinsic dissipation) is not modeled in the finite element procedure because the numerical temperature field will be compared to the experimental thermal increment, ϑ_{exp}^{crack}, provoked only by the presence of the internal crack.

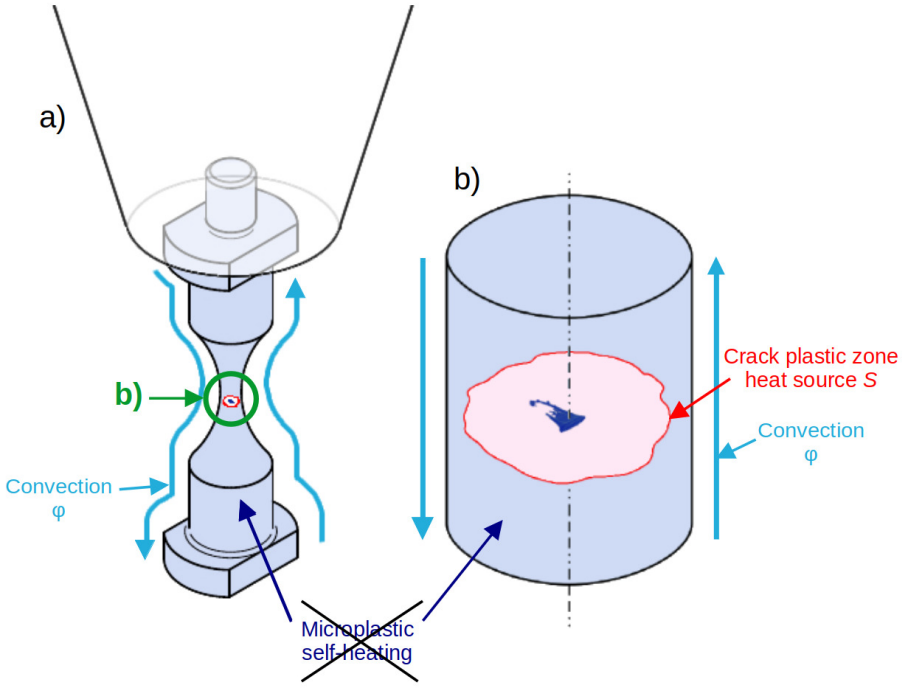

Figure 2.31 | **Sources considered in the finite element model used for thermal analyses** (a) Global scheme of a specimen. (b) Detailed view of the specimen central part. In the model, an adiabatic relation has been imposed between the two crack lips (not shown in the figure).

- the heat source originating from the plastic activity in the reversed cyclic plastic zone around the crack tip, $S(s)$, is modeled to be linear along the crack front (where s is the curvilinear abscissa along the crack front) since the area of this plastic zone remains negligible (compared with the specimen size and the crack length) and given that stress and plastic strain fields are not known. This is equivalent to integrating the plastic energy rate in the reversed cyclic plastic zone (if it is supposed to be entirely dissipated in heat). The SIF values along the crack front - which are determined as explained in Section 2.4.2 - are imported in the finite element model to estimate this source with the η proportionality coefficient:

$$S(s) = \eta \Delta K(s)^4 \tag{2.15}$$

By considering the reversed cyclic plastic zone heat source, the heat equation can be written as follows for each M point in the modeled volume:

$$\rho C_p \frac{\partial \vartheta}{\partial t} = \lambda \nabla^2 \vartheta + \delta(M) S(s) \tag{2.16}$$

with ρ the volumetric mass, C_p the heat capacity and λ the thermal conductivity of Ti64. $\delta(M)$

is the Dirac function along the crack front.

The procedure described in this section aims to determine the value of the η proportionality coefficient from the experimental temperature increase, ϑ_{exp}^{crack}, provoked only by the presence of the internal crack (for example, measured in Figure 2.30a for Block nb 20 after $t = 15$ s). This procedure is based on the fact that the temperature field and η are proportionnal because they are linear with the sources. In that case, the finite element model is applied with the assumption of $\eta = 1$ W.m^{-3}.MPa^{-4} to obtain a normalized temperature field and to calculate the numerical thermal increment, ϑ_{FE}^{crack}. Hence, it is possible to calculate the experimental η_{exp} value from a linear relation (Eq. 2.17) between the two temperature increments, ϑ_{exp}^{crack} and ϑ_{FE}^{crack} (measured at the same location after a similar, t_i, amount of cycling time). The overall procedure is summarized in Figure 2.32.

$$\frac{\vartheta_{FE}^{crack}(t_i)}{\eta_{FE}=1} = \frac{\vartheta_{exp}^{crack}(t_i)}{\eta_{exp}} \iff \eta_{exp} = \frac{\vartheta_{exp}^{crack}(t_i)}{\vartheta_{FE}^{crack}(t_i)} \tag{2.17}$$

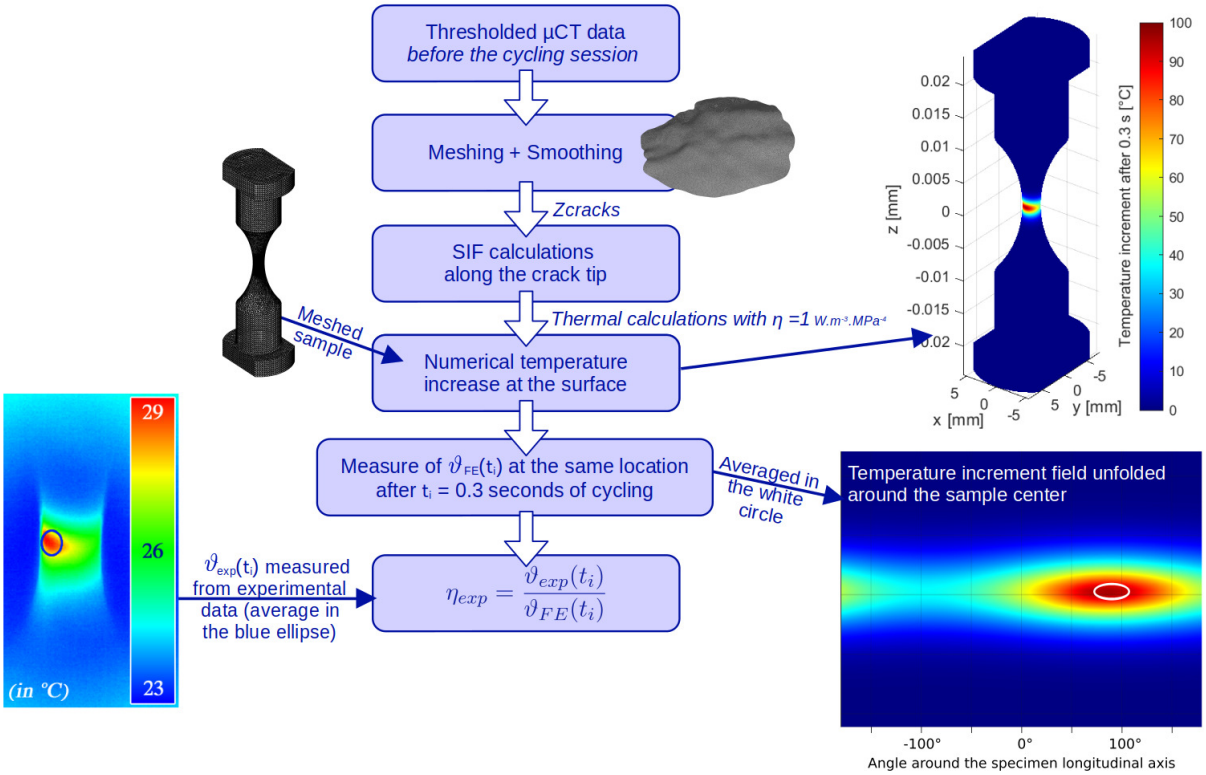

Figure 2.32 | **Graphical abstract showing the thermal approach** carried out to evaluate the η parameter. Usually, the cycling duration t_i after which the temperatures are measured is short (around 0.3 sec) to avoid being too much influenced by external thermal phenomena. A detailed description of the successive steps is given in the text.

Because micro-tomography acquisitions are carried out between the successive fatigue cycling blocks, the crack shape during the blocks is not known. For this reason, the estimation of η_{exp} corresponding to a given block is carried out by using the meshed crack obtained from the tomographic acquisition *prior to* the considered block. For this purpose, Equation 2.17 is used with $t_i = 0.3$ sec corresponding to the very early beginning of the cycling block (the 6000 first cycles). As presented in the next chapters, crack growth rates have been measured between 10^{-12} and 10^{-8} m/cycle, so 6000 cycles at these rates corresponds to a crack propagation between 0.006 and 60 μm. Those values are negligible compared to the measured crack sizes.

The results obtained from this method will be presented in Chapter 4 to evaluate if the plastic activity around a propagating crack changes when a chimney links the internal crack to the specimen surface.

2.5 Graphical Overview of the Chapter

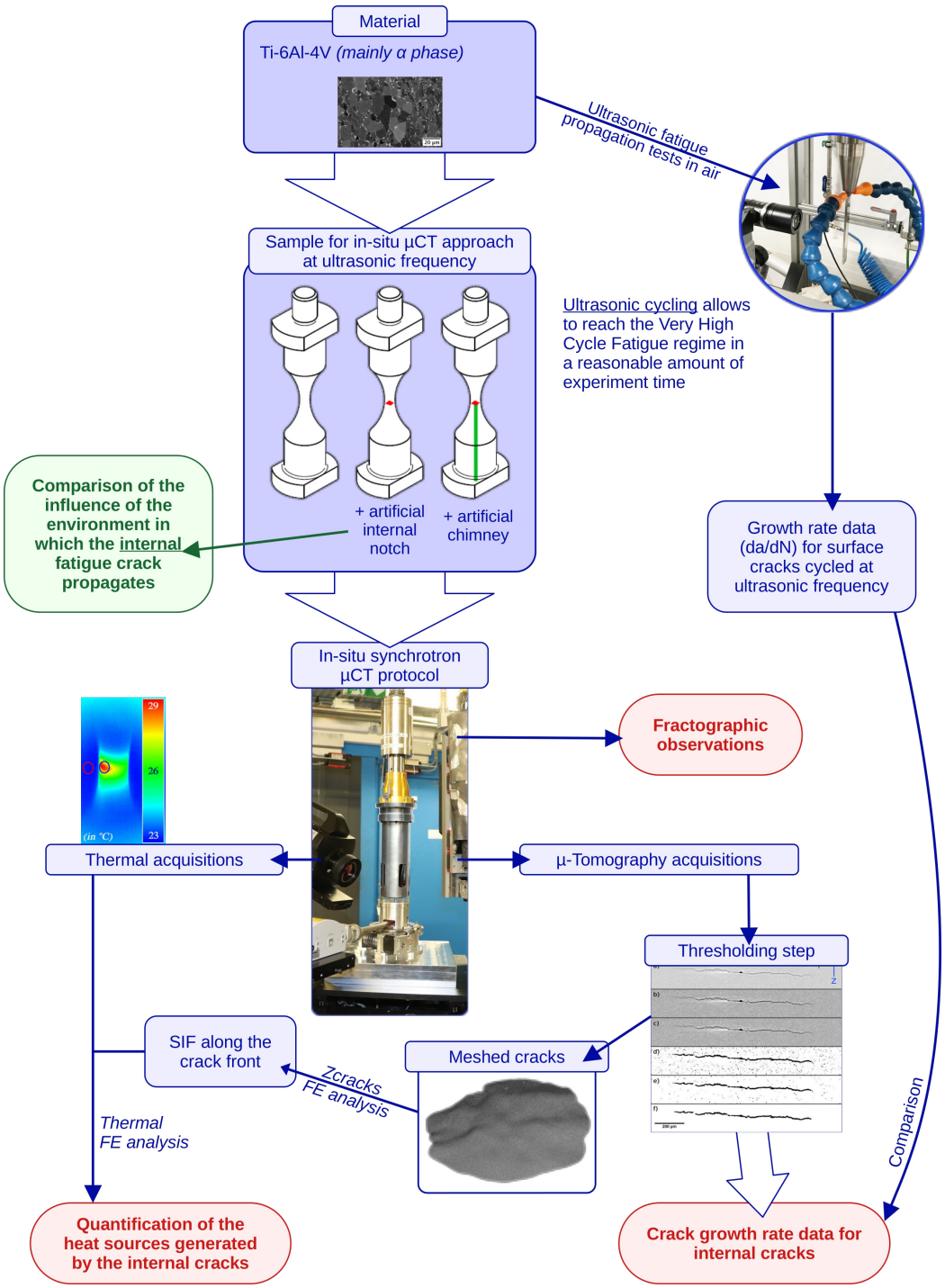

Figure 2.33 | Overview of the experimental and numerical procedures employed in this work. The red boxes represent the experimental data analyzed to evaluate the environment effect on the fatigue crack propagation.

Chapter 3

Internal Fatigue Crack in Ti64

Contents

To study the Very High Cycle Fatigue regime and internal cracks, the experimental protocol described in Chapter 2 (ultrasonic fatigue machine adapted to in-situ tomography and used to cycle internally notched specimens) has been used. The fatigue lives and fracture surfaces have been analyzed and growth rates have been measured from the crack 3D shapes acquired with micro-tomography. These results are presented in this chapter to evaluate the fatigue crack propagation obtained with such a protocol.

3.1 Fatigue Tests Results in an S-N Diagram

3.1.1 Ultrasonic Fatigue Specimens Without Artificial Internal Defect

A first series of experiments has been carried out with the ultrasonic fatigue system to cycle specimens *without* any artificial internal defect. Their geometry is similar to the one illustrated in Figure 2.21 but no internal notch was added. The aim of these preliminary experiments was to compare fatigue data obtained for the chosen Ti64 alloy with literature results on the same alloy at ultrasonic and conventional loading frequencies.

These unnotched specimens are listed in Table 3.1; they were loaded at different nominal stress amplitudes. Their fatigue lives are shown in an S-N graph in Figure 3.1 (purple star symbols). The fatigue lives obtained with our setup are in good agreement with the values from the literature showing decreasing S-N curves with a very low slope and scattered fatigue lives. For example, at 500 MPa, some specimens failed after 10^7 cycles whereas others did not fail after 10^9 cycles [HUA 14, ZUO 08, TAK 08]. This observation is also true for the specimens tested in the present study.

Specimen nb	Stress ampl. (MPa)	Nb of cycles before fracture*	Remarks
2	500	1.5×10^6	surface
3	500	$> 1 \times 10^9$	not broken
6	600	9.41×10^8	subsurface
7	580	3.3×10^6	surface
8	620	2.98×10^6	surface
9	560	$> 1 \times 10^9$	not broken
10	600	6.67×10^7	surface
11	640	4.3×10^4	surface
13	620	4.2×10^5	surface
14	580	6.53×10^7	subsurface
15	600	7.94×10^6	internal
16	580	4×10^5	surface
17	560	3.45×10^6	surface
19	540	$> 3.78 \times 10^9$	not broken
20	500	1.5×10^7	internal
21	560	4.77×10^7	subsurface
23	500	2×10^9	not broken
27	500	4.06×10^6	surface
32	480	$> 1.82 \times 10^9$	not broken
35	480	$> 1.74 \times 10^9$	not broken
36	480	$> 1.49 \times 10^9$	not broken
37	480	$> 2.25 \times 10^9$	not broken

Table 3.1 | Ti64 specimens (without any artificial internal sharp notch) cycled in this study. Represented by purple datapoints in Figure 3.1.

*As specified in Chapter 2, this is the total number of cycles applied to the specimen until it cannot resonate anymore because the crack has fractured almost all the specimen section.

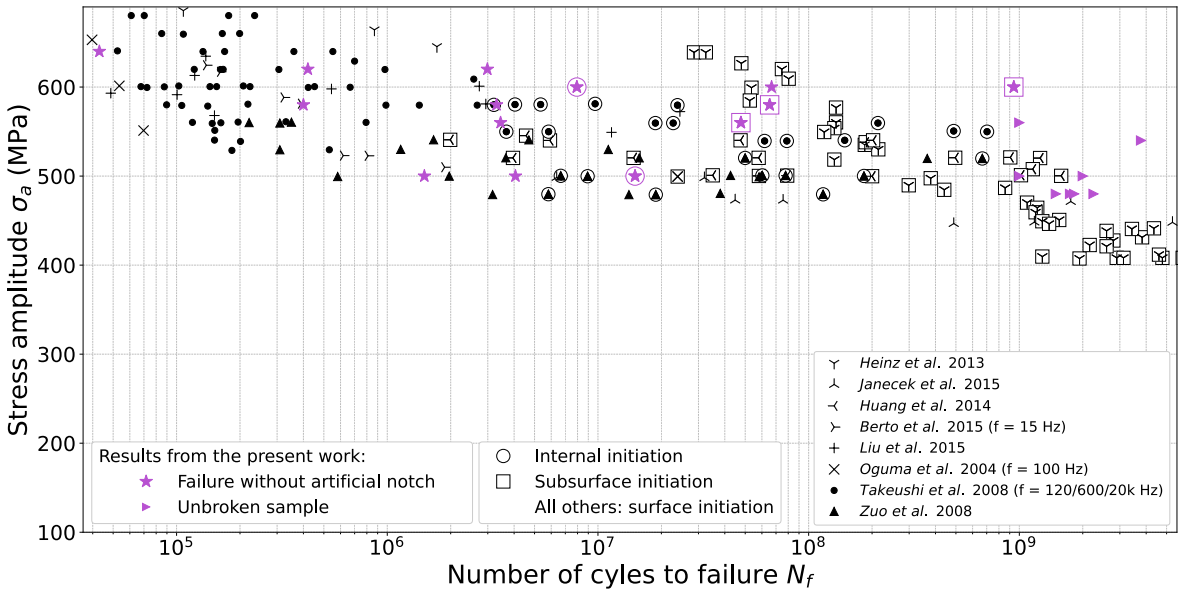

Figure 3.1 | **Fatigue lives of smooth ultrasonic specimens without artificial internal defect** (purple symbols) compared with data from literature obtained for smooth Ti64 specimens (black symbols) [HEI 13, JAN 15, HUA 14, BER 15, LIU 15, OGU 04, TAK 08, ZUO 08]. Unless specified in the legend, the literature data were obtained at ultrasonic frequency (20 kHz). The experimental conditions of the literature references are listed in Appendix H. The fatigue lives obtained with the ultrasonic machine agree with the literature.

A second observation concerns the crack initiation location. In the unnotched specimens, the large majority of the fatigue cracks initiated from the surface (Fig. 3.2a) or the subsurface (Fig. 3.2b) of the specimens, a few internal initiations occurred (Fig. 3.2c). This is reported in Figure 3.1 by the data points that are surrounded by a square (subsurface initiation) or those that are not surrounded (surface initiation). This observation is in agreement with the literature for VHCF of titanium. For example, Nikitin remarked in a VT3-1 titanium alloy, that a lot of subsurface initiation occurred in specimens cycled at low stress amplitude [NIK 15]. It can be noticed, however, that either for literature data or for the data from this study, the surface fatigue crack initiation concerns mostly the specimens with the shortest lives (smaller than $\sim 3 \times 10^6$ cycles).

3.1.2 Specimens With an Internal Artificial Defect

The present work focuses on the study of internal fatigue crack propagation. As pointed out by the results obtained for specimens without internal defect, internal crack initiation occurs for low stress amplitudes leading to very long fatigue lives.

To have access to the crack shapes with tomography during an important fraction of the

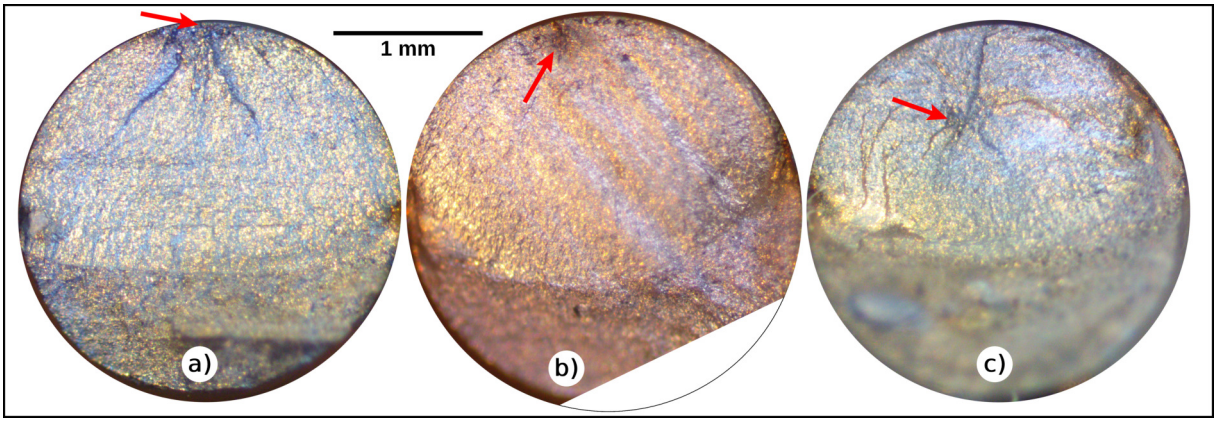

Figure 3.2 | Optical microscope view of the fracture surface for three specimens without artificial internal notch (a) Surface crack initiation (Specimen nb 8 cycled during $N = 2.98 \times 10^6$ cycles at $\sigma_a = 620$ MPa), (b) Subsurface initiation (Specimen nb 14: $N = 6.53 \times 10^7$ cycles at $\sigma_a = 580$ MPa) and (c) internal initiation (Specimen nb 15: $N = 7.94 \times 10^7$ cycles at $\sigma_a = 600$ MPa). The red arrows locate the crack initiation sites.

propagation stage, it is necessary to acquire the first 3D shape of the internal crack not long after the initiation. But, as explained in Section 2.2.2, the laser vibrometer used for crack initiation detection can report false detections. Consequently, before starting the propagation phase of the protocol, it is necessary to check if an internal crack did initiate in the acquired tomographied volume or not. Knowing in advance the location of crack initiation reduces the time required to look for a potentially initiated crack in the 3D volume. In the case of synchrotron experiments which only last a few days, this is a crucial issue.

Also, during the first stages of the propagation of a fatigue crack, the crack size and opening are very small making it difficult to distinguish it in tomographic data especially if one has to look for the initiation location everywhere in the volume of the specimen. Hence, to know from where the crack will initiate, it has been decided to insert a sharp notch in the specimen which will act as an artificial internal defect concentrating the stress field around it and fostering internal fatigue crack initiation from a specific zone in the material. The notch needs to be sharp in order to be as close as possible from a natural crack.

The notching procedure developed by Junet *et al.* (femtosecond laser notching of a Ti64 sheet then welded to another one with SPS) [JUN 19] has been adapted to the ultrasonic specimens as described in Section 2.3. Preliminary femtosecond laser tests have been made on the same material to adjust the laser power in order to precisely control the notch size. Similar laser control parameters were used for every notch. This procedure is easily reproducible given that every specimen presented in this study (except Specimen nb 43) has been notched from the same batch. Hence, every notch is small, very sharp and geometrically quasi-similar to the others (cf. Fig. 3.3). As detailed by Junet *et al.*, one can expect minimal residual damage and reduced

microstructure alteration around such micro defects [JUN 19]. The list of the cycled specimens with an artificial internal sharp notch and the corresponding experimental conditions are given in Table 3.2.

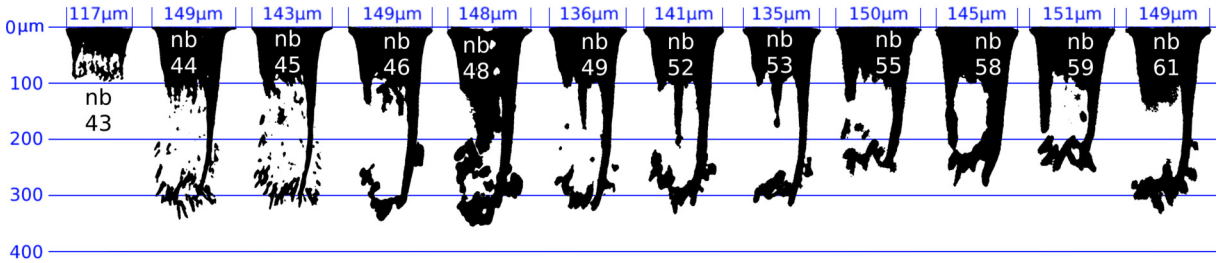

Figure 3.3 | Projection of all the notches of the specimens submitted to cyclic loading during this study All the notches, except for Specimen nb 43 were obtained in the same batch. This explains why the latter has a different shape. Specimens nb 46, 48, 52 and 53 will be analyzed in Chapter 4 because they contain a chimney.

Specimen nb	Stress ampl. (MPa)	Nb of cycles before fracture*	Nb of cycles when a crack is detected using μCT	Corresponding marker in Fig. 3.22
43	385	1.05×10^8	No μCT data	/
44	337	1.17×10^8	9.59×10^6	●
45	329	7.53×10^7	9.73×10^6	●
46	330	4.55×10^7	9.98×10^6	●
55	330	1.30×10^8	No μCT data	/
61	330	8.92×10^7	7.18×10^7	●
58	500	2.43×10^6	2.06×10^6	●
59	500	3.38×10^6	No μCT data	/

Table 3.2 | Ti64 specimens containing an artificial internal sharp notch which are cycled at 20 kHz in this study. The notches are internal and do not have any contact with ambient air.

With notched specimens, crack initiation always occurred (100% of the cases) from the artificial internal notch. The fatigue lives of these notched specimens are illustrated in Figure 3.4 (blue stars) which compares them with all the data points from Figure 3.1 where internal or subsurface initiations have been observed. From this figure, it can be seen that the insertion of an internal sharp notch ($\sim$ 300 μm $\times$ 120 μm with a thickness between 5 and 20 μm) shortens quite drastically the fatigue life. Besides, the fatigue behavior seems more reproducible because, for a given stress amplitude, the fatigue lives are scattered over half a decade whereas more than two decades can be found between the fatigue lives of two unnotched specimens loaded at

*As specified in Chapter 2, this is the total number of cycles applied to the specimen until it cannot resonate anymore because the crack has fractured almost all the specimen section.

the same amplitude. This reduction in fatigue life scatter is typical for specimens containing artificial notches of a given size.

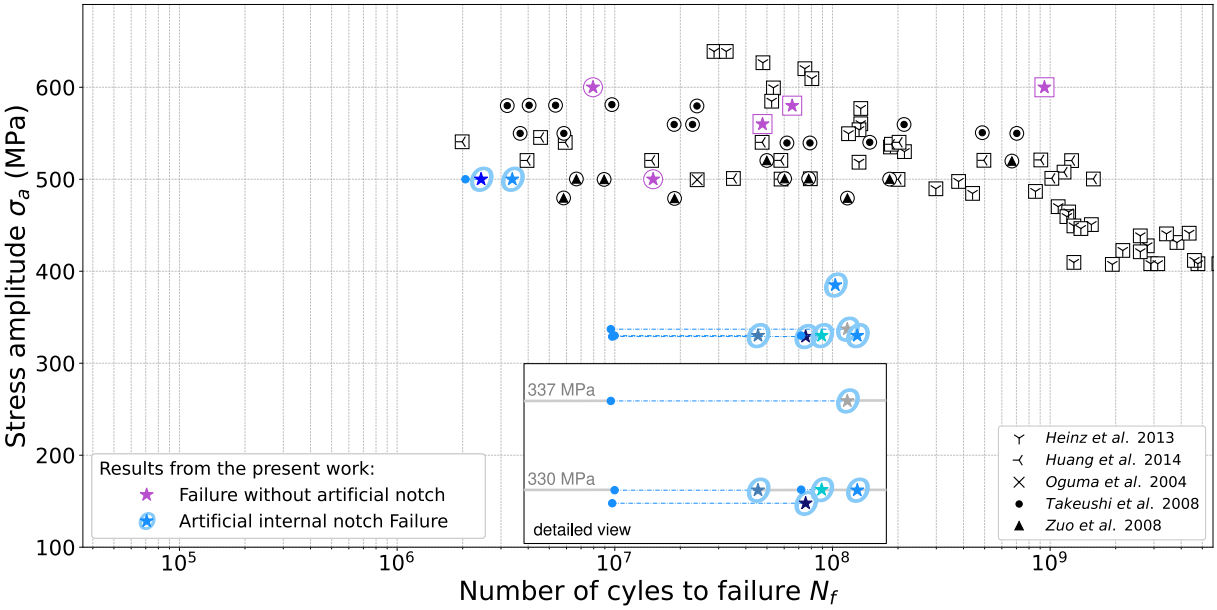

Figure 3.4 | **S-N graph for ultrasonic notched specimens with internal cracks** compared with data from literature and from unnotched specimens. The notched specimens have shorter fatigue lives than the unnotched ones. The detailed view in the black rectangle allows to distinguish the different points around 330 MPa. The horizontal dashed lines represent the number of cycles between the crack first detection and its final fracture.

An estimation of the number of cycles before crack initiation - not frequently measured in a direct way in the literature and especially at 20 kHz - can be obtained from the tomography data. When an initiated crack is observed on the tomographic 3D volume for the first time, the overall number of cycles applied before this micro-tomography acquisition is an upper bound estimation of the number of cycles needed to initiate the fatigue crack from the notch. For each specimen, this value is listed in Table 3.2 and represented in Figure 3.4 with a blue point. The horizontal dashed lines represent the number of cycles between the crack first detection and its final fracture. Several studies in the literature claim that, in Very High Cycle Fatigue, the major part of the fatigue life is spent in crack initiation [WAG 09, MCD 10, HON 14, XU 18]. For three specimens out of the four cycled around 330 MPa which could be tomographied in the present study, the amount of fatigue life before the first detection corresponds to a small fraction of the overall fatigue life (between 8 and 20%). It illustrates the decrease in fatigue life entailed by the presence of an internal notch which fosters crack initiation. Furthermore, it shows that, in the VHCF regime, the number of cycles needed for internal crack propagation only can be larger than 9×10^7 cycles. Similarly, A. Messager used micro-tomography to observe

VHCF crack initiation in an A357-T6 aluminum alloy containing an artificial casting defect and showed physical evidence that the duration of the propagation phase for a crack initiated from such an internal defect represents a substantial part of the VHCF life [MES 20].
Another example of early internal crack initiation has been reported by Yoshinaka *et al.* [YOS 19] who observed Ti64 specimens without any defect with a tomography approach. Internal crack initiation was observed after only 20% of the overall fatigue life and other numerous initiations were observed during a large proportion of the fatigue life (between 5×10^6 and 10^8 cycles).

In addition to fatigue life considerations, the other classic way to study fatigue cracks is the post-mortem observation of the specimen fracture surfaces. This is presented in the next section to evaluate if the internal fatigue cracks obtained with the presented protocol can be compared with the natural ones described in the literature.

3.2 Observation of the Fracture Surfaces

In this section, the characteristics of the ultrasonic fatigue crack surfaces are described and compared with literature to try to understand the crack propagation mechanisms.

3.2.1 Morphology of the Crack Surface

3.2.1.1 Influence of the Manufacturing Protocol on the Microstructure in Which the Crack Propagates

The manufacturing procedure used to obtain internally notched specimens (introduction of artificial notch and welding) may have an impact on the observed crack growth and the crack shape. For example, in his PhD thesis [JUN 21], A. Junet observed a slight difference in crack propagation rate between the part of the crack which is located in the titanium half-sheet containing the artificial notch and the crack located in the notch-free half-sheet. Such a difference has been explained by the fact that he used two titanium plates with different thicknesses (and therefore different rolling ratio reductions) welded together (with one that has been notched before). Consequently, after the plate sintering, two slightly different microstructure textures were observed on each side of the joint plane (near the internal notch). To avoid this drawback in the present work, it has been decided to use a thicker plate which was cut in its middle. One half was then notched before welding the two parts in a configuration similar as the initial one (as summarized in Figure 2.22). This was done to have the same original microstructure on both sides of the welding plane.

As the notch was obtained with a femtosecond laser, a very short interaction with the material was expected during the notching procedure. As shown by Weck *et al.* [WEC 06], close to the notch, the material can be harder but a thermal treatment - such as the one used during SPS welding - is very efficient to reduce this extra hardness. Furthermore, the present study deals

with the *propagation* of cracks, not their *initiation* and 3D characterization starts when the crack is long enough not to be influenced by the internal notch anymore (see for example, the crack fronts in Figure 3.7).

The SPS welding has been carried out at the same temperature as that of the hot rolling - used to form the initial Ti plates - but during a shorter amount of time (10 minutes compared to one hour). This diffusion bonding process has been described in a previous study on a similar Ti64 alloy [JUN 19] and no difference could be observed with EBSD in the grain structure. Also, the tensile properties of the material were almost similar before and after the SPS welding. In the present case, again, no difference in the microstructure could be observed after SPS by EBSD (cf. Fig. 3.5). Although the tensile properties were not tested this time, only a small reduction in hardness (HV 500g) was measured after SPS (from 348 ± 13 HV to 323 ± 18 HV *i.e.* a 7% reduction as referenced in Appendix I). Therefore, we feel confident that the welding process has hardly affected the studied material.

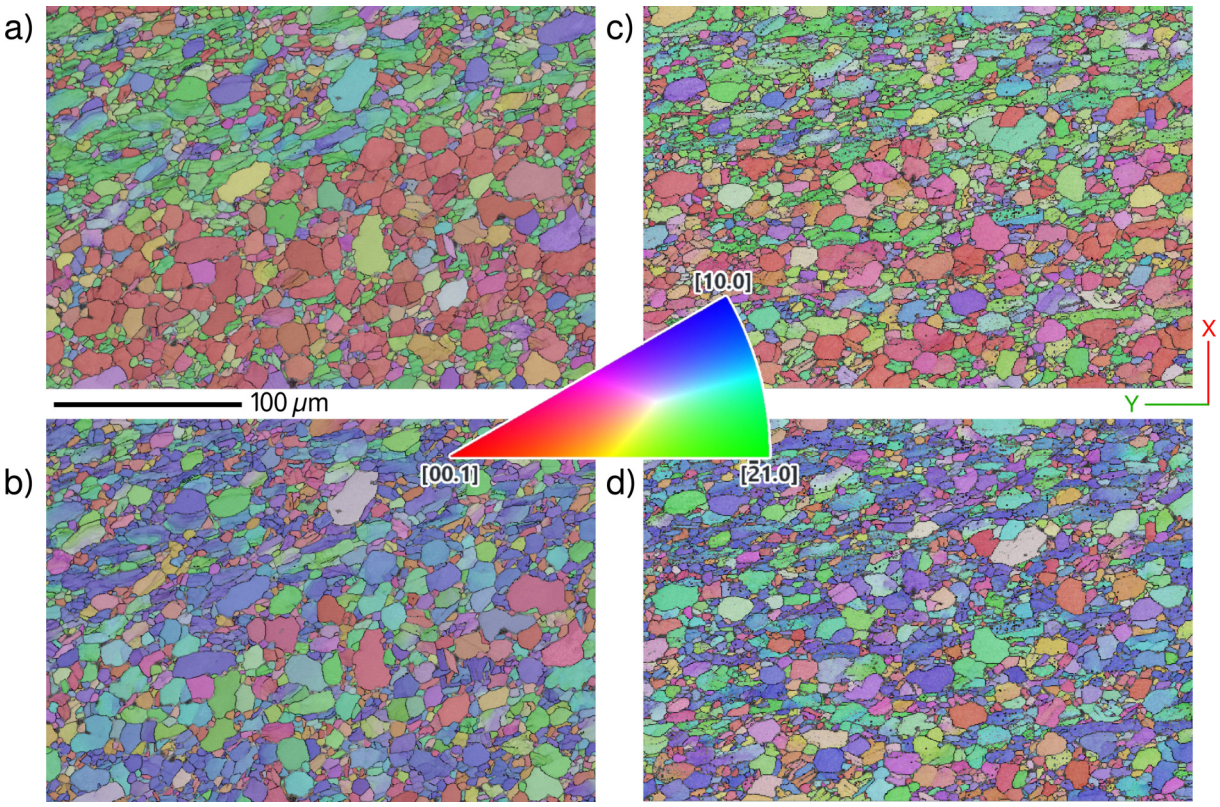

Figure 3.5 | EBSD maps (a) & (b) before and (c) & (d) after SPS bonding procedure (a) & (c) represent the Inverse Pole Figure (IPF) showing the crystal directions parallel to the specimen long dimension (Z direction) and (b) & (d) shows the crystal directions parallel to the width of the original Ti64 plate (X direction - *cf.* also Fig. 2.3). No major microstructure modifications are observed before and after SPS.

3.2.1.2 Observation of the Crack Shape

Because the notching and welding processes should have reduced influence on the crack growth, the shape of the cracks should only be influenced by the material original microstructure. As explained before, the use of in-situ synchrotron micro-computed tomography allows to access the 3D shape of the cracks at several instants of their propagation. Figure 3.6a represents a crack obtained with the described protocol. As illustrated by the two sections views from this figure, the crack has a relatively smooth shape, *i.e.* planar without strong macroscopic variation in the orientation of the crack surface normal vector (mode I growth). This is representative of almost all the crack shapes obtained in this study which are summarized in Appendix G. Only one specific crack obtained in the present work has a relatively complex shape; it is illustrated in Figure 3.6b. These cracks differ from the fatigue cracks obtained in A. Messager's PhD thesis [MES 20] who used a very similar ultrasonic cycling machine.

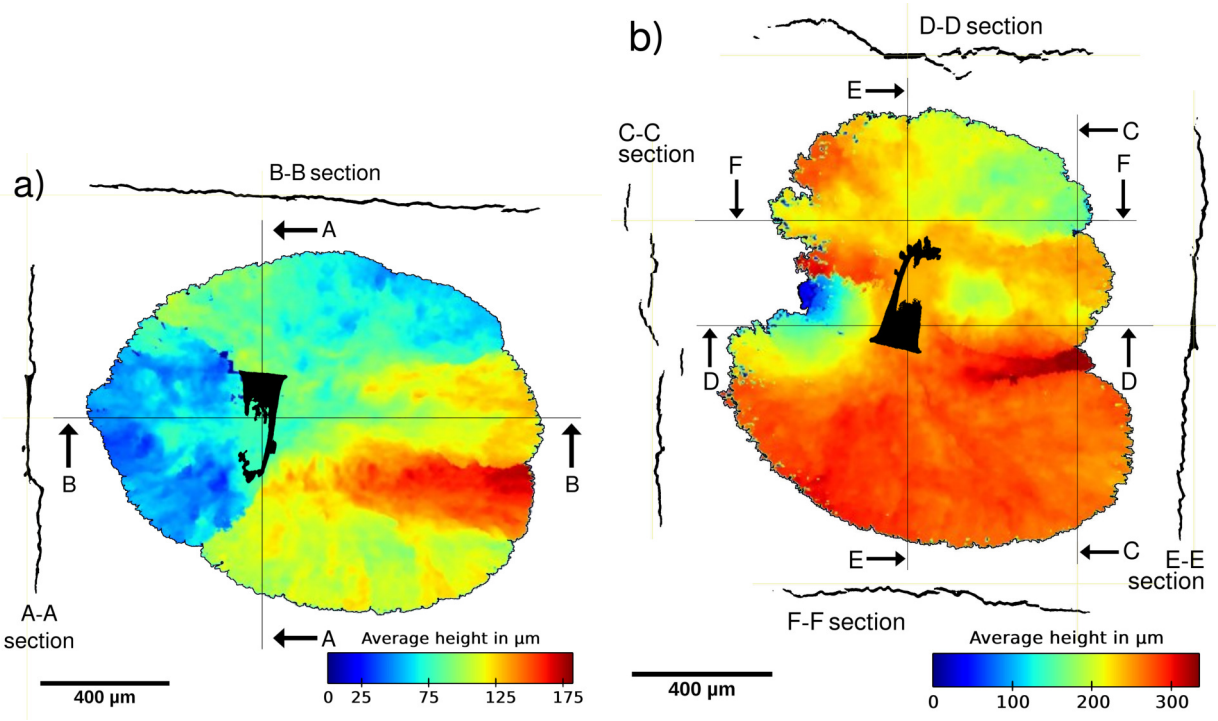

Figure 3.6 | **Average height of two fatigue cracks which propagated from an internal notch** (the zero is fixed at the lowest height of the crack). Maps plotted from the thresholded 3D shapes of the cracks (acquired with micro-tomography). The different section views correspond to the cut planes represented in black on the cracks. (a) The crack from Specimen nb 46, represented after 4.55×10^7 cycles at 330 MPa, has a regular shape representative of the cracks obtained in this study. (b) The crack from Specimen nb 61, represented after 8.92×10^7 cycles at 330 MPa, is the only one presenting a relatively complex shape.

The large grains of the cast Al alloy studied by A. Messager [MES 20] induced very irregular crack fronts and complex morphologies of the crack surfaces. In the present study, since the grain size is much smaller ($10.8 \pm 1 \mu$m), the observed internal cracks are not significantly affected by the microstructure and the crack fronts are relatively regular as soon as the crack exits the sharp notch influence (*cf.* the successive fronts depicted in Figure 3.7). It is not possible to estimate if local jagged aspect of the crack front is the real front aspect or if it is due to the thresholding procedure. Hence,the uncertainty on the crack front is evaluated to 5 pixels based on the capacity to distinguish the crack front in tomography data.

Figure 3.7 illustrates also the fact that the global shape of the crack fronts rapidly becomes circular after initiation. This shows that the artificial internal notches are sharp enough not to influence crack growth relatively rapidly after initiation. Hence they are comparable to small natural cracks, it is important with the purpose to obtain results comparable to naturally initiated fatigue internal cracks.

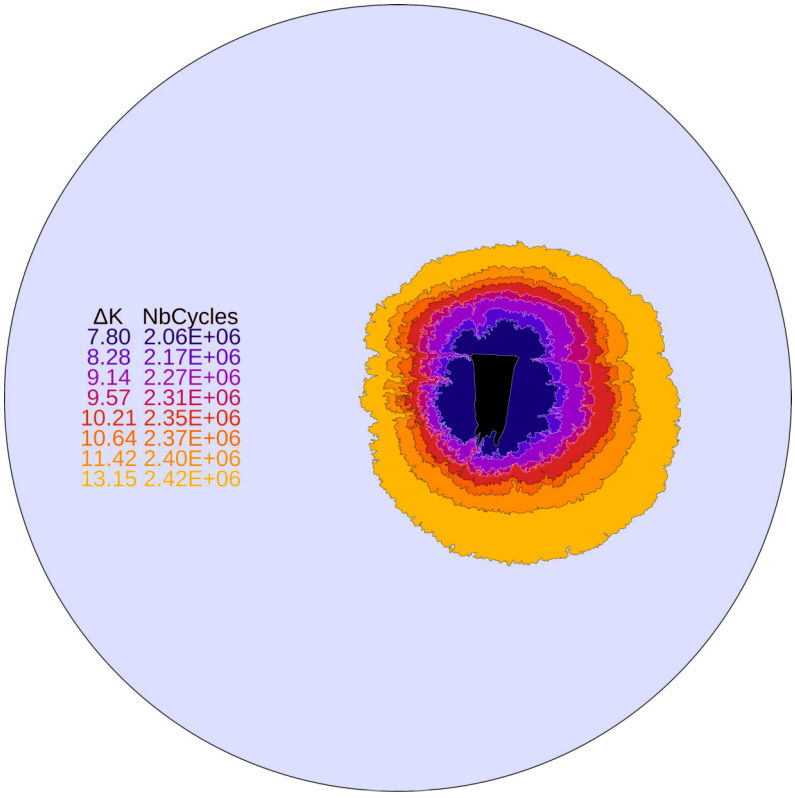

Figure 3.7 | Orthogonal projections of the crack fronts on a plane perpendicular to the cycling direction obtained from micro-tomography data of Specimen nb 58 cycled at 500 MPa. The blue circular shape represents the specimen section. The crack fronts are relatively regular when the crack is larger than the initial sharp notch.

3.2.2 Microscopic Observations

3.2.2.1 Observations of the Fracture Surfaces

Figure 3.8 shows an optical image of the fracture surface of a specimen which failed due to an internal fatigue crack (which has no link with the ambient atmosphere like all the other specimens presented in this chapter). As systematically observed for the specimens presented in this chapter, it presents the characteristic features described in the literature (by Hong & Sun for example [HON 17]). Three zones schematically shown in Figure 3.9 can be distinguished as follows:

- A zone with a dark aspect is present in the vicinity of the initiation site. In this so-called *Rough Area* (also called *Dark Area* in several references), the crack has a strong interaction with the microstructure which results in a relatively large roughness. More precisely, as shown in Figure 3.10, this zone contains smooth facets dispersed within larger «granular» areas. This is in agreement with many studies carried out on internal fatigue cracks observed in the same type of alloy [MCE 08, OGU 13, LIU 15].
- A circular zone surrounds the *Rough Area* and is more planar. Many literature references call the zone inside this circular area the *Fish-eye* zone.
- Finally, the *Steady Crack Growth Area* followed by the final fracture zone (where the SIF reaches the material toughness and propagates quickly) compose the last part of the fracture surface.

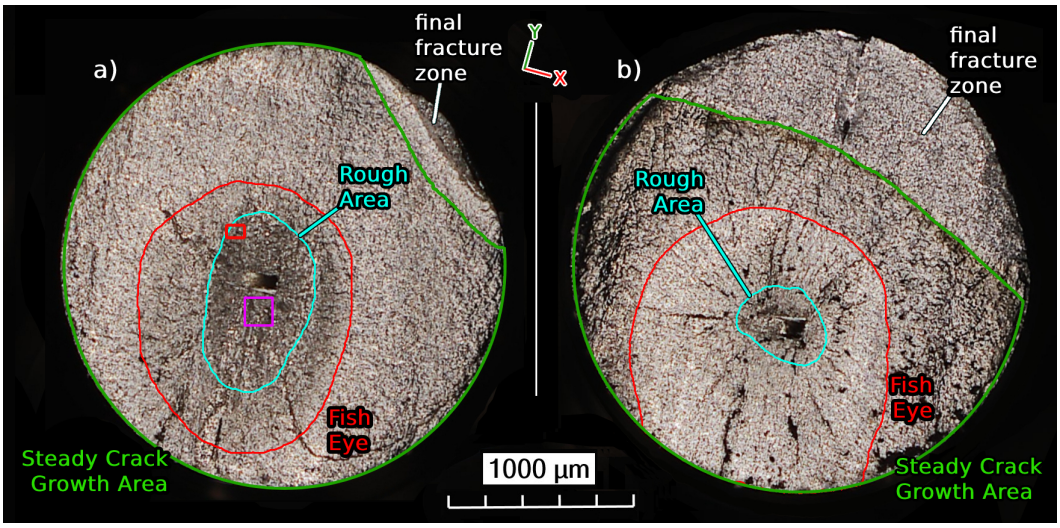

Figure 3.8 | **Optical microscopy observation of two fracture surfaces with internal fatigue cracks** (not linked with the specimen surface). (a) Specimen nb 46 cycled at 330 MPa during 4.55×10^7 cycles. (b) Specimen nb 59 cycled at 500 MPa during 3.38×10^6 cycles. The different zones schematized in Figure 3.9 are delimited in the present figure. The pink rectangle in (a) locates Figure 3.10a and the small red one localizes Figure 3.10b.

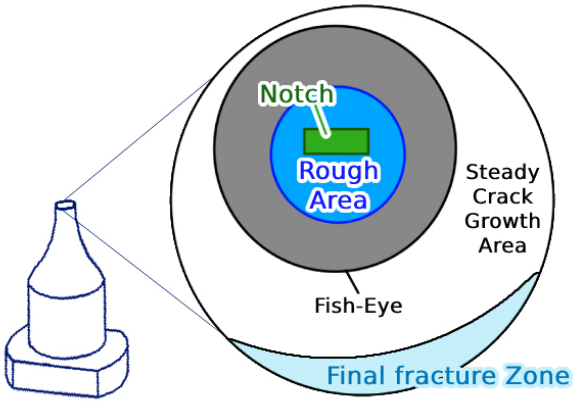

Figure 3.9 | **Scheme of the typical zones on the fracture surface of an internal crack**

In the literature, the normals of the facets observed on the *Rough Area* are usually roughly aligned with the $\vec{c}$ -axis of the HCP structure - also called the basal direction (cf. Fig. 1.3). For example, Pilchak *et al.* have used EBSD measurements to show that the angle between the facet normals and the $\vec{c}$ -axis is comprised between -20° and 40° [PIL 10]. The range of this interval is justified by the fact that when a propagating crack approaches a grain oriented for plastic deformation on the basal plane, it has to deviate to facilitate its propagation with the plastic slip system available in front of the crack. Hence, its normal is as close as possible to the $\vec{c}$ direction when it enters the considered grain. Consequently, the facet surface might not be perfectly parallel with a basal plane and present small steps. Other studies report that most of the facet normals are parallel to the $\vec{c}$ -axis [SIN 07, JHA 12]. A. Junet has estimated in his work that an important proportion of the facets comprised in the *Rough Area* were parallel to a basal plane but no quantitative measurement were carried out [JUN 21]. Conversely, a study by Evenaerts *et al.* was made on Ti64 wires which presented a strong prismatic texture (*i.e.* the grains have in majority their prismatic $\{10\bar{1}0\}$ planes aligned with the loading direction) [EVE 17b]. In this work, the authors observed an important majority of prismatic facets (*i.e.* which are parallel with a prismatic $\{10\bar{1}0\}$ plane of the HCP structure) and linked them with the original specimen texture.
In the present work, different experimental techniques have been employed to try to study more precisely the microstructural aspects of the different fractographic features reported above. The results of these observations are summarized in the following sections.

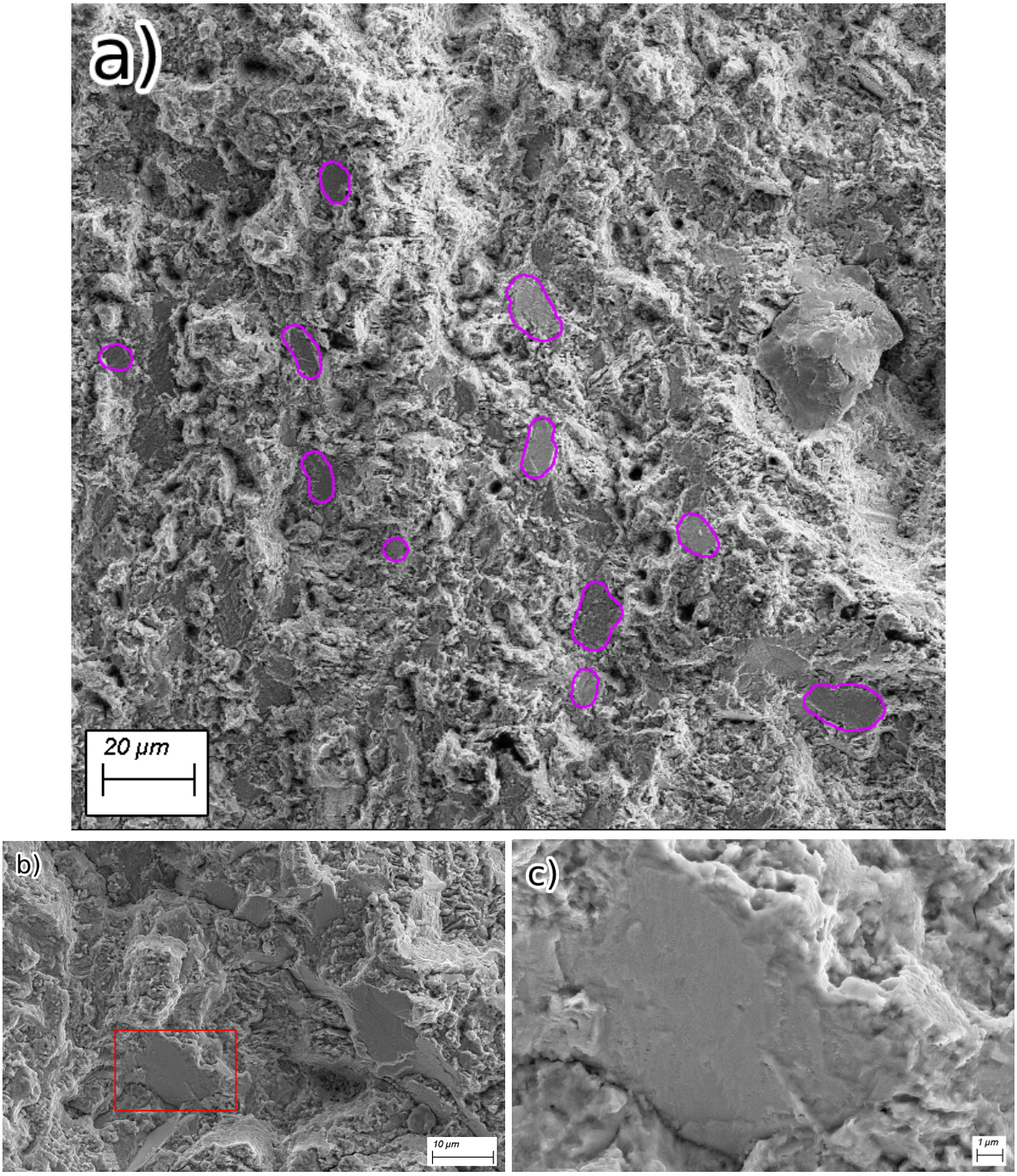

Figure 3.10 | **SEM detailed views of the *Rough Area* of an internal crack** (a) Global view showing a «granular» aspect with scattered facets (some of them are circled in pink). (b) View showing the «granular» aspect and some facets with a higher magnification. (c) Detailed view of a facet localized in the *Rough Area*. The red rectangle in (b) localizes (c).

3.2.2.2 Microstructural Observations of the Facets

As presented in the previous section, the formation of facets on the fracture surface of a propagating internal crack is controlled by the microstructure encountered by the crack immediately after initiation (short crack). This relation between facets and local microstructure has been analyzed with several methods to evaluate if the facet normals are aligned with a specific microstructural direction as reported by different studies.

a - *Large View of the Microstructure Under the Fracture Surface*

One specimen has been cut along the global normal direction of its fracture surface (*i.e.* in a plane parallel to the loading direction - *cf.* Fig. 3.11a) with a diamond wire saw. The obtained surface has been polished with an argon beam milling system (Gatan Ilion II) and it has been imaged with the EBSD method to observe the microstructure under the fracture surface (cf. Figure 3.11c).

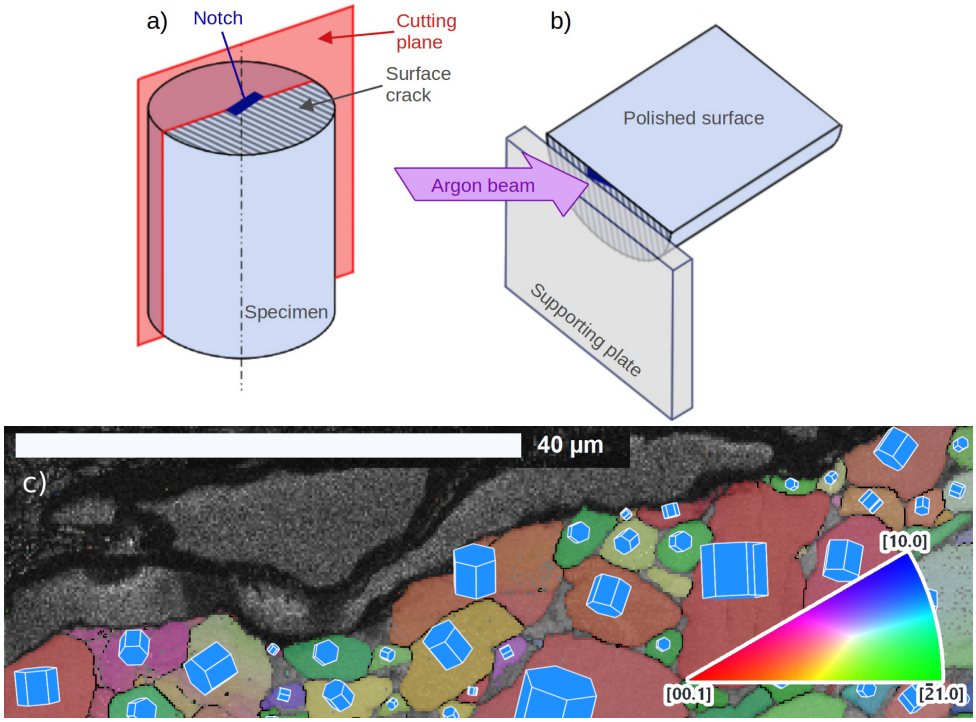

Figure 3.11 | EBSD map detail of the microstructure under the fracture surface Schemes of (a) the specimen cutting plane and (b) the polishing configuration. (c) EBSD map of the microstructure observed on the polished surface. The IPF shows the crystal direction parallel to the vertical direction of the picture. The crack depicted here was linked with the specimen surface (Specimen nb 49 cycled at 315 MPa during 8.16×10^5 cycles) as presented in Chapter 4 so the fractographic features are different but it allowed to evaluate the relevance of such an observation procedure.

This approach allows to observe a relatively large area showing the microstructure under the fracture surface. However, to carry out the polishing, the fracture surface has to be glued on a supporting plate (as schematized in Figure 3.11b), hence it is not possible to directly correlate the microstructure under the surface with the fractographic features observed from above the surface. So, it is not possible to know if the polished cut plane contains a facet.

b - *Local Microstructure Under One Facet*

To be sure to observe the microstructure under one facet, a thin lamella - hereafter called «wall» - of the fracture surface was extracted by Focused Ion Beam (FIB) milling. This allows to have access to the grains located just under the selected facet. This machining procedure is described in the following insert.

Focused Ion Beam Milling (FIB)

FIB milling is usually used to prepare small volumes extracted from a specimen for Transmission Electronic Microscope (TEM) observations. As summarized in Figure 3.12, a carbon or platinum protection layer has to be applied on the region of interest to prevent to damage it too much during the extraction (Fig. 3.12a). A gallium ion beam is then used to mill the material around the region of interest (Fig. 3.12b) before extracting the small wall and gluing it on a TEM holder - also called a grid (Fig. 3.12c). Finally, the wall thickness is diminished down to several dozens of nanometers (Fig. 3.12d) to carry out TEM observations (Fig. 3.12e). Such a FIB procedure has already been reported to study the microstructure under a fracture surface as described by Hong & Sun [HON 17].

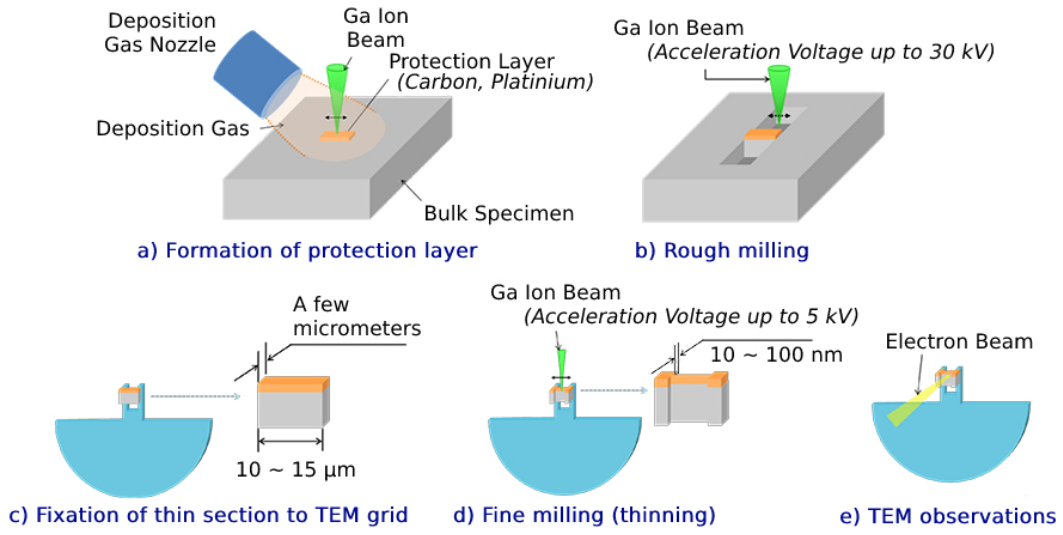

Figure 3.12 | Summary of the Focused Ion Beam milling procedure See text above for a description of the different steps. Scheme extracted from the JEOL website [FIB23].

A wall has been extracted under a specific facet located in the *Rough Area* of a specimen. The extraction plane is depicted in Figure 3.13 and the obtained wall is pictured in Figure 3.14a.

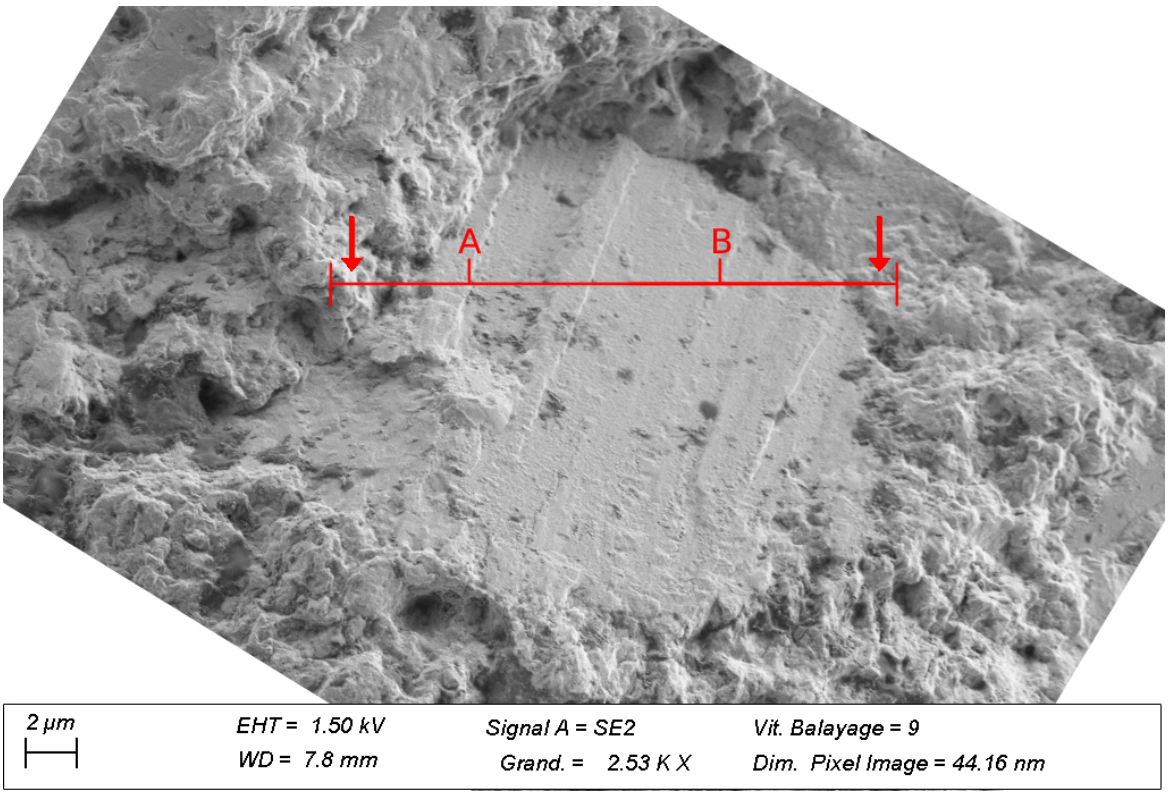

Figure 3.13 | **SEM picture representing a facet** located in the *Rough Area* of Specimen nb 44 cycled at 337 MPa during 1.17×10^8 cycles. The localization of the specimen wall extracted with FIB is represented by the red line and the face represented in Fig. 3.14a is depicted by the red arrows. *A* and *B* points are also represented in Figure 3.14a.

To analyze the microstructure of the wall, a Transmission Kikuchi Method (TKD) has been used* to obtain a better resolution than EBSD. This method is detailed in a following insert. This TKD method was applied to the extracted wall and the obtained map is represented in Figure 3.14b. It allows to observe that the facet is not completely planar because of a slip accommodation of the crack to propagate as close as it can from the basal plane (this is called *quasi-cleavage* and explained by Pilchak *et al.* [PIL 10]). The TKD map shows also that, underneath the facet, a single grain is found. Because the wall extraction procedure is a time-consuming process (several hours), no other facet was studied in such a way.
The orientation of the grain is displayed in the top left corner of Figure 3.14b. However, as the orientation between the facet normal and the cutting plane is unknown, it is not possible to

*We deeply thank Thierry Douillard for the time spent helping us with the FIB and TKD procedures.

precisely compare the direction of the facet normal with the crystal orientation (*i.e.* the angle between $\vec{n_m}$ and $\vec{n_F}$ from Figure 3.15 is unknown).

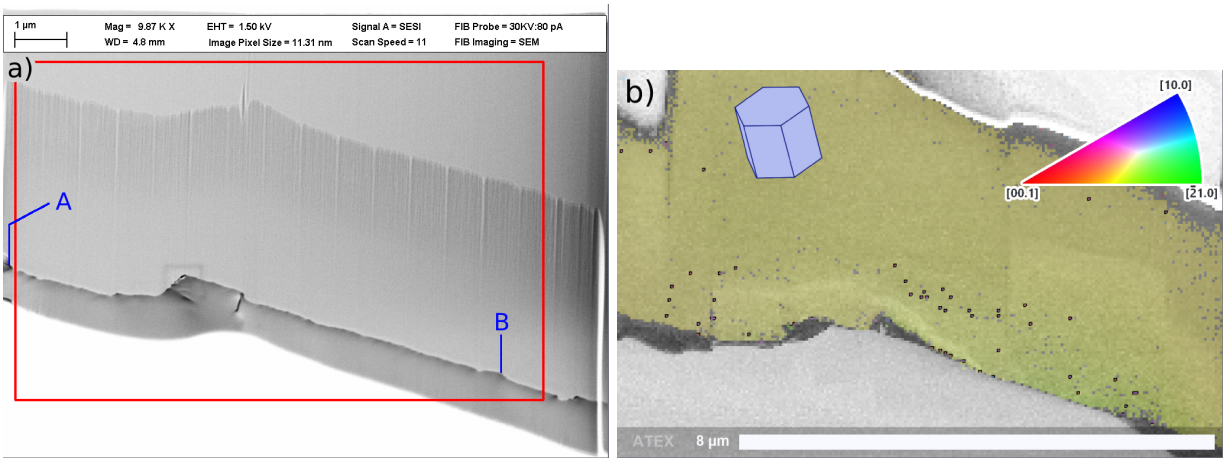

Figure 3.14 | **(a) SEM and (b) TKD pictures of the extracted wall located under the facet** depicted in Fig. 3.13. Only a single grain seems to be present under the facet. The EBSD map has been obtained with TKD method and the IPF presents the crystal direction which is normal to the picture. The red rectangle in (a) locates (b) and A and B are also represented in Figure 3.13.

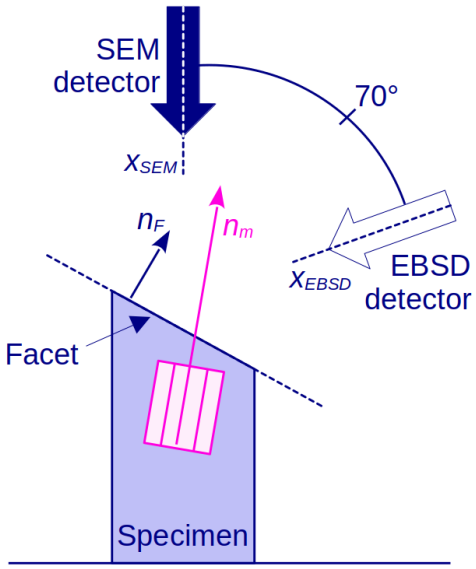

Figure 3.15 | **Scheme of the different directions used to describe the orientation of a facet in a specimen observed with SEM and EBSD** $\vec{x_{SEM}}$ and $\vec{x_{EBSD}}$ are respectively the observation direction of the SEM and the EBSD detectors. The angle between those two directions is known. $\vec{n_F}$ is the normal of the observed facet. $\vec{n_m}$ is the direction of the $\vec{c}$ - axis of the grain under the facet.

Transmission Kikuchi Diffraction Method (TKD)

TKD is used on thin specimens to collect the electrons which are transmitted through the region of interest to build an EBSD map from the collected diffraction patterns. As summarized in Figure 3.16, EBSD is usually used to study the surface microstructure of relatively bulky specimens whereas TKD is used to study reduced regions from thin specimens. When it can be used, the TKD method provides a better resolution than the classic EBSD.

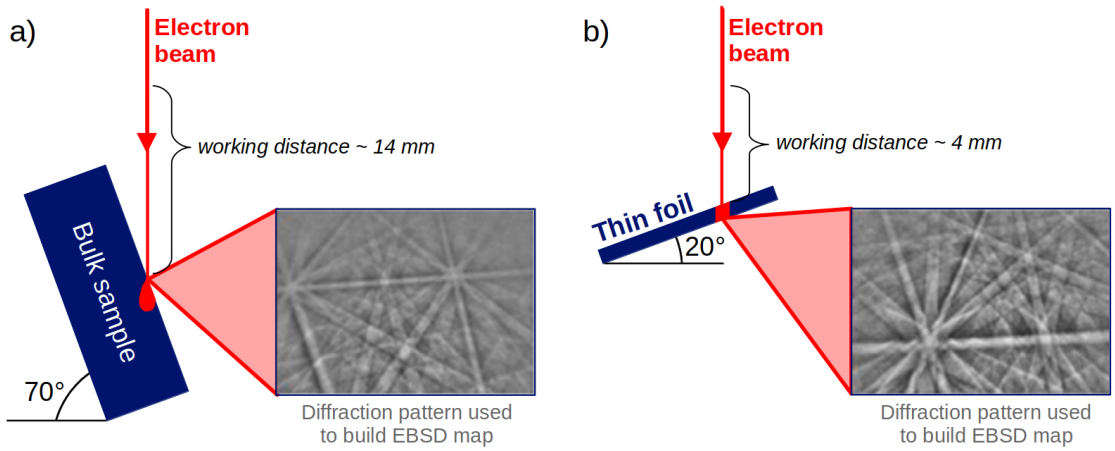

Figure 3.16 | Principle set-ups for (a) EBSD and (b) TKD methods. TKD is used for thin specimens and uses the electrons transmitting through the specimen. Figure adapted from the work of Liang *et al.* [LIA 19].

c - *Direct EBSD Mapping of the Facets*

Some EBSD acquisitions were carried out on the fracture surface directly pointing at the facets. The quality of the obtained maps may be not very good but it allows to obtain the angle between $\vec{n_m}$ and $x_{\vec{EBSD}}$ (from Figure 3.15) for the grains located under some facets (depending on their orientation and flatness). For example, a facet has been studied in such a way in Figure 3.17: the angle between the view direction, x_{EBSD}, and the grain $\vec{c}$-axis can be measured and seems to be close to 0°. So, it is highly likely that this facet corresponds to a basal plane but, as the orientation of the facet normal, n_F, is unknown, it is not possible to be sure of that.

To measure the angle between the facet normal and the SEM observation axis, the quantitative tilt fractography method has been employed as it was done by Sinha *et al.* [SIN 07] after the work from Themelis *et al.* [THE 90]. As described in Appendix B, this technique needs two pictures of the same facet acquired when the specimen is tilted with two different angles. From those two images, it is theoretically possible to obtain the angle between the facet normal, n_F,

and the view direction, x_{EBSD}. For the example of Figure 3.17, this angle between the facet plane and the $\vec{c}$ -axis, was determined to be 79° using this method (similar measurements for other facets are shown in Appendix F). When compared to the 3D rendering of the HCP cell on Figure 3.17, this value seems at least inaccurate and most probably wrong. This error might be due to the very small size of the analyzed facet which could lead to high uncertainties on the results obtained with the tilt fractography method. Another method based on roughness measurements using optical confocal microscopy was briefly tested to measure this angle and is presented in Appendix F. This last method was not more successful than the one previously described.

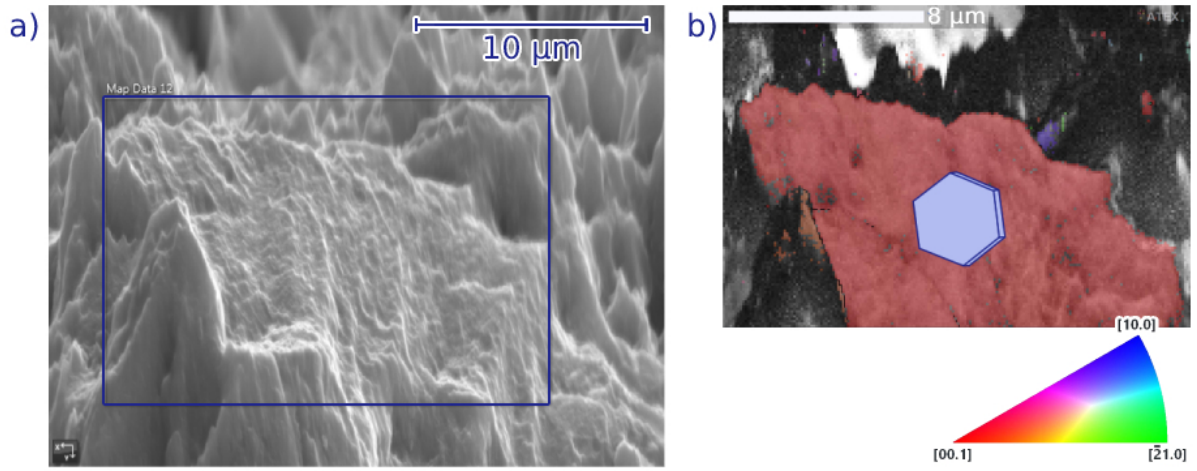

Figure 3.17 | **(a) SEM picture of a facet present in the *Rough Area* of an internal crack fracture surface and (b) its corresponding EBSD map** Because the axis of the EBSD camera has a 70° angle from the axis of the SEM camera (*cf.* Fig. 3.15), Picture (a) is artificially distorted to show the SEM picture with the same angle than the EBSD one (*i.e.* in a way such as the specimen is observed from a 0° view direction). The IPF shows the crystal direction normal to the picture. The depicted feature belongs to the fracture surface of Specimen nb 46 cycled at 330 MPa during 4.55×10^7 cycles.

d - *Concluding Remarks on the Micrstructural Analysis Under the Facets*

As reported by the literature, the carried out approach allowed to point out that, **only one grain is located under each facet**. The angle between the microstructure of such a grain and the normal of its corresponding facet is difficult to measure. However, from the variety of grain orientations reported under different facets in Appendix F, it emerges that **the facet normal is not systematically aligned with the basal direction of the grain**. This observation can be linked with the results described earlier from Evenaerts *et al.* who claimed that the facet normals are controlled by the texture of the original material. In the present work, the used Ti64 contains large macrozones where neighboring grains are similarly oriented. Specifically, as

the specimens are manufactured to have their length parallel to the rolling direction (presented in Figure 2.3), the $\vec{c}$ -axis of the macrozones are either oriented along the specimen's length (*i.e.* normal to the crack surface) or in the specimen's section (*i.e.* compatible with a prismatic direction normal to the crack surface). This could explain the presence of various alignments between the facet normals and the local microstructure.

3.2.2.3 Granular Areas

Between the facets present in the *Rough Area*, the fracture surface has a «granular» rough aspect. This type of fractographic feature is illustrated in Figure 3.18. A thin wall has been extracted from this area with the FIB method to observe the underlying microstructure. The observed section is shown in Figure 3.19a and the TKD maps are presented in Figures 3.19b, 3.20a and 3.20b. On these figures, it is possible to distinguish several regions immediately under the crack surface which are composed of nanograins. The size of those nanograins, around 150 nm, is approximately 100 times smaller than the average grain size of the original material, suggesting that this microstructure was not present in the initial material and might be due to the cyclic loading and the presence of the fatigue crack.

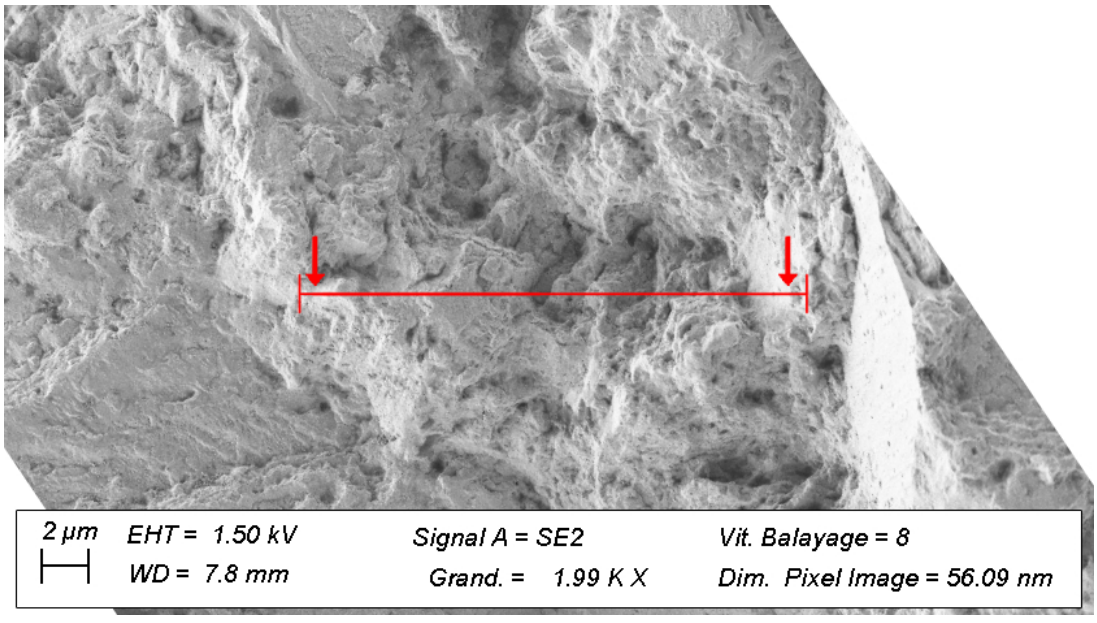

Figure 3.18 | SEM picture of a «granular» rough zone located in the *Rough Area* from the fracture surface of Specimen nb 44 cycled at 337 MPa during 1.17×10^8 cycles. The localization of the wall extracted with FIB is represented by the red line and the face observed in Fig. 3.19a is depicted by the red arrows. FIB milling was carried out on one of two crack surfaces (*i.e.* one side of the cracked specimen) and the presented picture was taken on the second one. That is the reason why the holes in the present figure correspond to the pikes of Figure 3.19a.

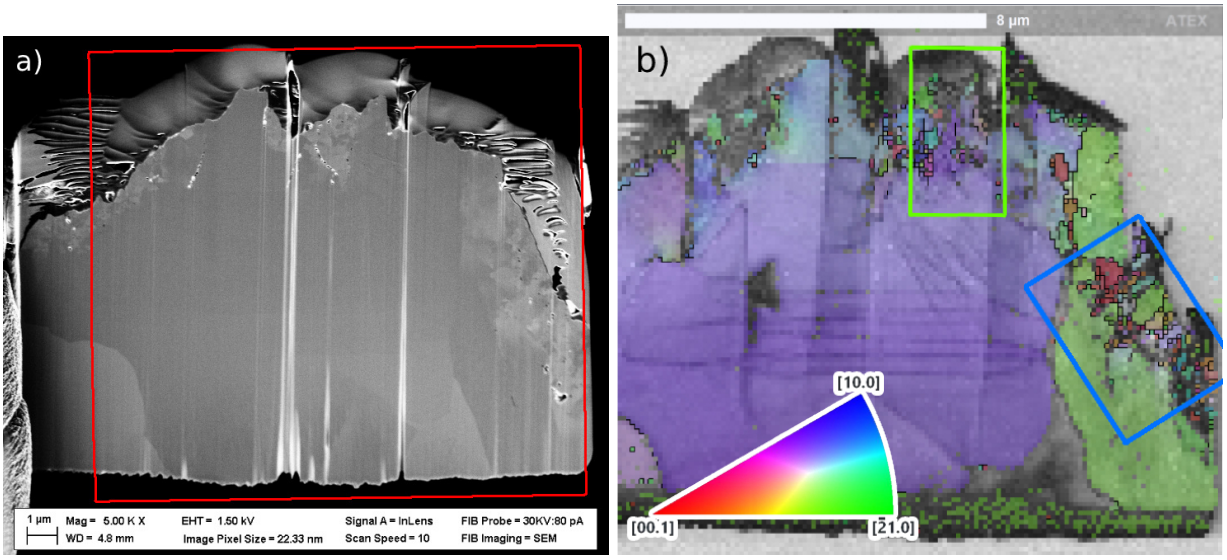

Figure 3.19 | **(a) SEM picture and (b) TKD map of the extracted wall located under the «granular» rough zone** depicted in Fig. 3.18. The red rectangle in (a) locates (b). The blue rectangle locates Fig. 3.20a and the green one locates Fig. 3.20b. The IPF presents the crystal direction normal to the picture.

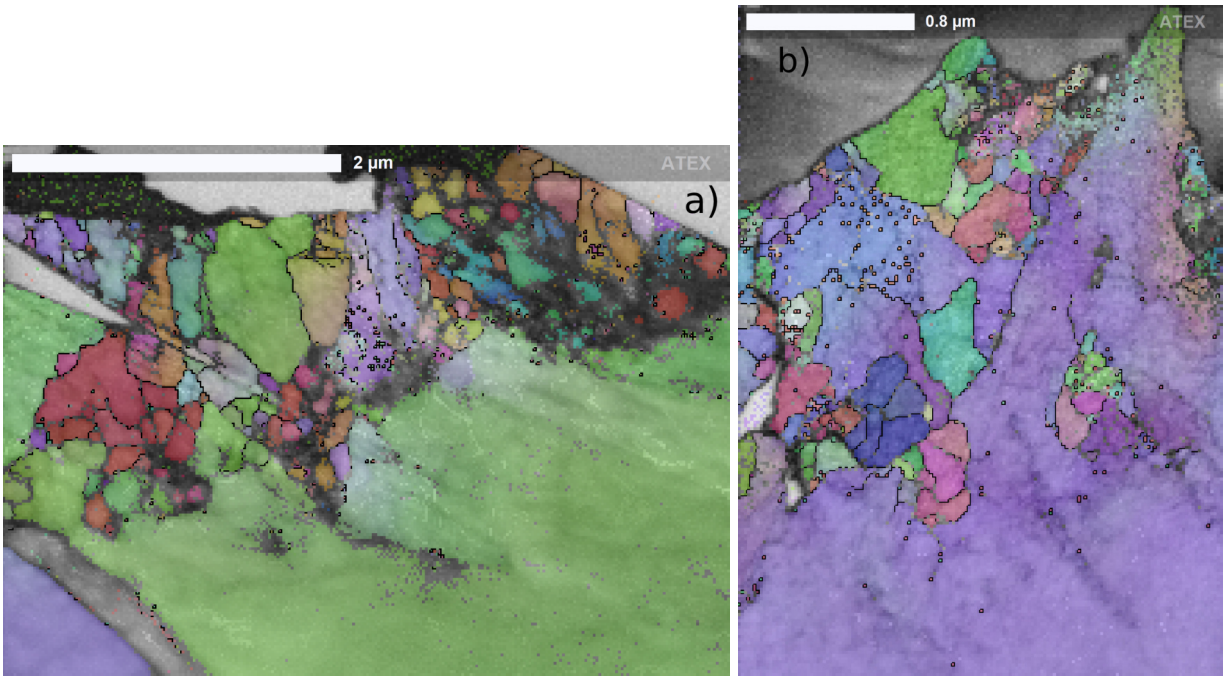

Figure 3.20 | **Detailed views of the map obtained with TKD under a «granular» rough zone** A nanograin layer is present just under the granular features of the crack surface (the grain size of the original material is $10.8 \pm 1 \mu$m).

Several studies report grain refinement under the crack surfaces in steels as reviewed by Sakai *et al.* [SAK 16]. Hong & Sun observed a wall extracted by FIB out of the fractographic surfaces of a high-strength steel and a Ti64 alloy which have been ultrasonically fatigue tested. Their Transmission Electron Microscope observations allowed them also to distinguish nanograins in a micrometer-thick layer under the crack surface [HON 17]. Su *et al.* observed the same type of microstructure in a bi-modal Ti64 alloy [SU 17], the nanograins average size of 105 nm was a bit smaller than those observed in this study and illustrated in Figure 3.20 (estimated to be around 150 nm). In this paper of Su *et al.*, different stress ratios were tested and it emerges that the *Rough Area* and the nanograins layer were absent from the initiation site of failed specimens which were cycled at $R = 0.5$ whereas they were observed at $R = -1$. Furthermore, Hong & Sun [HON 17] reported an absence of *Rough Area* for specimens ultrasonically cycled at $R = -1$ which failed after a short amount of cycles ($N = 1.28 \times 10^5$ cycles). In their study, the size of the *Rough Area* was reduced but still present for specimens cycled at $R = 0.1$. A. Junet observed a granular *Rough Area* on the same alloy at R = 0.1 (20 Hz) although no attempt was made to analyze the grain structure under the fracture surface [JUN 21].

To understand these observations, Hong *et al.* proposed the so-called Numerous Cyclic Pressing (NCP) model. The formation of the nanograins layer under the *Rough Area* is supposed to be caused by an accumulation of plastic deformation originating from the repeated pressing between the two crack lips [HON 16]. According to this model, the formation of the *Rough Area* and of the nanograins layer is favored by long fatigue lives and negative stress ratios.

Another hypothesis justifying the presence of the *Rough Area* and of nanograins is however claimed by Oguma *et al.* [OGU 13] who suppose that the repeated contact of the internal crack surfaces induces a cold-welding phenomenon. The cyclic loading provokes a repeated fracture of the cold-welded surfaces (not necessarily at the same location within the grains) leading to some microstructure refinement. Cold-welding provoked by cyclic loading has been experimentally observed in the case of pure platinum nanocrystals analyzed with Transmission Electron Microscope [BAR 23]. As it will be presented in Chapter 4, when air molecules are brought to an internal crack during its propagation, the fracture surfaces do not present a *Rough Area* nor nanograins. Assuming that the NCP mechanism could operate in air as well as in vacuum while cold-welding should be favored in vacuum (oxidized surfaces would be very difficult to weld), this brings an argument in favor of the cold-welding hypothesis to justify the presence of the *Rough Area*.

In a nutshell, as pointed out by the different zones of the crack surface, the crack path is impacted by the microstructure in the first stages of propagation. Furthermore, the presence of the nanograins layer shows that the crack itself induces some modifications in the microstructure. The different fractographic zones where different mechanisms are active could have an impact on the crack growth rate. The latter is analyzed in the next section.

3.3 Crack Growth Rate

The cracks obtained with tomography acquisitions carried out at different instants between the fatigue crack first detection and the specimen final fracture (represented in Figure 3.21a as an example) allows to estimate the crack growth rate of the studied internal fatigue cracks within each of the regions identified on the fracture surfaces. This type of data has only been obtained in the literature by Yoshinaka *et al.* [YOS 19] who also used synchrotron micro-tomography. However, in their case, the cycling frequency was 400 Hz, the stress ratio was $R = 0.1$, the cracks initiated naturally (*i.e.* without any artificial defect) and no relation was made with the fractographic features.

In the current study, the 3D crack fronts observed after different numbers of cycles are used to plot the crack growth rate curves ($da/dN = f(\Delta K)$ with $a = a_{eq}$ the crack size, N the number of cycles and ΔK the SIF range). To do this, an equivalent crack size a_{eq} is evaluated from the area of the 3D projected crack obtained thanks to the thresholding protocol described in Section 2.4.1. a_{eq} corresponds to the radius of a disk (*i.e.* penny-shape crack) with the same area as the projected crack: $a_{eq} = \sqrt{area/\pi}$. Figure 3.21b represents the crack radius measured at different polar coordinates around the notch for successive tomographic scans and the black curve represents a_{eq} measured for the same scans. It can be seen that the a_{eq} estimation is a good average (this is also the case for the other tomographied cracks).

The thresholding protocol could not be carried out for specimens nb 44 and 45 because of the presence of ring artifacts in the 3D images obtained at the ID19 beamline (ESRF). For these two specimens, the crack equivalent radius was therefore approximated by half the maximum crack dimension measured from several 2D sections of the 3D acquired volume. This approach was carried out for the other specimens as well to check that the difference between the two approaches is not important (around 15% difference in the measured values of a_{eq}).

The value of the SIF range, $\Delta K = K_{max} - K_{min}$, is estimated by using Eq. 3.1 where σ the applied stress, a_{eq} the equivalent crack radius and b the specimen gauge length radius [TAD 00].

$$K = \frac{2}{\pi}\sigma\sqrt{\pi a_{eq}}\ \frac{1 - \frac{a_{eq}}{2b} + 0.148\left(\frac{a_{eq}}{b}\right)^3}{\sqrt{1 - a_{eq}/b}}, \tag{3.1}$$

This equation is valid for a penny-shape crack at the center of a specimen with a circular cross-section (diameter $2b$) as explained above. This penny-shape has been assumed all along the fatigue life including the early stages of propagation where some cracks can have irregular 3D fronts (cf. the darker shapes of Figure 3.21a). This hypothesis entails an uncertainty on the measurement, it has been quantified and is detailed in Appendix A. This simplified data analysis - which also ignores the crack eccentricity - mainly aims at *comparing* a propagating internal crack with data from the literature.

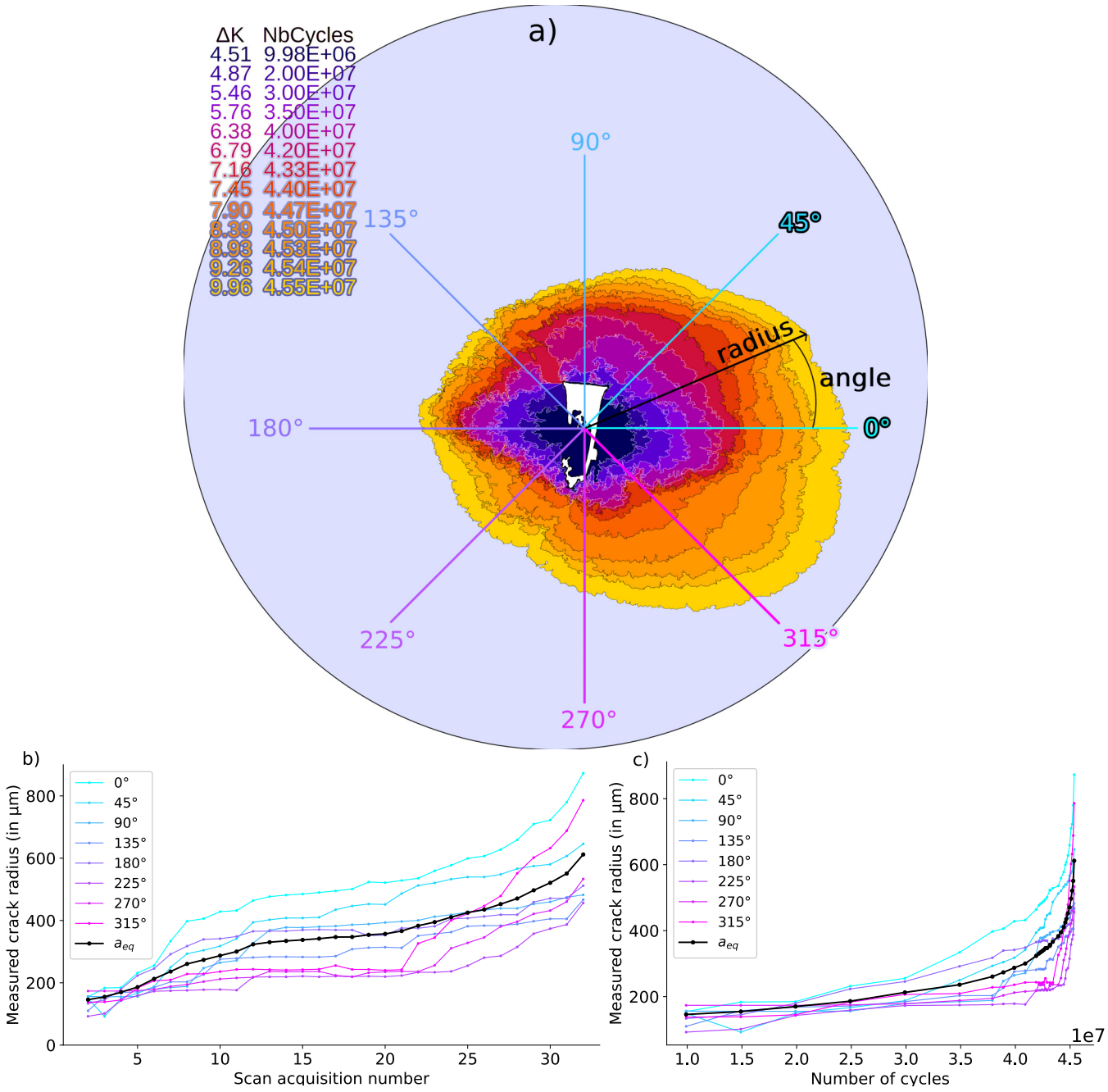

Figure 3.21 | **(a) Orthogonal projections of the crack fronts on a plane perpendicular to the cycling direction obtained from micro-tomography data. (b) & (c) Different crack radius measurements** estimated at the various polar coordinates represented in (a) for successive tomographic scans (as illustrated by the angle represented in black in (a)). The black curves in (b) & (c) correspond to the equivalent crack size estimated as $a_{eq} = \sqrt{area/\pi}$. The crack propagated in Specimen nb 46 cycled at 330 MPa during 4.55×10^7 cycles before final fracture.

It is generally supposed that the crack does not propagate when it is closed. Consequently, the effective SIF range ΔK_{eff} is approximated as $\Delta K_{eff} = K_{max} - K_{op}$ with K_{op} the minimum SIF value for which the crack is open. According to our knowledge, with an ultrasonic loading at 20 kHz, it is not possible to experimentally determine the value of K_{op}. Hence, as cycling was carried out under a loading ratio of $R = -1$, the crack is supposed to be closed when the applied stress is negative ($K_{op} = 0$ and consequently $\sigma_{max} = \Delta\sigma/2$). Equation 3.1 then transforms as follows (with $\Delta\sigma/2 = \sigma_a$ the stress amplitude):

$$\Delta K_{eff} \approx \frac{2}{\pi}\frac{\Delta\sigma}{2}\sqrt{\pi a_{eq}}\ \frac{1 - \frac{a_{eq}}{2b} + 0.148\left(\frac{a_{eq}}{b}\right)^3}{\sqrt{1 - a_{eq}/b}}, \tag{3.2}$$

The crack growth rate $\frac{da}{dN}$ is estimated from the crack size difference between two successive scans $a_{eq}(scan\ k+1) - a_{eq}(scan\ k)$. It is linked with an average of the two SIF evaluated for these two scans to obtain Figure 3.22. The estimated value is the mean value of the crack growth rate between (scan $k+1$ and scan k) for an equivalent penny-shape crack. The corresponding uncertainties on these measurements are detailed in Appendix A.

Figure 3.22 compares the crack growth rate data from this study with experimental data from the literature. The circle symbols correspond to specimens cycled in the present study with an internal sharp notch not in contact with ambient atmosphere *i.e.* without a chimney. Reference data include some cracks which had either internal initiation or surface initiation with the whole specimen put in vacuum. These two types of testing conditions will be called *vacuum-propagating* cracks hereafter. The fact that only one reference reports internal fatigue crack propagation rates [YOS 16a] illustrates the lack of in-situ observations of *internal* fatigue cracks in the literature. Besides, only one literature dataset could be found for cracks propagating under vacuum conditions at $R = -1$ (with a 20 kHz cycling frequency) [GEA 22]. Therefore, the crack growth rates could mainly be compared with literature experiments carried out at $R = 0.1$. It seems that the crack growth rates obtained in the present study are in very good agreement with the values from the literature for vacuum-propagating cracks. The only difference concerns the crack growth rates obtained by Junet *et al.* which are higher than the others [JUN 23]. In their study, the protocol used to manufacture the specimens and to acquire tomographic data is similar to the one used in the present work. The main difference is the cycling frequency (20 Hz for Junet *et al.* and 20 kHz in the present study). This point will be discussed in Chapter 4 when the influence of environment will be taken into account.

Another point seems in agreement with the literature concerning the crack propagation regime. As frequently observed by other studies, the crack growth rates seem more dispersed for low values of SIF range (*i.e.* $\Delta K < 7$ MPa $\sqrt{\text{m}}$) than for high values. This observation is also valid for the results obtained in the present study even though the crack size was averaged using a a_{eq} radius.

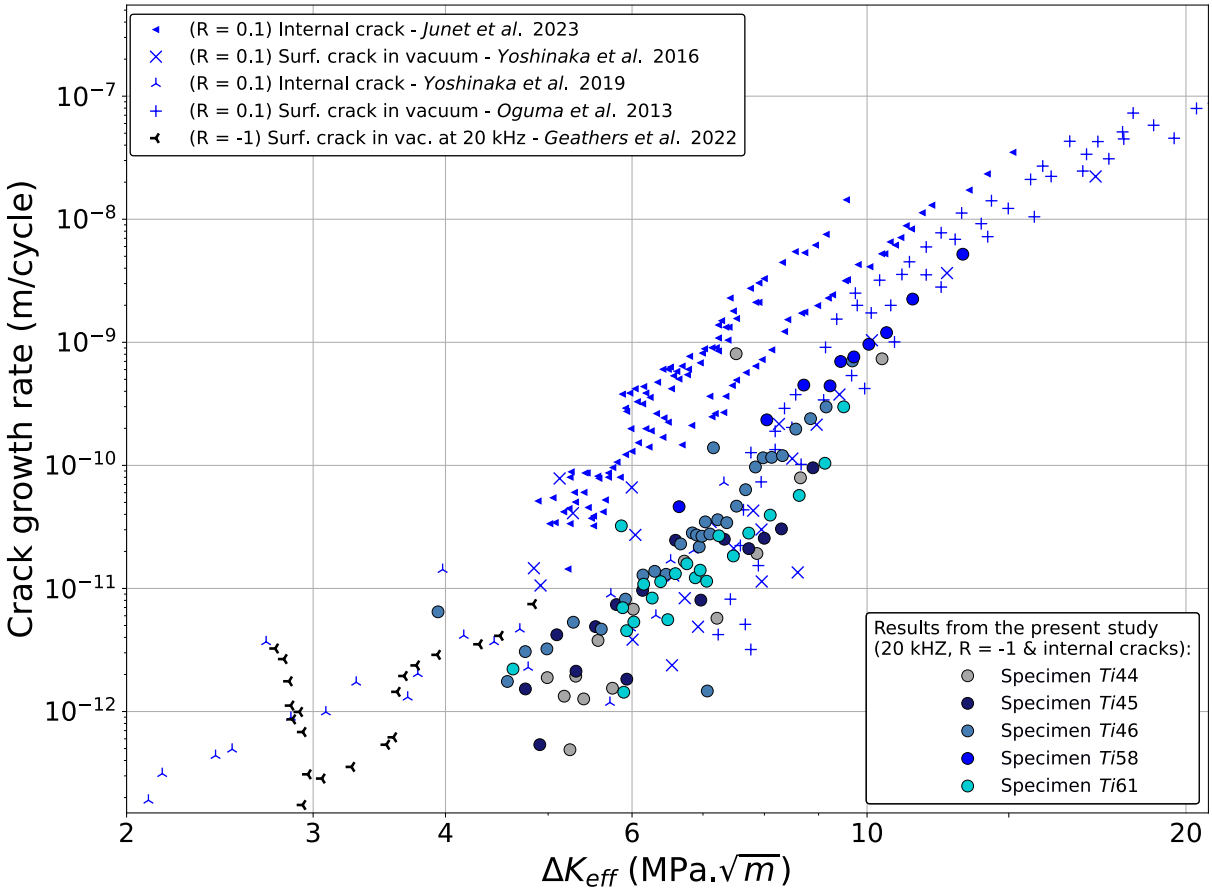

Figure 3.22 | **Crack growth rate data in a Paris diagram for the tested specimens with internal cracks** All the literature data points [OGU 13, YOS 16b, YOS 19, GEA 22, JUN 23] were obtained at low loading frequency *i.e.* between 20 and 400 Hz and under positive stress ratio ($R = 0.1$) except for Geathers *et al.* (20 kHz and R = -1). Table 3.2 links each marker type with a specimen. The experimental conditions of the literature references are listed in Appendix H. The growth rates of the cracks propagating from an artificial internal notch seem to be in agreement with the rates reported in the literature for crack propagating in vacuum and internal cracks (except for Junet *et al.* data points).

In addition to the fractographic observations, the crack growth rate measurements allow us to be confident in the fact that a crack initiated from an internal artificial sharp notch propagates in an environment comparable to vacuum. This means that the combination of the notching procedure and ultrasonic cycling provides internal notches with a vacuum level comparable to natural internal cracks. This allows to validate the data collected with the presented experimental protocol to study internal fatigue cracks.

However, the differences in crack growth rates with the results from Junet *et al.* who used

the same type of artificial internal notches need to be explained [JUN 23]. For that purpose, an approach where similar internal notches were linked with the specimen surface (with a chimney) has been carried out to obtain more elements but also to discuss (with some physical evidence and results) the influence of environment on propagating fatigue cracks.

3.4 Chapter Synthesis

In this chapter, the results obtained with the combination of a specimen artificial notching procedure and an ultrasonic cycling protocol coupled with micro-computed tomography have been presented and analyzed. The following points emerge from this work:

- Performing in-situ fatigue tests at very low-stress amplitudes results in long fatigue lives ($N > 10^8$ cycles). So ultrasonic cycling allows shortening VHCF experiments to be adapted to synchrotron procedures.
- The fatigue lives obtained on unnotched specimens are in agreement with fatigue data of Ti64 from the literature.
- The notch insertion is crucial to ensure a systematic internal initiation and to optimize the micro-tomography in-situ analysis.
- The notched specimens had lower fatigue lives which were more reproducible than the usual lives referenced in literature for Ti64.
- The microscopic analysis of the fracture surfaces confirms the typical presence of a *Rough Area* in the vicinity of the crack initiation site. It is composed of facets scattered in a «granular» aspect zone. Those facets are located within a single grain and their normal vector is not always parallel with the microstructural $\vec{c}$-axis of their underlying grain. The granular aspect seems to be related to microstructure refinement immediately under the fracture surface. This phenomenon has already been observed and is probably attributed to cold-welding under negative loading ratios.
- Fractographic and fatigue crack growth rates analysis allow to know that the cracks obtained with the internal notching procedure are propagating in an environment comparable to the one undergone by natural internal fatigue cracks.

Graphical Overview

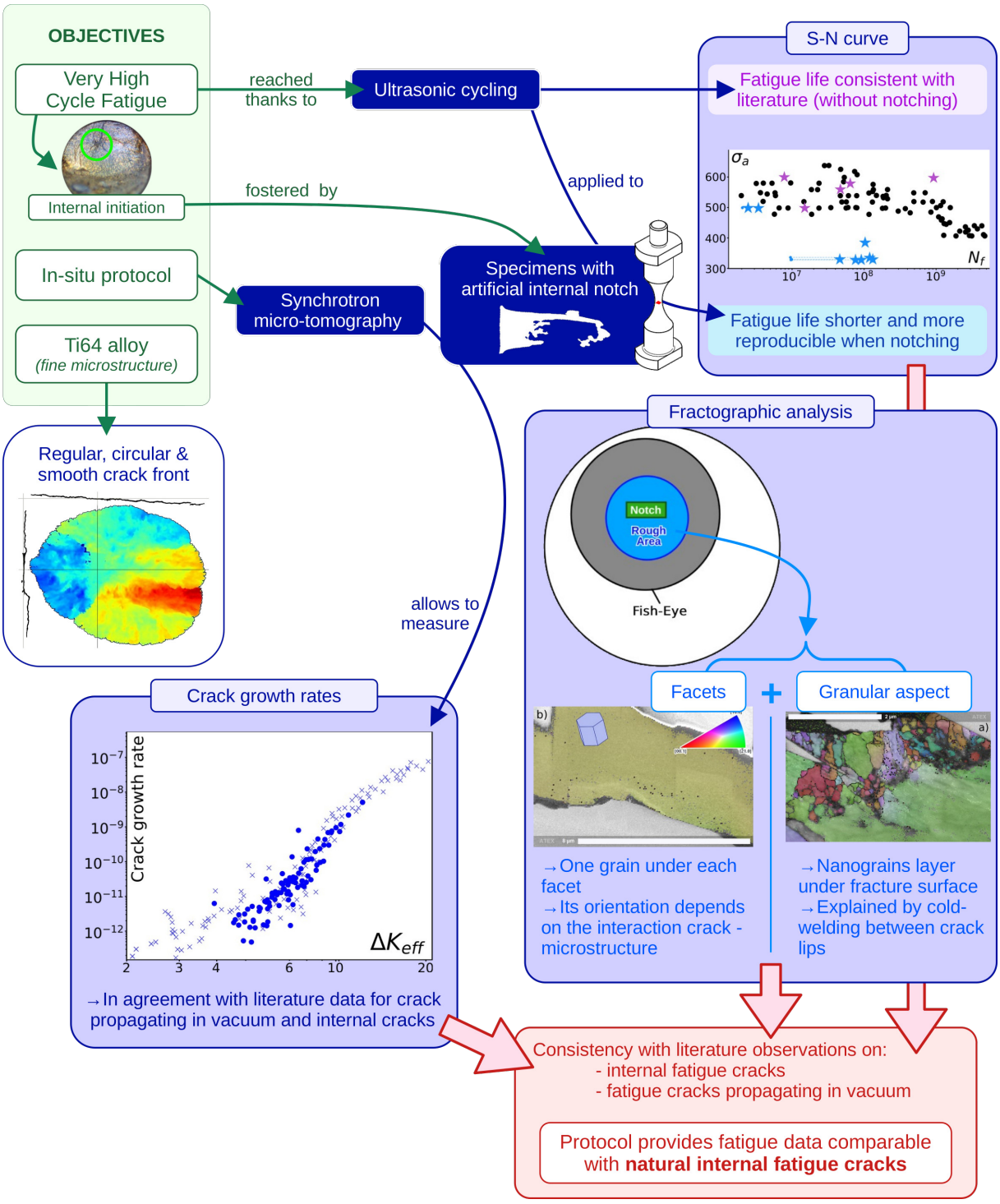

Figure 3.23 | **Synthesis of the experimental results** obtained with in-situ ultrasonic fatigue tests applied on specimens containting an artificial internal sharp notch.

Chapter 4

Environment Effect

Contents

The last chapter was focused on internal fatigue cracks which present lower growth rates than surface cracks growing in air [CHA 15, YOS 16a, SER 17, JUN 19]. The two differences between internal and surface cracks are their position within the specimen section and the environment in which they propagate. The crack position influences the stress field at the crack front because a small surface crack will undergo plane stress whereas internal cracks will mainly experience plane strain conditions. This may play a role in the plasticity at the crack tip and therefore, have an influence on the growth rate [VAR 11]. In the previous chapter, it was confirmed that surface cracks propagating in specimens cycled in vacuum present growth rates comparable to

the cracks emanating from internal artificial defects. To eliminate a potential effect of the stress field at the crack tip, the procedure to obtain internally notched specimens has been adapted to insert a chimney that links the artificial defect to the outside surface. «Bring air to internal fatigue cracks» has been developed to study cracks with shapes and stress fields similar to the ones studied in Chapter 3. This should allow to evaluate only the environment effect. It is assumed that, because of the small dimensions of the added chimney linking the internal notch with the specimen bottom surface (as represented in Figure 4.1), this one has a limited influence on the stress field around the notch. Furthermore, this study focuses on the crack propagation mechanisms away from the internal artificial sharp notch where this possible influence should be negligible.

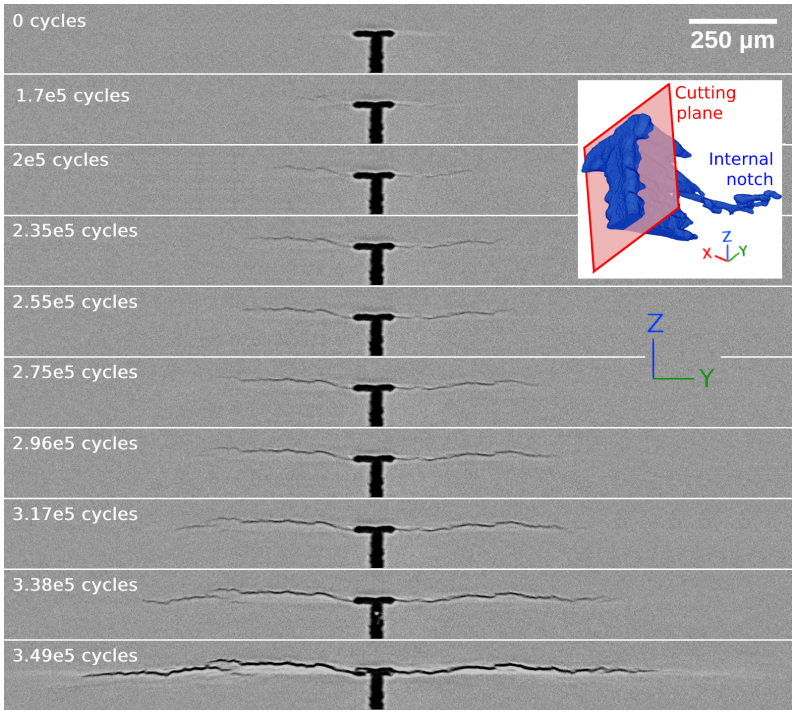

Figure 4.1 | Propagation of an internal crack in a specimen (nb 53) with a chimney visible on the pictures Data obtained by slicing the reconstructed tomographic volumes acquired at different numbers of cycles. The applied stress amplitude is 300 MPa and the loading direction is parallel to Z. The shapes of the notch and the top part of the chimney are illustrated in the insert along with the cutting plane used to represent the successive slices.

4.1 Fatigue Life

Four ultrasonic notched specimens had a chimney linking the internal crack to the specimen bottom surface. These specimens were cycled during synchrotron experiments to obtain tomographic data for three of them (see the list in Table 4.1).

Specimen nb	Stress ampl. (MPa)	Nb of cycles before fracture*	Nb of cycles when a crack is detected using μCT	Corresponding marker in Fig. 4.20
48	300	5.04×10^5	3.70×10^5	
49	315	8.16×10^5	No μCT data	
52	300	4.02×10^5	3.49×10^5	
53	300	3.60×10^5	6.21×10^4	

Table 4.1 | Internally notched ultrasonic specimens with a chimney

As it was done for specimens without the chimney, the total number of cycles before fatigue fracture was plotted in an S-N curve (Fig. 4.2). It can be seen in this figure that, for the investigated stress levels, the fatigue lives are shorter for internal cracks propagating in a specimen with a chimney than for cracks in specimens without a chimney. During his PhD thesis, A. Junet cycled fatigue specimens with a similar protocol but a lower frequency (20 Hz) at higher maximum stress σ_{max} and a positive nominal stress ratio $R = 0.1$ [JUN 21]. He measured a difference in fatigue life of approximately one decade between cracks in specimens with and without a chimney. In the present study where the maximum stress is about 50% lower than for his experiments, the difference in fatigue life reaches more than two decades.

This two decades difference can be explained by the number of cycles needed to start a long crack propagation because, as pointed out by Oguma & Nakamura [OGU 13], the ΔK_{th} value (below which long cracks do not propagate) is lower for a crack propagating in air than for a crack growing in vacuum. Also, as explained in the following sections, the cracks propagating in specimens with the chimney (*i.e.* linked with the specimen surface) have higher growth rates than the ones without a chimney. Hence, the number of cycles during which a crack propagates is also reduced if it is linked with the specimen surface.

A first order calculation was carried out to estimate the number of cycles during which a crack emanating from the internal sharp notch propagates. For that purpose, the Paris law described in Section 1.3.3 is integrated. If Equation 3.1 [TAD 00] is considered for a penny-shape crack located in the center of the circular section of a specimen (with b its radius), the number of cycles, N_f, needed to propagate from the a_i initial crack radius to a final size, a_f, can be evaluated as follows:

$$N_f = \frac{1}{C(2/\sqrt{\pi})^m \Delta\sigma^m} \int_{a_i}^{a_f} \frac{da}{a^{m/2} f(a/b)^m}, \text{ with } f\left(\frac{a}{b}\right) = \frac{1 - \frac{a}{2b} + 0.148\left(\frac{a}{b}\right)^3}{\sqrt{1 - a/b}} \tag{4.1}$$

*As specified in Chapter 2, this is the total number of cycles applied to the specimen until it cannot resonate anymore because the crack has fractured almost all the specimen section.

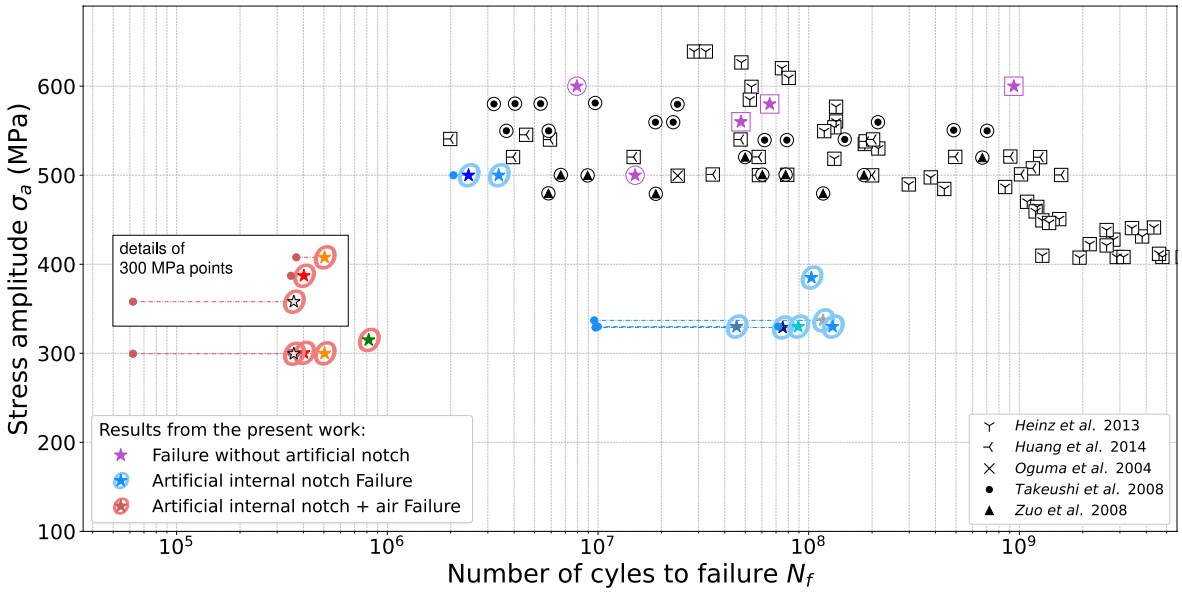

Figure 4.2 | **S-N graph for ultrasonic notched specimens with internal cracks linked to the surface with a chimney** compared with data from the literature, from unnotched specimens and from notched specimens without the chimney. The experimental conditions of the literature references are listed in Appendix H. The horizontal dashed lines represent the number of cycles between the crack first detection and its final fracture. A detailed view is added to distinguish the different points cycled at 300 MPa. The fatigue lives of specimens with an internal sharp notch are reduced when a chimney is inserted.

As explained in Section 4.3.2, micro-tomography data allows to measure the crack growth rates. From those values, the Paris law coefficients C and m can be estimated for the two experimental conditions (*cf.* red and blue dashed lines in Figure 4.19). Hence, the Paris laws of Equations 4.2 and 4.3 can be written.

$$\Delta a/\Delta N_{chimney} = 7.532 \times 10^{-11} \Delta K^{1.72} \text{ m/cycle} \tag{4.2}$$

$$\Delta a/\Delta N_{no\ chimney} = 4.393 \times 10^{-18} \Delta K^{8.00} \text{ m/cycle} \tag{4.3}$$

It is then possible to calculate the ratio between the numbers of cycles needed to propagate a crack from a $a_i = 300$ μm radius (the size of the internal notch) to the final fracture ($a_f = b = 1250$ μm, the specimen radius) at a 300 MPa stress amplitude for the two experimental conditions:

$$\frac{N_f(no\ chimney)}{N_f(chimney)} = 55 \tag{4.4}$$

This approximation seems consistent with the two decades difference observed in Figure 4.2. This suggests that the number of cycles needed to initiate the crack from the internal artificial notch is negligible and the difference in total fatigue lives is probably mainly due to a difference in crack growth rates between the two types of tested specimens.

All these elements tend to indicate that the propagation mechanisms for a cracks in a specimen with a chimney might be different from those of the internal cracks presented in Chapter 3. They could be comparable to propagation mechanisms in air. Additional observations and results described in the next sections will bring other elements to confirm this assertion.

As pointed out in Section 3.1.2 for internal cracks without a chimney, the low scatter of the fatigue life can also be observed in the present case. The numbers of cycles between the first detection and the final fracture are represented in Figure 4.2 by the horizontal dashed lines. Except for Specimen nb 53 where the cycling was automatically stopped soon enough, the other cracks were already long and propagating rapidly when they were monitored for the first time. For one specimen (nb 49), crack initiation was even missed and the final fracture occurred before the first tomographic acquisition. This shows that the propagation of internal cracks in contact with the specimen bottom surface (because of the chimney) was significantly faster than that of internal cracks not in contact with ambient atmosphere.

4.2 Fractographic Analysis

4.2.1 Crack Surface Zones

Similarly to specimens without the chimney, the fracture surfaces of internal cracks in specimens with the chimney have been analyzed with optical microscopy and SEM. These observed fracture surfaces are very different from the ones described in Chapter 3 as depicted in Figure 4.3a: two different zones are present in the *Fish-Eye* zone and can be distinguished with optical microscopy.

- *A small zone which appears dark* in the optical microscope is visible around the notch (it will be called hereafter the *Black Area*). Using SEM provides a closer look at this zone and reveals that this *Black Area* has a faceted aspect (*cf.* Fig. 4.4a and 4.4b). This suggests strong interactions of the crack with the microstructure.
- *Around this dark central region, another zone which appears bright* in the optical microscope can be observed (Figure 4.4c). A more detailed inspection by SEM reveals that this bright aspect is due to the presence of relatively large planar features present in this zone. The aspect of these features reminds that of a leaf and has been reported by Pilchak *et al.* and A. Junet [PIL 09, JUN 21]. They claim that this aspect is due to the so-called *quasi-cleavage* mechanism occurring when the crack reaches a grain with an angle between the propagation direction and the grain basal direction. In that case, the crack has to

accommodate the different grain orientations to propagate from one grain to the next one as close as it can from the basal plane, giving the fractographic feature a planar aspect containing steps. Hence, such a *quasi-cleavage* feature is created in more than one cycle. This is consistent with the fact that the planar features observed in the present study very frequently present extensive striations (Figure 4.4d). It illustrates the fact that such a planar feature is not created in one cycle.

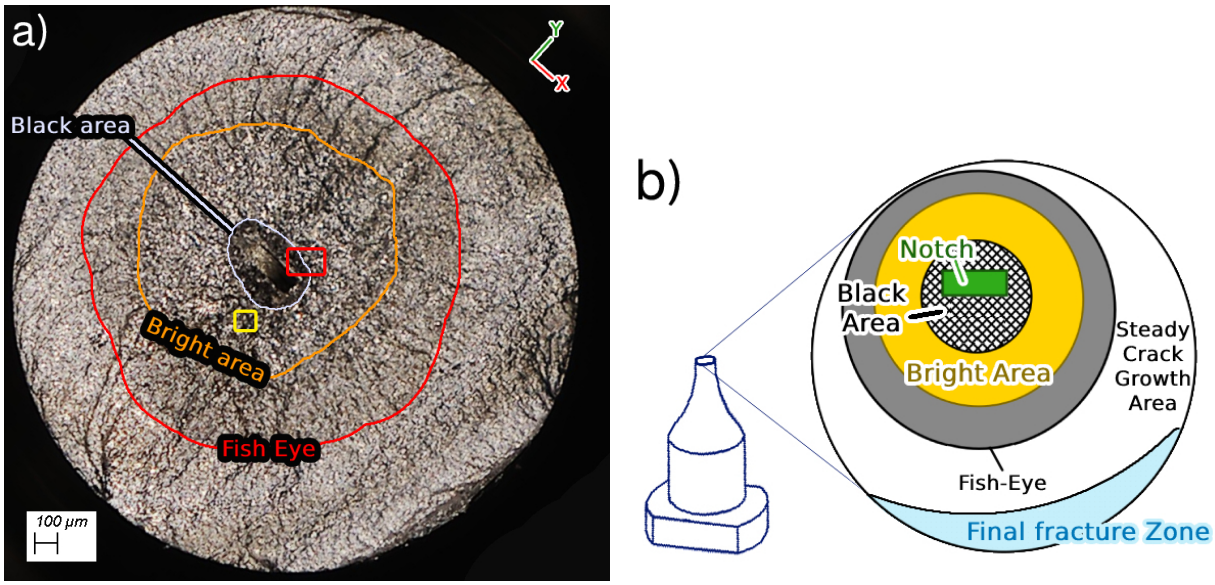

Figure 4.3 | **Fracture surface of an internal crack which propagated in a specimen containing a chimney** (Specimen nb 48 cycled at 300 MPa during 5.04×10^5 cycles). (a) Optical view of the fracture surface. The *Black Area* surrounds the initiation site and is surrounded itself by the *Bright Area*. These two zones are comprised in the *Fish-Eye* zone. The red rectangle locates Figure 4.4a. Figures 4.4c and 4.4d are located in the yellow rectangle where the value of the SIF range is estimated at $\Delta K \approx 5.4$ MPa $\sqrt{\text{m}}$ (Eq. 3.2). (b) Scheme of the typical zones present on such a fracture surface.

These differences in crack surface features observed between specimens with and without chimney are in very good agreement with the fractographic observations of Yoshinaka *et al.* who performed fatigue tests on Ti64 specimens in various environments (from air at the atmospheric pressure ~ 0.1 MPa to a vacuum with a pressure of 10^{-4} Pa) to evaluate the difference in crack surface aspect under different environments [YOS 21]. As described in Chapter 1 (Section 1.4.1 and Figure 1.13), these authors describe - for the surface cracks which propagated in air - an «angular and sharp aspect» close to the initiation site (around $\Delta K = 6$ MPa $\sqrt{\text{m}}$) surrounded by a «larger flat striated zone» (which is still visible at $\Delta K = 18$ MPa $\sqrt{\text{m}}$). For surface cracks in a vacuum environment, they observe a «granular and round aspect» in the vicinity of the initiation site which is surrounded by a «flat zone without striation».

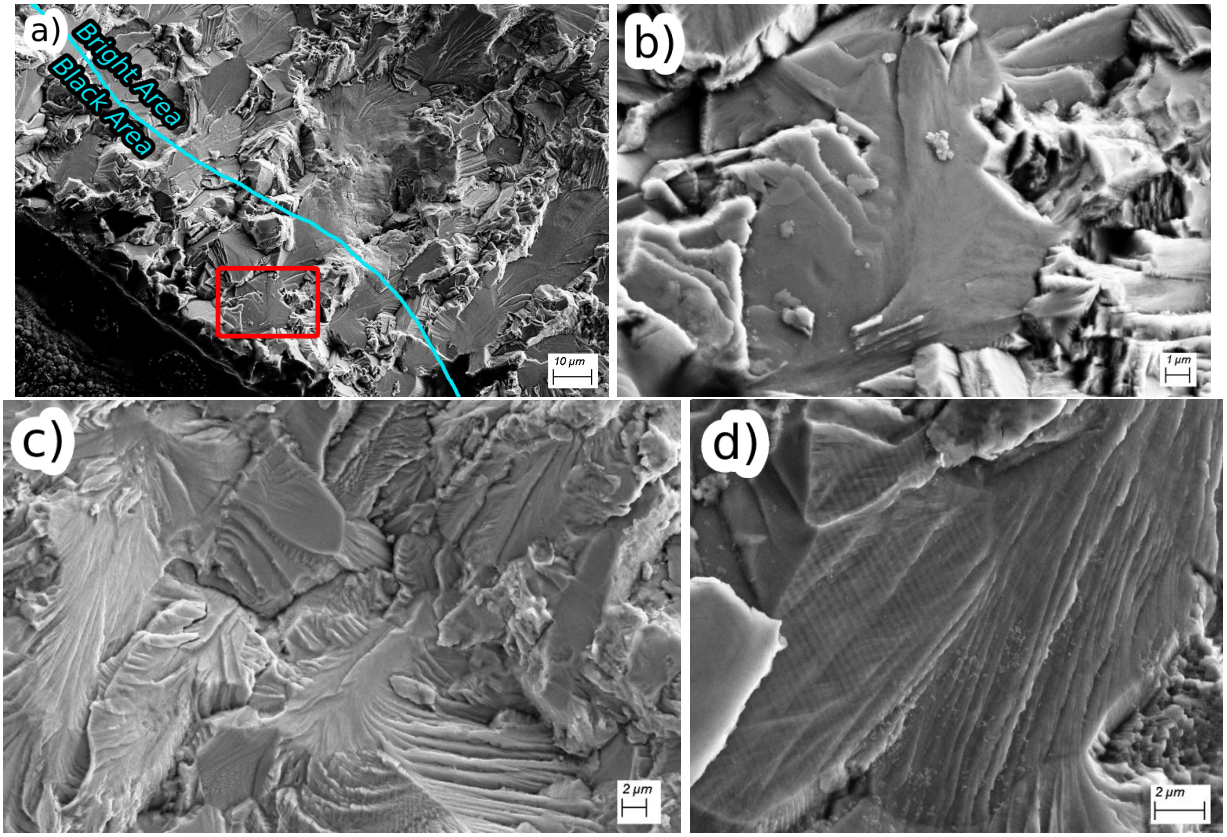

Figure 4.4 | SEM detailed views of the *Black Area* and the *Bright Area* of a crack fracture surface which propagated in a specimen with a chimney (Specimen nb 48 cycled at 300 MPa during 5.04×10^5 cycles). (a) zoom on the *Black Area* with crystallographic aspect located in the red rectangle of Figure 4.3a. The blue curve separates the *Bright Area* and the *Black Area* which is very narrow. (b) detailed view of a facet in the *Black Area* located in the red rectangle of (a). (c) zoom on the *Bright Area* with planar features. (d) detailed view of a planar feature from the *Bright Area* showing extensive striations. (c) and (d) are located in the yellow rectangle of Figure 4.3a.

These observations match very well with the fractographic features observed in the present work for internal cracks respectively with and without the chimney. This confirms that, in spite of its narrow dimensions, the chimney allows air molecules under atmospheric pressure, to reach the interior of the notch and, from there, the crack tip despite the ultrasonic loading frequency. These fractographic observations also confirm that, for internal cracks, the propagation mechanisms differ between the two environments, at least until the cracks are long enough to enter into the *Fish-Eye* zone external area (which appears grey in Figure 4.3b). In this last region, the fracture surfaces belonging to specimens with and without a chimney appear similar as illustrated in Figure 4.5.

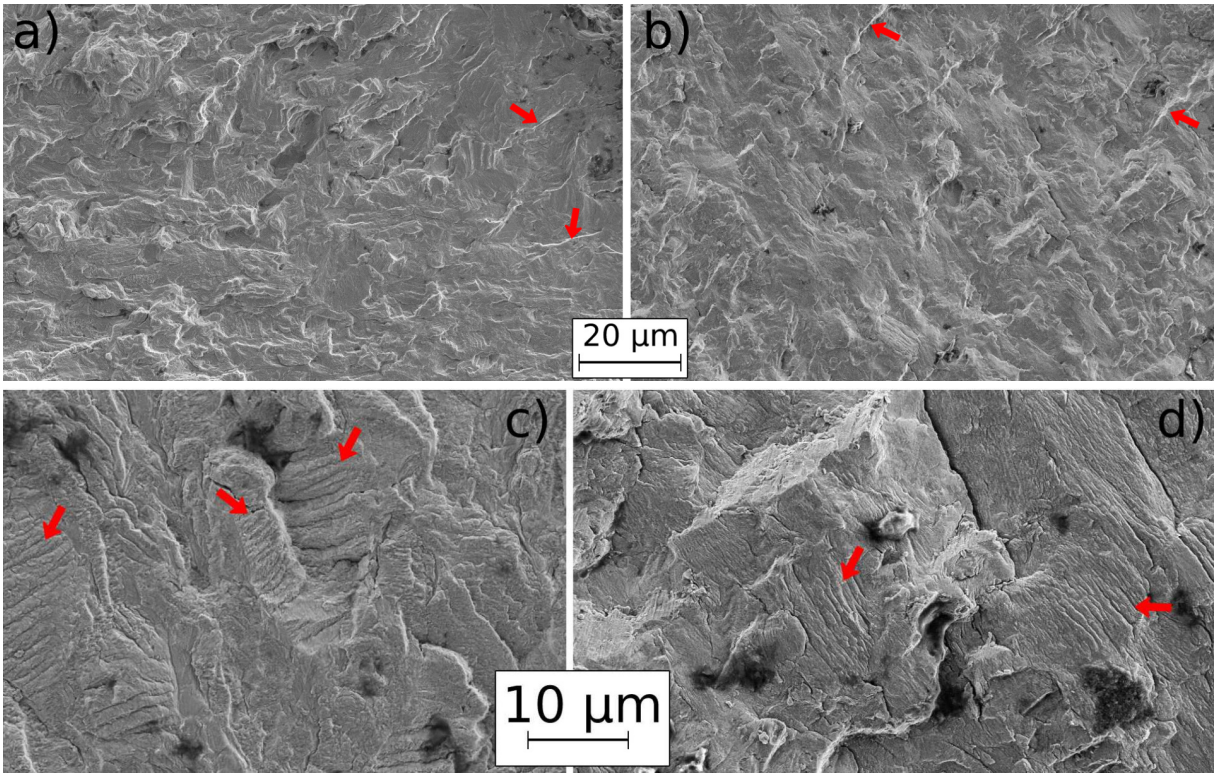

Figure 4.5 | **Fractographic aspect of the external area of the *Fish-Eye* zone observed with SEM for specimens with (b & d) and without (a & c) a chimney** Low magnification pictures (a & b) show that the fracture surface presents a combination of rough and planar zones (the latter being less planar than the facets) with many step lines (*cf.* red arrows). Also, a higher magnification (c & d) allows to remark the presence of ridges in the external area of the *Fish-Eye* zone (also located by red arrows) for the two types of specimen.
(a) corresponds to $\Delta K \approx 11.2$ MPa $\sqrt{\text{m}}$ for Specimen nb 44 cycled at 337 MPa.
(b) corresponds to $\Delta K \approx 10.1$ MPa $\sqrt{\text{m}}$ for Specimen nb 49 cycled at 315 MPa.
(c) corresponds to $\Delta K \approx 12.4$ MPa $\sqrt{\text{m}}$ for Specimen nb 59 cycled at 500 MPa.
(d) corresponds to $\Delta K \approx 10.9$ MPa $\sqrt{\text{m}}$ for Specimen nb 49 cycled at 315 MPa.

The section below the fracture surface of Specimen nb 49 which is presented in Figure 3.11 allows to observe the microstructure under the *Black* and *Bright Area*. The cutting plane is represented in Figure 4.6a and the zones are observed with SEM (Fig. 4.6b). EBSD observations have also been carried out in those two regions but no crucial difference emerges (*cf.* Figures 4.6c and 4.6d).

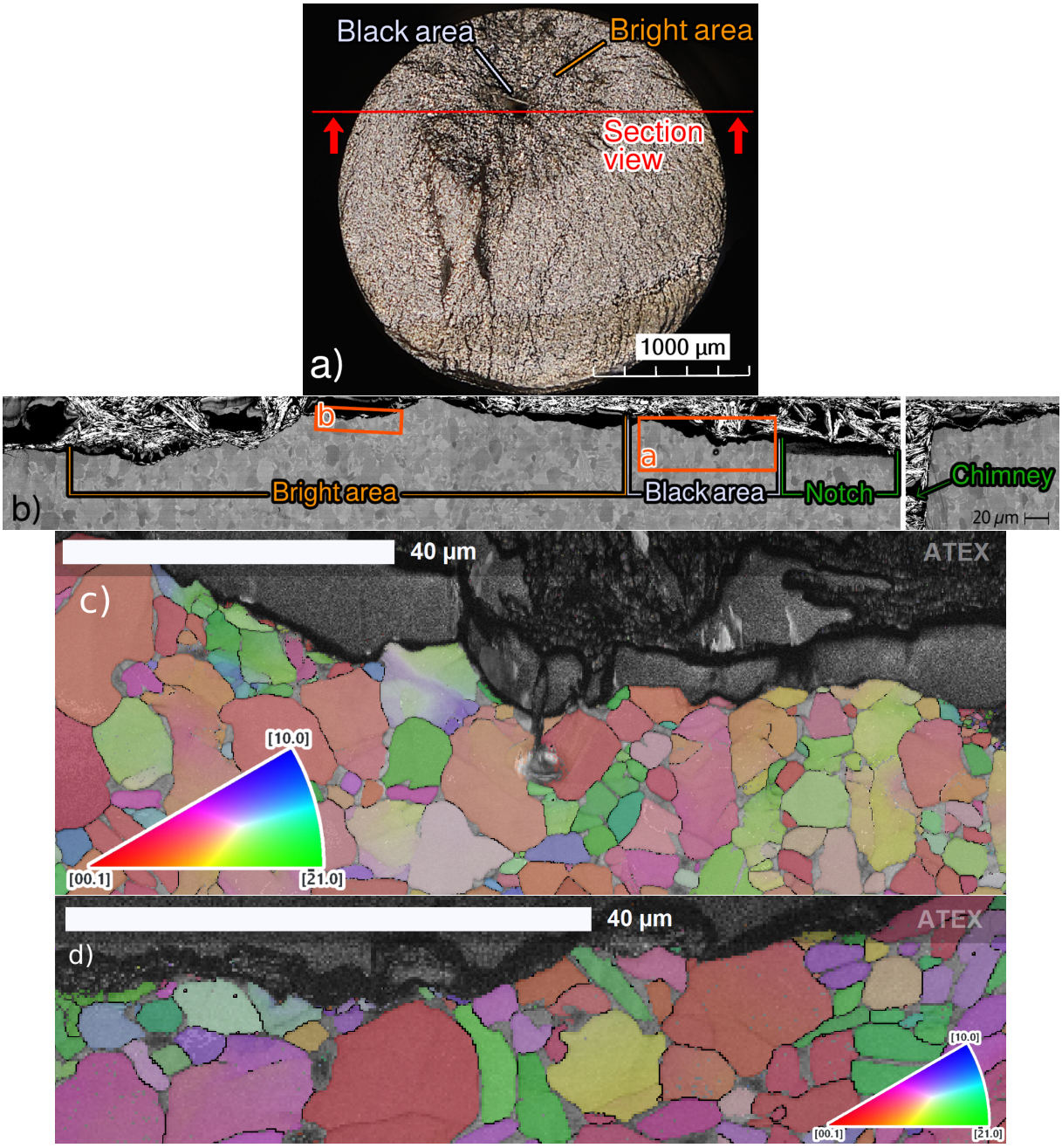

Figure 4.6 | **Section perpendicular to the average crack plane for a specimen with a chimney** (Specimen nb 49 cycled at 315 MPa during 8.16×10^5 cycles). (a) Location of the section. (b) SEM picture of the polished section observed in back-scattered mode to distinguish the microstructure under the fracture surface around the internal notch. EBSD map details of the (c) *Black* and (d) *Bright* zones. In (b), the notch and the chimney are represented in green, *Black Area* is located in white and *Bright Area*, in orange. (c) & (d) are located within the orange rectangles in (b). The IPF shows the crystal direction parallel to the vertical direction of the picture ($\sim$ direction of the loading). No major microstructural difference has been observed under these two fractographic zones.

4.2.2 Striation Analysis

As illustrated in Figure 4.4d, the planar zones present in the *Bright Area* contain many straight parallel marks. These features are specific to fatigue crack propagation in air environment as explained in Section 1.4.1. The inter-striation spacing has been used to locally estimate the crack growth rate within the planar features. For this, the crack is assumed to propagate the distance measured between two striations in one loading cycle. The measurements have been carried out for at least 10 planar features per specimen at ΔK values ranging from 4 to $10\,\mathrm{MPa}\sqrt{\mathrm{m}}$. Within this range, the crack growth rate does not seem to vary with ΔK values, its average value is $2.7 \times 10^{-7} \pm 1.0 \times 10^{-7}$ m/cycle (*cf.* Fig. 4.7). As it was done in Section 3.3, the averaged macroscopic crack growth rate has been estimated thanks to tomography data for the specimens with a chimney. These results will be presented in Section 4.3 but they allow to remark that the local crack growth rate measured from the striation spacing is two orders of magnitude higher than the maximum value of the macroscopic one estimated from tomographic data. This observation matches also with the results from Yoshinaka *et al.* [YOS 21] who measures the striation spacing to be 1.4×10^{-7} m when $\Delta K = 18\,\mathrm{MPa}\sqrt{\mathrm{m}}$ for a crack propagating in air environment in the same alloy loaded in tension at $R = 0.1$. Differences about the same order of magnitude have been measured between striations-determined crack growth rate and macroscopic one by Pilchak *et al.* for another titanium alloy [PIL 13].
A possible explanation for this apparently high crack growth rate in the planar fractographic features has been suggested by Williams *et al.*. It consists in the fact that the propagation is not homogeneous along the crack front so the macroscopic crack growth rate - which is an averaged value - can differ from the local one (measured in the planar fractographic features for example) [WIL 11]. However, for such long cracks, the microstructure influence on the propagation is reduced. Another explanation might be that the crack in such flat zones could stay arrested during several cycles (between 10 and 100) before propagating again. The microstructure under such striations has been observed and will be presented in the next section.

4.2.3 Microstructure Analysis Under the Striations

The FIB extraction procedure described in Section 3.2.2.2b has been applied to a planar fractographic feature containing striations. A wall was extracted perpendicularly to the striation marks as illustrated in Figure 4.8. This procedure allows to observe the microstructure immediately under the fracture surface (*cf.* Fig. 4.9).

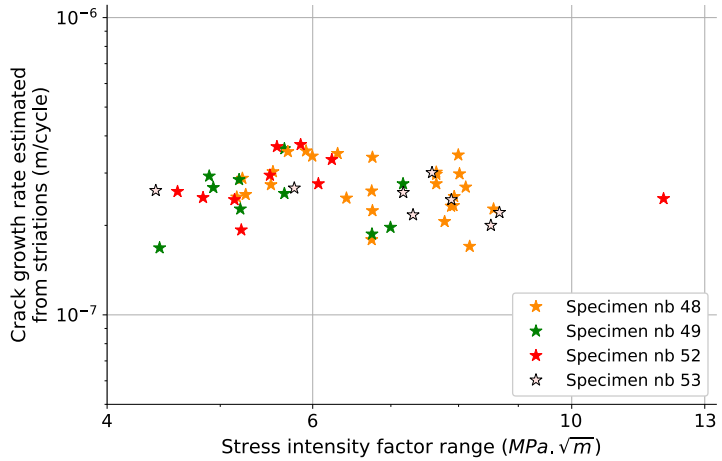

Figure 4.7 | **Crack growth rates estimated from the distance between striations** located in the crack surface of different specimens with a chimney. Those measured values do not seem to depend on the stress intensity factor range between $\Delta K = 4$ and $\Delta K = 9$ MPa $\sqrt{\text{m}}$ (*cf.* Fig. 4.20 for comparison with macroscopic growth rates estimated from tomographic data). The color of each marker corresponds to one specimen as referenced in Table 4.1.

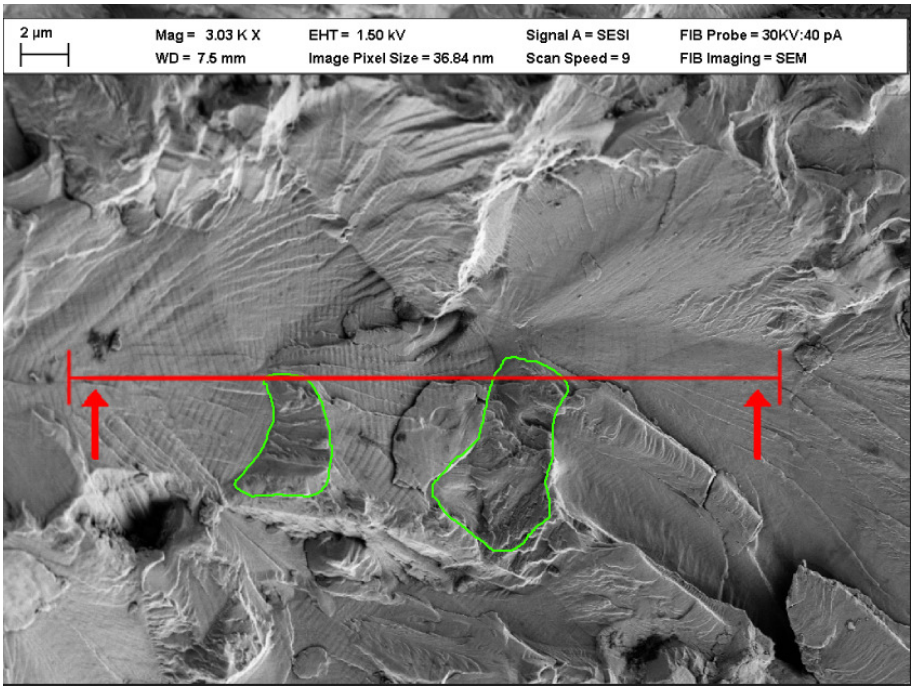

Figure 4.8 | **SEM picture representing a planar striated zone in the *Bright Area*** from the fracture surface of Specimen nb 48 cycled at 300 MPa during 5.04×10^5 cycles. The localization of the wall extracted with FIB is represented by the red line and the face represented in Fig. 4.9 is depicted by the red arrows. The green zones correspond to the grains which do not contain any parallel microstructural marks, they seem to present, instead, a sharper aspect.

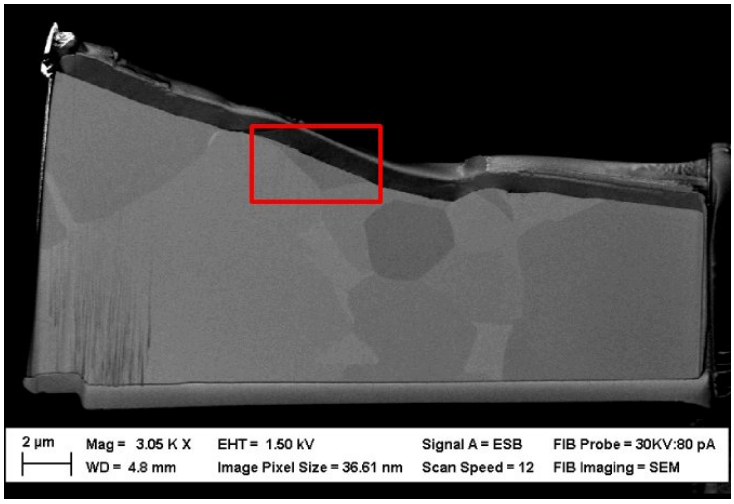

Figure 4.9 | SEM picture of the extracted wall located under the striated zone depicted in Fig. 4.8. The red rectangle locates Fig. 4.10a.

A detailed view of the microstructure under a striation pattern allows to remark small *marks* (*cf.* SEM observations in Fig. 4.10a and TEM observations* in Fig. 4.10c). These marks which have a wedge shape are oriented in the direction of the crack propagation (the crack propagates from left to right in Figure 4.10c), they have a length ranging from 200 to 600 nm and a thickness between 20 and 80 nm. Also, the average angle between the direction of these marks and the crack average surface is approximately equal to 60° (*cf.* angle ζ in Figure 4.10c). This is not far from the typical 70° angle between the direction of the plastic zone longest dimension ahead of a crack tip and the crack propagation direction in the case of an isotropic material [MCC 91]. Furthermore, from the distance between the analyzed marks and the internal notch ($\sim 320\ \mu$m), an estimation of the SIF range at which those marks were created can be calculated from Equation 3.2 (~ 6.1 MPa $\sqrt{\text{m}}$). This value is used to estimate the plastic zone size (*cf.* Eq. 1.4) when the crack front was near the created marks. Hence, the plastic radius was approximately 500 nm which is comparable to the length of those marks (the average length of the marks in Fig. 4.10c is 360 nm). All those elements point toward a link between the presence of the marks and the plastic activity at the crack tip.

The inter-striation distance has been measured (Fig. 4.10b) and compared with the distance between two successive marks observed in the microstructure under those striations (Fig. 4.10a); these two values are in very good agreement.
Figure 4.14 summarizes the presence or not of parallel marks in the different grains observed in the extracted wall from a more general point of view. This can be compared to the fracture surface of Figure 4.8 to remark that every time striations are observed on the fracture surface, parallel marks are also present in the grain located under those striations. Conversely, the

*We thank Nicholas Blanchard and Thierry Douillard for the time spent on all the TEM observations.

fractographic aspect above the grains which do not contain any parallel mark is sharper and does not present any striations (zones circled in green in Figure 4.8). All these observations suggest that a microstructural mark is present under each striation. However, as pointed out by the red line from Figure 4.10c, the inter-striation distance is larger than the thickness of a microstructural mark.

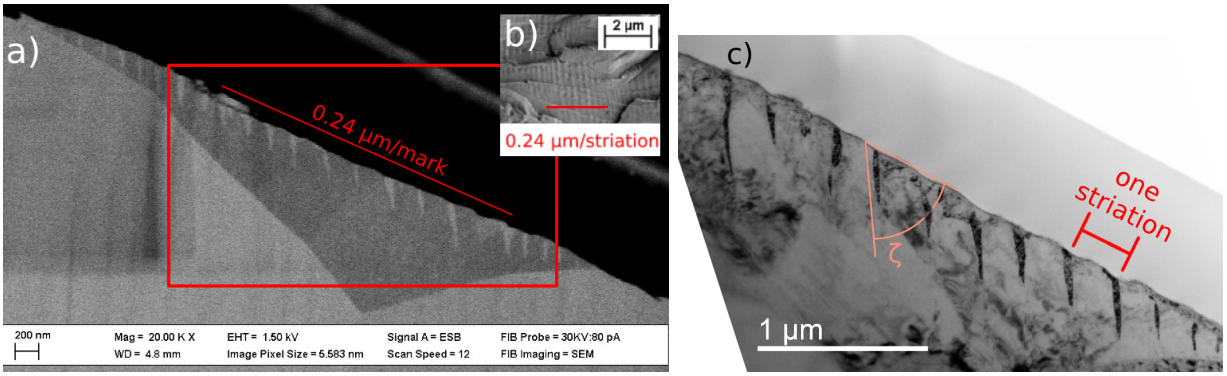

Figure 4.10 | **Marks observed under the striations** (a) SEM picture of the marks. (b) Striations visible above the marks represented in (a). (c) Transmission Electron Microscope detail picture of the marks. (c) is localized in the red rectangle of (a). ζ is the average angle between the direction of the marks and the crack average surface. The distance measured between two striations seems to match with the distance between two marks meaning that one mark is present under each striation.

The extracted wall has also been analyzed by EBSD to obtain the microstructure orientation just under the crack surface. However, as illustrated in Figure 4.12a, the EBSD spatial resolution does not allow to distinguish the marks observed with Scanning and Transmission Electron Microscope. For this reason, the TKD procedure described in Section 3.2.2.2b has been used (Fig. 4.12b). From this data, it was possible to measure the misorientation between the regions corresponding to the marks and the one of the overall grain in which they are included (*cf.* unit cells depicted in Fig. 4.12b). The misorientation between those two regions has been measured to be a **rotation of 87° around the [11$\bar{2}$0] direction**. This value has been confirmed with measurements of misorientations carried out from TEM diffraction patterns (*cf.* Fig. 4.13).
As summarized in the PhD thesis of L. Nervo [NER 15], four twin systems have been reported in titanium. Particularly, two of them can occur when the material is loaded in compression, and the two others concern tension loadings [MUN 97]. The misorientation relation measured in the present study is very close to the so-called {10$\bar{1}$2} tensile-twinning relation referenced in titanium which is a rotation of 85° around the [11$\bar{2}$0] direction [LAV 18a]. This suggests that one tensile-twin forms under each striation mark. The *half-lens* shape of these twins has been reported in Section 17.5 of the book written by Abbaschian *et al.* (*cf.* Fig. 4.11) in the case where a twin intersects only with one free surface [ABB 10]. In this case, the lattice around the

twin is distorted to accommodate to the shearing strain. It leads to the formation of surface kinks adjacent to the twins. Similar features can be observed in Figure 4.10c along the profile of the wall.

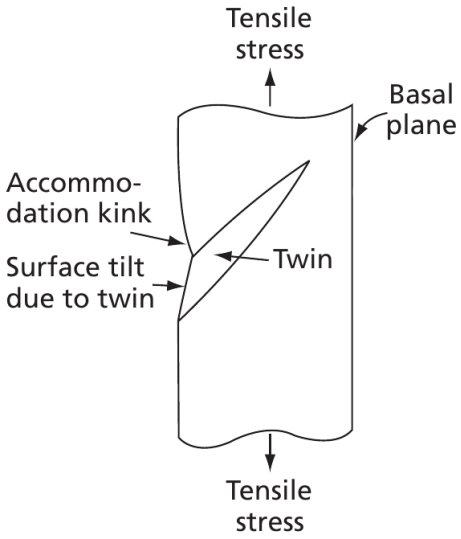

Figure 4.11 | **Half-lens shape of tensile twins** described by Abbaschian *et al.* [ABB 10]

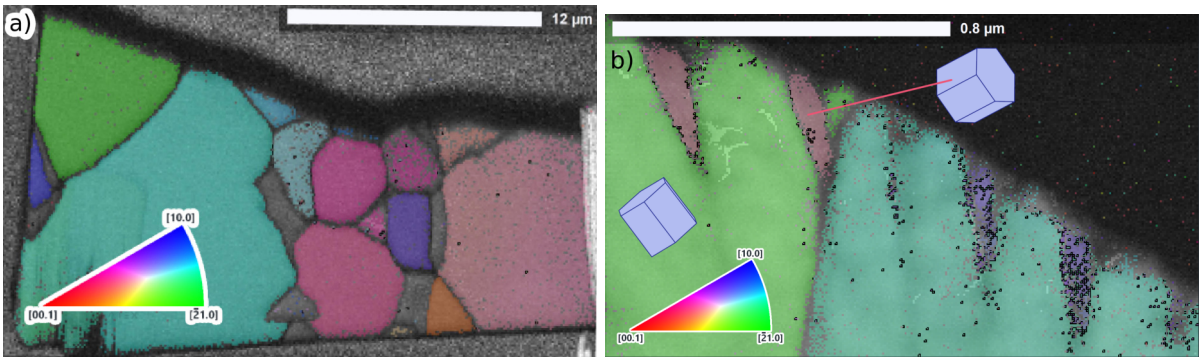

Figure 4.12 | **Microstructure orientation maps of the extracted wall located under the striated zone** (a) EBSD global view of the section depicted in Fig. 4.9. (b) detailed view of the twinning marks for two adjacent grains. (b) picture was obtained with TKD method. The IPF presents the crystal direction normal to the pictures. The crystal misorientation between the marks and the bulk corresponds to the $\{10\bar{1}2\}$ tensile-twinning relation.

Twinning in a fatigue-cycled Ti64 specimen has already been reported in several studies but, to the best of our knowledge, it has never been related to striations. For example, Lavogiez *et al.* observed that tensile-twinning occurs at the surface of a cycled specimen [LAV 18a]. When slip bands try to pass from a soft grain (*i.e.* whose orientation is favorable for slip with a high Schmid factor [RUG 07]) to a neighboring hard grain (*i.e.* low Schmid factor), they do so by forming a

twin in the latter. Also, Ma *et al.* studied a cycled lamellar Ti64 and reported tensile-twinning in the grains near the crack [MA 17b]. In this study, they calculated the Schmid factor to find out that $\{10\bar{1}2\}$ tensile-twinning principally occurs in grains with low values of the Schmid factor for basal slip. It means that, when the $\vec{c}$ -axis is aligned with the loading direction, basal slip is difficult to trigger and twinning tends to be favored. This interplay between $\vec{c}$ -axis direction and twinning occurrence is also claimed by Chi *et al.* [CHI 23].

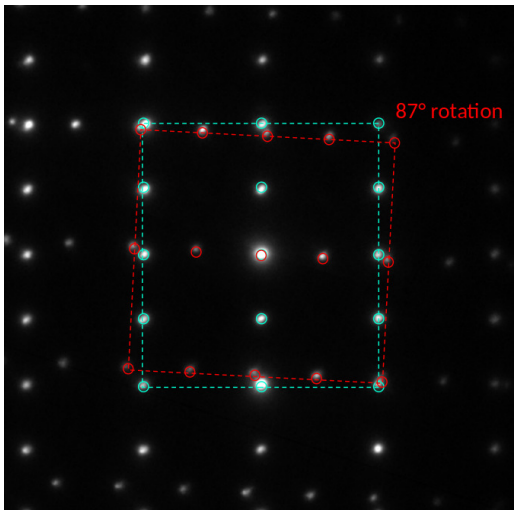

Figure 4.13 | **Diffraction patterns of a microstructural mark (in red) and of the grain in which it is located (in blue)** Acquisition carried out with Transmission Electron Microscope. An 87° misorientation is measured between these two matrixes. It is typical of the $\{10\bar{1}2\}$ tensile-twinning relation in titanium [NER 15, LAV 18a].

Conversely, Sun *et al.* cycled a Ti64 alloy and observed that $\{10\bar{1}2\}$ tensile-twinning occurred in grains with high Schmid factor for basal slip [SUN 23]. To explain this, they claim that high stress can provoke dislocation accumulation in some grains until a point when twinning is triggered to accommodate the plastic strain.

Munroe *et al.* [MUN 97] report that the presence of twinning in titanium can be observed in grains with $\vec{c}$ -axis aligned with the loading direction but also in the case of high Schmid factors for basal slip. In this paper, different results from several studies are listed and claim that $\{10\bar{1}2\}$ twinning was dominant in titanium monocrystals if the Ω angle between the $\vec{c}$ -axis and the loading direction is equal to 12°, 30°, close to 0° or between 30° and 40°.

Figure 4.14 summarizes the presence or not of twinning in the different grains from the wall analyzed in the present study. Hence, in our case, it emerges that tensile-twinning is not observed in the grains with a $\vec{c}$ -axis almost aligned with the loading direction and twinning marks are present when $37° < \Omega < 44°$.

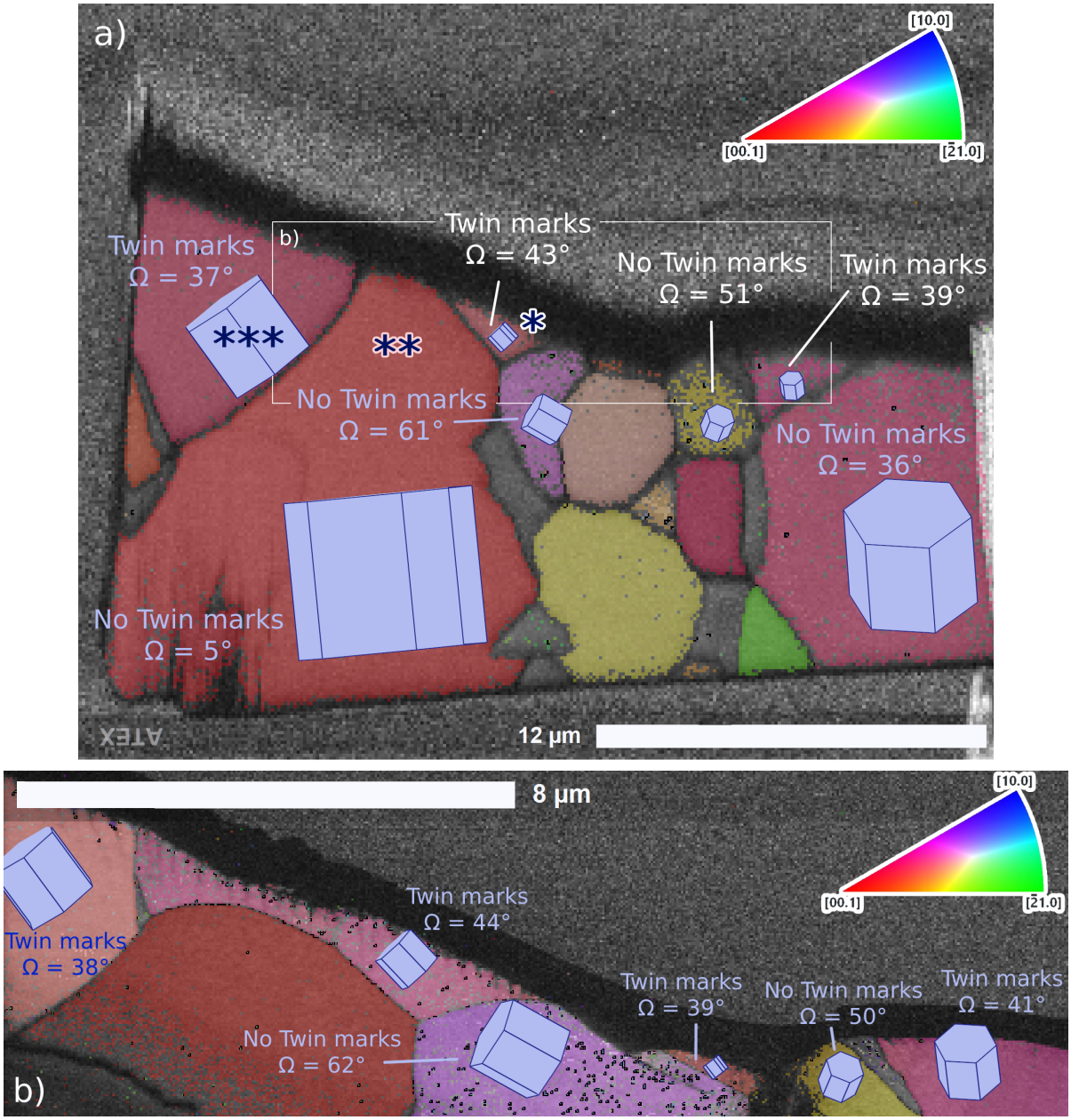

Figure 4.14 | Summary of the presence of striations and the Ω angle between $\vec{c}$ - axis and vertical loading direction for each grain located in the extracted wall which is represented in Fig. 4.9. (a) Low magnification TKD map. (b) Detailed view of (a) after a supplementary polishing session using a precision ion polishing system. The white rectangle in (a) locates (b) and the IPF shows the crystal direction parallel to the vertical direction of the picture (assumed to be approximatively the stress direction). The grains which do not present any striations are the ones circled in green in Figure 4.8. The Schmid factors of the three grains with «*» markers have been analyzed.

To try to explain the presence of tensile-twinning in the grains under some of the fractographic regions presenting striation marks, a numerical Schmid factor analysis has been carried out*. For that purpose, a crack is inserted within a 2D mesh under plane strain conditions (because the crack is internal) with a symmetric boundary condition on its left lateral boundary (*cf.* Fig. 4.15). An elastic Finite Element calculation on this mesh allows to obtain the stress field at the crack tip. As the study has only been carried out for the three grains represented with «*» markers in Figure 4.14a, the numerical crack is slightly tilted in the grain (*cf.* Fig. 4.15) to be more representative of the experimental crack (assuming a nearly vertical loading in Figure 4.14).

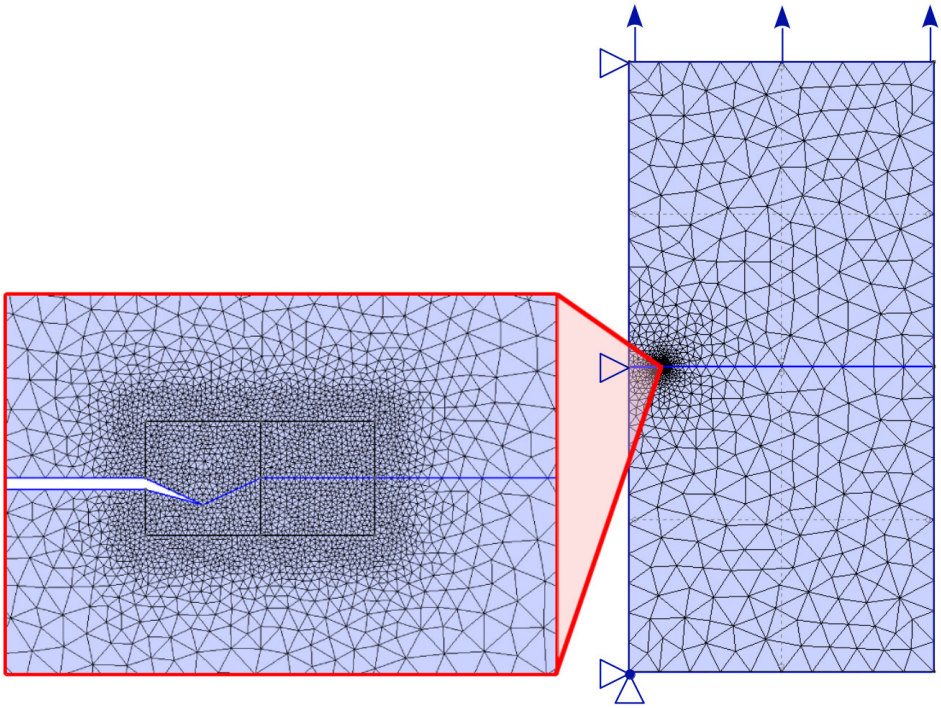

Figure 4.15 | 2D model used for the elastic finite element calculation carried out to obtain the stress field at the crack tip

Then, for each crystallographic orientation, the obtained stress field at the crack tip is used to calculate a resolved shear stress, τ^s, for each slip system s listed in Table 4.2.

$$\tau^s = \boldsymbol{b}^T \sigma \boldsymbol{n} \tag{4.5}$$

with $\boldsymbol{n}$ the slip plane normal, $\boldsymbol{b}$ the slip direction and σ the stress field (*cf.* Figure 4.16 for a scheme of the different notations). Note that, in contrast to the uniaxial sketch of Figure 4.16,

*We sincerely thank Sylvain Dancette for the time dedicated to Schmid factor analysis carried out from halfway around the world!

the stress state at the crack tip, σ, is triaxial as computed by the finite element analysis described above.

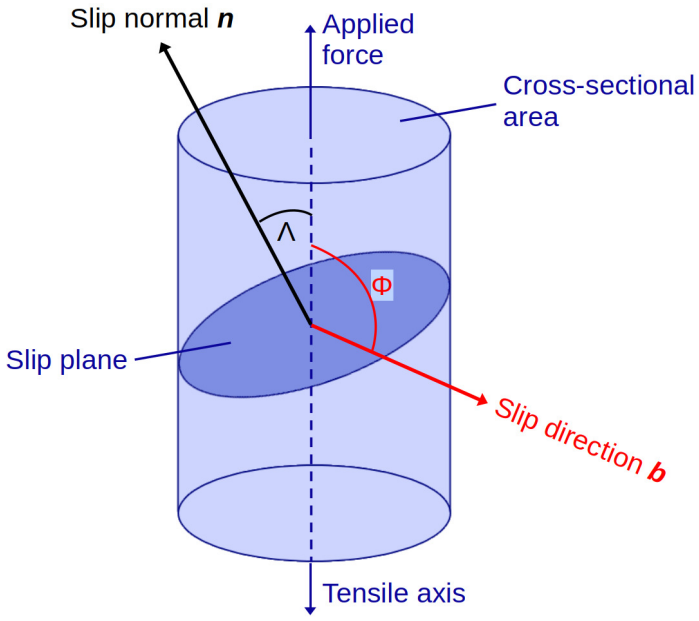

Figure 4.16 | Notations used to calculate the resolved shear stress on a given slip system

This «slip approach» is also applied to the twin mechanisms to obtain an equivalent shear rate. For that purpose, the twinning plane and the twinning direction (as defined by Bilby & Crocker [BIL 65]) are considered respectively as the slip plane with the normal, $\boldsymbol{n}$, and the slip direction, $\boldsymbol{b}$. This approach has been carried out for the tensile and compressive twinning systems summarized in Table 4.2. However, contrary to slip modes, the twin modes are uni-directional. Therefore, only positive resolved shear stresses on the specified twin systems might activate deformation twinning in the grain.

Slip system	Slip plane	Slip direction
Basal	(0002)	$< 11\bar{2}0 >$
Prismatic	$\{10\bar{1}0\}$	$< 11\bar{2}0 >$
Pyramidal <c+a>	$\{10\bar{1}1\}$	$< 11\bar{2}3 >$
Twinning type	**Twinning plane**	**Twinning direction**
Tensile	$\{10\bar{1}2\}$	$< \bar{1}010 >$
Compressive	$\{11\bar{2}2\}$	$< 11\bar{2}3 >$

Table 4.2 | Slip and twin systems used in the Schmid factors analysis The twinning planes and directions are used for the tensile and compressive twin mechanisms which are modeled by a «slip approach» to determine an equivalent shear rate.

The Critical Resolved Shear Stress (CRSS) for the different slip systems in titanium has been computed by several studies as reported by Castioni *et al.* [CAS 21] and summarized in Table 4.3. For the twinning systems, the CRSS have been taken equal to the higher one *i.e.* corresponding to the CRSS of the "harder" system (the $< c+a >$ pyramidal slip system in the case of Ti64 according to Bridier *et al.* [BRI 09]).

τ_c^{prism}	τ_c^{basal}	$\tau_c^{pyr<c+a>}$	τ_c^{Ttwin}	τ_c^{Ctwin}
1.0	1.14	1.59	1.59	1.59

Table 4.3 | Relative critical resolved shear stresses used in the Schmid factor analysis for the different slip and twin systems. The values are normalized by the lowest CRSS (corresponding to the prismatic slip). Extracted from the work of Bridier *et al.* [BRI 09].

To predict the active slip or twin mechanism for each crystallographic orientation, the corresponding resolved shear stress, τ^s, is normalized by the CRSS corresponding to the mechanism, τ_c^s to obtain a shear rate $\dot{\gamma} = \dot{\gamma_0}|\tau^s/\tau_c^s|^{1/m}\ sign(\tau^s)$ with $\dot{\gamma_0}$ a reference slip rate and m a strain-rate sensitivity exponent (as described in Appendix A from the paper of Lavogiez *et al.* [LAV 18b]). By comparing the maximum shear rate in each family of slip or twin systems, it is possible to obtain the "preferential" deformation mode for a grain of a given crystallographic orientation as summarized by the IPF triangle in Figure 4.17.

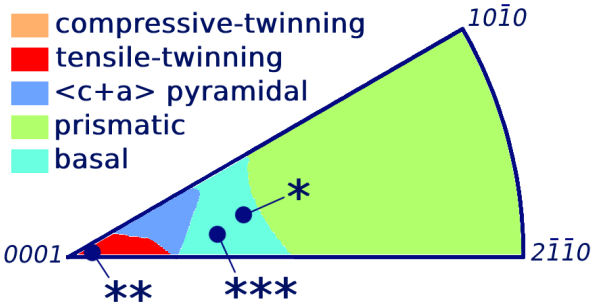

Figure 4.17 | Deformation system activated for each microstructure orientation according to the Schmid factor analysis. The «*» markers correspond to the three grains indexed by similar markers in Figure 4.14.

The three studied grains (indexed with «*» markers in Fig. 4.14) are located in this figure. It emerges that the Schmid factor analysis predicts twinning in the grain with «**» but no twinning in the two others. Those predictions are the opposite of what has been experimentally observed but they agree with the results of Ma *et al.* and Chi *et al.* [MA 17b, CHI 23] who claim that twin is favored when the local $\vec{c}$ -axis is normal with the loading direction because slipping is impossible to activate in this case. The mismatch between these Schmid factor analysis results and the experimental observations could be explained by the fact that the CRSS might be

impacted by the environment. This impact could change the order of activation between the different systems [BRI 15].

With the considered hypotheses, the presence of twinning under each striation has not been explained with the Schmid factor analysis. However, this phenomenon can be considered to try to understand some crack propagation mechanisms. As described in Section 4.2.2, the crack growth rates measured thanks to the striations are two orders of magnitude higher than the macroscopic one. Consequently, this brings two different hypotheses: either **(i)** each striation mark needs one cycle to be created and the local crack growth rate is lower outside of the planar fractographic features where the striations are observed or **(ii)** the crack stays arrested during many cycles between the creation of two successive striation marks. The second hypothesis lies in the fact that the crack stays arrested for several cycles between the formation of two successive twinning marks. It can be linked with the explanation from Chi *et al.* about tensile twinning in Ti64 [CHI 23]. In this paper, the authors suggest that twin nucleation occurs in α grains when the plastic strain accumulation reaches a certain level. By considering this assertion in the present study, the cracks can be supposed to discontinuously propagate as the number of cycles increases and to produce a twin at the crack tip every time the propagation starts again because of plastic strain accumulation.

To summarize, the observations of the microstructure located under the fracture surface in the *Bright Area* reveal the presence of $\{10\bar{1}2\}$ tensile-twinning under each striation in this region. To the best of our knowledge, this had never been reported in this alloy before. This mechanism has not been observed under the un-striated fractographic planar areas and in particular, under the facets observed in the fractographic surface of the cracks propagating internally without a chimney. This suggests that the propagation mechanisms are strongly modified when the crack propagates in a specimen which has an internal chimney. In particular, the plastic activity at the crack tip seems to be impacted.

4.3 Crack Growth Rate

4.3.1 Surface Cracks Propagating Under Ultrasonic Cyclic Loading

The majority of the fatigue data found in the literature concerning Ti64 have been obtained at low loading frequency with $R = 0.1$ and have to be considered with caution in a comparison with the measurements acquired at 20 kHz and $R = -1$ in the present study. To our knowledge, this type of data is almost not present in the literature except in one study carried out with SEM imaging by Geathers *et al.* [GEA 15, GEA 22]. Therefore, an experiment has been carried out - as presented in Section 2.2.3 - on flat pre-cracked specimens designed for resonating at

20 kHz under axial tension (so-called *ultrasonic CT-like specimen* in the following) to obtain crack growth rate data for Ti64 at ultrasonic frequency with a nominal stress ratio $R = -1$. These tests provided a reference dataset to compare with the crack growth rates of internal fatigue cracks cycled at 20 kHz and linked to the surface with a chimney.
The standard test method used to collect fatigue propagation data imposes two conditions on the propagation blocks to be valid (*cf.* Section 2.2.3.3) [AST13]. All the data points corresponding to this experiment fulfill these two conditions; however, during a cycling block, the crack can propagate while another branch is created in parallel (Fig. 4.18a). The other branch can also propagate further than the original one (Fig. 4.18b). In these two cases, it has been chosen to measure the crack length increase, da, as the propagation of the longest branch (*cf.* Figure 4.18). But, as these specific cases are not considered in the standard method, the corresponding data points are represented in white circles in Figures 4.19 and 4.20 and should be considered with caution.

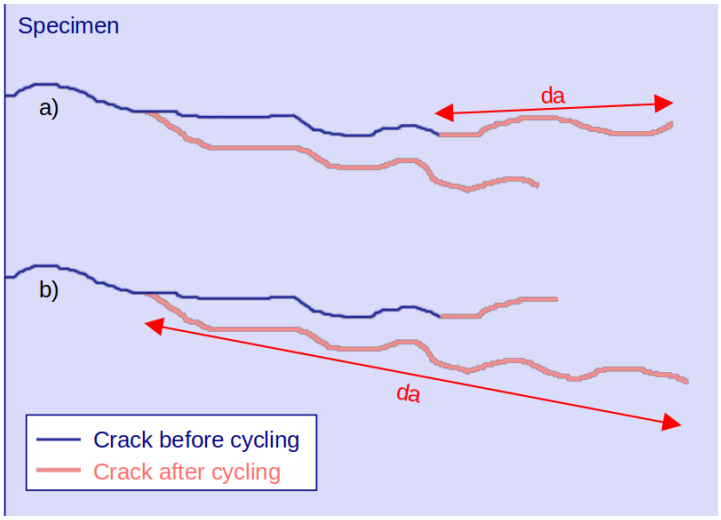

Figure 4.18 | **Two specific crack propagation cases not considered by the ASTM E647 standard test method** [AST13]. da represents the crack length increase measured during one loading block of the CT ultrasonic propagation tests presented in this section.

4.3.2 Crack Growth Rates Comparisons

The procedure described in Section 3.3 to calculate the crack growth rates from tomographic data has been applied to the specimens with a chimney. In Figure 4.20, the crack growth rates are plotted versus the SIF range in a Paris diagram and compared with data from the literature and from other experiments presented in this manuscript (ultrasonic surface crack propagation and in-situ internal crack propagation without a chimney). Figure 4.19 presents only the data acquired at $R = -1$. The data from the work of Junet *et al.* [JUN 23] are not represented in

those figures for the sake of clarity but it will be discussed later in Section 4.3.4. The crack growth rate uncertainties for the internal tomographied data and the CT ultrasonic propagation ones are presented in Appendix A.

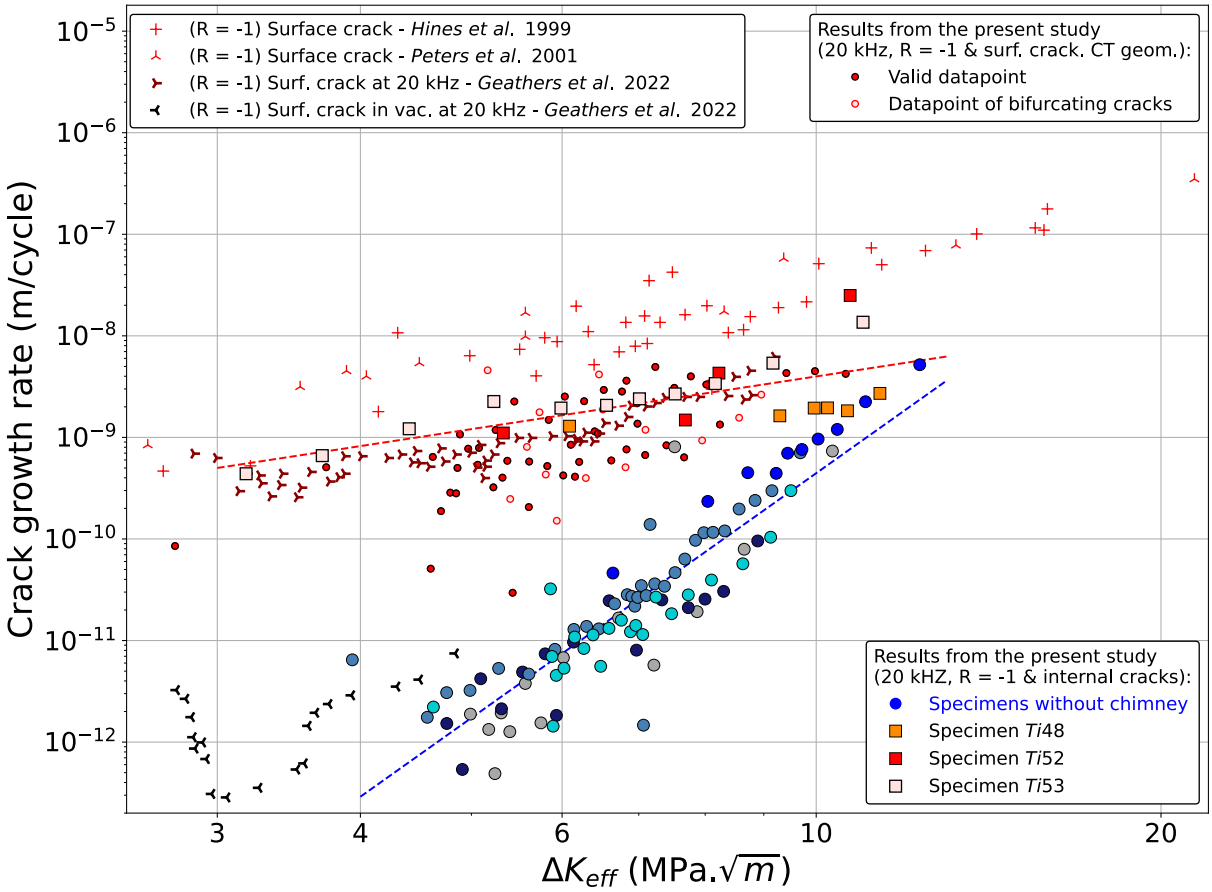

Figure 4.19 | Crack growth rate data in a Paris diagram for all the tested specimens compared with literature data obtained at $R = -1$ [HIN 99, PET 01, GEA 22]. The latter were obtained at low loading frequency *i.e.* between 20 and 400 Hz except for Geathers *et al.* (20 kHz). The red circles correspond to the ultrasonic fatigue propagation data acquired with surface cracks. The red and blue dashed lines correspond to a fit of the in-situ data obtained for specimens respectively with and without a chimney. The presence of a chimney in the specimens provokes higher crack growth rates than for specimens without such a chimney.

First of all, the fatigue tests of specimens with an internal chimney provide fewer data points than in the case of specimens without any chimney because the crack growth rates are higher. Consequently, the propagation length is more important between two successive micro-tomography acquisitions. Also, the initial propagation is so rapid that, when cycling is stopped for the first time, the crack is generally already quite long and few data points could be acquired at low SIF range values ($\Delta K < 6$ MPa $\sqrt{\text{m}}$).

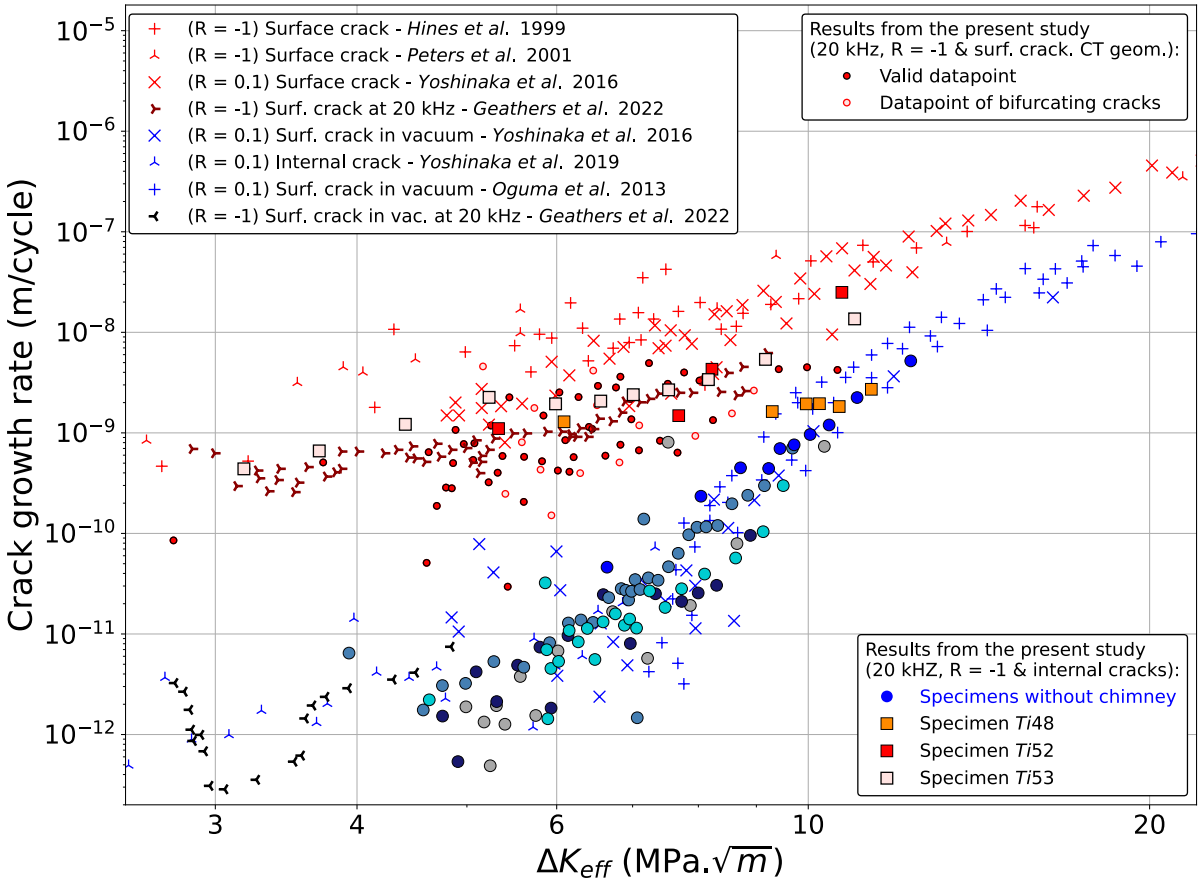

Figure 4.20 | **Crack growth rate data in a Paris diagram for all the tested specimens** compared with literature data [HIN 99, PET 01, YOS 16b, GEA 22, YOS 19, OGU 13]. The latter were obtained at low loading frequency *i.e.* between 20 and 400 Hz except for Geathers *et al.* (20 kHz). The experimental conditions of the literature references are listed in Appendix H. Tables 3.2 and 4.1 link each marker type with a specimen. The red circles correspond to the ultrasonic fatigue propagation data. These growth rates have the same order of magnitude than the rates reported in the literature for crack propagating in air from the surface of specimens.

The growth rates of cracks propagating in a specimen with a chimney are clearly higher than the ones measured in specimens without a chimney for $\Delta K < 10$ MPa $\sqrt{\text{m}}$. As they agree with the rates obtained at ultrasonic loading frequencies for CT-like specimens (Section 4.3.1) and with the only reference from literature at 20 kHz and $R = -1$ [GEA 22], this tends to prove again the efficiency of the chimney to bring air to the internal cracks. For high SIF range values, the growth rates obtained for specimens with a chimney tend towards the values acquired in the case of specimens without any chimney (*i.e.* internal propagation behavior). This observation is also valid for the datapoints obtained at ultrasonic frequencies with CT-like specimens and for Geathers *et al.* datapoints [GEA 22]. However, this is less the case for other literature data

points which have been acquired at conventional cycling frequency. This will be discussed in the rest of the section.

If more attention is paid to the cycling frequency, it is possible to remark that for vacuum-propagating cracks, the ultrasonic and conventional (low frequency) data are similar. However, this is no longer true for cracks in contact with air. There is a difference in crack growth rates between the datapoints acquired at ultrasonic and low frequency [HIN 99, PET 01, YOS 16b]. This difference increases at large SIF range values ($\Delta K > 8$ MPa $\sqrt{\text{m}}$ *i.e.* for longer cracks). In other words, as the SIF range increases, the growth rate at 20 kHz for a crack in contact with air tends to be lower than for a crack in a similar situation but cycled at low frequency. For SIF range values around 10 MPa $\sqrt{\text{m}}$, the crack growth rates at 20 kHz in air were even measured (for one specimen) to reach the values obtained for vacuum-propagating cracks.

The previous observations concerning the impact of cycling frequency on Ti64 fatigue behavior are in agreement with the observations of Holper *et al.* on aluminum alloys [HOL 03] (*cf.* Chap. 1). According to these authors, if a crack is cycled at ultrasonic frequency in air, at high SIF range values (*i.e.* when it is a long crack), the air molecules cannot reach the crack front as well as they could if the frequency was low. Hence, the crack growth rates tend to become similar to that of a crack propagating in vacuum (the latter not being influenced by the frequency because of the absence of air molecules). This paper, cite the study of Wei *et al.* [WEI 80, GAO 88] who showed that a water vapor pressure of 5 Pa is sufficient to make a fatigue crack undergo full environment effect at 5 Hz (with $R = 0.05$). With this frequency, the crack front is submitted to 5 Pa during an exposure time of less than 0.2 seconds (because crack closure might prevent the crack to be open during the total tensile part of the cycles). Holper *et al.* consider then a 1200 Pa water vapor in a standard experimental case (ambient temperature of 20°C with 40 to 60% relative humidity). So, with atmospheric pressure, the exposure time mentioned before can only be reached with cycling frequencies below 1.2 kHz at a positive stress ratio or even below 600 Hz at $R = -1$ (in reality, the cracks stay open for an even shorter time because of the crack closure effect).
If the same mechanism is assumed for the Ti64 alloy, at 20 kHz, one can expect a small difference between crack growth rates in air and in vacuum at high SIF range values (corresponding to long cracks here). This is exactly what we observe in Figure 4.20. This assertion can be supported by Mayer who reviewed that the fatigue lives of specimens that have failed from internal cracks in titanium alloys are not impacted by the cycling frequency whereas specimens having failed from surface fatigue cracks present longer lives if they are ultrasonically cycled [MAY 15].

Concerning the stress ratio, Boyce *et al.* report several crack growth rate datasets acquired for surface cracks loaded at different frequencies (from 30 Hz to 20 kHz) with positive stress ratios (R=0.1 or 0.8) [BOY 01]. No frequency influence was reported in this context. It can be linked to the fact that, at positive stress ratios, the crack is closed during a shorter amount of time than at negative stress ratios (because the specimen is never in compression), consequently,

air molecules can almost always reach the crack front even if ultrasonic frequencies are used.

As a summary, the observations presented in this section point out that the crack growth rates are higher if a crack propagates in a specimen with a chimney than if it propagates in a specimen without a chimney. It means that the chimney most probably efficiently brings air molecules to the internal notch. However, at high SIF range values, the growth rates obtained for cracks propagating in air are lower for ultrasonic frequency than for conventional ones. This might mean that air molecules cannot reach the front of a long crack if it is loaded at ultrasonic frequency. Consequently, its growth rates tend towards the ones of vacuum-propagating cracks. This phenomenon should be reduced for fatigue tests at positive stress ratios because, in that case, the cracks stay usually open during a longer proportion of the cycles. More data are needed to confirm these observations, but as explained, **tracking internal cracks propagating in air with micro-tomography is difficult**.

4.3.3 Link Between Crack Growth Rates and Fractographic Features

The sizes of the fractographic zones of specimens with and without chimney (described in Sections 3.2.2.1 and 4.2.1) were measured and used to estimate an equivalent SIF range value corresponding to the crack exiting the considered zones. For this purpose, Equation 3.2 was applied with the equivalent crack size a_{eq} as explained at the beginning of Section 3.3. These values are plotted in Figure 4.21.

The typical fractographic features of internal fatigue crack have already been linked to SIF range values in the literature. Hong & Sun estimated the characteristic SIF value for crack initiation in VHCF regime in titanium alloys as $\Delta K = 3.39$ MPa $\sqrt{\text{m}}$ [HON 17]. Junet *et al.* [JUN 23], who also studied internal crack propagation in Ti64, evaluated the ΔK value at the end of the *Rough Area* as $\Delta K_{RA/FiE} = 9.14 \pm 1.19$ MPa $\sqrt{\text{m}}$. They claim that this value is in agreement with other studies: Li *et al.* reported that this value increases if the stress ratio decreases, they report $\Delta K_{RA/FiE} = 8.03$ MPa $\sqrt{\text{m}}$ for negative stress ratio ($R = -0.3$) [LI 17]. Cao & Ravi Chandran measured $\Delta K_{RA/FiE}$ between 7 & 9 MPa $\sqrt{\text{m}}$ [CAO 17]. Heinz & Eifler estimated it to be $\Delta K_{RA/FiE} = 6.76 \pm 0.39$ MPa $\sqrt{\text{m}}$ [HEI 16] and Yoshinaka *et al.* reported $\Delta K_{RA/FiE} = 9.1$ MPa $\sqrt{\text{m}}$ [YOS 16b]. All these literature values seem to match with the equivalent SIF range estimated in the present study which is around $\Delta K_{RA/FiE} = 9$ MPa $\sqrt{\text{m}}$.

Another observation concerns the transitions from the *Bright Area* to the external area of the *Fish-Eye* zone (crack propagating in air) and from the *Rough Area* to the external area of the *Fish-Eye* zone (crack propagating in vacuum) which seem to occur at the same SIF range values ($\Delta K \approx 9$ or 10 MPa $\sqrt{\text{m}}$). Above, this value, the crack growth rates tend to be close for the two environments. This suggests similar propagation mechanisms between those two environments when the cracks are very long and cycled at ultrasonic frequency (because, in this case, the air molecules hardly reach the crack front).

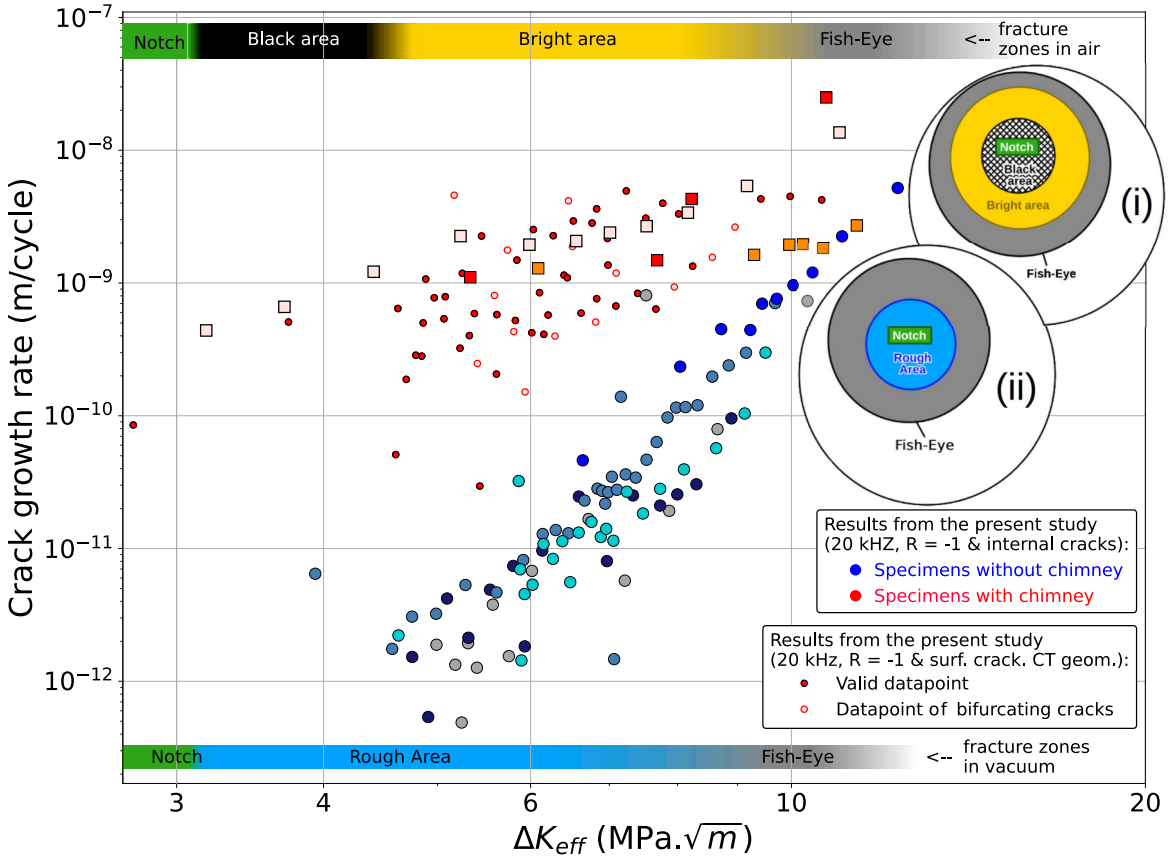

Figure 4.21 | **Estimations of the equivalent SIF range corresponding to each zone of the fracture surfaces represented in a Paris diagram** The SIF range corresponding to the different regions of the fracture surfaces in specimens without and with chimney are shown by the colored bars respectively at the bottom and the top of the curve. These values are compared with crack growth rate data for all the specimens tested in this study. The colors correspond to the fractographic zones schematized in (i) for specimens with a chimney and (ii) for specimens without a chimney.

4.3.4 Effect of the Cycling Frequency on Specimens with an Internal Notch

As evoked in Chapter 3, the crack growth rates measured in the present study for internal cracks without chimney seem to match with most of the literature data (whatever the cycling frequency) but notably *not* with the data obtained during the thesis of A. Junet even though this author used the same experimental protocol (artificial internal notch made with a femtosecond laser and SPS plate welding + in-situ synchrotron μCT acquisitions) [JUN 19]. The only difference was the cycling frequency which was set as 20 Hz in A. Junet's work. During his experiment, this author also used a chimney to bring air to the internal crack, hence, crack growth rate data were also obtained for specimens with chimney and are represented in Figure 4.22 to be compared with the datasets already presented in the current chapter.

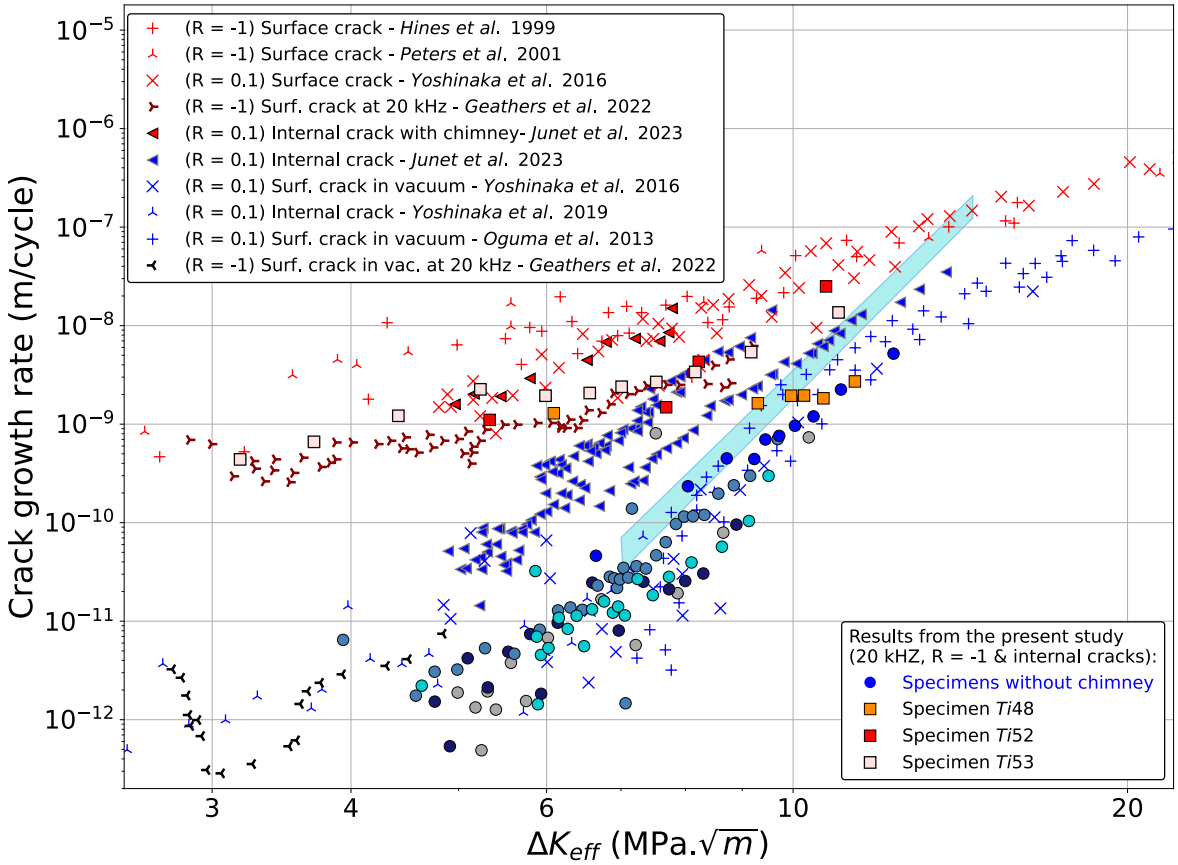

Figure 4.22 | **Comparison of crack growth rate with internal crack data cycled at 20 Hz by Junet *et al.*** [JUN 23]. The experimental conditions of the literature references are listed in Appendix H. The blue quadrilateral represents the order of magnitude of the crack growth rates estimated by A. Junet from Paris's law integration for specimens which did not undergo any dwell effect (no static loading).

The crack growth rates obtained by A. Junet for specimens with chimney match the literature data at low frequency but his internal cracks without chimney present higher growth rates than the rest of the literature and than the results from the present study. A hypothesis to explain this difference is that, after the SPS welding protocol, the vacuum level inside the artificial notch is not high enough to have cracks comparable to natural internal ones. Consequently, the crack growth rate for this type of specimen is located between the air and the vacuum fatigue behaviors. It can be called «*vacuum-like*» environmental conditions. In the present study, the previous analyses allow us to claim that ultrasonic cyclic loading «enhances» the vacuum conditions inducing a decrease in crack growth rates of the *vacuum-like* propagating cracks obtained from artificial internal notches. That could explain why the internal cracks ultrasonically cycled without a chimney in the present study have similar crack growth rates than other vacuum propagating cracks from the literature while it is not the case for the specimens of A. Junet which were cycled at low frequency.

In his thesis [JUN 21], A. Junet gives another explanation for this relatively high internal crack growth rates of specimens without chimney: the time during which the static loading is applied to the specimen while a tomography scan is acquired could induce a dwell effect [BAN 78, BAC 03]. This phenomenon is known to influence the fatigue life, particularly for titanium alloys, and could entail an increase in crack growth rates. To confirm this hypothesis, he estimated the crack growth rates by integrating Paris's law (with the C and m parameters taken from his previous propagation studies on the same material) for fatigue-failed specimens which did not undergo any static loading in order not to be influenced by a potential dwell phenomenon (hence they were not tomographied). These estimations are represented by the blue quadrilateral in Figure 4.22. They present lower values than the A. Junet's in-situ data which led him to his hypothesis. However, the quadrilateral remains still slightly higher than most of the literature datasets and than the ultrasonic dataset acquired during the present study. This entails that the dwell effect might have an impact on fatigue crack propagation rates but this effect alone does not explain the high crack growth rates measured by A. Junet.

4.4 Thermal Analysis

According to the observations reported in the previous section, coupled frequency and environment effects might contribute to the drop in crack growth rate undergone by long fatigue cracks propagating in air conditions. The environment in which a crack propagates might influence the cyclic plastic activity at the crack tip. Since this plastic energy is dissipated in heat, it constitutes a heat source in the reversed cyclic plastic zone at the crack tip. Consequently, the temperature field around the crack tip might differ when the crack grows in different environments. To evaluate this assertion, a thermal analysis has been carried out from temperature measurements acquired during the in-situ fatigue tests realized on specimens with and without a chimney.

4.4.1 Determination of the η Parameter

The η parameter from the model described in Section 1.4.2.1 is the proportionality coefficient between the crack tip lineic heat source and ΔK^4. Hence, this parameter characterizes the heat source at the crack tip independently of the applied stress amplitude. So, to evaluate the influence of the environment on the plastic activity at the crack tip, the η parameter will be determined in the case of ultrasonic fatigue tests carried out on specimens with and without a chimney.

The procedure summarized in Figure 2.32 has been applied to several cycling blocks of some specimens to determine the corresponding η parameter. In a nutshell, from tomographic scans, the crack shape has been meshed (*cf.* Section 2.4.1) to carry out numerical SIF estimations

along the crack fronts (with the Zcracks module of the Zset finite element software [ZCR21] as described in Section 2.4.2). This SIF evolution along the crack front is used to calculate a lineic heat source with the assumption of $\eta = 1$ W.m^{-3}.MPa^{-4}. Then, the heat source along the front is implemented in a finite element procedure which integrates the heat equation to obtain the temperature field at the surface of the specimen (the hypotheses used in this finite element model are detailed in Section 2.4.3.2). Because the temperature field is linear versus the heat source, it depends linearly on the η parameter. Consequently, a ratio between the numerical thermal increment (obtained with $\eta = 1$ W.m^{-3}.MPa^{-4}) and the experimental one gives the experimental value of the η parameter (*cf.* Eq. 2.17).

Because the temperature is monitored during each cycling block, a corresponding η value can be identified for the different blocks. It is supposed to be constant during each block and, as explained in Section 2.4.3.2, it is estimated from a temperature measurement acquired after 0.3 sec of cycling. All these values are represented versus the SIF range averaged along the meshed crack front in Figure 4.23.

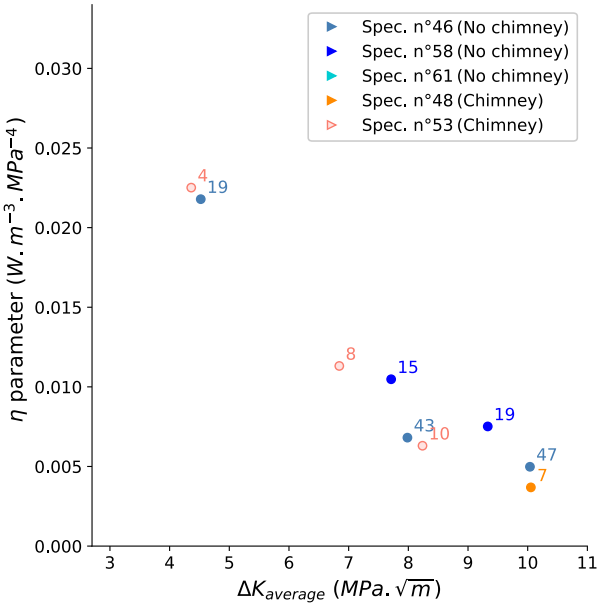

Figure 4.23 | **Results of the η calculation protocol represented versus the SIF range averaged along the meshed crack front for several cycling blocks recorded for some specimens with and without chimney** The number displayed near each data point corresponds to the studied cycling block during which the temperature has been monitored. The color of the marker corresponds to the studied specimen (colors are matched with Tables 3.2 and 4.1).

As illustrated in Figure 4.23, the η parameter seems to depend on the SIF range value. It means that the linear relation versus ΔK^4 claimed by the used model (Eq. 2.15) might not be very accurate. Also, the η parameters measured for specimens without a chimney seem

slightly higher than the ones corresponding to specimens with a chimney (at similar SIF range values). To try to understand these observations, the influence of certain parameters on the measured η values will be evaluated in the following sections to estimate some uncertainties in those measurements.

4.4.2 Influence of the Crack Size on the Thermal Measurements

According to Equation 2.17, the experimental temperature increase is needed to estimate the η parameter. As it is explained in Section 2.4.3.1, the measured experimental temperature values are averaged in a small zone surrounding the hot spot (*cf.* Fig. 2.28). Consequently, the spatial standard deviation of this measurement can be evaluated to estimate the impact of experimental temperature increase on the η parameter. It is represented by the error bars on Figure 4.24 showing the η parameter versus the meshed crack front total length.

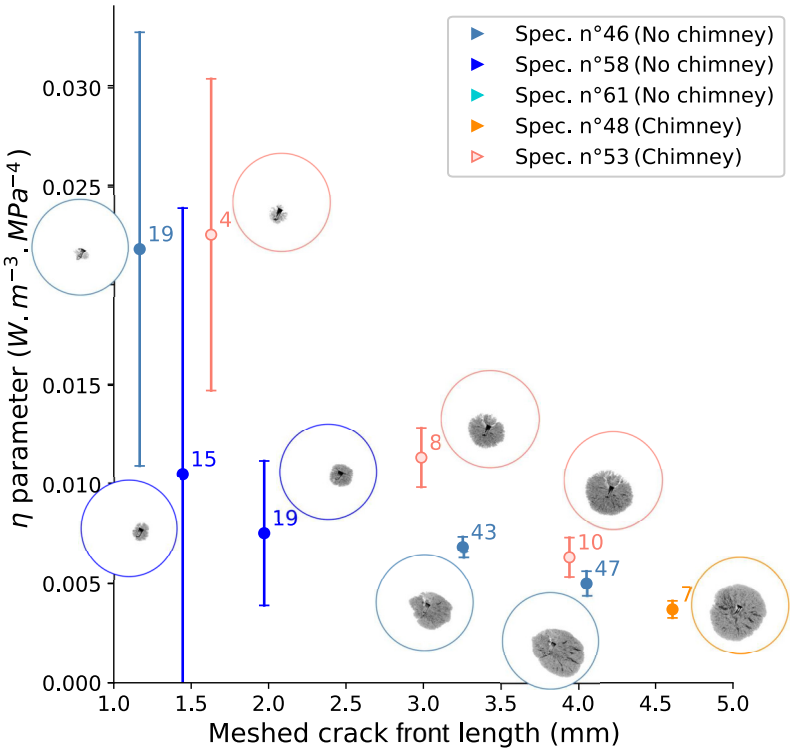

Figure 4.24 | **Results of the η calculation protocol represented versus the front total length for several cycling blocks recorded for some specimens with and without chimney** The number displayed near each data point corresponds to the studied cycling block during which the temperature has been monitored. The color of the marker corresponds to the studied specimen (colors are matched with Tables 3.2 and 4.1). The uncertainties due to experimental temperature averaging are presented along with each crack projection in the corresponding specimen cross-section. Small cracks with a crack front length shorter than 2.5mm produce a small temperature increment at the surface leading to very large uncertainties.

It points out that the temperature increase monitored during the cycling of specimens containing small cracks is too weak to obtain meaningful measurements. The values of η obtained for those small cracks are then too uncertain to be considered. Consequently, it has been chosen not to consider the values for cracks with a total crack front length shorter than 2.5 mm.

4.4.3 Influence of Mesh Smoothing on the Heat Source Identification

The influence on the η parameter of the smoothing level employed to generate crack meshes has been evaluated. As described in Section 2.4.1, the mesh is obtained from tomographic scan data that have been thresholded. The procedure comprises at least one smoothing step to get rid of the mesh elements which are too distorted. This smoothing procedure has been carried out with the *Laplacian Smooth* tool from *Meshlab* software [SOR 05]. Smoothing can then be applied again with different amounts of steps interspersed by several remeshing steps (also to avoid strong element distortion). Two different amounts of smoothing steps (10 and 100) were tried as depicted by Figure 4.25b & 4.25c.

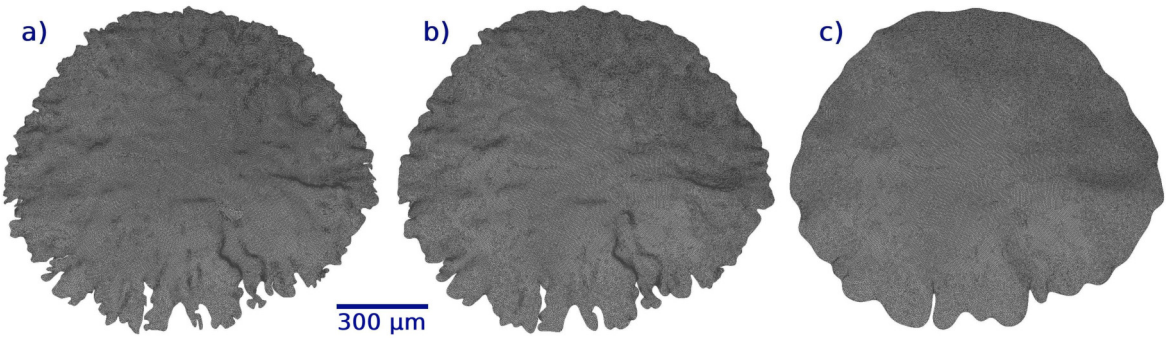

Figure 4.25 | **Three types of smoothing applied to a meshed crack** (a) no smoothing except the first one carried out to remesh the distorted elements, (b) & (c) mesh after applying respectively 10 and 100 steps of Meshlab's *Laplacian Smooth*.

It is possible to remark that the smoothing level has an influence on the irregularity of the crack front; consequently, the calculated SIF range along the front is impacted. A smoother front presents fewer variations in its SIF range evolution but the extreme values of the SIF range are enhanced (the green arrow in Fig. 4.26a corresponds to the SIF range value of the crack front portion circled in green in Fig. 4.26c). The smoothing procedure has also an impact on the total crack tip length because a lightly smoothed crack (Fig. 4.25a) will be more irregular so it will have more concavities than an extensively smoothed one (Fig. 4.25c). Since the heat source located in the reverse cyclic plastic zone is a lineic source in the proposed model, mesh smoothing has an influence on the estimation of the total energy rate dissipated by the crack (as illustrated by the values reported in Figure 4.26b).

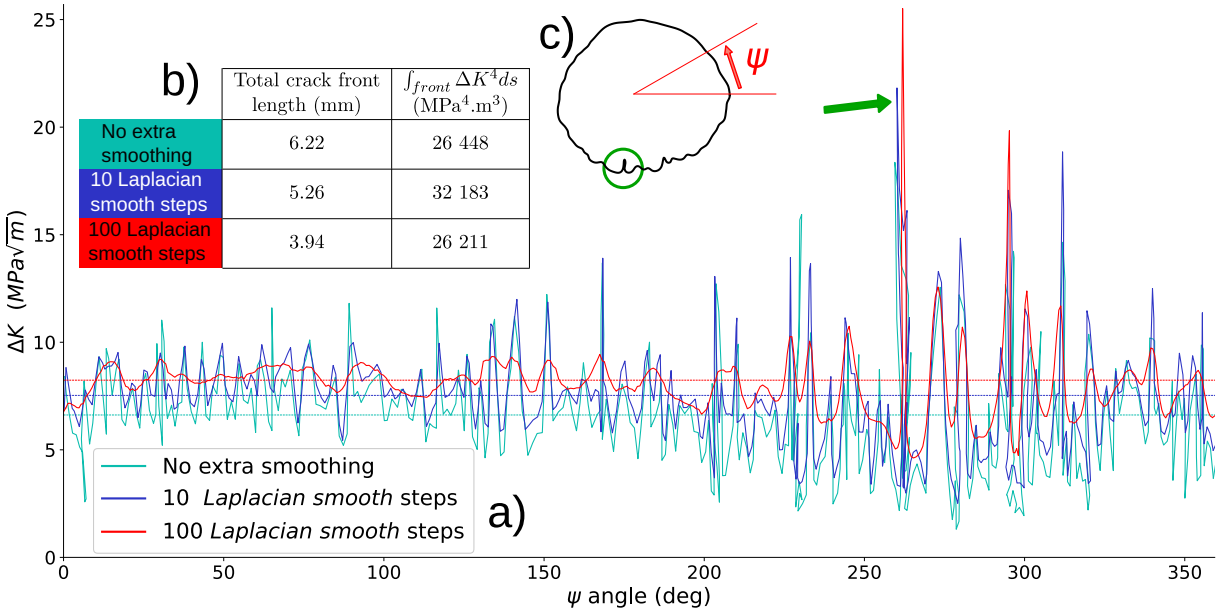

Figure 4.26 | SIF range ΔK_I evaluated from Eq. 2.11 along the tip of differently smoothed crack meshes (a) The three curves correspond to the three smoothing levels depicted in Figure 4.25 and dashed lines are the corresponding average values. (b) Total crack front length and integral of ΔK^4 along the crack front for each smoothing level. (c) Projected crack used to define the ψ angle. The high local SIF range values correspond to the crack irregularities. It is illustrated by the green arrow corresponding to the SIF range value of the crack front portion circled in green in (b).

This influence is depicted by Figure 4.27a representing the lineic heat source $S = \eta \Delta K^4_{average}$ for each cycling block thermally evaluated. In this graph, the shape of the markers (circle, star or square) corresponds to the used mesh smoothing procedure. The points obtained for the same cycling block with different smoothing levels can be used to evaluate the influence of the smoothing approach on the plastic zone heat source. To take into account this influence, the points corresponding to a specific cycling block have been merged into a single point with uncertainty bars (*cf.* Fig. 4.27b).

4.4.4 Considerations on the Measured Internal Crack Tip Plasticity Heat Source

The described protocol allowed us to estimate the lineic heat source due to the cyclic plastic zone at the crack tip thanks to the evaluation of the η parameter. It is represented in Figure 4.28 with the measured uncertainties. Hence, from the in-situ temperature field measurements carried out on Ti64, this parameter has been estimated between 2.7×10^{-3} and 1.3×10^{-2} W.m^{-3}.MPa^{-4}.

Only very few papers report reference values for the η linearity coefficient on different materials [KLI 03, RAN 14a, PIP 83, RAN 14b]. This makes uncertain the quantification of this parameter so it has to be considered with caution.

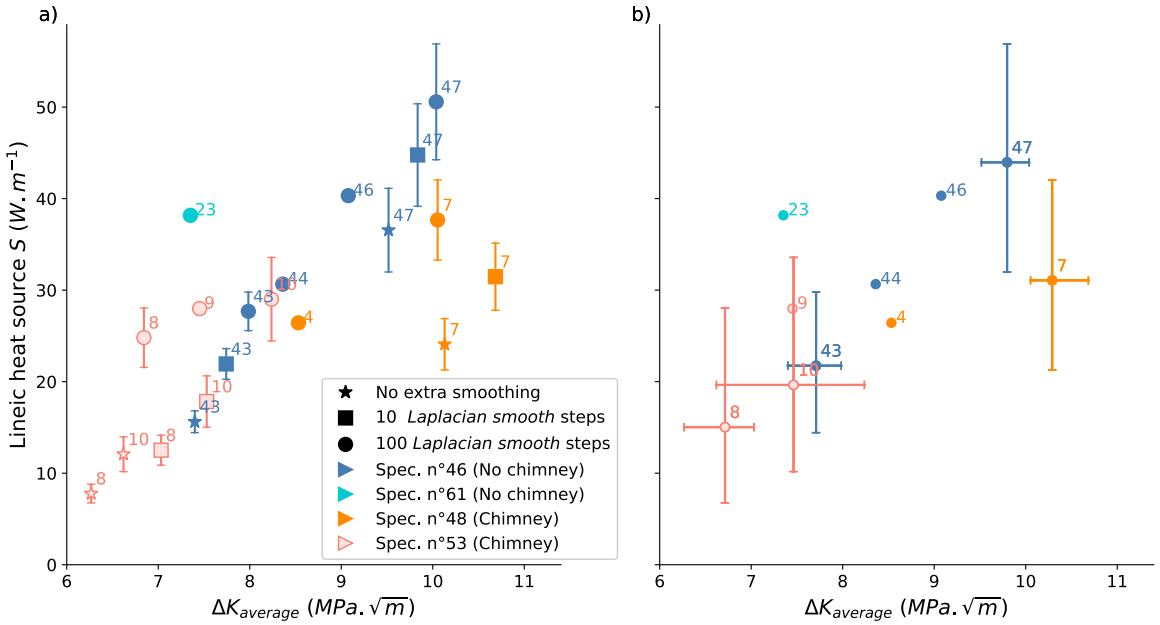

Figure 4.27 | **Value of the lineic heat source estimated** (a) for different smoothing levels of several cycling blocks recorded for some specimens with and without chimney. (b) The points corresponding to the same mesh with different smoothing have been grouped with uncertainty bars which take into account the influence of the smoothing protocol. The points without error bars have not undergone a smoothing sensitivity analysis. The number displayed near each data point corresponds to the studied cycling block. The color of the marker corresponds to the studied specimen.

The values from the present study were obtained from different specimens cycled either with or without a chimney. As pointed out by Figure 4.28, it appears that the η values seem *slightly higher for cracks propagating internally without a chimney than for cracks in a specimen with a chimney*. This could mean that, for similar SIF range values, the dissipated energy (represented by the heat source purple curves), and consequently the plastic activity at the crack front, is more important for a crack propagating internally with no contact with ambient atmosphere than for a crack propagating in air environment.

As explained in Section 4.2.3, tensile twinning was observed near the cracks that propagated in a specimen with a chimney but not in the vicinity of cracks propagating in a specimen without a chimney. Twinning is a displacive transformation so very little dissipation occurs when this mechanism is triggered [BAN 07]. This could mean that twinning is a weak heat source and, consequently, heat emission at the crack tip would be reduced when twinning occurs. This might explain the small differences in the η parameter measured between the fatigue cracks propagating in the two types of environment.

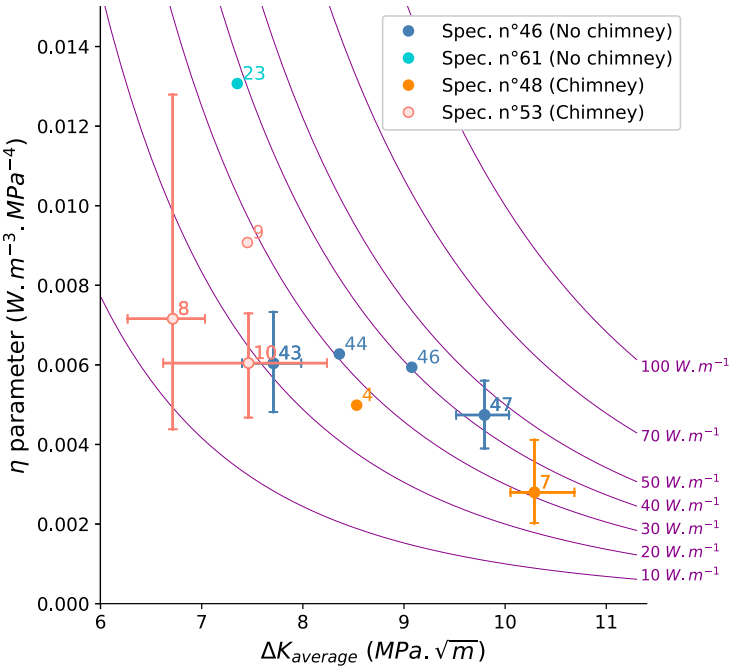

Figure 4.28 | **Values of the η parameter estimated for different cycling blocks** corresponding to some specimens with and without chimney. The points without error bars have not undergone a mesh smoothing sensitivity analysis. Purple curves represent different lineic heat source values as represented in Figure 4.27 (according to Equation 2.15). The number displayed near each data point corresponds to the studied cycling block. The color of the marker corresponds to the studied specimen.

However, this difference between heat sources at the front of cracks propagating in air or in vacuum is of the same order of magnitude as the uncertainty bars. Hence, it is not possible to be more assertive on the impact of the environment on crack tip cyclic plasticity without having a procedure producing fewer uncertainties (*c.f.* the important influence of mesh smoothing).

Finally, this approach models the lineic plastic zone heat source to have a linear dependence on ΔK^4 because it is the only model available in the literature. However, the experimental results presented in this section tend to show that the η parameter varies with the value of ΔK. So, the considered model might not be very accurate. This could be because it does not consider the crack closure effect which may have different influences on the plastic activity at the crack tip depending on the environment and the SIF range. It is a limit of the heat source estimation protocol described here.

4.5 Chapter Synthesis

The in-situ ultrasonic fatigue protocol applied to internally notched specimens was adapted to bring air to the initiated cracks thanks to a chimney linking the internal notch to the specimen surface and allowing air molecules to reach the crack front. The following points emerge from the analysis of the results obtained with this procedure:

- The fatigue lives of cracks propagating in a specimen with a chimney are lower than those of specimens without the chimney by about two decades. This difference in fatigue lives might be essentially due to a difference in crack growth rates. As it was the case for specimens without a chimney, the S-N data is very reproducible also in the case of chimney specimens.
- At ultrasonic cycling frequency, the cracks propagating from the internal notch with a chimney have similar fractographic aspect and crack growth rates than fatigue cracks initiating from the surface in ambient atmosphere (from this study and from the literature).
- Fatigue crack growth rates for ultrasonically cycled specimens containing a chimney are lower than the rates obtained at conventional frequencies, particularly at high SIF ranges (*i.e.* long cracks). This observation is also valid for surface cracks loaded at ultrasonic frequency. The fatigue behavior (growth rates and fractography) for *air-propagating long cracks* cycled at ultrasonic frequencies looks like the one of cracks propagating in vacuum (which does not depend on the cycling frequency). To explain this, it is supposed that, at ultrasonic frequencies, the cracks are not open long enough to allow the air molecules to reach the crack front. Consequently, the environment effect is drastically reduced.
- Temperature field acquisitions carried out during the ultrasonic cyclings allow to observe experimental evidence of a slightly higher plastic activity at the front of an internal crack with no link with specimen surface compared to the activity at the front of an internal crack propagating in air. However, as this approach has been used to evaluate a very local material characteristic (the cyclic plasticity at the crack tip), it still needs improvements to reduce the uncertainties and to improve the heat source model.
- Fractographic observations point out that the *Rough Area* presents on the crack surface of Ti64 internal crack (not in contact with ambient atmosphere) is replaced by a *Bright Area* which comprises a *Black Area* around the initiation site if a chimney is added inside the specimen. The *Black Area* presents a sharp crystallographic aspect whereas the *Bright Area* comprises planar and striated zones. Assuming that one cycle is needed to create one striation, these features allow to estimate a local crack growth rate two decades larger than the macroscopic one. This could be explained by the fact that cracks propagate discontinuously in the planar features.
- The striation marks (observed on specimens with chimney only) are created by $\{10\bar{1}2\}$

tensile-twinning which have been observed in section views. In this work, the occurrence of this type of twin in a grain might be controlled by a microstructural criterion: the grain $\vec{c}$-axis direction has to be oriented from 37° to 44° with the loading direction to allow the twinning to occur.

Graphical Overview

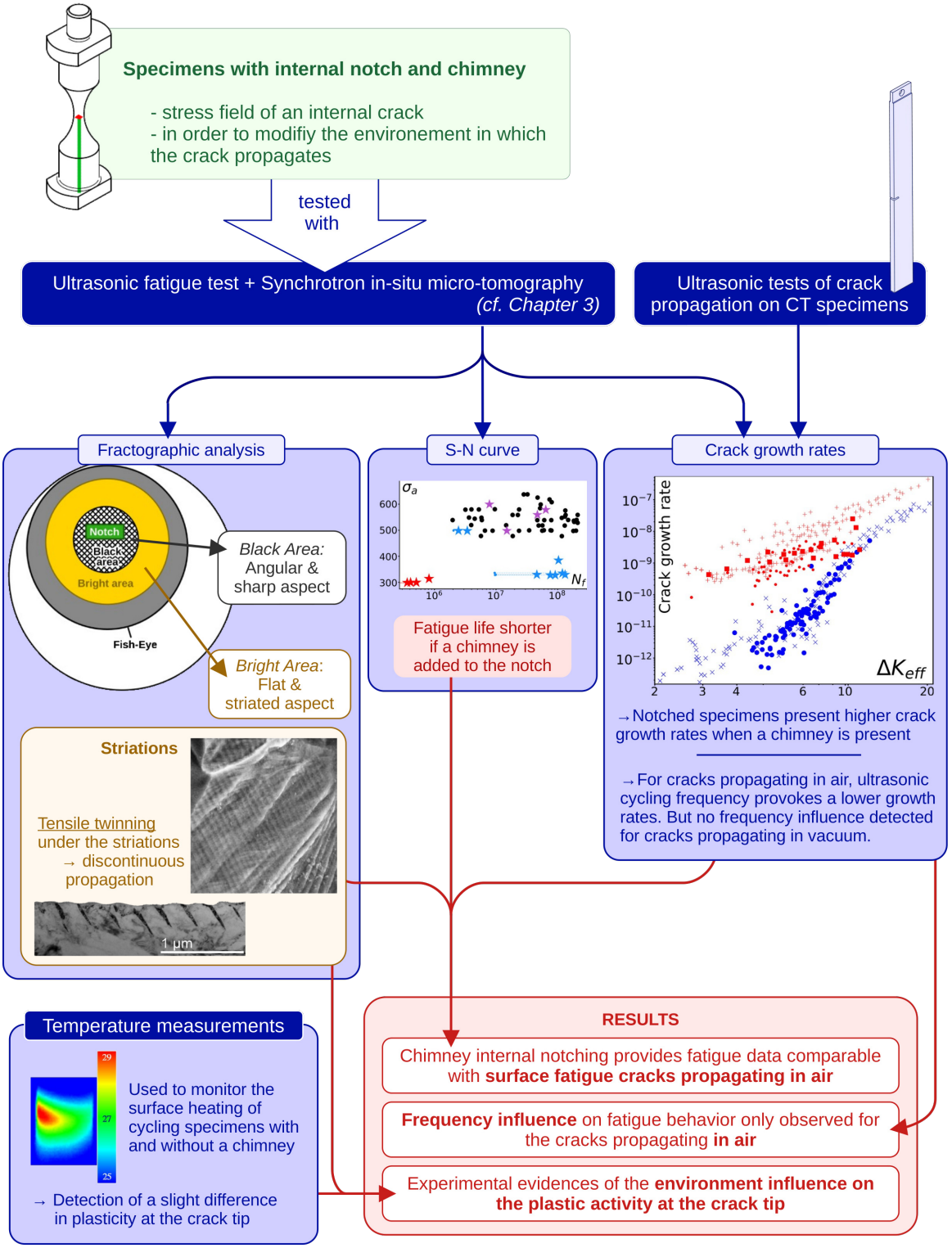

Figure 4.29 | **Synthesis of the environement effect on fatigue crack propagation** observed from the results obtained with in-situ ultrasonic fatigue tests applied on specimens containting an artificial internal notch and a chimney.

Concluding Remarks and Prospects

Internal fatigue cracks are impossible to detect with visual surface observation methods used during classic maintenance procedures. Hence, the fatigue behavior of internal cracks has to be precisely known in order to prevent critical part fractures from occurring [KLI 13, BEA 20]. For this purpose, different in-situ experimental methods (such as temperature measurements, system nonlinearities analysis or X-ray imaging) have been developed to acquire robust fatigue data on internal cracks [WAG 09, KUM 09, LUO 18]. X-ray micro-tomography is the only method providing direct 3D images of a propagating crack. However, very few papers in the literature report such observations on internally initiated fatigue cracks [CHA 15, YOS 16a, MES 19, JUN 19, XUE 22]. For this reason, an experimental protocol has been developed in this study by combining in-situ synchrotron micro-tomography and ultrasonic fatigue cycling in order to acquire the 3D shape of internal fatigue cracks at different instants of their propagation up to the Very High Cycle Fatigue regime. From these crack shapes, growth rates can be estimated but also meshes can be generated to be used in some numerical finite element approaches estimating the mechanical or thermal parameters of the studied crack.

The fatigue lives obtained in the present study with the ultrasonic fatigue testing machine are consistent with the literature data. However, to optimize the experimental sessions at the synchrotron, the cycled specimens were internally notched. The fatigue lives of those sharp notched specimens are reduced but the cracks could be monitored more efficiently. The observed fractographic features and the crack growth rates measured on those specimens are similar to those reported by different studies on fatigue cracks propagating in vacuum and natural internal ones in the same Ti64 alloy. For example, a layer of nanograins has been observed under the *Rough Area* of the fracture surface obtained in the present study. This can be linked with the observations of Oguma et al. [OGU 13] who justify this aspect with cold-welding. All the observations allow to claim that the fatigue cracks obtained in this study are comparable to natural internal fatigue cracks in Ti64. It validates the data acquired with the experimental protocol presented in this thesis.

Fatigue tests in vacuum on specimens containing a surface crack have been used in the literature to reproduce the behavior of internal fatigue cracks. However, surface fatigue cracks do not exactly experience the same mechanical conditions as internal cracks. The latter are

fully enclosed in the bulk of the specimen (with a potential effect of constraint on plasticity) but surface cracks are not (plane stress condition at the surface). To get rid of this effect and *isolate the effect of environment* on internal cracks, the notching procedure has been adapted by adding a chimney that links the internal notch to the bottom surface of the specimen in order to bring air molecules to the internally initiated crack. According to our knowledge, this procedure permitted to carry out the first direct observations of internal cracks propagating in Ti64 with and without air. In this case (*i.e.* with a chimney), it is possible to observe shorter fatigue lives, higher crack growth rates and fractographic features typically reported for cracks propagating in air (*i.e.* striations). These observations confirm that the chimney properly brings air molecules to the internal crack. Hence, the obtained fatigue data are comparable to the surface fatigue cracks grown in air reported in the literature.

Literature reports temperature acquisitions on cycling specimens carried out to detect crack initiation [WAG 09, MES 20] or to monitor the propagation [KRE 13, RAN 22]. In the present study, from temperature field measurements at the surface of the specimens during cycling, a thermal analysis has been carried out in order to point out the influence of the environment on the plasticity at the crack tip. Although the difference has the same order of magnitude as uncertainties, it appears that the heat source generated by internal crack tip cyclic plasticity is slightly higher than the one observed around internal cracks linked with air. The microstructure under the striations mentioned above has been analyzed with TEM and EBSD and reveals the presence of tensile-twins under each striation mark. As no striation and twinning marks are observed in the fractographic surface of internal cracks propagating without being in contact with air, this phenomenon can be linked with the difference in heat source. That would mean that twinning phase transformation generates little dissipation.

Because cycling was carried out at ultrasonic frequencies, crack growth rate measurements allow to evaluate the influence of cycling frequency on fatigue. For cracks cycled in air at ultrasonic frequency, the growth rates are lower than those measured on the same alloy at low frequency. For high SIF range values (and long cracks), the data acquired at ultrasonic frequency even tend towards the growth rates obtained for cracks propagating in vacuum. The very short amount of time during which cracks are open when they are cycled at ultrasonic frequencies might prevent the air molecules from reaching the front of long cracks [HOL 03].

These results* - which are focused on the effect of environment on fatigue crack propagation - illustrate the type of investigations which can be carried out with the in-situ protocol applied to internally notched specimens. This would allow to collect crucial fatigue data in the VHCF domain which could prevent critical failure of mechanical components. However, additional investigations are needed to confirm the interpretations and to study more precisely several phenomena reported in this thesis.

*A part of these results have been published during the PhD thesis [HEB 23]

Surface Crack Propagation in Vacuum at Ultrasonic Frequency

The growth rates of internal cracks linked to the ambient atmosphere with a chimney have been compared with surface crack growth rates acquired also at ultrasonic frequency (CT-like specimens). It allowed to point out that the crack growth rates in an internally notched specimen with a chimney are comparable to the surface crack growth rates. Similarly, *ultrasonic propagation tests should be carried out in vacuum for CT-like specimens with a surface crack*. For that purpose, the ultrasonic machine has to be adapted with a vacuum chamber to carry out ultrasonic fatigue tests with in-situ tomography on such surface cracks propagating in vacuum. Similar growth rates between internal cracks and surface cracks put in vacuum would add an experimental confirmation that the behavior of these two types of fatigue crack is comparable even at ultrasonic frequency. Such a result could confirm that the difference in growth rates between internal and surface cracks is principally due to the influence of the environment, the difference in the stress field undergone by the crack being less impactful.

Further Experimental Evidence to Confirm the Frequency Effect

The experimental observations described in Section 4.3.2 allow to claim that the effect of cycling frequency on crack growth rates is linked with the influence of the environment because, for high values of the stress intensity factor range, air molecules cannot reach the crack front if an ultrasonic cycling frequency is used. In that case, it only affects cracks in contact with air as observed in the presented results. Also, fatigue tests at positive stress ratios should not be impacted by the cycling frequency. This last point has already been observed for cracks propagating in air by Stanzl-Tschegg [STA 06] but no comparison with internal cracks was presented. For that purpose, a setup to cycle internally notched specimens at ultrasonic frequency with a positive stress ratio is needed. The results would be compared to the propagation data acquired in the present study at $R = -1$ to evaluate the effect of stress ratio at ultrasonic frequency.

Improvements of the Thermal Model to Quantify Crack Tip Plastic Activity

The evaluation of the plastic activity at the tip of a propagating crack under cyclic loading - which was carried out from temperature measurements - was done to evaluate the environment influence on this plasticity. However, this difference was slight and about the order of magnitude of the uncertainties. Consequently, this approach should be adapted to reduce the noise in the thermal measurements. For that purpose, the camera setups could be optimized to collect more data once the crack has initiated. More importantly, tests could be carried out at a higher cycling frequency (40 kHz) in order to have a bigger heat source needed to gain more accuracy in the temperature measurements.

If signals with a higher signal-to-noise ratio are acquired, the model used to evaluate the different heat sources could be improved. Particularly, the linearity between the lineic heat source at the cyclic plastic zone and ΔK^4 seems not accurate. This could be explained by the fact that the crack closure is not taken into account by the model.

Improvements on the Schmid Factor Analysis to Understand Twinning

As described in Section 4.2.3, a Schmid factor analysis has been carried out to try to understand the presence of twinning in some grains around the crack path in specimens with a chimney. For that purpose, twinning activation has been modeled with a criterion based on the critical resolved shear stress. Since no such data exist in the literature, the value of this critical resolved shear stress was supposed to be equal to the highest one among the different slip systems. However, the numerical results obtained with this approach were different from the experimental observations. Consequently, a study should be carried out to find out if specific twin CRSS values could allow to obtain simulation results similar to the experimental observations. Furthermore, the influence of environement on the values of the critical resolved shear stress was not considered and could change the order of activation between the different systems.

Improvements on the Crack Initiation Detection System

In the protocol described in this manuscript, a laser vibrometer was used to detect the fatigue cracks as soon as possible after they initiated to acquire a first micro-tomography. In the case of internal cracks not in contact with the ambient atmosphere, this first acquisition occurred when the crack size was relatively small compared to the specimen diameter. It allowed to regularly obtain the 3D crack shape during its whole propagation until final fracture. However, in the case of specimens with a chimney, since the growth rates were important, the initial tomography occurred once the crack was large and, consequently, only a limited number of acquisitions could be carried out before the final fracture. To obtain more tomographic acquisitions in the case of cracks propagating in contact with air, it is necessary to improve the detection system. For that purpose, a system with two laser vibrometers could be set up to monitor the oscillation at the bottom surface of the vibrating specimen but also at the bottom of the horn. A difference between these two acquired signals would allow to evaluate only the specimen nonlinearities. In that case, the detection procedure could be less impacted by parasitic nonlinearities and a smaller threshold could be set on the specimen free-end displacement second or third harmonics to detect earlier the crack initiation. This would allow to obtain more propagation data for cracks propagating in air or even to monitor specimens without any artificial internal notch.

Internal Fatigue Crack Initiation

The present work was focused on internal fatigue crack propagation. For that purpose, internal notching was used to foster the initiation and to locate it in the tomography field of view. Consequently, the initiation mechanisms might be different from the natural ones. A study on internal fatigue crack initiation could complement the present results in order to have more robust data on Very High Cycle Fatigue regime. To do so with the protocol described in this study, initiation should occur without the notch. For that purpose, materials with natural inclusions could be used (such as steel 42CrMo4, for example) to know in advance the possible natural initiation location in the material. However, if no internal notch is used, the initiation

can occur in a relatively large volume. Hence, as the acquired volume has to be inspected when a potential initiation is detected with the laser vibrometer, it will be time-consuming to check with tomography if an internal crack properly initiated. So this approach has to be carried out as long as an improvement in the detection system is considered (as evoked above).

Appendix A

Measurement Uncertainties

The different measurements used to calculate the experimental data points in the Paris diagrams ($da/dN = f(\Delta K)$ in Fig. 3.22 and 4.19) have uncertainties that need to be estimated. This has been done for the SIF and the crack growth rate using Equation A.1.

$$\delta f(x_j) = \sqrt{\sum_j \left[\left(\frac{\partial f}{\partial x_j} \right)^2 \delta x_j^2 \right]}. \tag{A.1}$$

As shown in the next figures, the uncertainty on the crack growth rate is negligible for high SIF ranges but increases for smaller cracks; mainly because the crack growth rate is very low. The uncertainty on the SIF range can be important specifically for cracks with a non-circular shape but the uncertainty level does not seem to contradict the result interpretation as the curves conserve their shape and still match with literature data.

A.1 Paris Diagram Uncertainties for Tomographied Cracks

For tomographied cracks, the SIF range is calculated from Equation 3.2 so uncertainties need to be quantified for the stress amplitude $\sigma_a = \Delta\sigma/2$, the equivalent crack radius a_{eq} and the specimen gauge length radius b. However, as detailed in Section 3.3, the use of Equation 3.2 supposes the cracks to have a penny shape which is not properly the case. Hence, the uncertainty on a_{eq} was evaluated from the radius of the smallest circle containing the projection of the crack and the radius of the largest circle contained in the projected crack. The uncertainty on the equivalent crack radius δa_{eq}, is equal to the difference between these two circles radiuses.
The crack growth rate is evaluated as the ratio between the crack size increase and the number of cycles between two tomographic acquisitions, so uncertainties are needed for the crack size increment δa_{eq} and the increment of the number of cycles δN. The uncertainty on the extension of the projected crack area depends on the difference in the projected crack area between two

successive tomographic scans. The uncertainty on a_{eq} is subjectively evaluated to 5 pixels based on the capacity to distinguish the crack front in tomography data.

A summary of the uncertainties estimations is presented in Table A.1 and the uncertainty bars are depicted in Figure A.1.

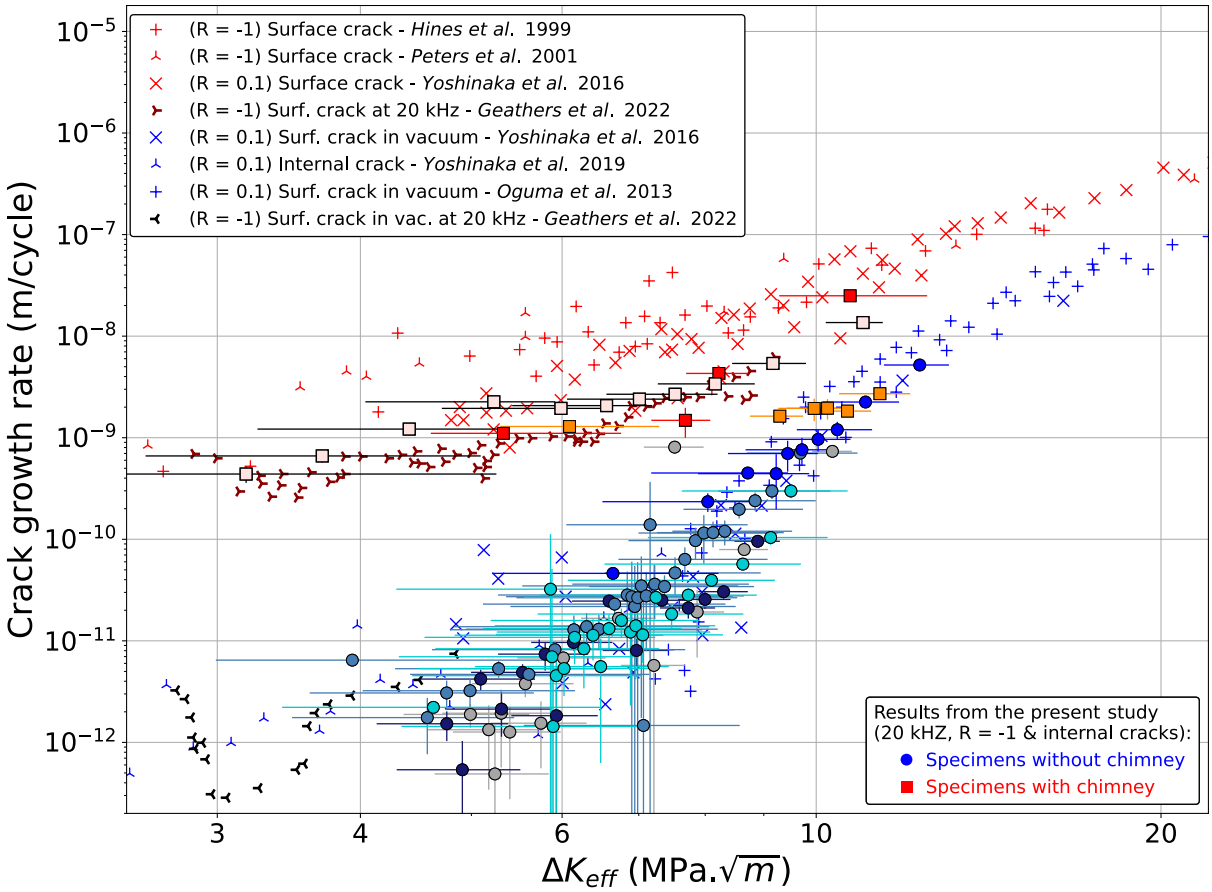

Figure A.1 | **Uncertainties for tomographied cracks represented in a Paris diagram** from Figure 4.20. The observations described in Chapter 3 and Chapter 4 do not seem to be contradicted as the curves conserve their shape and still match with literature data.

Table A.1 Measurement uncertainties taken into account in the case of the tomographied cracks

$\delta(\Delta\sigma)$	δb	δa_{eq} (for $\frac{da}{dN}$)	$\delta(\Delta N)$
2 %	40 μm	5 pixels (3.5 μm)	20 cycles (1 ms)

A.2 Paris Diagram Uncertainties for Surface Cracks in Ultrasonic CT-Like Specimens

For surface cracks studied during ultrasonic fatigue tests carried out on CT-like specimens, the SIF is calculated from Equation 2.5 so uncertainty is quantified for the displacement amplitude, U_0, as the difference between the amplitude measured with the laser vibrometer and the one calculated with the used linear regression. The projected crack length uncertainty, δa_{proj}, is also needed. It has been estimated from repeated measurements carried out on a few crack pictures. Furthermore, δa_{proj} has been individually adjusted for each crack propagation block because the accuracy of the alignment between two successive pictures was not always similar. Also, a chamfer was present on the specimen edges but it is not similar for every specimen. This has been considered as well in the estimation of δa_{proj}.
The crack growth rate uncertainty is evaluated from δN and δa_{curv}. The curvilinear crack length uncertainty has been estimated from repeated measurements carried out on a few crack pictures.

All the uncertainties estimations are presented in Table A.2 and the uncertainty bars are depicted in Figure A.2.

Table A.2 Measurement uncertainties taken into account in the case of surface cracks propagating in ultrasonic CT specimens

$\delta(U_0)$	δa_{proj} (for ΔK)	δa_{curv} (for $\frac{da}{dN}$)	$\delta(\Delta N)$
0.3 μm	8% max.	13 μm	20 cycles (1 ms)

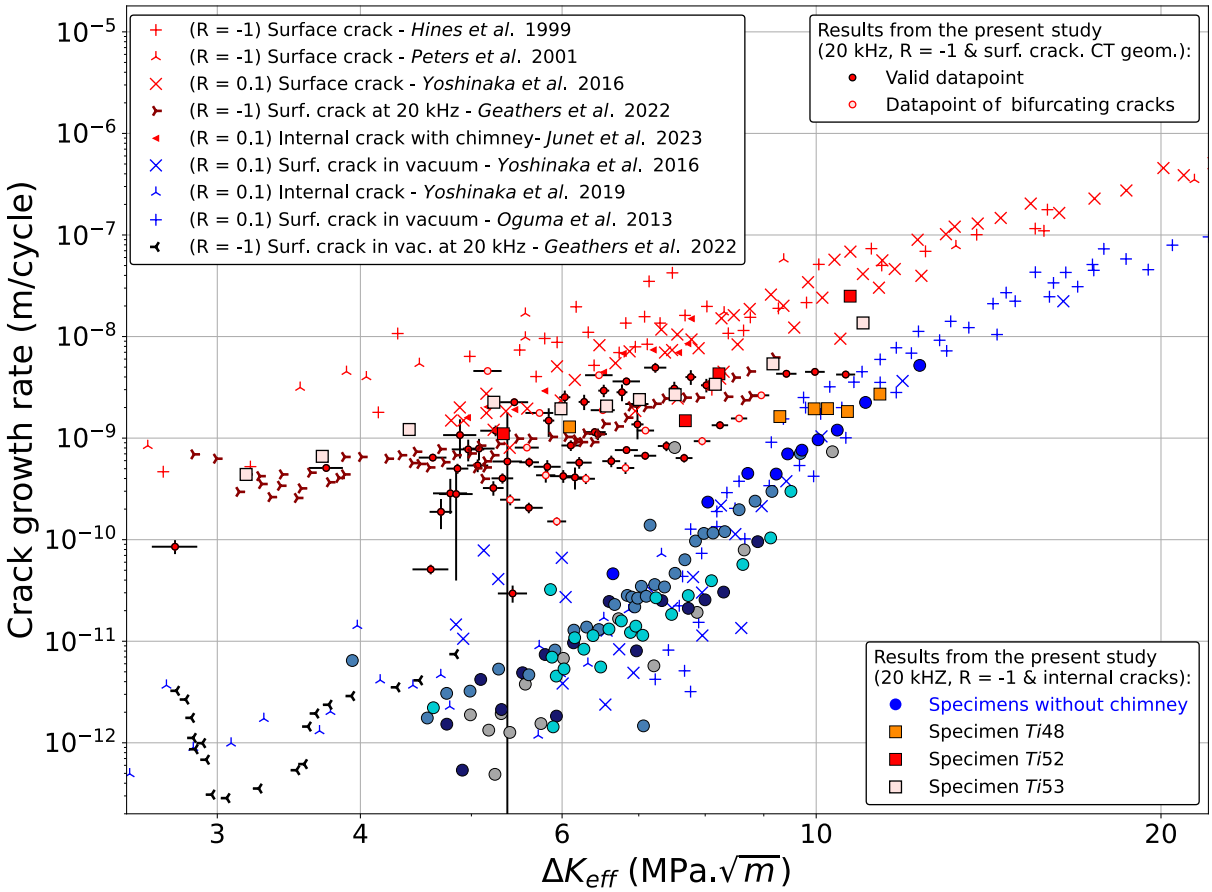

Figure A.2 | **Uncertainties for surface cracks propagating in ultrasonic CT specimens represented in a Paris diagram** from Figure 4.20. The observations described in Chapter 4 do not seem to be contradicted as the uncertainties remain small.

Appendix B

Tilt Fractography Method

The tilt fractography protocol has been described by Themelis *et al.* and Sinha *et al.* [THE 90, SIN 07] and is used in Chapter 3 to measure the inclination angle of a plane facet localized on the specimen fracture surface.

For that purpose, the coordinates of three non-colinear fracture features have to be measured when the specimen is tilted at two different angles. The protocol is based on the following equations.

x, y and z, the coordinates of a feature in the SEM stage axis system can be measured from the features coordinates obtained at two different tilt angles. According to Figure B.1, it is possible to write for each tilt angle θ_i:

$$x_i = x cos\theta_i - z sin\theta_i \tag{B.1}$$

Consequently, the coordinates of a fracture feature in the SEM stage axis system (i, j, k) can be written depending on its coordinates at tilt angles θ_1 and θ_2:

$$\begin{bmatrix} x_1 \\ z_1 \end{bmatrix} = \begin{bmatrix} cos\theta_1 & -sin\theta_1 \\ cos\theta_2 & -sin\theta_2 \end{bmatrix} \begin{bmatrix} x \\ z \end{bmatrix} \iff \begin{bmatrix} x \\ z \end{bmatrix} = \frac{1}{cos\theta_2 sin\theta_1 - cos\theta_1 sin\theta_2} \begin{bmatrix} -sin\theta_2 & sin\theta_1 \\ -cos\theta_2 & cos\theta_1 \end{bmatrix} \begin{bmatrix} x_1 \\ x_2 \end{bmatrix} \tag{B.2}$$

Specifically, for the fracture feature «A» with (x^A, y^A, z^A) its coordinates in the SEM stage axis system and (x_i^A, y_i^A) its coordinates at tilt angle θ_i:

$$\begin{cases} x^A = (x_1^A sin\theta_2 - x_2^A sin\theta_1)/sin(\theta_2 - \theta_1) \\ y^A = y_1^A = y_2^A = (y_1^A + y_2^A)/2 \\ z^A = (x_2^A cos\theta_1 - x_1^A cos\theta_2)/sin(\theta_2 - \theta_1) \end{cases} \tag{B.3}$$

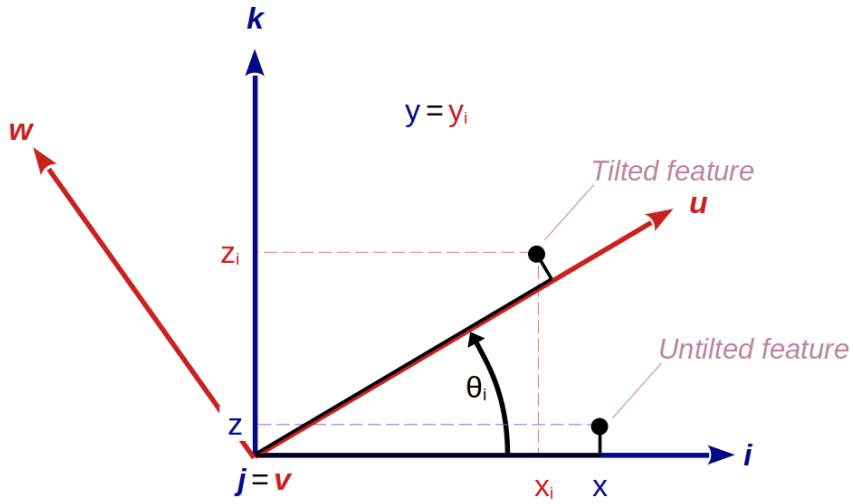

Figure B.1 | **Coordinates situation of a feature which is on a tilted specimen** The tilting is a θ_i rotation around $j = v$ axis. x, y and z are the feature coordinates in the SEM stage axis system (i, j, k). x_i, y_i and z_i are the coordinates in the tilted system (u, v, w) at tilt angle θ_i.

If the approach described above to obtain the feature coordinates in the SEM stage axis system is carried out for three non-colinear features «A», «B» and «C», it is possible to obtain two non-colinear vectors included in the facet plane:

$$\vec{AB} = \begin{bmatrix} (x^B - x^A) \\ (y^B - y^A) \\ (z^B - z^A) \end{bmatrix} \quad \text{and} \quad \vec{BC} = \begin{bmatrix} (x^C - x^B) \\ (y^C - y^B) \\ (z^C - z^B) \end{bmatrix} \tag{B.4}$$

Consequently, the cross product of these two vectors gives a vector colinear to the facet normal:

$$\vec{n} = \vec{AB} \times \vec{BC} = \begin{bmatrix} (y^B - y^A)(z^C - z^B) - (y^C - y^B)(z^B - z^A) \\ (x^B - x^A)(z^C - z^B) - (x^C - x^B)(z^B - z^A) \\ (y^C - y^B)(x^B - x^A) - (y^B - y^A)(x^C - x^B) \end{bmatrix} \tag{B.5}$$

Finally, the angle between the observation direction $\vec{k}$ and the facet normal $\vec{n}$ can be calculated as follows:

$$\gamma = arccos\left(\frac{\vec{n}.\vec{k}}{\|\vec{n}\|}\right) \tag{B.6}$$

Appendix C

Notes on the Crack Initation Detection System

Figure C.1 | **System used to support the laser vibrometer** installed on ID19 beamline in ESRF synchrotron.

During the first synchrotron experimental sessions, the limits of the laser vibrometer system were pointed out. A large amount of false detections occurred in reason of parasitic vibrations present in the experimental synchrotron environment. The new clamping system shown in Section (S) from Figure 2.5 allows the reduction of this detected noise but the detections were still occurring too frequently without any crack initiation. Finally, the major improvement was to replace the tripod which supported the laser vibrometer with a more rigid solution. As shown in Figure C.1, a rigid part was fixed to the beamline granite table and the translating support of the laser vibrometer was fixed on this rigid part. By choosing this solution and plugging - when it was possible - the power supply of the acquisition devices on the electric network isolated from the grounds and specifically dedicated to the measurements, the detection system was considerably less sensitive to external vibrations and had only very few false detections.

Appendix D

Experimental Measurements of the Material Properties

Two material properties are needed to design ultrasonic specimens. To measure the Young modulus in the case of ultrasonic loading, E_{US}, and the volumetric mass of the material, ρ, a cylindrical specimen has been manufactured with the same material according to the drawing from Figure D.1. For such a geometry, Bathias & Paris propose the resonance frequency f such as defined in Equation D.1 (with l the cylinder length) [BAT 05].

$$f = \frac{1}{2l}\sqrt{\frac{E_{US}}{\rho}} \tag{D.1}$$

The presented geometry allows to measure $\rho = 4422\ \mathrm{kg\,m^{-3}}$. It has been loaded with an ultrasonic machine to measure its resonance frequency, f, according to Equation D.2 [CHA 97]. A measured resonance frequency $f = 20\ 433$ Hz leads to $E_{US} = \rho(2fl)^2 = \mathbf{117.4\ GPa}$

$$f_g = \frac{2f_v f}{f_v + f} \iff f = \frac{f_v f_g}{2f_v - f_g} \tag{D.2}$$

with $f_v = 20\ 387$ Hz the loading frequency of the ultrasonic machine without any specimen and $f_g = 20\ 410$ Hz the frequency of the machine with the cylindrical specimen.

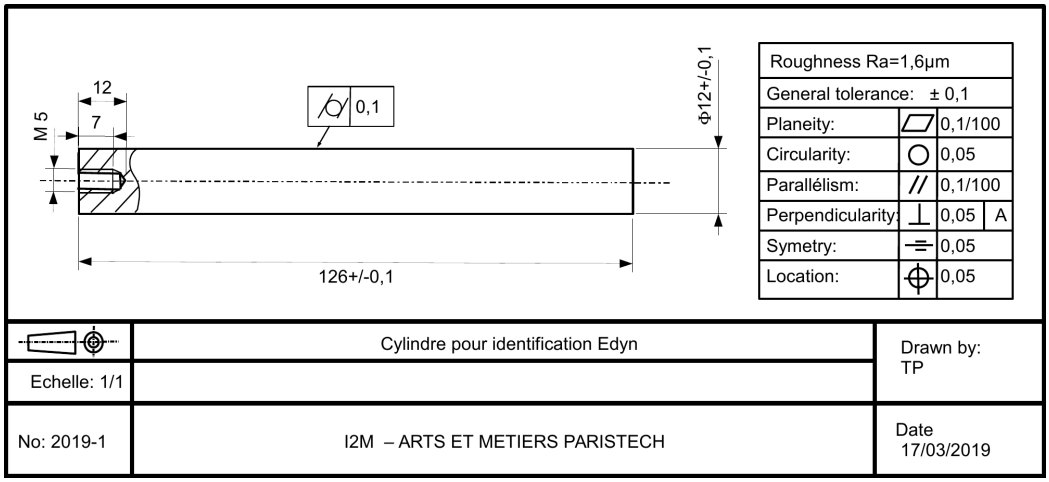

Figure D.1 | Drawing of the cylinder specimen used to determine E_{US}

Appendix E

G-θ Method

The G-θ method is used to calculate the SIF range along the crack tip of a complicatedly shaped crack. It is detailed in the software users manual [ZCR21] (reproduced below) and summarized in French in Section 3.2.3.1 from Messager's thesis [MES 20].

G-theta method theory

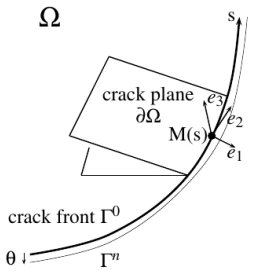

Transformations F^n of domain Ω to Ω^n due purely to crack propagation

$$F^n \; : \; M \rightarrow M \; + \; \eta \, \theta(M)$$

θ : crack extension virtual field that modifies only the position of the crack front Γ_0

$\theta \in \Theta \; = \; \{\mu \; \textit{such that} \; \mu.e_3 = 0\}$ (tangent to the crack plane)

The stress energy release rate $G(\theta)$ for crack extension θ is given by the Lagrangian derivative of potential energy W:

$$G(\theta) \; = \; -\frac{\partial W}{\partial \eta}$$

For thermo-elasticity the right-hand side reduces to :

$$\frac{\partial W}{\partial \eta} \; = \; \int_\Omega \left[\frac{1}{2} \left(\sigma : \left(\epsilon - \epsilon^{th} \right) \right) \nabla\theta \; - \; \sigma : \left(\nabla u \nabla\theta \right) \right] d\Omega$$

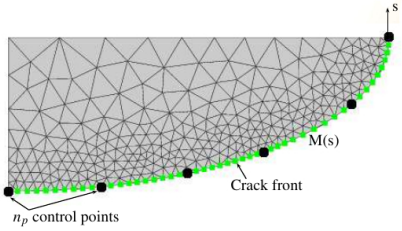

The left-hand side is obtained by integration on the crack front Γ^0:

$$G(\theta) \; = \; \int_{\Gamma_0} G(s) \; \theta(s) \; e_1(s) \; ds$$

Discretization by n_p control points with shape functions $N_j(s)$:

$$G(s) = \sum_{j=1}^{n_p} G_j\, N_j(s) \quad , \quad G(\theta) = \sum_{j=1}^{n_p} G_j \int_{\Gamma_0} \theta(s)\, N_j(s)\, ds \;,\; \forall \theta \in \Theta$$

For θ^i $(i = 1, n_p)$ virtual fields $\theta^i(s).e_1(s) = N_i(s)$:

$$\begin{aligned} G(\theta^i) &= \sum_{j=1}^{n_p} G_j \int_{\Gamma_0} N_i(s)\, N_j(s) ds \qquad i = 1, n_p \\ &= \int_{\Omega} \left[\frac{1}{2} \left(\sigma : \left(\epsilon - \epsilon^{th} \right) \right) \nabla \theta^i \; - \; \sigma : \left(\nabla u \nabla \theta^i \right) \right] d\Omega \end{aligned}$$

a system with n_p unknowns G_j $(j = 1, n_p)$

SIF extraction using the G-theta method

Introducing the same discretization of a G^v value on the crack front Γ^0 as the one defined for G previously:

$$G^v(s) = \sum_{j=1}^{n_p} G_j^v\, N_j(s)$$

it is possible to evaluate an interaction integral using any virtual displacement field v in combination of the FEA obtained displacement u in the following formulation:

$$\sum_{j=1}^{n_p} G_j^v \int_{\Gamma_0} N_i(s)\, N_j(s) ds = \int_{\Omega} \left[\frac{1}{2} \left(\sigma(u) : \left(\epsilon(v) \right) \right) \nabla \theta^i \; - \; \sigma(v) : \left(\nabla U . \nabla \theta^i \right) \right] d\Omega$$

Introducing, in the previous equation, any pure mode I, II or III Westergaard displacement solutions $v^{I,II,III}$, defined in the crack front vicinity, allows to compute associated $G^{v,I,II,III}$ values. The following Irwin formula for a given isotropic linear elastic behavior, leads to each associated SIF $K_j^{I,II,III}$ along the front discretization:

$$\sum_{j=1}^{n_p} G_j^{v,I,II,III} \int_{\Gamma_0} N_i(s)\, N_j(s) ds = \sum_{j=1}^{n_p} \frac{1 - \nu^2}{E} \left(K_j^I\, K_j^{v,I} + K_j^{II}\, K_j^{v,II} \right) + \frac{1}{2\mu} K_j^{III}\, K_j^{v,III} \int_{\Gamma_0} N_i(s)\, N_j(s) ds$$

Appendix F

Analysis of the Microstructure Under the Facets

F.1 Direct EBSD Mapping of Other Facets

A study on the facets located in the Rough Area of specimens cycled without a chimney is presented in Chapter 3. The method described in Section 3.2.2.2 to obtain the microstructural orientation of the grains under such facets was carried out for several of them. The next figures present, for each of them, a SEM picture of the studied facet with its corresponding EBSD map. Because the axis of the EBSD camera has a 70° angle from the axis of the SEM camera (*cf.* Fig. 3.15), all Pictures (a) are artificially distorted to show the SEM pictures with the same angle than the EBSD ones (*i.e.* in a way such as the specimen is observed from a 0° view direction). The IPF shows the crystal direction normal to the pictures.

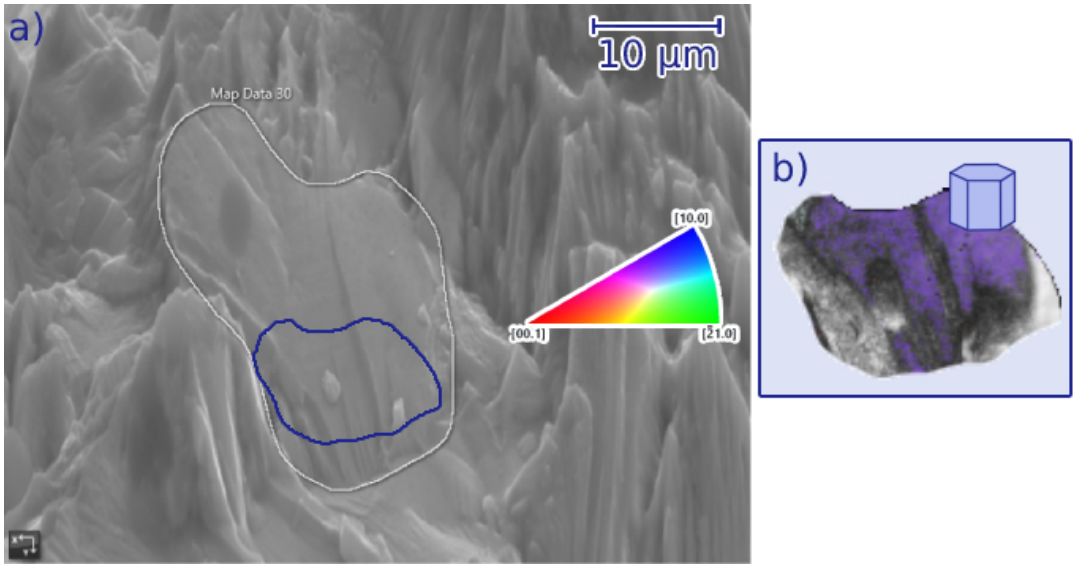

Figure F.1 | **(a) SEM picture of the facet and (b) its corresponding EBSD map** The depicted feature belongs to the fracture surface of Specimen nb 48 cycled at 300 MPa during 5.04×10^5 cycles. The tilt fractography method was used on this facet, the angle between its normal and the view direction is evaluated to 61°.

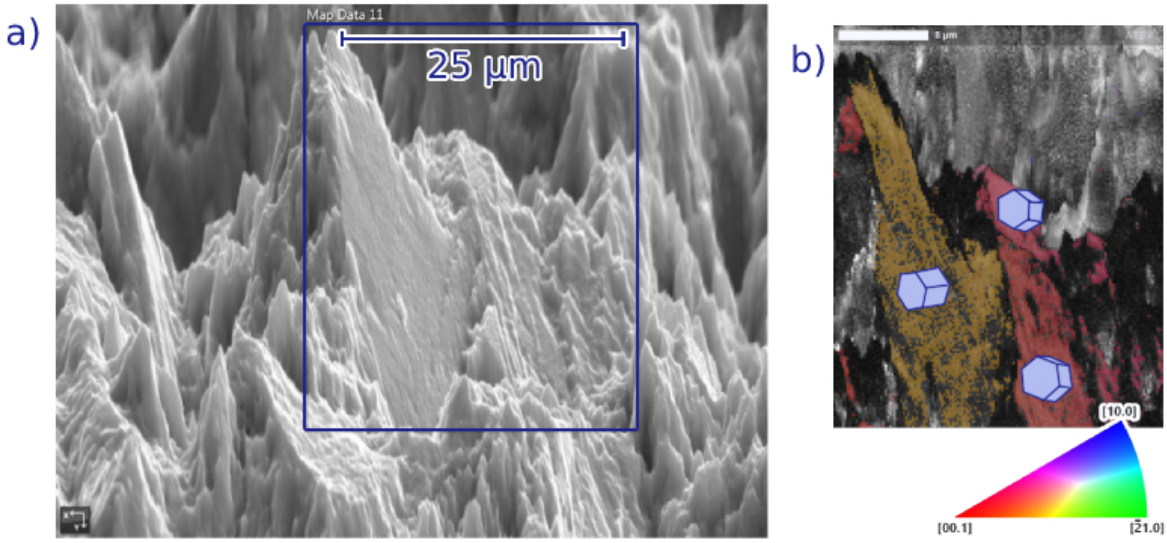

Figure F.2 | **(a) SEM picture of the facet and (b) its corresponding EBSD map** The depicted feature belongs to the fracture surface of Specimen nb 46 cycled at 330 MPa during 4.55×10^7 cycles. The tilt fractography method was used on this facet, the angle between its normal and the view direction is evaluated to 81°.

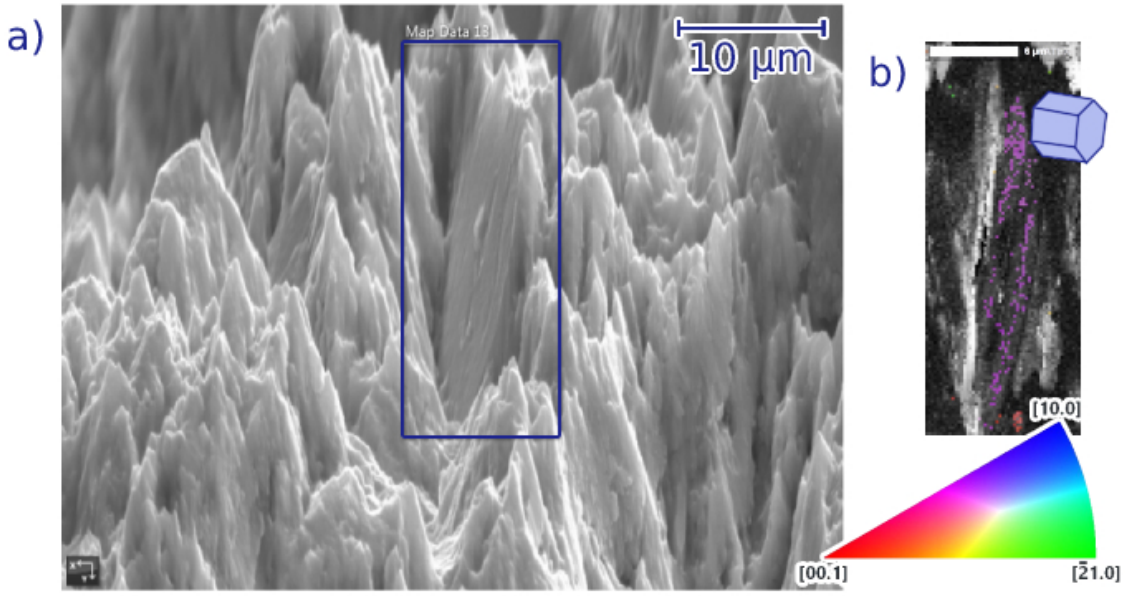

Figure F.3 | **(a) SEM picture of the facet and (b) its corresponding EBSD map** The depicted feature belongs to the fracture surface of Specimen nb 46 cycled at 330 MPa during 4.55×10^7 cycles. The tilt fractography method was used on this facet, the angle between its normal and the view direction is evaluated to 82°.

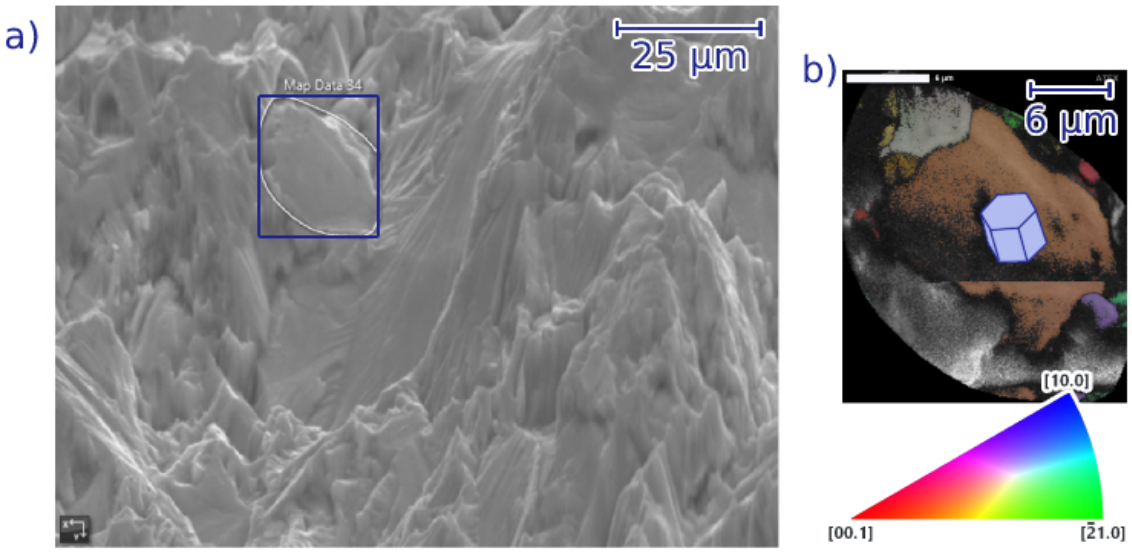

Figure F.4 | **(a) SEM picture of the facet and (b) its corresponding EBSD map** The depicted feature belongs to the fracture surface of Specimen nb 48 cycled at 300 MPa during 5.04×10^5 cycles. The tilt fractography method was used on this facet, the angle between its normal and the view direction is evaluated to 58°.

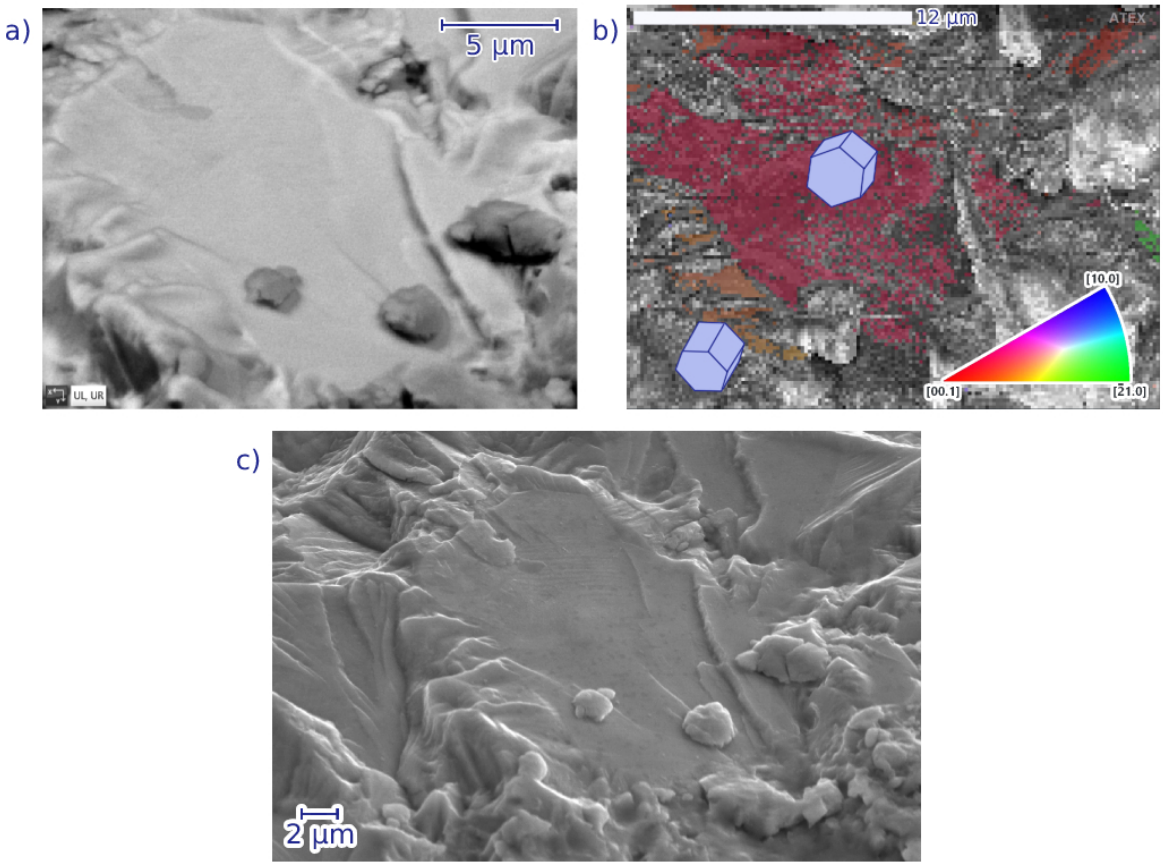

Figure F.5 | **(a) SEM picture of the facet and (b) its corresponding EBSD map** The depicted feature belongs to the fracture surface of Specimen nb 49 cycled at 315 MPa during 8.16×10^5 cycles. The tilt fractography method was used on this facet, the angle between its normal and the view direction is evaluated to 54°.

F.2 Another Tested Method to Determine the Facet Orientation

In reason of the lack of confidence in the results from the tilt fractography method, another approach has been used to evaluate the facet orientation. The studied facet is observed with a Hirox RH-2000 high-resolution optical microscope (cf. Figure F.6) and the automatized focus tool from this microscope allows to obtain a 3D map of the observed surface (cf. Figure F.7). The example illustrated in Figure F.6 corresponds to the facet observed with SEM from Figure F.5. Its normal angle was measured to be 51° with tilt fractography but only around 22° with the optical microscopy approach. This approach was not pushed further for a matter of time so no evaluation of the accuracy of such a method could be carried out.

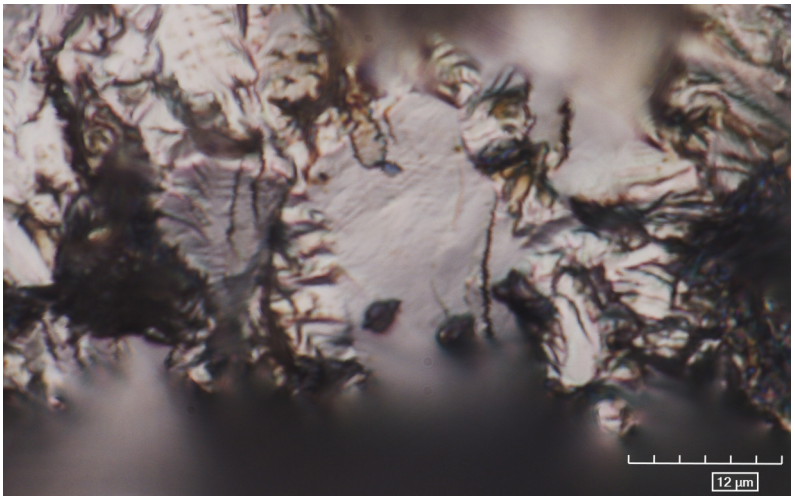

Figure F.6 | **Optical microscopic observation of a facet used to measure its orientation** The facet was also observed with SEM in Figure F.5.

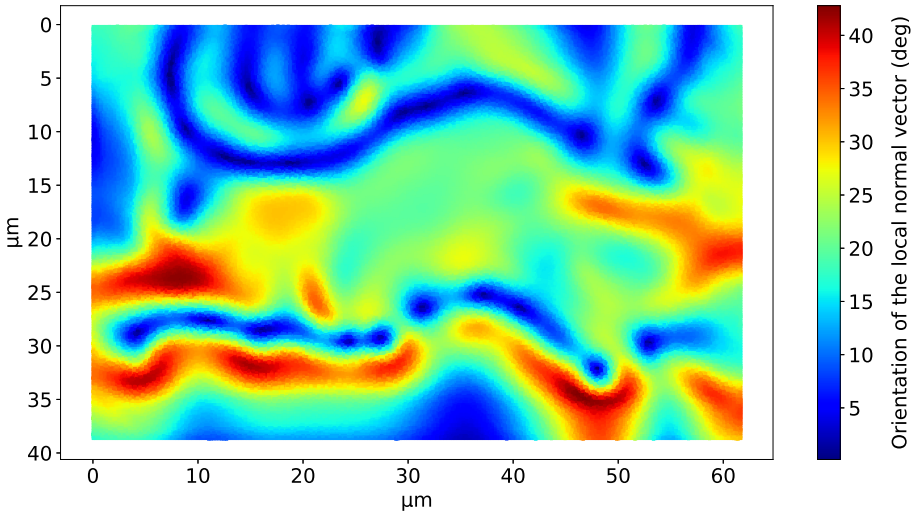

Figure F.7 | **Angle the local normal makes with the picture normal** This map has the same dimensions than the optical microscopy picture presented in Figure F.6. This facet was also observed with SEM in Figure F.5.

Appendix G

Studied Internal Cracks

The fracture surfaces of the internal cracks which propagated in a specimen with an artificial notch are illustrated in this Appendix.

G.1 Specimens Which Have Been Tomographied

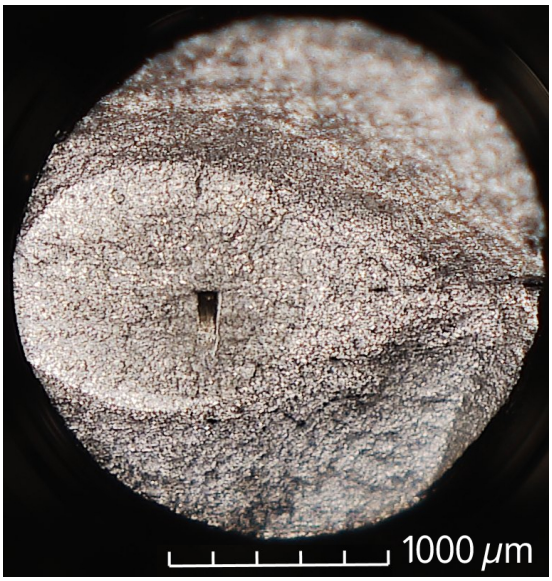

Figure G.1 | **Optical microscopy observation of the fracture surface** of Specimen nb 44 which has been cycled at 337 MPa during 1.17×10^8 cycles. It does not contain a chimney.

The following figures represent (a) the average heights of the fatigue cracks (the zero is fixed at the lowest height of the crack). The different sections correspond to section views along the planes represented in black on the cracks. (b) Optical microscopy observation of the fracture

surfaces.

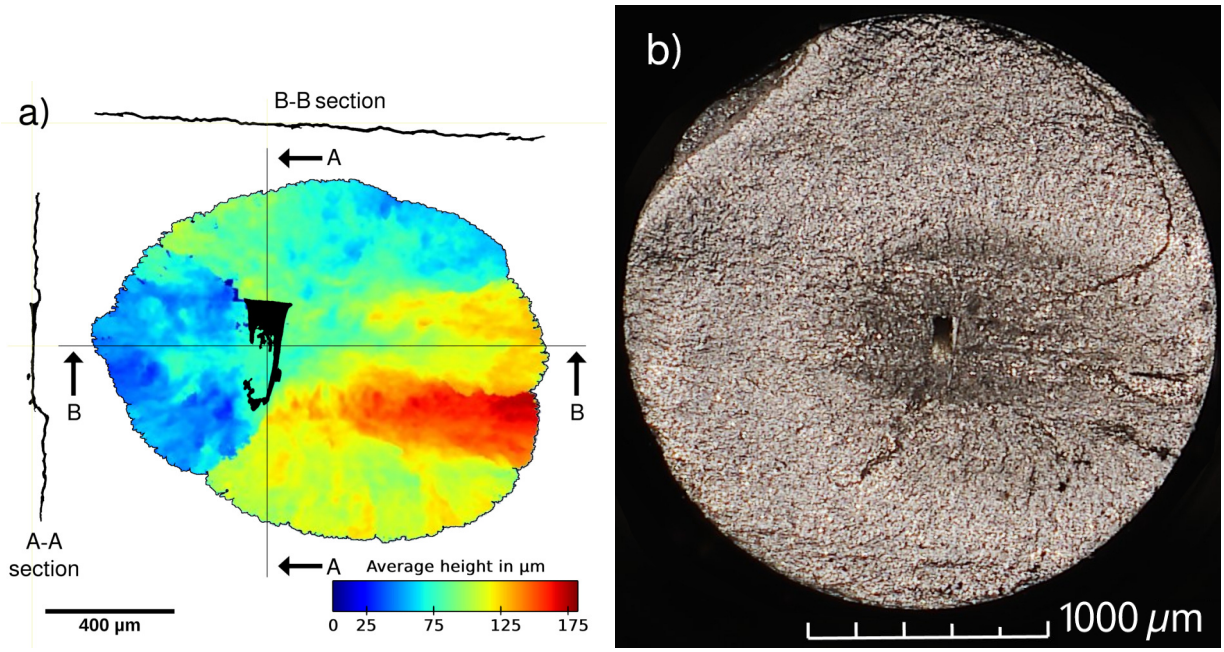

Figure G.2 | Specimen nb 46 has been cycled at 330 MPa during 4.55×10^7 cycles. (a) represents the crack shape 3.8×10^4 cycles before final fracture. It does not contain a chimney.

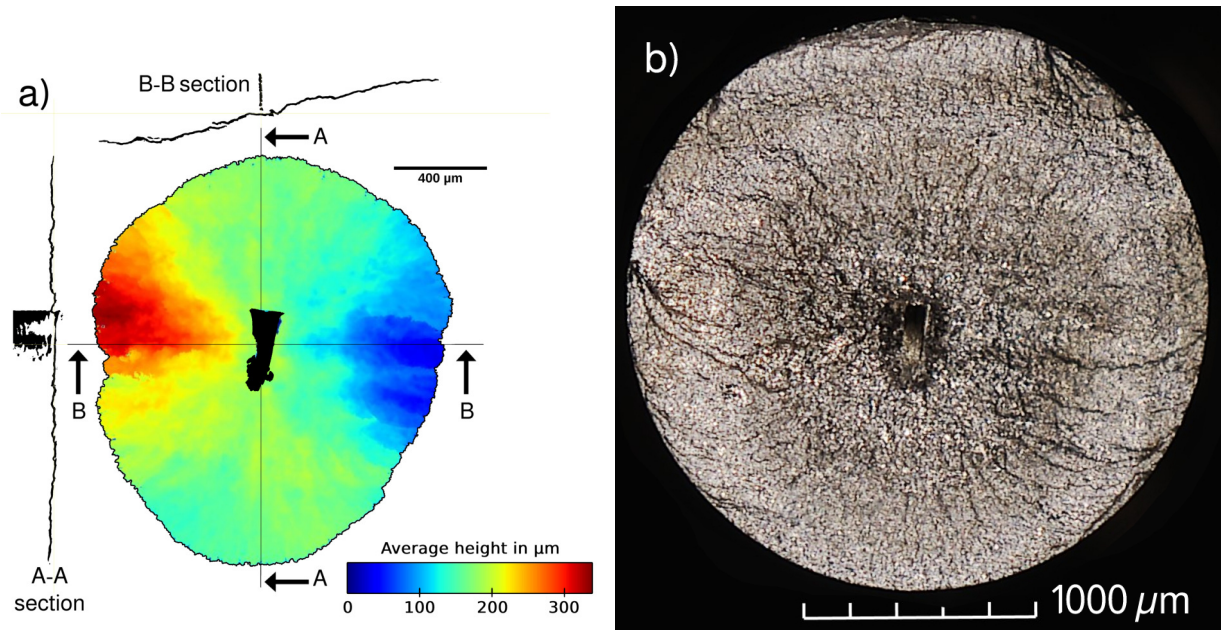

Figure G.3 | Specimen nb 48 has been cycled at 300 MPa during 5.04×10^5 cycles. (a) represents the crack shape 1.3×10^4 cycles before final fracture. It contains a chimney.

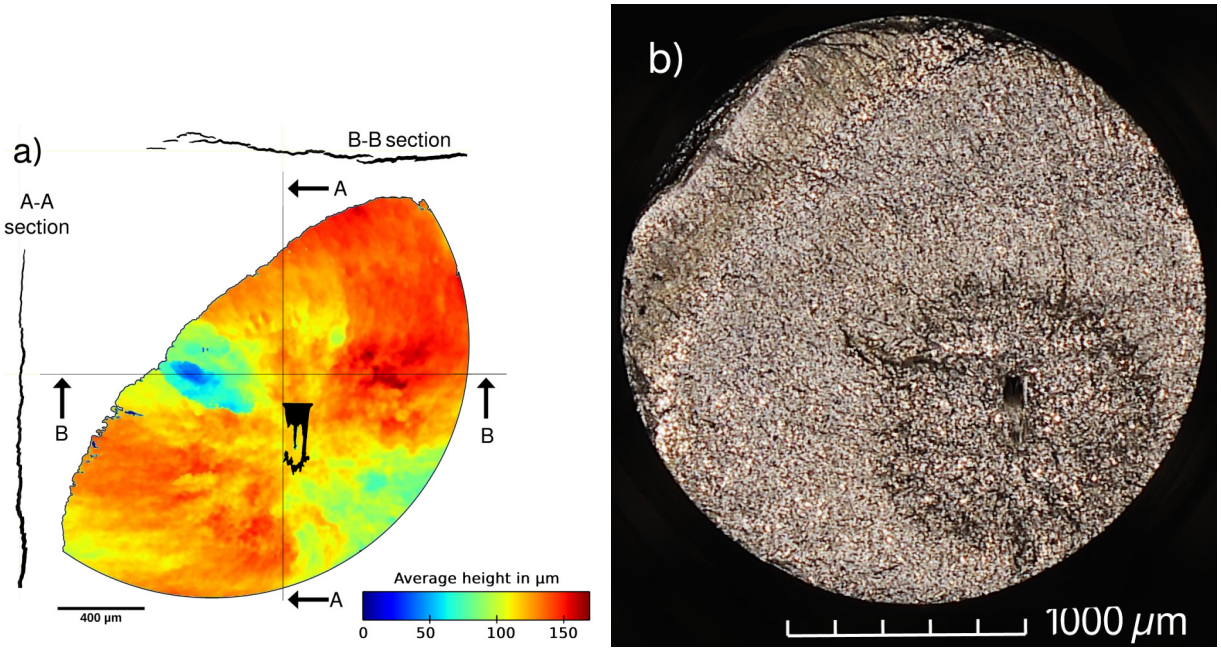

Figure G.4 | Specimen nb 52 has been cycled at 300 MPa during 4.02×10^5 cycles. (a) represents the crack shape 1.1×10^4 cycles before final fracture. It contains a chimney.

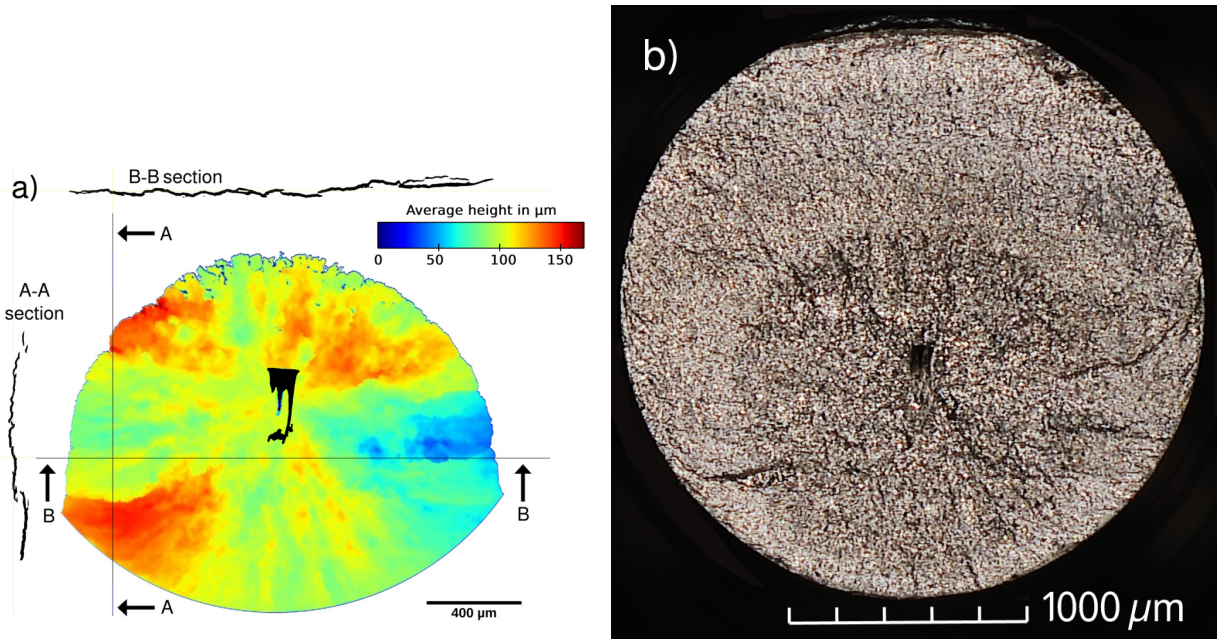

Figure G.5 | Specimen nb 53 has been cycled at 300 MPa during 3.6×10^5 cycles. (a) represents the crack shape 1.1×10^4 cycles before final fracture. It contains a chimney.

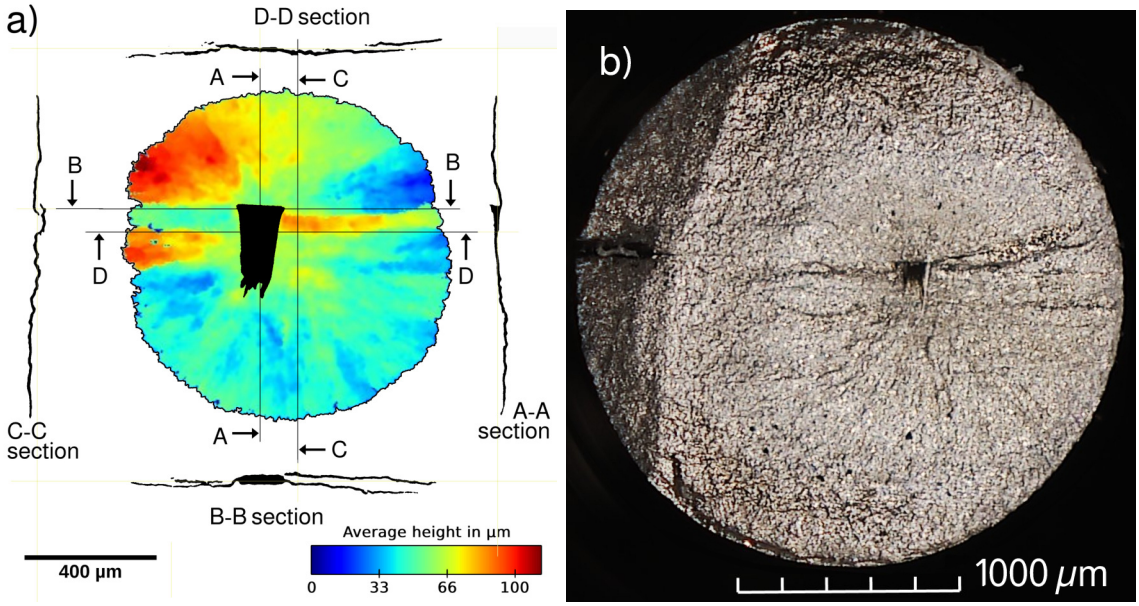

Figure G.6 | Specimen nb 58 has been cycled at 500 MPa during 2.43×10^6 cycles. (a) represents the crack shape before the final fracture which occurred during the static loading (necessary for the tomographic acquisition). It does not contain a chimney.

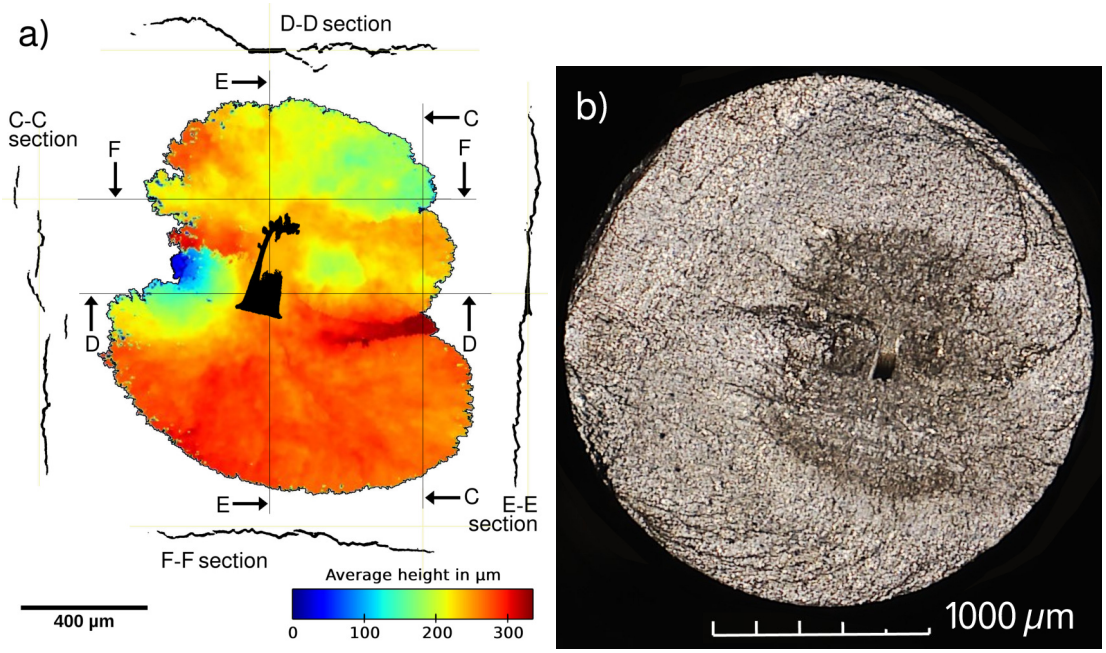

Figure G.7 | Specimen nb 61 has been cycled at 330 MPa during 8.92×10^7 cycles. (a) represents the crack shape 7.0×10^4 cycles before final fracture. It does not contain a chimney.

G.2 Specimens Which Have Not Been Tomographied During the Crack Propagation

The following figures represent only an optical microscopy observation of the fracture surface.

Figure G.8 | Specimen nb 49 has been cycled at 315 MPa during 8.16×10^5 cycles. It contains a chimney.

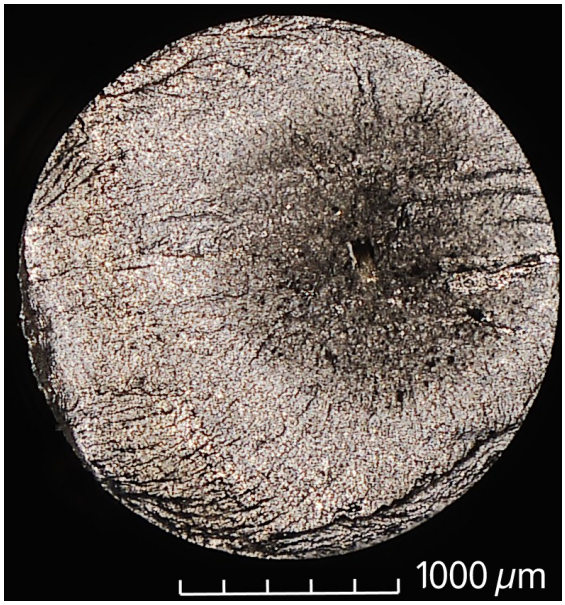

Figure G.9 | Specimen nb 55 has been cycled at 330 MPa during 1.30×10^8 cycles. It does not contain a chimney.

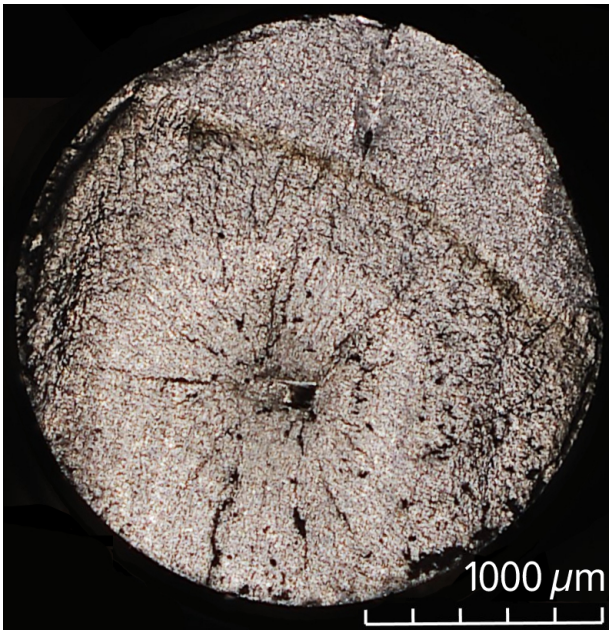

Figure G.10 | Specimen nb 59 has been cycled at 500 MPa during 3.38×10^6 cycles. It does not contain a chimney.

Appendix H

Experimental Conditions of the Ti64 Fatigue Tests from the Literature

This Appendix lists the experimental conditions of the fatigue tests extracted from the literature to be compared with the results from this work (*cf.* Figures 3.1, 3.22, 4.2, 4.20 and 4.22).

Authors & year	Cycling frequency (Hz)	Stress ratio R	Crack initiation	Reference
Berto *et al.* - 2015	15	-1	Natural	[BER 15]
Geathers *et al.* - 2022	20 000	-1	Surf. notches	[GEA 22]
Heinz *et al.* - 2013	20 000	-1	Natural	[HEI 13]
Hines *et al.* - 1999	90	-1	Natural	[HIN 99]
Huang *et al.* - 2014	20 000	-1	Natural	[HUA 14]
Janecek *et al.* - 2015	20 000	-1	Natural	[JAN 15]
Junet *et al.* - 2023	20	0.1	Int. notches	[JUN 23]
Liu *et al.* - 2015	20 000	-1	Natural	[LIU 15]
Oguma *et al.* - 2004	100	-1	Natural	[OGU 04]
Oguma *et al.* - 2013	60	0.1	CT specimens	[OGU 13]
Peters *et al.* - 2001	30	-1	Surf. notches	[PET 01]
Takeushi *et al.* - 2008	120, 600 20 000	-1	Natural Surf. notches	[TAK 08]
Yoshinaka *et al.* - 2016	60	0.1	Surf. notches	[YOS 16b]
Yoshinaka *et al.* - 2019	400	0.1	Natural	[YOS 19]
Zuo *et al.* - 2008	20 000	-1	Natural	[ZUO 08]

Table H.1 | **Fatigue test experimental conditions of the literature results** compared with the data obtained during the present study on Ti64

Appendix I

Hardness Measurements

This Appendix lists the hardness measurements carried out before and after the SPS bonding procedure as presented in Section 3.2.1.1.

Before SPS (HV)	After SPS (HV)
336	338
329	306
327	323
351	300
345	286
336	332
358	307
358	355
359	336
358	319
338	324
	330
	336
	336

Table I.1 | **Hardness measurements before and after the SPS bonding procedure** (HV 500g)

Appendix J

List of Scientific Communication Contributions

This Appendix lists the different communications carried out by Louis Hébrard to present the PhD thesis project and some results:

- **Research paper - 2023** - Environment effect on internal fatigue crack propagation studied with in-situ X-ray microtomography - L. Hébrard, J.Y. Buffiere, T. Palin-Luc, N. Ranc, M. Majkut, A. King, A. Weck - Materials Science and Engineering: A - Vol. 882, 145462 - https://doi.org/10.1016/j.msea.2023.145462
- **International conference - Apr. 4th, 2022** - Presentation (20 min.) at the 11th European Solid Mechanics Conference (Cambridge - United Kingdom): *3D characterization of internal fatigue cracks in Ti-6Al-4V during gigacycle fatigue*
- **International conference - Jul. 5th, 2022** - Presentation (20 min.) at the 18th European Mechanics of Materials Conference (Galway - Ireland): *3D characterization of internal fatigue cracks in metallic material during gigacycle fatigue*
- **National conference - 2023** - Poster at Plasticité 2023 (Lyon - France)
- **International conference - Sept. 4th, 2023** - Presentation (20 min.) at FEMS Euromat 2023 (Frankfurt - Germany): *Observation of the environment effect on internal fatigue crack propagation in Ti-6Al-4V with in-situ X-ray microtomography*
- **Lab seminar - 2022** - Presentation (15 min.) at the Matéis-Métal yearly Team-building seminar
- **Lab seminar - 2022** - Poster at the Matéis yearly PhD student day
- **Lab seminar - 2023** - Presentation (50 min.) at the I2M monthly lab seminar

Nomenclature

α	Non-linearity parameter used in the present study
β	Kumar *et al.*'s non-linearity parameter [KUM 09]
β_{rel}	Relative value of Kumar *et al.*'s non-linearity β parameter [KUM 09]
ΔK	Stress intensity factor range
ΔK^+	Positive part of the SIF range ($= \Delta K_{eq}$ in the study because $R = -1$)
$\Delta K_{average}$	SIF range averaged along the crack tip
ΔK_{eff}	Effective stress intensity factor range taking into account the closure effect
ΔK_{eq}	Equivalent stress intensity factor range (taking all $K_{I,II,III}$ into account)
$\Delta K_{RA/FiE}$	SIF range value at the transition from Rough Area to Fish-Eye region
ΔK_{th}	Threshold value of SIF range for long crack propagation
δ(M)	Dirac function along the crack front
$\Delta\sigma$	Stress range: $\sigma_{max} - \sigma_{min}$
$\dot{\gamma}$	Shear rate
η	Proportionality coefficient between heat source and ΔK^4
$\Gamma(a)$	Dimensionless function depending on the crack length to define the SIF
λ	Thermal conductivity
μ	Shear modulus
ν	Poisson ratio
Ω	Angle between the c-axis of a grain and the loading direction
ψ	Angle around a projected crack (defined in Figure 4.26)
ρ	Volumetric mass
σ	Nominal value of the applied stress
σ_Y	Yield stress
σ_a	Stress amplitude
σ_{max}	Maximum value per cycle of the nominal applied stress

σ_{min}	Minimum value per cycle of the nominal applied stress
τ^s	Resolved shear stress for the slip system s
τ_c^s	Critical resolved shear stress for the deformation mechanism s
θ	Polar position of a M point
φ	Convection heat flux
ϑ^{crack}	Difference in specimen surface temperature increment (due to the presence of a crack)
ϑ_{exp}	Temperature increase: $T_{surf}^{exp} - T_0^{exp}$
$\vec{n_F}$	Normal direction of the studied facet
$\vec{n_m}$	$\vec{c}$ - axis direction of the microstructure of the single grain located under the studied facet
$x_{E\vec{B}SD}$	EBSD detector observation direction
$x_{S\vec{E}M}$	SEM detector observation direction
ζ	Angle between the direction of a twin mark and the crack average surface (defined in Figure 4.10c)
a	Crack radius
a_{curv}	Crack length (used to calculate growth rates in ultrasonic propagation tests - Fig. 2.17b)
a_{eq}	Equivalent crack size
A_i	Area of i grain
a_{proj}	Projected crack length (used to calculate SIF in ultrasonic propagation tests - Fig. 2.17b)
A_{tot}	Total area of an EBSD map
b	Specimen gauge length radius
C	Paris law coefficient
C_p	Heat capacity
C_{air}	Paris law coefficient for a crack propagating in air
C_{vac}	Paris law coefficient for a crack propagating in vacuum
$D(gs)$	Number of voxels having a grayscale equal to gs
$D_{average}$	Average grain size
d_{bot}	Specimen free-end surface displacement amplitude
d_{in}	Self-heating (or intrinsic dissipation) heat source
D_i	Equivalent i grain diameter
da	Crack length increase

E	Elasticity modulus
E_{US}	Elasticity modulus measured in the case of ultrasonic loading
f	Frequency resonance of the ultrasonic specimen
$F(a/W)$	Shape function linking displacement amplitude and SIF for ultrasonic fatigue crack growth specimens
$f_{i,j}^{I,II,III}$	Functions defining the polar stress spatial distribution (resp. for 3 fract. modes)
G	Shear modulus
gs	Grayscale value (8-bits digital level)
gs_{20}	Grayscale threshold value such as $D(gs_{20}) = 0.2\max(D)$
h	Convection coefficient
k	$= \frac{3-\nu}{1+\nu}$ (in the plane stress conditions)
k_1	$= 2\pi f\sqrt{\rho/E_{dyn}}$ (used to design the specimen geometry)
k_2	$= \operatorname{arcosh}(R_2/R_1)/L_1$ (used to design the specimen geometry)
k_3	$= \sqrt{k_2^2 - k_1^2}$ (used to design the specimen geometry)
$K_{I,II,III}$	Stress intensity factors respectivelly for the three fracture modes
K_{op}	Smallest SIF value at which the crack is open
L	Length of the ultrasonic crack growth (CT) specimen
L_1	Length of the ultrasonic specimen part having a section with variable radius
L_2	Length of the ultrasonic specimen head
M	Point in a volume
m	Paris law exponent
m_{air}	Paris law exponent for a crack propagating in air
m_{vac}	Paris law exponent for a crack propagating in vacuum
N	Number of cycles
N_f	Number of cycles to fracture
R	Nominal stress ratio, $\frac{\sigma_{min}}{\sigma_{max}}$
r	Distance between a M point and the crack (*i.e.* its radial distance in a cylindrical coordinate system)
R_0	Radius of the ultrasonic specimen median torus
R_1	Radius of the ultrasonic specimen central section
R_2	Radius of the ultrasonic specimen head
R_a	Ultrasonic line amplification ratio

R_K	Stress intensity factor ratio, $\frac{K_{min}}{K_{max}}$
$r_{p,cycl}$	Reversed cyclic plastic zone radius
$r_{p,mono}$	Monotonic plastic zone radius
s	Curvilinear abscissa
$S(s)$	Lineic heat source originating from the reversed cyclic plastic zone
T_0^{exp}	Initial value of the experimental specimen surface temperature
T_{surf}^{exp}	Experimental value of the specimen surface temperature
U_0	Displacement amplitude
u_x, u_y, u_z	Displacement field around a crack tip
U_{PC}	Computer input vibration displacement amplitude
V_1	Amplitude of the fundamental frequency of the velocity
V_2	Amplitude of the second harmonics of the velocity
V_{ctrl}	Converter power control voltage
W	Thickness of the ultrasonic crack growth (CT) specimen
X,Y, Z	Original material laminated plate directions

Acronyms

μCT micro-Computed Tomography.

AIDE Adsorption-Induced Dislocation Emission.

BCC Body-Centred Cubic.

CGR Crack Growth Rate.
CRSS Critical Resolved Shear Stress.
CT Compact Tension (specimen).
CTOD Crack Tip Openning Displacement.

EBSD Electron Backscatter Diffraction.
EDX Energy-Dispersive X-ray spectroscopy.
ESRF European Synchrotron Radiation Facility.

FE Finite Element.
FEA Finite Element Analysis.
FFT Fast Fourier Transform.
FGA Fine Grain Area.
FIB Focused-Ion Beam.
FiE Fish-Eye.

HCF High Cycle Fatigue.
HCP Hexagonal Close-Packed.
HELP Hydrogen Enhanced Localized Plasticity.

IPF Inverse Pole Figure.

LCF Low Cycle Fatigue.
LEFM Linear Elastic Fracture Mechanics.

NCP Numerous Cyclic Pressing.

OPS Oxide Polishing Suspension.

PMMA Polymethyl methacrylate.

RA Rough Area.

S-N Graphics representing the cyclic stress applied to a specimen represented versus the number of cycles to failure.

SEM Scanning Electron Miscroscope.

SIF Stress Intensity Factor.

SPS Spark Plasma Sintering.

TEM Transmission Electron Miscroscope.

Ti64 Ti-6Al-4V.

TKD Transmission Kikuchi Diffraction.

US Ultrasonic.

VHCF Very High Cycle Fatigue.

Bibliography

[ABB 10] Abbaschian R., Abbaschian L., Reed-Hill R. E. – *Physical metallurgy principles*. Cengage Learning, 4th ed, si édition, 2010. ⟶ cited p. 115, 116

[ASM 04] ASM.Handbook – *Fractography*, vol. 12. ASM International - The Material Information Company, 2004. ⟶ cited p. 23

[AST13] ASTM E647 - Standard Test Method for Measurement of Fatigue Crack Growth Rates. American Society for Testing and Materials, Pennsylvania, USA, 2013. ⟶ cited p. 57, 123

[ATR 83] Atrens A., Hoffelner W., Duerig T. W., Allison J. E. – Subsurface crack initiation in high cycle fatigue in Ti-6Al-4V and in a typical martensitic stainless steel. *Scripta Metallurgica*, vol. 17, n° 5, 1983, p. 601-606. ⟶ cited p. 8, 23

[BAC 03] Bache M. – A review of dwell sensitive fatigue in titanium alloys: the role of microstructure, texture and operating conditions. *International Journal of Fatigue*, vol. 25, n° 9-11, 2003, p. 1079–1087. ⟶ cited p. 18, 130

[BAN 78] Bania P. J., Eylon D. – Fatigue crack propagation of titanium alloys under dwell-time conditions. *Metallurgical Transactions A*, vol. 9, n° 6, 1978, p. 847–855. ⟶ cited p. 18, 130

[BAN 07] Banerjee S., Mukhopadhyay P. – *Phase Transformations: Examples from Titanium and Zirconium Alloys*. Pergamon, 2007. ⟶ cited p. 135

[BAR 23] Barr C. M., Duong T., Bufford D. C., Milne Z., Molkeri A., Heckman N. M., Adams D. P., Srivastava A., Hattar K., Demkowicz M. J., Boyce B. L. – Autonomous healing of fatigue cracks via cold welding. *Nature*, vol. 620, n° 7974, 2023, p. 552–556. ⟶ cited p. 20, 96

[BAT 99] Bathias C. – There is no infinite fatigue life in metallic materials. *Fatigue & Fracture of Engineering Materials & Structures*, vol. 22, n° 7, 1999, p. 559–565. ⟶ cited p. 1, 7, 33

[BAT 05] Bathias C., Paris P. C. – *Gigacycle Fatigue in Mechanical Practice*. Marcel Dekker Ed. New-York, USA, 2005. ⟶ cited p. 7, 9, 58, 155

[BAT 10] Bathias Claude; Pineau A. – *Fatigue of Materials and Structures - Fundamentals*. John Wiley & Sons, 2010. ⟶ cited p. 7, 8, 15

[BEA 20] BEA A. C. – Accident to the AIRBUS A380-861 equipped with Engine Alliance GP7270 engines registered F-HPJE operated by Air France on 30 September 2017 in cruise over Greenland (Denmark). rapport, 2020. ⟶ cited p. 1, 2, 141

[BER 15] Berto F., Campagnolo A., Lazzarin P. – Fatigue strength of severely notched specimens made of Ti-6Al-4V under multiaxial loading. *Fatigue & Fracture of Engineering Materials & Structures*, vol. 38, n° 5, 2015, p. 503–517. ⟶ cited p. 77, 171

[BIL 65] Bilby B., Crocker A. – The theory of the crystallography of deformation twinning. *Proceedings of the Royal Society of London. Series A. Mathematical and Physical Sciences*, vol. 288, n° 1413, 1965, p. 240–255. ⟶ cited p. 120

[BIR 71] Birkbeck G., Inckle A., Woldron G. – Aspects of Stage II fatigue crack propagation in low-carbon steel. *Journal of Materials Science*, vol. 6, 1971, p. 319-323. ⟶ cited p. 24

[BON 12] Bonakdar A., Wang F., Williams J. J., Chawla N. – Environmental Effects on Fatigue Crack Growth in 7075 Aluminum Alloy. *Metallurgical and Materials Transactions A*, vol. 43, n° 8, 2012, p. 2799–2809. ⟶ cited p. 18, 20

[BOY 01] Boyce B. L., Ritchie R. O. – Effect of load ratio and maximum stress intensity on the fatigue threshold in Ti-6Al-4V. *Engineering Fracture Mechanics*, , 2001, Page 19. ⟶ cited p. 18, 126

[BRI 09] Bridier F., McDowell D. L., Villechaise P., Mendez J. – Crystal plasticity modeling of slip activity in Ti–6Al–4V under high cycle fatigue loading. *International Journal of Plasticity*, vol. 25, n° 6, 2009, p. 1066–1082. ⟶ cited p. 121

[BRI 15] Britton T. B., Dunne F. P. E., Wilkinson A. J. – On the mechanistic basis of deformation at the microscale in hexagonal close-packed metals. *Proceedings of the Royal Society A: Mathematical, Physical and Engineering Sciences*, vol. 471, n° 2178, 2015, Page 20140881. ⟶ cited p. 122

[BUE23] Titanium polishing protocol from Buehler. https://www.buehler.com/assets/solutions/methods-by-material/8_summet_refractory%20metals.pdf, consulted Jun. 1st 2023. ⟶ cited p. 60, 61

[BUF 06] Buffiere J. Y., Ferrie E., Proudhon H., Ludwig W. – Three-dimensional visualisation of fatigue cracks in metals using high resolution synchrotron X-ray micro-tomography. *Materials Science and Technology*, vol. 22, n° 9, 2006, p. 1019–1024. ⟶ cited p. 32

[BUL 10] Bulloch J., Callagy A. – A detailed study of the relationship between fatigue crack growth rate and striation spacing in a range of low alloy ferritic steels. *Engineering Failure Analysis*, vol. 17, n° 1, 2010, p. 168–178. ⟶ cited p. 26

[CAL 20] Callegari B., Oliveira J., Aristizabal K., Coelho R., Brito P., Wu L., Schell N., Soldera F., Mücklich F., Pinto H. – In-situ synchrotron radiation study of the aging response of Ti-6Al-4V alloy with different starting microstructures. *Materials Characterization*, vol. 165, 2020, Page 110400. ⟶ cited p. 41

[CAM 06] Campos-Pozuelo C., Vanhille C., Gallego-Juarez J. – Comparative study of the nonlinear behavior of fatigued and intact samples of metallic alloys. *IEEE Transactions on Ultrasonics, Ferroelectrics and Frequency Control*, vol. 53, n° 1, 2006, p. 175–184. ⟶ cited p. 29

[CAO 17] Cao F., Ravi Chandran K. – The role of crack origin size and early stage crack growth on high cycle fatigue of powder metallurgy Ti-6Al-4V alloy. *International Journal of Fatigue*, vol. 102, 2017, p. 48–58. ⟶ cited p. 8, 127

[CAS 21] Castioni F., Cazottes S., Rollett A. D., Dancette S. – Plastic behavior of the α' phase in Ti-6Al-4V alloys. *Materials Letters*, vol. 283, 2021, Page 128719. ⟶ cited p. 9, 121

[CAT 12] Caton M., John R., Porter W., Burba M. – Stress ratio effects on small fatigue crack growth in Ti–6Al–4V. *International Journal of Fatigue*, vol. 38, 2012, p. 36–45. ⟶ cited p. 26

[CHA 97] Chati M., Rand R., Mukherjee S. – Modal analysis of a cracked beam. *Journal of Sound and Vibration*, vol. 207, n° 2, 1997, p. 249–270. ⟶ cited p. 155

[CHA 10] Chan K. S. – Roles of microstructure in fatigue crack initiation. *International Journal of Fatigue*, vol. 32, n° 9, 2010, p. 1428–1447. ⟶ cited p. 12

[CHA 15] Chapman T., Kareh K., Knop M., Connolley T., Lee P., Azeem M., Rugg D., Lindley T., Dye D. – Characterisation of short fatigue cracks in titanium alloy IMI 834 using X-ray microtomography. *Acta Materialia*, vol. 99, 2015, p. 49–62. ⟶ cited p. 2, 18, 32, 103, 141

[CHA 20] Chang Y., Pan X., Zheng L., Hong Y. – Microstructure refinement and grain size distribution in crack initiation region of very-high-cycle fatigue regime for high-strength alloys. *International Journal of Fatigue*, vol. 134, 2020, Page 105473. ⟶ cited p. 24

[CHI 23] Chi W., Wang W., Wu L., Duan G., Sun C. – Nanograin formation mechanism under fatigue loadings in additively manufactured Ti-6Al-4V alloy. *International Journal of Fatigue*, vol. 175, 2023, Page 107821. ⟶ cited p. 117, 121, 122

[CLO 97] Cloetens P., Pateyron-Salomé M., Buffière J. Y., Peix G., Baruchel J., Peyrin F., Schlenker M. – Observation of microstructure and damage in materials by phase sensitive radiography and tomography. *Journal of Applied Physics*, vol. 81, n° 9, 1997, p. 5878–5886. ⟶ cited p. 32

[DAV 03] Davidson D., Chan K., McCLUNG R., Hudak S. – 4.05 Small Fatigue Cracks. *Small Fatigue Cracks*, vol. 4, 2003, p. 129–164. ⟶ cited p. 11, 17

[DUQ 71] Duquette D. J., Gell M. – The effect of environment on the mechanism of Stage I fatigue fracture. *Metallurgical Transactions*, vol. 2, n° 5, 1971, p. 1325–1331. ⟶ cited p. 20

[ENG 07] Engler-Pinto C. C., Frisch R. J., Lasecki J. V., Mayer H., Allison J. E. – Effect of frequency and environment on high cycle fatigue of cast aluminum alloys. *Fourth International Conference on Very High Cycle Fatigue (VHCF-4)*, , 2007. ⟶ cited p. 21

[EVE 16] Everaerts J., Verlinden B., Wevers M. – Internal fatigue crack initiation in drawn Ti–6Al–4V wires. *Materials Science and Technology*, vol. 32, n° 16, 2016, p. 1639–1645. ⟶ cited p. 8

[EVE 17a] Everaerts J. – Fatigue crack initiation and facet formation in Ti-6Al-4V wires. PhD thesis, KU Leuven, Belgium, 2017. ⟶ cited p. 23

[EVE 17b] Everaerts J., Verlinden B., Wevers M. – Investigation of fatigue crack initiation facets in Ti-6Al-4V using focused ion beam milling and electron backscatter diffraction: Investigation of crack initiation facets. *Journal of Microscopy*, vol. 267, n° 1, 2017, p. 57–69. ⟶ cited p. 86

[FAT23] History of Fatigue. https://community.sw.siemens.com/s/article/history-of-fatigue, consulted Aug. 14th 2023. ⟶ cited p. 6

[FIB23] Focused Ion Beam Principle. https://www.jeol.com/words/emterms/20121023.042959.php, accessed: 12.09.2023. ⟶ cited p. 89

[FIT 14] Fitzka M., Mayer H., Schuller R., Stanzl-Tschegg S. E., Przeorski T., Krug P. – Variable amplitude loading of spray-formed hypereutectic aluminium silicon alloy DISPAL® S232 in the VHCF regime: Variable amplitude loading of DISPAL® S232. *Fa-*

tigue & Fracture of Engineering Materials & Structures, vol. 37, n° 9, 2014, p. 945–957. ⟶ cited p. 29

[FRO 99a] Frouin J., Matikas T. E., Na J. K., Sathish S. – In-Situ Monitoring of Acoustic Linear and Nonlinear Behavior of Titanium Alloys during Cycling Loading. *SPIE Conference on Nondestructive Evaluation of aging Materials and Composites III*, , 1999. ⟶ cited p. 29

[FRO 99b] Frouin J., Sathish S., Matikas T. E., Na J. K. – Ultrasonic Linear and Nonlinear Behavior of Fatigued Ti–6Al–4V. *Journal of Materials Research*, vol. 14, n° 4, 1999, p. 1295–1298. ⟶ cited p. 29

[FU 22] Fu R., Zheng L., Ling C., Zhong Z., Hong Y. – An experimental investigation of fatigue performance and crack initiation characteristics for an SLMed Ti-6Al-4V under different stress ratios up to very-high-cycle regime. *International Journal of Fatigue*, vol. 164, 2022, Page 107119. ⟶ cited p. 9, 24

[FUR 14] Furuya Y., Takeuchi E. – Gigacycle fatigue properties of Ti–6Al–4V alloy under tensile mean stress. *Materials Science and Engineering: A*, vol. 598, 2014, p. 135–140. ⟶ cited p. 23

[GAO 88] Gao M., Wei R. P., Pao P. S. – Chemical and metallurgical aspects of environmentally assisted fatigue crack growth in 7075-T651 aluminum alloy. *Metallurgical Transactions A*, vol. 19, n° 7, 1988, p. 1739–1750. ⟶ cited p. 126

[GEA 15] Geathers J., Torbet C., Jones J., Daly S. – Investigating environmental effects on small fatigue crack growth in Ti–6242S using combined ultrasonic fatigue and scanning electron microscopy. *International Journal of Fatigue*, vol. 70, 2015, p. 154–162. ⟶ cited p. 18, 23, 122

[GEA 22] Geathers J., Torbet C., Jones J., Daly S. – Examining the role of water vapor on small fatigue crack growth behavior in Ti-6242S using ultrasonic fatigue and scanning electron microscopy. *International Journal of Fatigue*, vol. 156, 2022, Page 106672. ⟶ cited p. 9, 21, 99, 100, 122, 124, 125, 171

[GRI 82] Grinberg N. – The effect of vacuum on fatigue crack growth. *International Journal of Fatigue*, vol. 4, n° 2, 1982, p. 83–95. ⟶ cited p. 17, 18, 20, 25, 26

[HEB 23] Hebrard L., Buffiere J.-Y., Palin-Luc T., Ranc N., Majkut M., King A., Weck A. – Environment effect on internal fatigue crack propagation studied with in-situ X-ray microtomography. *Materials Science and Engineering: A*, vol. 882, 2023, Page 145462. ⟶ cited p. 142

[HEI 13] Heinz S. – Analysis of fatigue properties and failure mechanisms of Ti6Al4V in the very high cycle fatigue regime using ultrasonic technology and 3D laser scanning vibrometry. *Ultrasonics*, , n° 53, 2013, p. 1433-1440. ⟶ cited p. 9, 12, 77, 171

[HEI 16] Heinz S., Eifler D. – Crack initiation mechanisms of Ti6Al4V in the very high cycle fatigue regime. *International Journal of Fatigue*, vol. 93, 2016, p. 301–308. ⟶ cited p. 127

[HEN 95] Henaff G., Marchal K., Petit J. – On fatigue crack propagation enhancement by a gaseous atmosphere: Experimental and theoretical aspects. *Acta Metallurgica et Materialia*, vol. 43, n° 8, 1995, p. 2931–2942. ⟶ cited p. 18, 19, 20

[HEN 07] Henaff G., Odemer G., Tonneaumorel A. – Environmentally-assisted fatigue crack growth mechanisms in advanced materials for aerospace applications. *International Journal of Fatigue*, vol. 29, n° 9-11, 2007, p. 1927–1940. ⟶ cited p. 20

[HEN 23] Henaff G., Sarrazin-Baudoux C. – Environmentally Assisted Fatigue in the Gaseous Atmosphere. *Comprehensive Structural Integrity*, p. 45–130 Elsevier, 2023. ⟶ cited p. 2, 18, 19, 20, 33

[HIN 99] Hines J. A., Lutjering G. – Propagation of microcracks at stress amplitudes below the conventional fatigue limit in Ti-6Al-4V. *Fatigue and Fracture of Engineering Materials and Structures*, vol. 22, n° 8, 1999, p. 657–665. ⟶ cited p. 124, 125, 126, 171

[HOL 03] Holper B., Mayer H., Vasudevan A., Stanzl-Tschegg S. – Near threshold fatigue crack growth in aluminium alloys at low and ultrasonic frequency: Influences of specimen thickness, strain rate, slip behaviour and air humidity. *International Journal of Fatigue*, vol. 25, n° 5, 2003, p. 397–411. ⟶ cited p. 9, 21, 22, 33, 126, 142

[HON 14] Hong Y., Lei Z., Sun C., Zhao A. – Propensities of crack interior initiation and early growth for very-high-cycle fatigue of high strength steels. *International Journal of Fatigue*, vol. 58, 2014, p. 144–151. ⟶ cited p. 80

[HON 16] Hong Y., Liu X., Lei Z., Sun C. – The formation mechanism of characteristic region at crack initiation for very-high-cycle fatigue of high-strength steels. *International Journal of Fatigue*, vol. 89, 2016, p. 108–118. ⟶ cited p. 96

[HON 17] Hong Y., Sun C. – The nature and the mechanism of crack initiation and early growth for very-high-cycle fatigue of metallic materials – An overview. *Theoretical and Applied Fracture Mechanics*, vol. 92, 2017, p. 331–350. ⟶ cited p. 12, 24, 33, 85, 89, 96, 127

[HUA 14] Huang Z. Y., Wang Q. Y., Wagner D., Bathias C. – A very high cycle fatigue thermal dissipation investigation for titanium alloy TC4. *Materials Science and Engineering: A*, vol. 600, 2014, p. 153–158. ⟶ cited p. 9, 28, 76, 77, 171

[HUA 15] Huang Z. Y., Liu H. Q., Wang C., Wang Q. Y. – Fatigue life dispersion and thermal dissipation investigations for titanium alloy TC17 in very high cycle regime: VHCF Scatter for TC17. *Fatigue & Fracture of Engineering Materials & Structures*, vol. 38, n° 11, 2015, p. 1285–1293. ⟶ cited p. 28

[HUD 76] Hudson C., Seward S. K. – A literature review and inventory of the effects of environment on the fatigue behavior of metals. *Engineering Fracture Mechanics*, vol. 8, n° 2, 1976, p. 315–329. ⟶ cited p. 18, 20

[IRW 48] Irwin G. R. – *Fracture Dynamics, Fracturing of Metals*. American Society for Metals, 1948. ⟶ cited p. 66

[IRW 58] Irwin G. R. – *Fracture*. In Handbuch der Physik, page 551. Springer-Verlag, Berlin/ Heidelberg, 1958. ⟶ cited p. 12, 14

[IST 14] Istomin K., Dönges B., Schell N., Christ H.-J., Pietsch U. – Analysis of VHCF damage in a duplex stainless steel using hard X-ray diffraction techniques. *International Journal of Fatigue*, vol. 66, 2014, Page 177–182. ⟶ cited p. 31

[JAN 15] Janeček M., Nový F., Harcuba P., Stráský J., Trško L., Mhaede M., Wagner L. – The Very High Cycle Fatigue Behaviour of Ti-6Al-4V Alloy. *Acta Physica Polonica A*, vol. 128, n° 4, 2015, p. 497–503. ⟶ cited p. 77, 171

[JHA 99] Jhang K.-Y., Kim K.-C. – Evaluation of material degradation using nonlinear acoustic effect. *Ultrasonics*, vol. 37, n° 1, 1999, p. 39-44. ⟶ cited p. 29

[JHA 09] Jhang K.-Y. – Nonlinear ultrasonic techniques for nondestructive assessment of micro damage in material: A review. *International Journal of Precision Engineering and Manufacturing*, vol. 10, n° 1, 2009, p. 123–135. ⟶ cited p. 29

[JHA 12] Jha S. K., Szczepanski C. J., Golden P. J., Porter W. J., John R. – Characterization of fatigue crack-initiation facets in relation to lifetime variability in Ti–6Al–4V. *International Journal of Fatigue*, vol. 42, 2012, p. 248–257. ⟶ cited p. 86

[JIA 16] Jiang Q., Sun C., Liu X., Hong Y. – Very-high-cycle fatigue behavior of a structural steel with and without induced surface defects. *International Journal of Fatigue*, vol. 93, 2016, p. 352–362. ⟶ cited p. 24

[JUN 19] Junet A., Messager A., Boulnat X., Weck A., Boller E., Helfen L., Buffiere J.-Y. – Fabrication of artificial defects to study internal fatigue crack propagation in metals. *Scripta Materialia*, vol. 171, 2019, p. 87–91. ⟶ cited p. 32, 39, 59, 61, 78, 79, 82, 103, 128, 141

[JUN 21] Junet A. – Étude tridimensionnelle de la propagation en fatigue de fissures internes dans les matériaux métalliques. PhD thesis, Université de Lyon, France, 2021. ⟶ cited p. 3, 18, 23, 24, 38, 62, 81, 86, 96, 105, 107, 130

[JUN 23] Junet A., Messager A., Weck A., Nadot Y., Boulnat X., Buffiere J.-Y. – Internal fatigue crack propagation in a Ti-6Al-4V alloy: An in situ study. *International Journal of Fatigue*, vol. 168, 2023, Page 107450. ⟶ cited p. 2, 59, 62, 99, 100, 101, 123, 127, 129, 171

[KIK 65] Kikukawa M., Ohji K., Ogura K. – Push-Pull Fatigue Strenght of Mild Steel at Very High Frequencies of Stress Up to 100 kc/s. *Journal of Basic Engineering - Transactions of the AS M E*, , 1965, p. 857–864. ⟶ cited p. 21

[KLI 03] Klingbeil N. – A total dissipated energy theory of fatigue crack growth in ductile solids. *International Journal of Fatigue*, vol. 25, n° 2, 2003, p. 117–128. ⟶ cited p. 27, 134

[KLI 13] Klinger C., Bettge D. – Axle fracture of an ICE3 high speed train. *Engineering Failure Analysis*, vol. 35, 2013, p. 66–81. ⟶ cited p. 1, 2, 141

[KRE 13] Krewerth D., Weidner A., Biermann H. – Application of in situ thermography for evaluating the high-cycle and very high-cycle fatigue behaviour of cast aluminium alloy AlSi7Mg (T6). *Ultrasonics*, vol. 53, n° 8, 2013, p. 1441–1449. ⟶ cited p. 2, 27, 28, 142

[KRU 07] Krupp U. – *Fatigue crack propagation in metals and alloys: microstructural aspects and modelling concepts*. Wiley-VCH, Weinheim, 2007. ⟶ cited p. 13, 14, 15

[KUM 09] Kumar A., Torbet C. J., Jones J. W., Pollock T. M. – Nonlinear ultrasonics for *in situ* damage detection during high frequency fatigue. *Journal of Applied Physics*, vol. 106, n° 2, 2009, Page 024904. ⟶ cited p. 2, 29, 30, 34, 45, 141, 177

[LAN 85] Lankford J. – The influence of microstructure on the growth of small fatigue cracks. *Fatigue & Fracture of Engineering Materials and Structures*, vol. 8, n° 2, 1985, p. 161–175. ⟶ cited p. 15, 16

[LAV 18a] Lavogiez C., Hémery S., Villechaise P. – Concurrent operation of ⟨c + a⟩ slip and twinning under cyclic loading of Ti-6Al-4V. *Scripta Materialia*, vol. 157, 2018, p. 30–33. ⟶ cited p. 115, 116, 117

[LAV 18b] Lavogiez C., Dancette S., Cazottes S., Le Bourlot C., Maire E. – In situ analysis of plasticity and damage nucleation in a Ti-6Al-4V alloy and laser weld. , 2018. ⟶ cited p. 121

[LAV 20] Lavogiez C., Hémery S., Villechaise P. – Analysis of deformation mechanisms operating under fatigue and dwell-fatigue loadings in an α/β titanium alloy. *International Journal of Fatigue*, vol. 131, 2020, Page 105341. ⟶ cited p. 18

[LEB 00] Le Biavant-Guerrier K. – Etude de l'amorçage de fissures de fatigue dans le Ti-6Al-4V. PhD thesis, Ecole Centrale Paris, France, 2000. ⟶ cited p. 11

[LEC 00] Lecomte J.-S. – Étude de la plasticité de l'alliage Ta6v entre 25° et 800°. PhD thesis, 2000. ⟶ cited p. 10

[LEN 00] Lenets Y. – Crack propagation life prediction for Ti-6Al-4V based on striation spacing measurements. *International Journal of Fatigue*, vol. 22, n° 6, 2000, p. 521–529. ⟶ cited p. 26

[LEY 03] Leyens C., Peters M. – *Titanium and Titanium Alloys: Fundamentals and Applications*. Wiley-VCH Verlag GmbH and Co. KGaA, 2003. ⟶ cited p. 9

[LI 12] Li S. X. – Effects of inclusions on very high cycle fatigue properties of high strength steels. *International Materials Reviews*, vol. 57, n° 2, 2012, Page 23. ⟶ cited p. 24

[LI 17] Li W., Zhao H., Nehila A., Zhang Z., Sakai T. – Very high cycle fatigue of TC4 titanium alloy under variable stress ratio: Failure mechanism and life prediction. *International Journal of Fatigue*, vol. 104, 2017, p. 342–354. ⟶ cited p. 127

[LIA 19] Liang X., Dodge M., Jiang J., Dong H. – Using transmission Kikuchi diffraction in a scanning electron microscope to quantify geometrically necessary dislocation density at the nanoscale. *Ultramicroscopy*, vol. 197, 2019, p. 39–45. ⟶ cited p. 92

[LIU 08] Liu L., Husseini N. S., Torbet C. J., Kumah D. P., Clarke R., Pollock T. M., Jones J. W. – In Situ Imaging of High Cycle Fatigue Crack Growth in Single Crystal Nickel-Base Superalloys by Synchrotron X-Radiation. *Journal of Engineering Materials and Technology*, vol. 130, n° 2, 2008. 021008. ⟶ cited p. 31

[LIU 11] Liu L., Husseini N., Torbet C., Lee W.-K., Clarke R., Jones J., Pollock T. – In situ synchrotron X-ray imaging of high-cycle fatigue crack propagation in single-crystal nickel-base alloys. *Acta Materialia*, vol. 59, n° 13, 2011, p. 5103–5115. ⟶ cited p. 2, 31

[LIU 15] Liu X., Sun C., Hong Y. – Effects of stress ratio on high-cycle and very-high-cycle fatigue behavior of a Ti–6Al–4V alloy. *Materials Science and Engineering: A*, vol. 622, 2015, p. 228–235. ⟶ cited p. 18, 23, 24, 77, 85, 171

[LIU 16] Liu X., Sun C., Hong Y. – Faceted crack initiation characteristics for high-cycle and very-high-cycle fatigue of a titanium alloy under different stress ratios. *International Journal of Fatigue*, vol. 92, 2016, p. 434–441. ⟶ cited p. 9

[LUN 14] Lunt D. – A thesis submitted to The University of Manchester for the degree of Doctor of Philosophy in the Faculty of Engineering and Physical Sciences. PhD thesis, The University of Manchester, United Kingdom, 2014. ⟶ cited p. 11, 39

[LUO 18] Luo Y., Wu S. C., Hu Y. N., Fu Y. N. – Cracking evolution behaviors of lightweight materials based on in situ synchrotron X-ray tomography: A review. *Frontiers of Mechanical Engineering*, vol. 13, n° 4, 2018, p. 461–481. ⟶ cited p. 31, 32, 141

[LUT 98] Lutjering G. – Influence of processing on microstructure and mechanical properties of $(\alpha + \beta)$ titanium alloys. *Materials Science and Engineering A*, vol. 243, 1998, p. 32–45. ⟶ cited p. 11

[LUT 07] Lutjering G., Williams J. C. – *Titanium*. Springer, 2007. ⟶ cited p. 9, 10

[LYN 88] Lynch S. – Environmentally assisted cracking: Overview of evidence for an adsorption-induced localised-slip process. *Acta Metallurgica*, vol. 36, n° 10, 1988, p. 2639–2661. ⟶ cited p. 20

[MA 17a] Ma X., Li F., Cao J., Li J., Chen H., Zhao C. – Vickers microhardness and microstructure relationship of Ti-6Al-4V alloy under cyclic forward-reverse torsion and monotonic torsion loading. *Materials & Design*, vol. 114, 2017, p. 271–281. ⟶ cited p. 41

[MA 17b] Ma Y., Xue Q., Wang H., Huang S., Qiu J., Feng X., Lei J., Yang R. – Deformation twinning in fatigue crack tip plastic zone of Ti-6Al-4V alloy with Widmanstatten microstructure. *Materials Characterization*, vol. 132, 2017, p. 338–347. ⟶ cited p. 117, 121

[MAT 15] Matlack K. H., Kim J.-Y., Jacobs L. J., Qu J. – Review of Second Harmonic Generation Measurement Techniques for Material State Determination in Metals. *Journal of Nondestructive Evaluation*, vol. 34, n° 1, 2015, Page 273. ⟶ cited p. 29

[MAY 13] Mayer H., Fitzka M., Schuller R. – Constant and variable amplitude ultrasonic fatigue of 2024-T351 aluminium alloy at different load ratios. *Ultrasonics*, vol. 53, n° 8, 2013, p. 1425-1432. Ultrasonic Fatigue of Advanced Materials. ⟶ cited p. 29

[MAY 15] Mayer H. – Recent developments in ultrasonic fatigue. *Fatigue & Fracture of Engineering Materials & Structures*, , 2015. ⟶ cited p. 8, 9, 18, 21, 23, 29, 126

[MCC 91] McClung R. C. – Crack closure and plastic zone sizes in fatigue. *Fatigue & Fracture of Engineering Materials and Structures*, vol. 14, n° 4, 1991, p. 455–468. ⟶ cited p. 114

[MCD 10] McDowell D., Dunne F. – Microstructure-sensitive computational modeling of fatigue crack formation. *International Journal of Fatigue*, vol. 32, n° 9, 2010, p. 1521–1542. ⟶ cited p. 80

[MCE 08] McEvily A., Nakamura T., Oguma H., Yamashita K., Matsunaga H., Endo M. – On the mechanism of very high cycle fatigue in Ti–6Al–4V. *Scripta Materialia*, vol. 59, n° 11, 2008, p. 1207–1209. ⟶ cited p. 85

[MES 19] Messager A., Junet A., Palin-Luc T., Buffiere J.-Y., Saintier N., Ranc N., May M. E., Gaillard Y., King A., Bonnin A., Nadot Y. – In situ synchrotron ultrasonic fatigue testing device for 3D characterisation of internal crack initiation and growth. *Fatigue Fract Eng Mater Struct. 2019*, , 2019. ⟶ cited p. 2, 30, 31, 32, 141

[MES 20] Messager A. – Étude de l'amorçage et de la propagation de fissures de fatigue internes courtes en régime gigacyclique dans un alliage d'aluminium de fonderie. PhD thesis, École Nationale Supérieure d'Arts et Métiers, France, 2020. ⟶ cited p. 3, 27, 29, 38, 41, 50, 51, 52, 55, 57, 70, 81, 83, 84, 142, 157

[MOR 05] Morrissey R., Nicholas T. – Fatigue strength of Ti–6Al–4V at very long lives. *International Journal of Fatigue*, vol. 27, n° 10-12, 2005, p. 1608–1612. ⟶ cited p. 23

[MUG 02] Mughrabi H. – On 'multi-stage' fatigue life diagrams and the relevant life-controlling mechanisms in ultrahigh-cycle fatigue: On 'multi-stage' fatigue life diagrams. *Fatigue & Fracture of Engineering Materials & Structures*, vol. 25, n° 8-9, 2002, p. 755–764. ⟶ cited p. 6, 7

[MUG 06] Mughrabi H. – Specific features and mechanisms of fatigue in the ultrahigh-cycle regime. *International Journal of Fatigue*, vol. 28, n° 11, 2006, p. 1501–1508. ⟶ cited p. 6

[MUN 97] Munroe N., Tan X., Gu H. – Orientation dependence of slip and twinning in HCP metals. *Scripta Materialia*, vol. 36, n° 12, 1997, p. 1383–1386. ⟶ cited p. 115, 117

[MUR 00] Murakami Y., Nomoto T., Ueda T., Murakami Y. – On the mechanism of fatigue failure in the superlong life regime (N $>10^7$ cycles). Part I: influence of hydrogen trapped by inclusions. , 2000. ⟶ cited p. 24

[NAK 16] Nakamura T., Yoshinaka F., Nakayama S., Oguma H., Shiozawa D., Nakai Y., Uesugi K. – Detection of small internal fatigue cracks in Ti-6Al-4V by using synchrotron radiation µCT imaging. *Mechanical Engineering Letters*, vol. 2, n° 0, 2016, p. 16–00233–16–00233. ⟶ cited p. 32, 42

[NAR 17] Naragani D., Sangid M. D., Shade P. A., Schuren J. C., Sharma H., Park J.-S., Kenesei P., Bernier J. V., Turner T. J., Parr I. – Investigation of fatigue crack initiation from a non-metallic inclusion via high energy x-ray diffraction microscopy. *Acta Materialia*, vol. 137, 2017, p. 71–84. ⟶ cited p. 32

[NEA 75] Neal D. F., Blenkinsop P. A. – Internal fatigue origins in $\alpha - \beta$ titanium alloys. *Acta Metallurgica*, vol. 24, 1975, p. 59–63. ⟶ cited p. 12

[NER 15] Nervo L. – Characterisation of the deformation mechanisms in HCP metals by combined use of X-ray imaging and diffraction techniques. PhD thesis, The University of Manchester, United Kingdom, 2015. ⟶ cited p. 115, 117

[NEW 83] Newman J. – A nonlinear fracture mechanics approach to the growth of small cracks. In Behavior of Short Cracks in Airframe Components. *Neuilly sur Seine (France): Advisory Group for Aerospace Research and Development. Proceedings*, vol. 328, 1983, p. 6.1-20. ⟶ cited p. 26

[NIK 15] Nikitin A. – La Fatigue Gigacyclique d'un alliage de Titane. PhD thesis, Université Paris Ouest Nanterre La Defense, France, 2015. ⟶ cited p. 11, 12, 23, 77

[NIK 16a] Nikitin A., Palin-Luc T., Shanyavskiy A. – Crack initiation in VHCF regime on forged titanium alloy under tensile and torsion loading modes. *International Journal of Fatigue*, vol. 93 Part 2, 2016, p. 318–325. ⟶ cited p. 11, 12

[NIK 16b] Nikitin A., Palin-Luc T., Shanyavskiy A., Bathias C. – Comparison of crack paths in a forged and extruded aeronautical titanium alloy loaded in torsion in the gigacycle fatigue regime. *Engineering Fracture Mechanics*, vol. 167, 2016, p. 259–272. ⟶ cited p. 1

[OBE 11] Oberwinkler B. – Modeling the fatigue crack growth behavior of Ti-6Al-4V by considering grain size and stress ratio. *Materials Science and Engineering: A*, vol. 528, n° 18, 2011, p. 5983–5992. ⟶ cited p. 18

[OGU 04] Oguma H., Nakamura T. – The Effect of Stress Ratios on Very High Cycle Fatigue Properties of Ti-6Al-4V. *Key Engineering Materials*, vol. 261-263, 2004, p. 1227–1232. ⟶ cited p. 77, 171

[OGU 10] Oguma H., Nakamura T. – The effect of microstructure on very high cycle fatigue properties in Ti–6Al–4V. *Scripta Materialia*, vol. 63, n° 1, 2010, p. 32–34. ⟶ cited p. 12

[OGU 13] Oguma H., Nakamura T. – Fatigue crack propagation properties of Ti–6Al–4V in vacuum environments. *International Journal of Fatigue*, vol. 50, 2013, p. 89–93. ⟶ cited p. 18, 20, 23, 25, 85, 96, 100, 105, 125, 141, 171

[OLI 07] Oliveira P. C. G., Adabo G. L., Ribeiro R. F., Rocha S. S. d., Ávila F. A., Valle A. L. d. – Influence of the final temperature of investment healting on the tensile strength and Vickers hardness of CP Ti and Ti-6Al-4V alloy. *Journal of Applied Oral Science*, vol. 15, n° 1, 2007, p. 44–48. ⟶ cited p. 41

[OUA 18] Ouarabi M. O. – Influence de la fréquence de chargement sur la résistance à l'amorçage et la croissance des fissures de fatigue dans des aciers utilisés pour des applications mécaniques exigeantes. PhD thesis, Université Paris Nanterre, France, 2018. ⟶ cited p. 9, 50, 52, 54, 57

[PAL 10] Palin-Luc T., Pérez-Mora R., Bathias C., Domínguez G., Paris P. C., Arana J. L. – Fatigue crack initiation and growth on a steel in the very high cycle regime with sea water corrosion. *Engineering Fracture Mechanics*, , 2010, Page 11. ⟶ cited p. 9

[PAN 20] Pan X., Qian G., Wu S., Fu Y., Hong Y. – Internal crack characteristics in very-high-cycle fatigue of a gradient structured titanium alloy. *Scientific Reports*, vol. 10, n° 1, 2020, Page 4742. ⟶ cited p. 22

[PAR 63] Paris P., Erdogan F. – A Critical Analysis of Crack Propagation Laws. *Journal of Basic Engineering*, vol. 85, n° 4, 1963, p. 528–533. ⟶ cited p. 16

[PEA 75] Pearson S. – Initiation of fatigue cracks in commercial aluminium alloys and the subsequent propagation of very short cracks. *Engineering Fracture Mechanics*, vol. 7, n° 2, 1975, p. 235–247. ⟶ cited p. 16

[PEL 69] Pelloux R. – Mechanisms of formation of ductile fatigue striations. *Transactions of the American Society for Metals*, vol. 62, 1969, p. 281-5. ⟶ cited p. 26

[PER 10] Perez Mora R. – Study of the fatigue strength in the gigacycle regime of metallic alloys used in aeronautics and off-shore off shore industries. PhD thesis, École Nationale Supérieure d'Arts et Métiers ParisTech, France, 2010. ⟶ cited p. 50, 52, 57

[PER 15] Perez-Mora R., Palin-Luc T., Bathias C., C. Paris P. – Very high cycle fatigue of a high strength steel under sea water corrosion: A strong corrosion and mechanical damage coupling. *International Journal of Fatigue*, vol. 74, 2015, p. 156–165. ⟶ cited p. 9

[PET 01] Peters J. O., Lutjering G. – Comparison of the Fatigue and Fracture of $\alpha + \beta$ and β Titanium Alloys. *Metallurgical and Materials Transactions A*, , 2001, Page 14. ⟶ cited p. 124, 125, 126, 171

[PET 03] Petit J., Hénaff G., Sarrazin-Baudoux C. – Environmentally Assisted Fatigue in the Gaseous Atmosphere. *Comprehensive Structural Integrity – Chapter 6*, p. 211–280 Elsevier, 2003. ⟶ cited p. 19, 20, 33

[PET 06] Petit J., Sarrazin-Baudoux C. – An overview on the influence of the atmosphere environment on ultra-high-cycle fatigue and ultra-slow fatigue crack propagation. *International Journal of Fatigue*, vol. 28, n° 11, 2006, p. 1471–1478. ⟶ cited p. 8, 18, 20, 22

[PET 07] Petit J., Sarrazin-Baudoux C., Martinez J., Stanzl-Tschegg S., Mayer H. – Very High Cycle Fatigue Behavior of a Ti6246 Alloy in Air and in High Vacuum. *Fourth International Conference on Very High Cycle Fatigue (VHCF-4)*, , 2007. ⟶ cited p. 18, 19, 21

[PET 10] Petit J., Sarrazin-Baudoux C. – Some critical aspects of low rate fatigue crack propagation in metallic materials. *International Journal of Fatigue*, vol. 32, n° 6, 2010, p. 962–970. ⟶ cited p. 16

[PIL 09] Pilchak A., Bhattacharjee A., Rosenberger A., Williams J. – Low ΔK faceted crack growth in titanium alloys. *International Journal of Fatigue*, vol. 31, n° 5, 2009, p. 989–994. ⟶ cited p. 107

[PIL 10] Pilchak A. L., Williams J. C. – Observations of Facet Formation in Near-α Titanium and Comments on the Role of Hydrogen:. *Metallurgical and Materials Transactions A*, vol. 42A, 2010, p. 1000–1027. ⟶ cited p. 86, 90

[PIL 13] Pilchak A. L. – Fatigue crack growth rates in alpha titanium: Faceted vs. striation growth. *Scripta Materialia*, vol. 68, n° 5, 2013, p. 277–280. ⟶ cited p. 26, 112

[PIP 83] Pippan R., Stüwe H. P. – Thermische Bestimmung der plastischen Deformation um die Rißfront eines Ermüdungsbruches. *International Journal of Materials Research*, vol. 74, n° 11, 1983, p. 699–704. ⟶ cited p. 27, 134

[PIP 17] Pippan R., Hohenwarter A. – Fatigue crack closure: a review of the physical phenomena: Fatigue Crack Closure. *Fatigue & Fracture of Engineering Materials & Structures*, vol. 40, n° 4, 2017, p. 471–495. ⟶ cited p. 15, 18

[RAN 08] Ranc N., Wagner D., Paris P. – Study of thermal effects associated with crack propagation during very high cycle fatigue tests. *Acta Materialia*, vol. 56, n° 15, 2008, p. 4012–4021. ⟶ cited p. 27, 28, 29

[RAN 14a] Ranc N., Palin-Luc T., Paris P., Saintier N. – About the effect of plastic dissipation in heat at the crack tip on the stress intensity factor under cyclic loading. *International Journal of Fatigue*, vol. 58, 2014, p. 56–65. ⟶ cited p. 134

[RAN 14b] Ranc N. – Contribution à l'étude du comportement hermomécanique des matériaux solides et des structures. Habilitation à Diriger des Recherches de l'Université Pierre et Marie Curie, France, 2014. ⟶ cited p. 134

[RAN 22] Ranc N., Messager A., Junet A., Palin-Luc T., Buffière J., Saintier N., Elmay M., Mancini L., King A., Nadot Y. – Internal fatigue crack monitoring during ultrasonic fatigue test using temperature measurements and tomography. *Mechanics of Materials*, vol. 174, 2022, Page 104471. ⟶ cited p. 2, 27, 29, 142

[RIC 67a] Rice J. R. – Mechanics of Crack Tip Deformation and Extension by Fatigue. *ASTM STP 415, Am. Soc. Testing Mats*, , 1967, Page 247. ⟶ cited p. 14

[RIC 67b] Rice J. R., Rosengren F. – Plane strain deformation near a crack tip in a power-law hardening material. *J. Mech. Phys. Solids*, vol. 16, 1967, p. 1–12. ⟶ cited p. 27

[ROC 06] Rocha S. S. d., Adabo G. L., Henriques G. E. P., Nóbilo M. A. d. A. – Vickers hardness of cast commercially pure titanium and Ti-6Al-4V alloy submitted to heat treatments. *Brazilian Dental Journal*, vol. 17, n° 2, 2006, p. 126–129. ⟶ cited p. 41

[ROD 02] Rodopoulos C. – Theoretical analysis on the behaviour of short fatigue cracks. *International Journal of Fatigue*, vol. 24, n° 7, 2002, p. 719–724. ⟶ cited p. 16

[RUG 07] Rugg D., Dixon M., Dunne F. P. E. – Effective structural unit size in titanium alloys. *The Journal of Strain Analysis for Engineering Design*, vol. 42, n° 4, 2007, p. 269–279. ⟶ cited p. 116

[SAK 09] Sakai T. – Review and Prospects for Current Studies on Very High Cycle Fatigue of Metallic Materials for Machine Structural Use. *Journal of Solid Mechanics and Materials Engineering*, vol. 3, n° 3, 2009, p. 425–439. ⟶ cited p. 7

[SAK 16] Sakai T., Nakagawa A., Oguma N., Nakamura Y., Ueno A., Kikuchi S., Sakaida A. – A review on fatigue fracture modes of structural metallic materials in very high cycle regime. *International Journal of Fatigue*, vol. 93, 2016, p. 339–351. ⟶ cited p. 8, 96

[SAR 97] Sarrazin-Baudoux C., Lesterlin S., Petit J. – Atmospheric Influence on Fatigue Crack Propagation in Ti Alloys at Elevated Temperature. , 1997. ⟶ cited p. 18

[SAR 16] Sarrazin-Baudoux C., Stanzl-Tschegg S., Schönbauer B., Petit J. – Ultra-slow Fatigue Crack Propagation in Metallic Alloys. *Procedia Engineering*, vol. 160, 2016, p. 151–157. ⟶ cited p. 18, 21, 22, 33

[SCH 78] Schijve J. – Internal Fatigue Cracks Are Growing in Vacuum. *Engineering Fracture Mechanics*, vol. 10, 1978, p. 359-370. ⟶ cited p. 21

[SCH 09] Schijve J. – *Fatigue of structures and materials*. Springer, Dordrecht, second edition édition, 2009. OCLC: 836585646. ⟶ cited p. 1, 12, 14, 17, 18, 23

[SER 17] Serrano-Munoz I., Buffiere J.-Y., Mokso R., Verdu C., Nadot Y. – Location, location & size: defects close to surfaces dominate fatigue crack initiation. *Scientific Reports*, vol. 7, n° 1, 2017, Page 45239. ⟶ cited p. 32, 103

[SHA 23] Shanyavskiy A., Nikitin I., Nikitin A. – The in-service fatigue fracture mechanisms for the I-stage low-pressure compresser disk of the aircraft engine D30KU-154. *Fatigue & Fracture of Engineering Materials & Structures*, vol. 46, n° 2, 2023, p. 728–741. ⟶ cited p. 1

[SIN 07] Sinha V., Mills M. J., Williams J. C. – Determination of crystallographic orientation of dwell-fatigue fracture facets in Ti-6242 alloy. *Journal of Materials Science*, vol. 42, n° 19, 2007, p. 8334–8341. ⟶ cited p. 86, 92, 151

[SIN 12] Sinha V., Larsen J. M. – Vacuum Levels Needed to Simulate Internal Fatigue Crack Growth in Titanium Alloys and Nickel-Base Superalloys: Thermodynamic Considerations. *Metallurgical and Materials Transactions A*, vol. 43, n° 10, 2012, p. 3433–3441. ⟶ cited p. 18, 20

[SMI 98] Smith W., Piascik S. – The Effect of 02, H20, and N 2 on the Fatigue Crack Growth Behavior of an $\alpha + \beta$ Titanium Alloy at 24 °C and 177 °C. *Fatigue Behavior of Titanium Alloys. Chicago, IL: The Minerals, Metals & Materials Society. (TMS Fall Meeting).*, , n° 2, 1998, Page 357–364. ⟶ cited p. 20

[SOR 05] Sorkine O. – Laplacian Mesh Processing. Chrysanthou Y., Magnor M., Eds., *Eurographics 2005 - State of the Art Reports* The Eurographics Association, 2005. ⟶ cited p. 65, 133

[STA 80] Stanzl S., Tschegg E. – Fatigue crack growth and threshold measured at very high frequencies (20 kHz). *Metal Science*, vol. 14, n° 4, 1980, p. 137–143. ⟶ cited p. 9

[STA 06] Stanzl-Tschegg S. – Fatigue crack growth and thresholds at ultrasonic frequencies. *International Journal of Fatigue*, vol. 28, n° 11, 2006, p. 1456–1464. ⟶ cited p. 21, 33, 143

[STA 13] Stanzl-Tschegg S. – Very high cycle fatigue measuring techniques. *International Journal of Fatigue*, vol. 60, 2013, p. 2-17. ⟶ cited p. 9

[SU 17] Su H., Liu X., Sun C., Hong Y. – Nanograin layer formation at crack initiation region for very-high-cycle fatigue of a Ti-6Al-4V alloy: Nanograin Formation for VHCF of TI Alloy. *Fatigue & Fracture of Engineering Materials & Structures*, vol. 40, n° 6, 2017, p. 979–993. ⟶ cited p. 23, 96

[SUG 89] Sugano M., Kanno S., Satake T. – Fatigue behavior of titanium in vacuum. *Acta Metallurgica*, vol. 37, n° 7, 1989, p. 1811–1820. ⟶ cited p. 20, 21

[SUN 23] Sun C., Wu H., Chi W., Wang W., Zhang G.-P. – Nanograin formation and cracking mechanism in Ti alloys under very high cycle fatigue loading. *International Journal of Fatigue*, vol. 167, 2023, Page 107331. ⟶ cited p. 117

[SUR 98] Suresh S. – *Fatigue of materials*. Cambridge University Press, Cambridge ; New York, 2nd ed édition, 1998. ⟶ cited p. 17, 20, 26

[TAD 00] Tada H., Paris P. C., Irwin G. R. – *The stress Analysis of Cracks Handbook, Third Edition*. American Society of Mechanical Engineers Press, 2000. ⟶ cited p. 66, 97, 105

[TAK 08] Takeuchi E., Furuya Y., Nagashima N., Matsuoka S. – The effect of frequency on the giga-cycle fatigue properties of a Ti-6Al-4V alloy. *Fatigue & Fracture of Engineering Materials & Structures*, vol. 31, n° 7, 2008, p. 599–605. ⟶ cited p. 23, 76, 77, 171

[TAY 81] Taylor D., Knott J. F. – Fatigue crack propagation behaviour of short cracks; the effect of microstructure. *Fatigue & Fracture of Engineering Materials and Structures*, vol. 4, n° 2, 1981, p. 147–155. ⟶ cited p. 16

[TER 16] Teranishi M., Kuwazuru O., Gennai S., Kobayashi M., Toda H. – Three-dimensional stress and strain around real shape Si particles in cast aluminum alloy under cyclic loading. *Materials Science and Engineering: A*, vol. 678, 2016, p. 273–285. ⟶ cited p. 32

[THE 90] Themelis G., Chikwembani S., Weertman J. – Determination of the orientation of Cu-Bi grain boundary facets using a photogrammetric technique. *Materials Characterization*, vol. 24, n° 1, 1990, p. 27–40. ⟶ cited p. 92, 151

[THI 19] Thielen M., Schaefer F., Gruenewald P., Laub M., Marx M., Meixner M., Klaus M., Motz C. – In situ synchrotron stress mappings to characterize overload effects in fatigue crack growth. *International Journal of Fatigue*, vol. 121, 2019, p. 155–162. ⟶ cited p. 31

[TOK 92] Tokaji K., Ogawa T. – The growth behaviour of microstructurally small fatigue cracks in metals. *Mechanical Engineering Publications*, vol. ESIS 13, 1992, p. 85–99. ⟶ cited p. 16

[UME 97] Umezawa O., Nagai K. – Subsurface Crack Generation in High-cycle Fatigue for High Strength Alloys. *ISIJ International*, vol. 37, n° 12, 1997, p. 1170–1179. ⟶ cited p. 8

[VAR 11] Varfolomeev I., Luke M., Burdack M. – Effect of specimen geometry on fatigue crack growth rates for the railway axle material EA4T. *Engineering Fracture Mechanics*, vol. 78, n° 5, 2011, p. 742–753. ⟶ cited p. 103

[VEL 07] Velasquez J. D. P. – Etude des copeaux et de l'intégrité de surface en usinage à grande vitesse de l'alliage de titane TA6V. PhD thesis, Université Paul Verlaine - Metz, France, 2007. ⟶ cited p. 41

[VEN 01] Venkatesh T. A., Conner B. P., Suresh S., Giannakopoulos A. E., Lindley T. C., Lee C. S. – An experimental investigation of fretting fatigue in Ti-6Al-4V: the role of contact conditions and microstructure. *Metallurgical and Materials Transactions A*, vol. 32, n° 5, 2001, p. 1131–1146. ⟶ cited p. 41

[WAG 09] Wagner D., Ranc N., Bathias C., Paris P. – Fatigue crack initiation detection by an infrared thermography method. *Fatigue & Fracture of Engineering Materials & Structures*, , 2009. ⟶ cited p. 27, 28, 34, 80, 141, 142

[WAN 75] Wanhill R. J. H. – Fractography of fatigue crack propagation in 2024-T3 and 7075-16 aluminum alloys in air and vacuum. *Metallurgical Transactions A*, vol. 6, n° 8, 1975, Page 1587. ⟶ cited p. 20

[WAN 89] Wanhill R. J. H., Galatolo R., Looije C. E. W. – Fractographic and microstructural analysis of fatigue crack growth in a Ti-.6A1-4V fan disc forging". , 1989, Page 10. ⟶ cited p. 24, 26

[WEC 06] Weck A., Crawford T., Borowiec A., Wilkinson D., Preston J. – Femtosecond laser-based fabrication of a new model material to study fracture. *Applied Physics A*, vol. 86, n° 1, 2006, p. 55–61. ⟶ cited p. 81

[WEI 80] Wei R. P., Pao P. S., Hart R. G., Weir T. W., Simmons G. W. – Fracture mechanics and surface chemistry studies of fatigue crack growth in an aluminum alloy. *Metallurgical Transactions A*, vol. 11, n° 1, 1980, p. 151–158. ⟶ cited p. 126

[WEI 81] Wei R. P., Simmons G. W. – Recent progress in understanding environment assisted fatigue crack growth. *International Journal of Fracture*, vol. 17, n° 2, 1981, p. 235–247. ⟶ cited p. 20, 33

[WEL 94] Welsch G., Boyer R., Collings E. W., Eds. *Materials properties handbook: titanium alloys*. ASM International, Materials Park, OH, 1994. ⟶ cited p. 11

[WIL 11] Williams J. J., Yazzie K. E., Connor Phillips N., Chawla N., Xiao X., De Carlo F., Iyyer N., Kittur M. – On the Correlation Between Fatigue Striation Spacing and Crack Growth Rate: A Three-Dimensional (3-D) X-ray Synchrotron Tomography Study. *Metallurgical and Materials Transactions A*, vol. 42, n° 13, 2011, p. 3845–3848. ⟶ cited p. 26, 112

[WU 94] Wu T., Bathias C. – Application of fracture mechanics concepts in ultrasonic fatigue. *Engineering Fracture Mechanics*, vol. 47, n° 5, 1994, p. 683–690. ⟶ cited p. 51

[WU 13] Wu G., Shi C., Sha W., Sha A., Jiang H. – Effect of microstructure on the fatigue properties of Ti–6Al–4V titanium alloys. *Materials & Design*, vol. 46, 2013, p. 668–674. ⟶ cited p. 11, 18

[WU 17] Wu S., Xiao T., Withers P. – The imaging of failure in structural materials by synchrotron radiation X-ray microtomography. *Engineering Fracture Mechanics*, vol. 182, 2017, p. 127–156. ⟶ cited p. 31, 32

[WU 21] Wu Z., Kou H., Chen N., Zhang Z., Qiang F., Fan J., Tang B., Li J. – Microstructural influences on the high cycle fatigue life dispersion and damage mechanism in a metastable β titanium alloy. *Journal of Materials Science & Technology*, vol. 70, 2021, p. 12–23. ⟶ cited p. 12

[XU 18] Xu L., Wang Q., Zhou M. – Micro-crack initiation and propagation in a high strength aluminum alloy during very high cycle fatigue. *Materials Science and Engineering: A*, vol. 715, 2018, p. 404–413. ⟶ cited p. 80

[XUE 22] Xue G., Tomoda Y., Nakamura T., Fujimura N., Takahashi K., Yoshinaka F., Takeuchi A., Uesugi M., Uesugi K. – Detection of small internal fatigue cracks in Ti-6Al-4V via synchrotron radiation nanocomputed tomography. *Fatigue & Fracture of Engineering Materials & Structures*, , 2022, p. 1-10. ⟶ cited p. 32, 141

[YOD 82] Yoder G. R., Cooley L. A., Crooker T. W. – On microstructural control of near-threshold fatigue crack growth in 7000-series aluminum alloys. , 1982. ⟶ cited p. 16

[YOS 16a] Yoshinaka F., Nakamura T., Nakayama S., Shiozawa D., Nakai Y., Uesugi K. – Non-destructive observation of internal fatigue crack growth in Ti–6Al–4V by using synchrotron radiation µCT imaging. *International Journal of Fatigue*, vol. 93, 2016, p. 397–405. ⟶ cited p. 1, 2, 31, 32, 99, 103, 141

[YOS 16b] Yoshinaka F., Nakamura T., Takaku K. – Effects of vacuum environment on small fatigue crack propagation in Ti–6Al–4V. *International Journal of Fatigue*, vol. 91, 2016, p. 29–38. ⟶ cited p. 19, 20, 21, 100, 125, 126, 127, 171

[YOS 19] Yoshinaka F., Nakamura T., Takeuchi A., Uesugi M., Uesugi K. – Initiation and growth behaviour of small internal fatigue cracks in Ti-6Al-4V via synchrotron radiation microcomputed tomography. *Fatigue & Fracture of Engineering Materials & Structures*, vol. 42, 2019, Page 2093–2105. ⟶ cited p. 81, 97, 100, 125, 171

[YOS 21] Yoshinaka F., Xue G., Fujimura N., Nakamura T. – Effect of vacuum pressure on small crack propagation in Ti-6Al-4V. *International Journal of Fatigue*, vol. 142, 2021, Page 105961. ⟶ cited p. 23, 25, 26, 34, 108, 112

[ZCR21] Z-cracks - 3D fracture mechanics simulation - 2020. http://zset-software.com/wordpress/wp-content/uploads/manuals/zcracks_tutorial.pdf, consulted Aug. 29th 2021. ⟶ cited p. 65, 66, 131, 157

[ZHA 98] Zhang J. Z., Halliday M. D., Bowen P. – High resolution *in situ* SEM observations of early stages of fatigue crack growth in IN 9052 aluminium alloy. *Materials Science and Technology*, vol. 14, n° 3, 1998, p. 193–200. ⟶ cited p. 20

[ZHA 02] Zhang X. P., Wang C. H., Ye L., Mai Y. W. – *In situ* investigation of small fatigue crack growth in poly-crystal and single-crystal aluminium alloys: fatigue crack growth in poly- and single-crystal Al alloys. *Fatigue & Fracture of Engineering Materials & Structures*, vol. 25, n° 2, 2002, p. 141–150. ⟶ cited p. 16

[ZHA 12] Zhao A., Xie J., Sun C., Lei Z., Hong Y. – Effects of strength level and loading frequency on very-high-cycle fatigue behavior for a bearing steel. *International Journal of Fatigue*, vol. 38, 2012, p. 46–56. ⟶ cited p. 24

[ZIM 12] Zimmermann M. – Diversity of damage evolution during cyclic loading at very high numbers of cycles. *International Materials Reviews*, vol. 57, n° 2, 2012, p. 73–91. ⟶ cited p. 25

[ZUO 08] Zuo J., Wang Z., Han E. – Effect of microstructure on ultra-high cycle fatigue behavior of Ti–6Al–4V. *Materials Science and Engineering: A*, vol. 473, n° 1-2, 2008, p. 147–152. ⟶ cited p. 8, 11, 12, 76, 77, 171

FOLIO ADMINISTRATIF

THÈSE DE L'INSA LYON, MEMBRE DE L'UNIVERSITÉ DE LYON

NOM : Hébrard

DATE de SOUTENANCE : le 21 décembre 2023

Prénom : Louis

TITRE : Study on the effect of the environment on internal fatigue crack propagation in Ti-6Al-4V

NATURE : Doctorat Numéro d'ordre : 2023ISAL0120

École doctorale : ED n°34 - Matériaux de Lyon Spécialité : Matériaux

RÉSUMÉ :

In the Very High Cycle Fatigue regime (fatigue lives longer than 10^7 cycles), fatigue cracks tend to initiate internally. This makes visual detection impossible during maintenance operations. Consequently, engineers need robust fatigue datasets to prevent such internal crack initiations that may lead to the fracture of a critical part. To obtain such data, in-situ experimental techniques are developed. In particular, micro-computed tomography allows to acquire direct images of internal fatigue cracks. In this study, a combination of in-situ micro-tomography and ultrasonic fatigue cycling has been applied to specimens that contain an internal sharp notch to study the propagation of internal fatigue cracks. More precisely, the crack shape of internal fatigue cracks has been monitored in 3D at different instants of their propagation up to the Very High Cycle Fatigue regime.

Some internal notches have been linked to the specimen surface given access to the ambient atmosphere. This was done to study the influence of the environment on internal fatigue cracks. This experimental procedure allowed to acquire for the first time, in-situ observations of internal fatigue cracks propagating with and without air in a Ti64 alloy. Temperature measurements were also carried out to evaluate the effect of the environment on the plasticity at the crack tip. Finally, the fatigue data obtained at ultrasonic frequencies allowed to evaluate the influence of the cycling frequency on the crack growth rates.

MOTS-CLÉS: Internal fatigue cracks propagation, Very High Cycle Fatigue, Micro-tomography, In-situ monitoring, Environment effect, Ti-6Al-4V, Artificial notching, Temperature field measurements.

Laboratoire de recherche :
MatéIS - UMR CNRS 5510 - INSA de Lyon
25 avenue Jean Capelle
69621 Villeurbanne Cedex (FRANCE)

Directeurs de thèse : Jean-Yves Buffiere (Professeur des Universités) , Thierry Palin-Luc (Professeur des Universités) et Nicolas Ranc (Professeur des Universités)

Présidente du jury : Véronique Aubin (Professeure des Universités)

Composition du jury : Nathalie Limodin (Directrice de Recherche, Rapporteuse)
Jonathan Cormier (Maître de Conférences - HDR, Rapporteur)
Charles Mareau (Maitre de Conférences, Examinateur)
Cédric Doudard (Professeur - HDR, Examinateur)